Studies of the Protein Interaction Network Required for Enterobactin Biosynthesis in *Escherichia coli*

Sofia Khalil

A Thesis

In the Department

of

Chemistry and Biochemistry

Presented in Partial Fulfillment of the Requirements for

the Degree of Doctor of Philosophy
at

Concordia University

Montreal, Quebec, Canada

December 2010

CONCORDIA UNIVERSITY

SCHOOL OF GRADUATE STUDIES

This is to certify that the thesis prepared

By: **Sofia Khalil**

Entitled: **Studies of the Protein Interaction Network Required for Enterobactin Biosynthesis in *Escherichia coli***

and submitted in partial fulfillment of the requirements for the degree of

DOCTOR OF PHILOSOPHY (Chemistry)

complies with the regulations of the University and meets the accepted standards with respect to originality and quality.

Signed by the final examining committee:

_____ Chair
Dr. A. Sen

_____ External Examiner
Dr. M. Mourez

_____ External to Program
Dr. R. Storms

_____ Examiner
Dr. J. Turnbull

_____ Examiner
Dr. A. English

_____ Thesis Supervisor
Dr. P. Pawelek

Approved by _____
Dr. H. Muchall, Graduate Program Director

December 16, 2010 _____
Dr. B. Lewis, Dean
Faculty of Arts and Science

Abstract

Studies of the Protein Interaction Network Required for Enterobactin Biosynthesis in *Escherichia coli*

Sofia Khalil, Ph.D.
Concordia University, 2010

Siderophores are small-molecule iron chelators that many bacteria synthesize and secrete in order to survive in iron-depleted environments. In *Escherichia coli*, biosynthesis of the siderophore molecule enterobactin requires the activities of six enzymes, EntA-EntF. These enzymes function sequentially to produce enterobactin molecule in the cytoplasm. The enterobactin biosynthesis pathway is divided into two modules. The first module involves the conversion of chorismate to 2,3-dihydroxybenzoic acid (2,3-DHB), and requires the activities of EntC, EntB (N-terminal domain) and EntA. The second module involves non-ribosomal peptide synthesis (NRPS) such that three molecules of 2,3-DHB are condensed with three molecules of L-serine to form the siderophore. The NRPS module requires the activities of EntE, EntB (C-terminal domain), EntD and EntF.

The overall goal of my research project is characterization of the enterobactin biosynthetic enzyme EntE. EntE catalyzes the activation of 2,3-DHB *via* adenylation producing DHB-AMP. I am interested in addressing the following questions: (i) How does EntE bind its 2,3-DHB substrate? (ii) How does it interact with its upstream and downstream partner proteins: EntA, which produces 2,3-DHB, and EntB, which uses the EntE product (DHB-AMP) as a substrate, respectively? My thesis is divided into three research-related chapters:

The first research chapter focused on the interaction of EntE with its substrate, 2,3-DHB, as well as the characterization of EntE-EntB interaction in the presence and absence of 2,3-DHB. A significant change in EntB conformation was observed upon the interaction with EntE when in the presence of 2,3-DHB. In the pull-down assay, EntB as bait protein pulled down more EntE in the presence of exogenous 2,3-DHB. We conclude from this chapter that the ligand-loaded state of the protein was necessary for efficient protein-protein interaction.

The second research chapter involves the characterization of a novel interaction between EntE and its upstream partner protein EntA. A significant increase in EntE activity was observed upon adding EntA. Furthermore, EntA reduces the FRET signal of EntE-bound 2,3-DHB in a saturable manner with increasing EntA concentrations. Using this fluorescence binding assay at 20 °C revealed a positive cooperativity in EntA-EntE interaction with Hill coefficient greater than one. The AUC experiments showed that EntA conformation is highly dependent on its concentration. In conclusion, the results of this chapter suggest that EntA-EntE interaction likely induces remodeling of EntE active site, resulting in the observed increase in EntE catalysis.

In the third research chapter, the EntA-EntE interaction interface was characterized using phage display. Based on the interaction interface predicted by phage display data, EntA variants containing single-site and double-site mutations were created (Q64A, A68Q, and Q64A/A68Q). Our *in vitro* biophysical techniques and growth phenotype experiments revealed that EntA (Q64A) and EntA (Q64A/A68Q) mutations have a more pronounced effect than EntA (A68Q) mutation on disruption of the EntA-EntE interaction interface.

Dedication

This thesis is dedicated to my parents, my husband, and my daughters who provided me with unconditional love and support during the course of this thesis.

Acknowledgements

I would like to express my sincere gratitude to my supervisor Dr. Peter D. Pawelek for his guidance, continued encouragement, and invaluable suggestions during the course of this work. His enthusiasm, inspiration, and detailed discussion to explain things are greatly appreciated.

I am also grateful for the contribution of my committee members, Dr. Joanne L. Turnbull and Dr. Ann English through their useful suggestions and encouragement. Special thanks go to "Dr. Joanne" who really advanced my knowledge by teaching me the biophysical techniques through Chem. 692.

I wish to acknowledge Dr. Judith Kornblatt and Dr. Jack Kornblatt for their invaluable inputs and useful discussions. Special thanks go to Dr. Jack Kornblatt for his kindly help in the ITC experiments.

I am forever grateful to all the professors in the Biochemistry department, Faculty of Science, Alexandria University, Egypt. They really enriched my knowledge in the "biochemistry basics" which helped me to continue my Ph.D. studies at Concordia University.

I am deeply and forever indebted to my beloved parents who have been a constant source of a never-ending support, love, and encouragement throughout my entire life. I want to thank in particular my husband, Samy, his encouragement, help, and patience made my thesis work possible. Finally, loving thanks go to my beloved girls Sarah and Monica who bring smiles to my life.

Contributions of Other Authors to This Work

Dr. Peter D. Pawelek generated EntE homology model. He also assisted me in the ITC and AUC experiments.

Table of Contents

List of Figures

CHAPTER ONE:

CHAPTER TWO:

List of Schemes

CHAPTER THREE:

CHAPTER FIVE:

List of Tables

CHAPTER TWO:

CHAPTER THREE:

CHAPTER FOUR:

APPENDIX:

List of Abbreviations

AMP	adenosine monophosphate
ArCP	aryl carrier protein
ATP	adenosine triphosphate
AUC	analytical ultracentrifugation
BSA	Bovine serum albumin
^{o}C	Celsius
CD	circular dichroism
2,3-DHB	2,3-dihydroxybenzoic acid
DNA	deoxyribonucleic acid
DTT	dithiothreitol
FRET	fluorescence resonance energy transfer
Hepes	(4-(2-hydroxyethyl)-1-piperazineethanesulfonic acid)
ICL	isochorismate lyase
IMAC	immobilized metal affinity chromatography
IPTG	isopropyl β-D-1-thiogalactopyranoside
ITC	isothermal titration calorimetry
LB	Luria broth
LC-MS/MS	liquid chromatography tandem mass spectrometry
NAD^{+}	nicotinamide adenine dinucleotide (oxidized form)
NADH	nicotinamide adenine dinucleotide (reduced form)
NADPH	nicotinamide adenine dinucleotide phosphate (reduced form)

NRPS	non-ribosomal peptide synthesis
rpm	revolutions per minute
SDS-PAGE	sodium dodecyl sulfate polyacrylamide gel electrophoresis
Sulfo-SMCC	sulfo-succinimidyl 4-[N-maleimidomethyl]cyclohexane-1-carboxylate
TBS	tris buffered saline
TCEP	tris(2-carboxyethyl)phosphine hydrochloride
Tris	tris(hydroxymethyl)aminomethane
TTBS	tris buffered saline containing 0.05% Tween 20

Statement of the Problem and Significance

In most bacterial pathogens, low levels of intracellular iron act as a signal to upregulate the expression of bacterial iron acquisition genes. The products of these genes are believed to contribute to the survival of the pathogenic bacteria inside the host and hence the pathogenesis of infection. Therefore bacterial proteins expressed under iron-limited conditions may be used as essential immuno- or chemotherapeutic targets.

Enterobactin, an *E. coli* chatecholate siderophore, is a low-molecular-weight iron chelating agent. The activities of six enzymes (EntA-EntF) are required for enterobactin biosynthesis in the *E. coli* cytoplasm. The enterobactin biosynthesis pathway is composed of two functional modules. The first module is the DHB biosynthetic module in which chorismate is converted into 2,3-DHB. This module involves the activities of EntC, EntB (N-terminal domain), and EntA. The second module involves non-ribosomal peptide synthesis (NRPS) which is comprised of the activities of EntE, EntB (C-terminal domain), EntF, and EntD. In the NRPS module, three molecules each of 2,3-DHB and L-serine residues are condensed to form enterobactin. This thesis focuses on the enterobactin biosynthetic enzymes EntA, EntE, and EntB which catalyze sequential reactions. EntA catalyzes the formation of 2,3-DHB which is then used as a substrate for EntE. EntE catalyzes the activation of 2,3-DHB in the form of 2,3-DHB-AMP which acts as a substrate for EntB.

Relatively little has been reported on the characteristics of these enzymes, and we are still far from comprehensively understanding how these enzymes work together in the same pathway. **An important unresolved question: to what extent are the activities of these enzymes coordinated through protein-protein interactions?** Such a network of

protein interactions may facilitate the direct channeling of enzymatic intermediates between sequentially related activities and increase efficiency of enterobactin biosynthesis under the iron-starved condition inside the host. In depth analysis of these enzymes and characterization of their interactions will enrich and advance our knowledge of the enzymology and molecular mechanisms of this pathway. Understanding of the molecular basis and the thermodynamics of complexes formation between those enzymes are extremely significant. Furthermore, identification of the interaction interfaces between the enzymes studied in this thesis will be crucial to design novel antimicrobial drugs.

All of these studies will guide us to better understand how pathogenic bacteria are able to use catecholate siderophores as virulence factors to accomplish their pathogenic effect inside the host. Recently, it has been reported that the mammalian cells synthesize a siderophore that plays an essential role in intracellular iron homeostasis (*1*). This siderophore uses 2,5-DHB in iron chelation instead of 2,3-DHB in *E. coli* enterobactin. BDH2, the EntA homologue, is responsible for the synthesis of 2,5-DHB. Thus mammalian homologues of *E. coli* EntA and EntE have been discovered for the first time. Our studies on the enterobactin enzymes will further shed light on the activities of the mammalian homologous enzymes and the possible interaction network between them during the mammalian siderophore biosynthesis.

CHAPTER ONE: GENERAL INTRODUCTION

1.1 Iron Chemistry and Availability

Iron is an important nutrient for most microorganisms due to its participation in many biological processes, including enzyme catalysis, electron transport, and DNA synthesis (*2*). Iron has two predominant charged ionic forms (Fe^{2+} and Fe^{3+}). Thus iron functions as a major cofactor in many processes. Under aerobic conditions at pH 7, iron is predominantly in the ferric form (*3*). Ferric ions have high affinity for hydroxyl ions, resulting in formation of insoluble ferric hydroxide ($Fe(OH)_3$) ions which have solubility constant less than 10^{-38} M (*4-5*). For this reason, the free ferric ions concentration in solution is 1.4×10^{-9} M (*6*). Most of iron in the living cell is complexed with proteins, making the free iron concentration (approximately 10^{-24} M) in the serum insufficient to support microbial growth (*2, 4, 7-9*). Consequently, most pathogens develop different strategies to obtain iron inside the host.

Unavailability of iron in host organisms has one more advantage in addition to limitation of microbial life. The very low iron concentration under physiological conditions protects the living cells from oxidation effects. This is because ferrous irons can react with superoxide and hydrogen peroxide, which are generated by many processes giving rise to reactive oxygen species (ROS) *via* the Fenton reaction (*10-11*). In this reaction, the hydrogen peroxide reacts with ferrous ions, producing very reactive hydroxyl radical. Then the oxidized iron (Fe^{3+}) is reduced by the cellular reducing component such as superoxide. The whole cycle is called Haber Weiss reaction (Figure 1 (*6*)). These ROS can cause harmful damage in the cell, including oxidative damage to DNA, membranes, and other cellular biomolecules (*12-13*). It has also been reported that iron accumulation leads to oxidative stress in many neurodegenerative diseases (*14-15*).

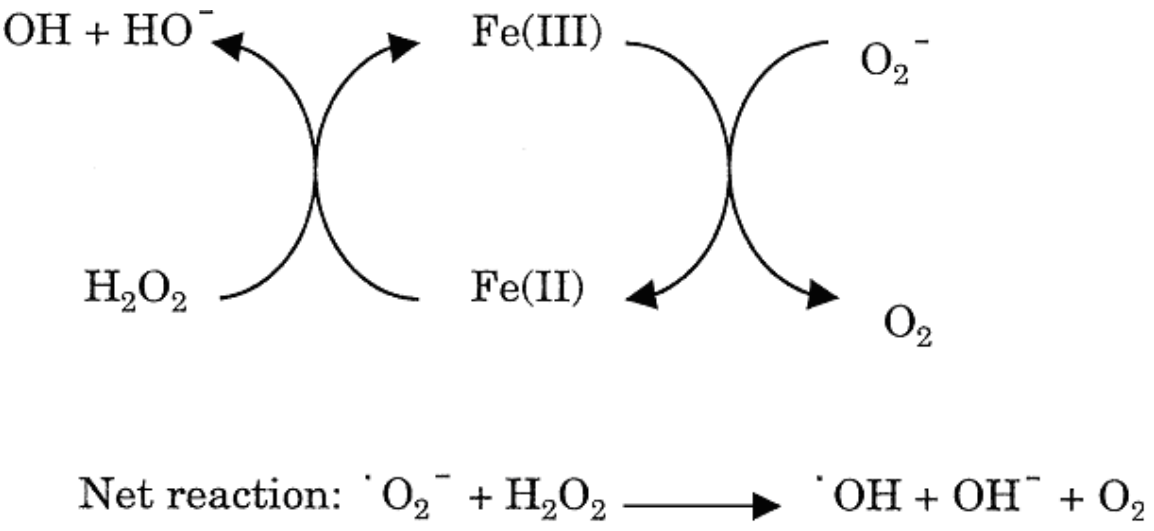

Figure 1: Haber Weiss cycle.

(Figure from Ratledge *et al* (*6*))

The superoxide radicals are provided by some reactions such as nitric oxide synthetases reactions.

1.2 Iron-Containing Proteins Used by Microorganisms

Iron is toxic to cell due its contribution to free radicals generation *via* Fenton reaction. Hence organisms have developed set of protective mechanisms to regulate iron homeostasis.

1.2.1 Extracellular Iron-Binding Proteins: Transferrins and Lactoferrin

In the mammalian cells, ferric iron is bound to extracellular iron binding glycoproteins called transferrin (Tf) and lactoferrin (Lf). Transferrin found in the serum while lactoferrin is found in extracellular fluid. Tf is usually partially saturated by iron so it has a protective role in addition to its iron delivery role (*16*). The protection role of Tf results from its ability to bind any iron released in the serum. Lf is one of the innate immune system that has a protective role in case of infections (*17*). Tf and Lf have

similar structures. Briefly, they have molecular weights of approximately 80 kDa and have two similar iron binding sites with binding constants approximately of 10^{20} M^{-1} for Fe^{+3} and 10^{3} M^{-1} for Fe^{2+} (*18*).

1.2.2 Intracellular Iron-Binding Protein: Ferritin

Ferritin is an intracellular iron storage protein that is present in most organsims. Ferritin stores and releases iron according to the cell need in a highly regulated way. Thus it plays an important role in iron homeostasis. Ferritin is found also in plants (phytoferritin) and in microorganisms (bacterioferritin) (*19*-*20*). Ferritins have similar structures except that bacterioferritins have attached heme (*21*). Ferritins are constructed of 24 protein subunits (each subunit ~ 20 kDa) with a central cavity that is capable of binding about 4500 ferric ions (*22*). In a mammalian cell, these subunits are divided into two types, the light (L) and the heavy (H) type. All native ferritins have the ability to oxidize Fe^{+2} and to store it as Fe^{+3}. Such catalytic centers present only in the H-type chain (*23*). In humans, ferritin holds approximately 30% of the iron pool (*24*).

1.3 Heme-Containing Proteins Used by Microorganisms

Heme is used as a prosthetic group in many enzymes. Plants and animals also have many heme-containing proteins, including myoglobin, catalase, and type b cytochrome. Heme is required by some bacteria that can not synthesize the tetrapyrole ring, including *Lactococcus lactis* and *Haemophilus influenzae*. Bacteria require heme in nanomolar levels in contrast iron which is required in micromolar levels (*25*).

1.3.1 Hemopexin

Inside the host, free heme is poisonous because its hydrophobicity leads to its partitioning in membranes. Hemopexin is a plasma heme binding glycoprotein which has a protective role via its binding with high affinity to any heme released into plasma with $K_D \sim 10^{-13}$ M (*26*). Heme-hemopexin binding protein "HxuA" has been identified in *Haemophilus influenzae (27)*. Here, HxuA mutant is deficient in using Heme-hemopexin as a source of iron. The heme-hemopexin-HxuA complex is recognized by an outer membrane receptor HxuC (*28*).

1.3.2 Hemoglobin

Hemoglobin acts as an oxygen transporter in red blood cells. It is composed of two α- and two β- subunits. Each subunit is tightly bound to a heme group that contains a penta-coordinated iron (*25*). Five iron binding sites are offered by the four nitrogen atoms in the porphyrin ring and the imidazole of one histidine residue from the protein. Hemoglobin can be classified based on the sixth coordination position into: (i) methemoglobin when the sixth coordination site is free, (ii) oxyhemoglobin when the sixth coordination site is occupied by oxygen, (iii) carboxyhemoglobin when the sixth coordination site is filled up by carbon dioxide (*25, 29*). In human, hemoglobin holds about two-thirds of the total iron in the body (*24*).

1.3.3 Hemoglobin- Haptoglobin

Haptoglobin is a glycoprotein located in the serum. Haptoglobin consists of two H chains joined by two smaller L chains. It has a protective role *via* its interaction with any hemoglobin released by hemolysis in the serum and thereby inhibits its oxidative activity

(30). This complex is irreversible and can be only separated after removal by the liver. The hemoglobin-haptoglobin complex provides iron for many bacteria, including *Haemophilus influenzae* type b and *Neisseria meningitidis* (31-32). Studies revealed that the TonB-dependent outer membrane receptor, HpuAB, utilizes hemoglobin- haptoglobin as an iron source in *N. meningitides* (33-34).

1.4 Iron and Heme Uptake Systems

As mentioned previously, iron is tightly bound to proteins in which it plays an essential role in overall structure or function. At the same time, there are many proteins that bind iron, heme, or hemoglobin to ensure removal of free iron or these iron-containing compounds from the circulation. Such clearance is a protective mechanism against the oxidative activity of iron or these iron-containing compounds as explained previously. This strict iron homeostasis results in free iron concentration in the serum of about 10^{-24} M (*35*). Hence the poor availability of iron at physiological pH under aerobic conditions is a serious obstacle to the growth of most microorganisms. Many microorganisms have developed direct and indirect mechanisms to scavenge iron or iron-containing heme under low-iron conditions.

However, some members of *Lactobacilli* can live without iron (*36*). These bacteria do not contain heme compounds and they use the cobalt – containing vitamin B12 form of ribonucleotide reductase (RNR) (*37*). RNR is required for biosynthesis of deoxyribonucleotides. RNR is classified into three classes. Class I is aerobic non haem-iron dependent RNR (in bacteria and eukaryotes) (*38*), class II is adenosylcobalamin-dependent RNR (in *Lactobacillus leichmannii*) (*39*), and class III is anaerobic iron-sulfur

dependent RNR (in bacteria and eukaryotes) (*38*). *E. coli* has class I and class III RNR systems, so it can adapt to aerobic and nonaerobic environments (*40*).

1.4.1 Direct Iron and Heme Uptake System

Direct uptake strategies involve direct contact between bacteria and iron or heme sources. The drawback of these strategies is that bacteria need specific receptors for each iron or heme source. In the direct iron uptake systems, bacteria have different mechanisms to release iron or heme upon binding of iron or heme sources by their receptors at the bacterial surface.

Direct Uptake of Iron

Bacteria could extract iron upon contact with the host iron source by direct removal of iron by its reduction and uptake (*6*). Anaerobes can get iron by creating their own environment by acidification of the environment inside the host cells, resulting in reduction of Fe^{3+} iron bound transferrin and lactoferrin causing release of Fe^{2+} iron (*41*). Facultative anaerobes *E. coli* and *S. typhimurium* have Feo uptake system for soluble ferrous ions (*42-43*). The Feo system is composed of three proteins, FeoA, FeoB, and FeoC. FeoB is an inner membrane protein but FeoA and FeoC are cytoplasmic proteins. Fe^{2+} uptake from the periplasm is accomplished by FeoB, probably with the assistance of FeoA and FeoC (*44*). It has also been reported that TbpA protein, TonB-dependent outer membrane receptor, serves as a channel to transport ferric iron after its release from Tf (*45*)**.** In *Mannheimia haemolytica*, a periplasmic Fe^{3+}-binding protein called FbpA mediates the transport of released ferric iron from Tf to the inner cytoplasmic membrane complex FbpB/C (*46*). This study demonstrated that FbpA adopts two conformations,

carbonate anion bound FbpA (closed conformation) and anion unbound FbpA (opened conformation). The closed conformation has higher affinity for ferric iron than the open conformation, indicating the important role of anion binding in iron uptake and release by FbpA.

Direct Uptake of Heme

The high affinity between heme and its heme-binding proteins rules out the possibity that bacteria can extract the heme molecules from these proteins by equilibrium displacement with the bacterial outer membrane receptors (*25*). It has been reported that heme could be released after hemoprotein degradation by surface proteinases in some microorganisms, such as RgpA and Kgp in *Porphyromonas gingivalis* (*47*). After heme release in the periplasm, heme will be transported to cytoplasm by the periplasmic-binding protein-dependent transport (PBT) system (*6*). Inside the cytoplasm, heme can be incorporated directly into enzymes or the iron can be removed by the porphyrin ring degredation (*48-49*).

1.4.2 Indirect Iron and Heme Uptake Systems

Indirect iron uptake systems are more common among microorganisms. In such systems, microorganisms synthesize and secrete iron-chelating molecules (siderophores) or heme-chelating proteins (hemophores) to scavenge iron and heme from various sources.

Indirect Heme Uptake System: Hemophores

Many bacteria pathogens have the ability to use heme as an iron source, including *V. cholerae, Shigella dysenteriae*, enterohemorrhagic *E. coli* O157:H7, and *H. influenzae*

(*41, 50-53*). The indirect heme uptake mechanism to scavenge heme from host heme sources involves secretion of soluble proteins called hemophores to interact with hemoproteins and bring heme to specific TonB dependent outer membrane receptors on the cell surface. HasA/HasR is a heme acquisition system identified in many pathogenic bacteria such as *Serratia marcescens*, and *P. aeruginosa (25)*. HasA is a heme-binding protein (hemophore) that binds free heme or pulls out heme from hemoglobin and transfers it to the outer membrane receptor HasR. HasA was purified as monomeric protein of 19 kDa that binds one heme with high affinity without conformational alteration (*54*). HasR is a TonB-dependent receptor that binds heme or HasA-heme complex (*55*).

Indirect Iron Uptake System: Siderophores

Under iron limiting conditions, most microorganisms synthesize and secrete small iron-chelating molecules called siderophores (from the Greek term for "iron carrying"). Siderophore-dependent iron uptake strategies are widely distributed among microorganisms. The number of different siderophores produced by bacteria, yeasts, and fungi is more than 500 (*56-58*). Siderophores are low molecular weight compounds, less than 1 kDa in size (*24*). Siderophores are characterized by their high affinity for Fe^{3+} and generally their stability constant for formation complex with Fe^{3+} ranges from 10^{25} to 10^{50} M^{-1} (*57*). This high affinity is enough to allow siderophore to extract iron from Tf and Lf (*59*). Ferric-siderophores are then transported into bacteria *via* specific active transport systems. In the bacterial cytoplasm, iron is used by iron-containing proteins or stored in heme-containing bacterioferritin (*22*). In many pathogenic microbes,

siderophore-mediated iron uptake systems are considered as important virulence factors (*60*).

1.5 Regulation of Iron Metabolism in Microorganisms

The first regulatory mechanism involves ferric uptake repressor (Fur) or diphtheria toxin repressor (DtxR). Fur and DtxR are metalloproteins that bind Fe^{2+}. In Gram-negative bacteria, the iron metabolism genes are regulated by Fur (*61*). Iron uptake genes are negatively regulated by Fur when iron is available within the bacteria. Under this iron sufficient condition, Fur is activated *via* its binding to Fe^{2+}. Active Fe^{2+}-Fur complex binds to the Fur box consensus sequence, located near or within the promoter of the gene to be regulated, resulting in repression the expression of Fur-regulated genes (such as genes involved in siderophore biosynthesis and secretion). Fe^{2+}-Fur complex also up regulates the translation of some of the iron-using proteins indirectly *via* inhibition of *RyhB* gene expression (Figure 2). RyhB is a small RNA that binds to the mRNAs of some of the iron-utilizing proteins and promotes their degradation (*62*). In contrast, under iron-limiting conditions, iron will dissociate from Fur, causing Fur inactivation and its release from the Fur box. This leads to upregulation of iron uptake genes expression in order to obtain iron from extracellular environment, and down regulation of the iron-using proteins mRNAs translation that are regulated by RyhB.

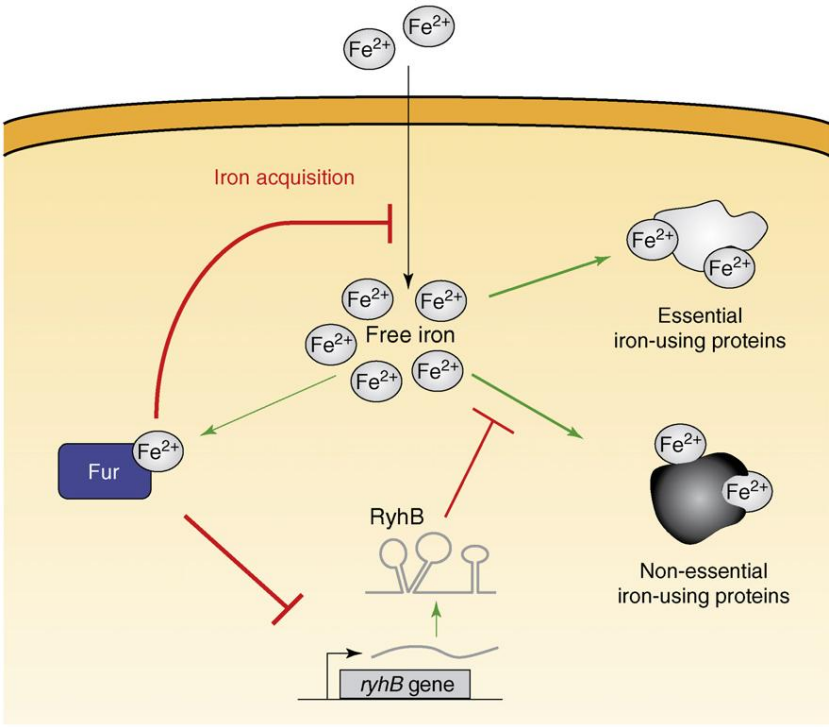

Figure 2: Iron metabolism regulation by Fur and RyhB.

(Figure from Salvail *et al* (*62*))

Under iron-limiting condition, Fe^{2+} will break up from Fe^{2+}-Fur complex, resulting in Fur inactivation. This will allow induction of the iron acquisition genes and the ryhB gene expression. Then Fe^{2+} will be taken from the extracellular environment by one or more iron acquisition mechanisms. Concomitantly, RyhB will inhibit the synthesis of the non-essential iron-containing proteins, ensuring the best use of Fe^{2+} by the essential iron-containing proteins. Once Fe^{2+} will be available in the cytoplasm, Fe^{2+} will be used by iron using proteins. Concurrently, Fe^{2+} will bind Fur, resulting in Fur activation. Then active Fe^{2+}-Fur complex will inhibit the expression of the iron acquisition genes and the ryhB gene.

Gram-positive bacteria produce proteins similar to Fur in order to regulate the iron uptake system. DtxR (diphtheria toxin repressor) was recognized as a repressor that binds iron as corepressor in *Corynebacterium diphtheriae* (*63*). DtxR-like proteins have been found in other Gram-positive bacteria such as and *S. epidermidis* (*64*) and

Brevibacterium lactofermentum (*65*). There are structural similarities between Fur and DtxR proteins in the domain organization and metal binding site (*66-67*). They are composed of DNA binding domain and metal binding domain. The metal binding domain contains two binding site for Zn^{+2} and Fe^{2+}. It was shown that Zn^{2+} binding to Fur has an essential role in stabilizing the protein quaternary structure (*66, 68*).

The second mechanism of regulation of bacterial iron metabolism is extra cytoplasmic function (ECF) sigma factors. This mechanism is commonly found in Gram-negative bacteria. Sigma factors are essential components that are able to bind RNA polymerase and DNA in order to stimulate transcription (*69*). Sigma factors are cytoplasmic proteins that can be sequestered by cytoplasmic membrane proteins (anti-sigma factors). However, some anti-sigma factors are cytoplasmic proteins and some sigma factors do not have anti-sigma factors. Generally, when an external ligand binds to an outer membrane receptor, the signal is transferred to a cytoplasmic membrane protein, resulting in degradation of the anti-sigma membrane proteins by inner membrane proteases. The released sigma factor then binds to RNA polymerase in order to stimulate the transcription of target genes (*69*). This mechanism is well characterized in the *E. coli* ferric citrate uptake system (*70*). In most bacteria, hemophore outer membrane receptors are regulated by Fur. HasR regulation involves ECF sigma and antisigma factors (*71*).

The third regulatory mechanism involves AraC-like transcriptional regulators. AraC-like proteins are located in the cytoplasm. They have DNA binding domain and Fe-siderophore binding domains (*24*). PchR, an AraC-type regulator, has been identified in *Pseudomonas aeruginosa (72).* PchR functions as activator for the pyochelin biosynthetic gene cluster *pchDCBA* and iron uptake gene expression. PchR requires

ferric-pyochelin to exert its action, suggesting that ferric-pyochelin acts as intratracellular effector that triggers the PchR-mediated activation.

1.6 Siderophores

1.6.1 Thermodynamics of Iron Binding by Siderophores

As mentioned previously, siderophores bind iron (Fe^{3+}) selectively with high affinity in order to compete with other iron chelators. In this part we will give more insight into the thermodynamics of iron-binding by siderophores.

Fe^{3+} is catagorized as a hard Lewis acid due to its high charge-to-radius ratio (*73*). Therefore, Fe^{3+} ions bind with high affinity to hard donor atoms (Lewis base) such as oxygen and amine nitrogen atoms. In contrast, Fe^{2+} ions have low charge-to-radius, making its capacity to form stable complex with siderophores quite low. Fe^{3+} forms octahedral complex ($Fe(H_2O)_6^{3+}$) in aqueous solution (*44*). Siderophore donor atoms replace the solvent water molecules and bind Fe^{3+} *via* strong ionic interactions in a hexadentate coordination that results in octahedral geometry. The stoichiometry of iron-siderophore complexes can be 1:1 if the siderophore provides six donor atoms. If the siderophore has less than 6 donor atoms, the water oxygen atoms will participate as donors or more than one siderophore will be involved in the chelation process. For example, pyochelin forms FeL and FeL_2 complexes (L is used here to indicate a siderophore molecule) (*74*).

In aqueous solution, both H^+ and Fe^{3+} compete for siderophore binding. Thus, the proton participation must be involved during the calculation of the Fe-siderophore complex formation constant (K_f) (*59*). The stability constant of Fe-siderophore complex formation is represented by β_{mlh} for the reaction "$mM + lL + hH = M_mL_lH_h$", where M is

metal, L is ligand, and H is proton (*24*). The catecholate siderophore enterobactin has a log β_{mlh} of 49 (*75, 76*). Another scale used to measure the stability of the Fe-siderophore complex is the pFe scale. The pFe value is -log $[Fe^{3+}]_{free}$ at fixed Fe^{3+}, ligand, and H^{+} concentrations. At pH 7.4, pFe values of enterobactin and aerobactin are 35.5 and 23.4, respectively (*24*).

The pKa values of the siderophore donor atoms also affect Fe-siderophore complex formation. The pKa values of the hydrogen removal from the catecholate siderophores hydroxyl groups are: from 6.5 to 8 for the first hydrogen and around 11.5 for the second hydrogen (*24*). The pKa values of hydroxamate siderophores range from 8 to 9 and those of carboxylate range from 3.5 to 5 (*24*). Thus, pH potentially plays a role in the ferric chelation process by siderophores. For this reason, microbes such as fungi inhabit acidic environments in which carboxylate siderophores are favored while enterobactin is a more effective iron-chelator in higher-pH environments (*77*).

1.6.2 Siderophores Structures

As explained previously, Fe^{3+} is hard Lewis acid and needs a hard donor atom to ensure strong interaction. Microbes take advantage of this property by incorporating iron-chelating molecules with catecholate, amine, hydroxamic acid, and α-hydroxycarboxylic acid binding moieties (Figure 3). These siderophores bind Fe^{3+} in hexadentate manner. Siderophores could be composed of one type of the chelating group, such as the tris-catecholate siderophore enterobactin and the tris-hydroxamate siderophore desferrioxamine (Figure 4). Alternatively, some siderophores are known as mixed siderophores because they have constructed of more than one type of the iron chelating groups (Figure 4). This type of siderophores includes the mixed citrate-hydroxamate

siderophore (aerobactin) that is produced by many pathogenic bacteria (*78-79*) and the mixed citrate-catecholate siderophore (petrobactin) that is produced by *Bacillus anthracis* (*24*, *80*). Hydroxamate donor groups are common in fungal siderophores such as ferrichrome (*81*).

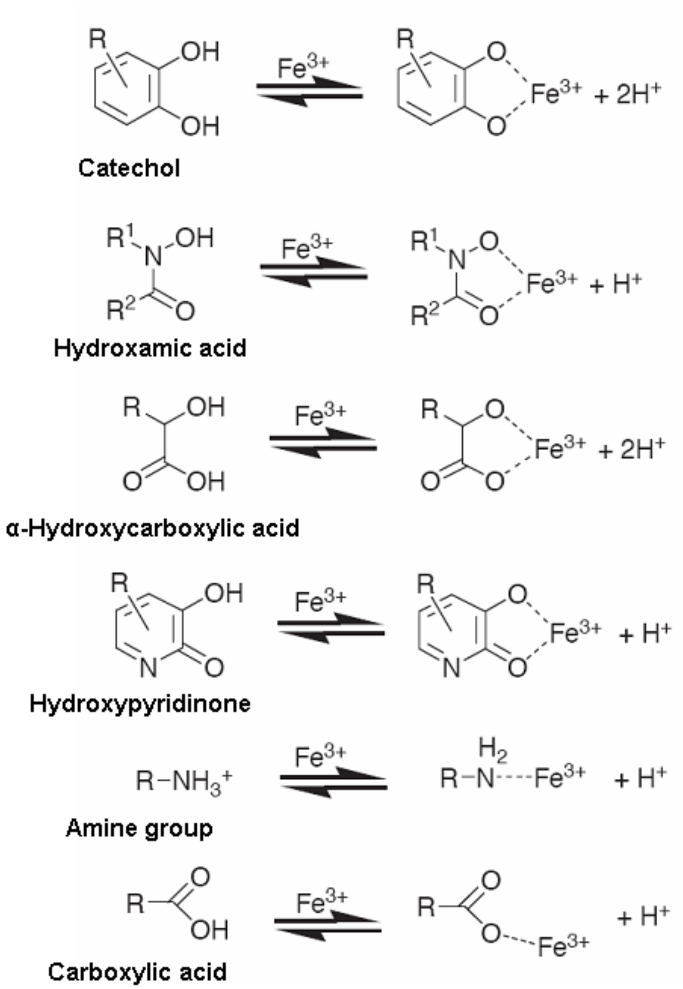

Figure 3: Chemical iron-binding groups used by microorganisms to build siderophores.

(Figure adapted from (*59*))

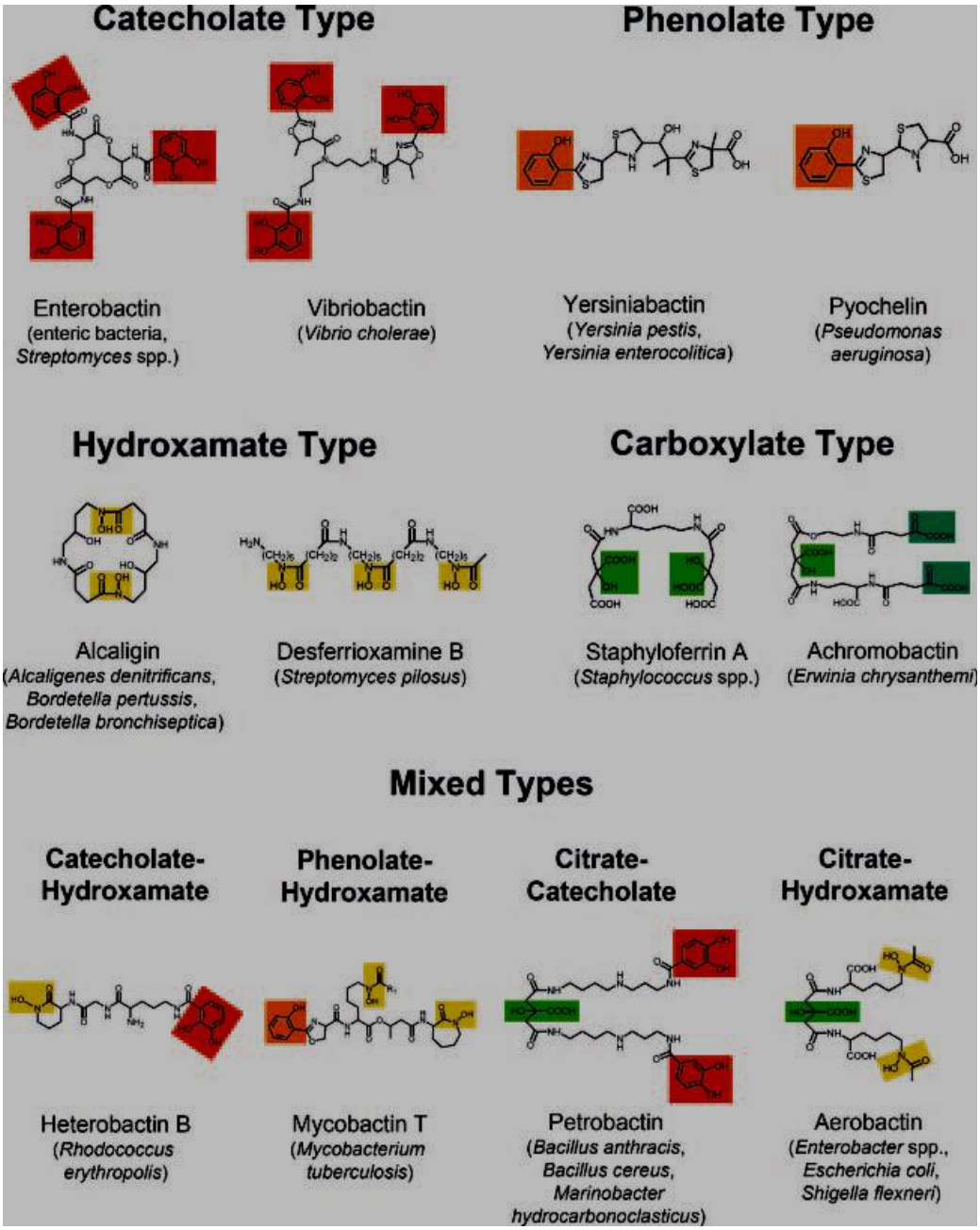

Figure 4: Chemical structure of some natural siderophores.

(Figure from Miethke *et al* (*24*))

Iron-binding groups are colored: catecholates (red), phenolate (orange,), hydroxymate (yellow), α-hydroxy-carboxylates (green), α-keto-carboxylates (blue-green).

1.6.3 Siderophores Biosynthesis

Non-Ribosomal Peptide Synthesis (NRPS) Processes

Large multienzyme complexes called non-ribosomal peptide synthetases (NRPS) are involved in biosynthesis of many siderophores (*24, 82-83*). NRPS enzymes catalyze amino acid activation and assemble siderophore backbones using specialized domains that will be explained later. NRPS mechanisms are used in the synthesis of aryl-capped siderophores which have been identified in many pathogenic bacteria, including enterobactin in *E. coli*, *Shigella* spp., and *Salmonella enterica*; mycobactin in *M. tuberculosis*; pyochelin and pyoverdin in *P. aeruginosa*; yersiniabactin in *Yersinia* spp.; vibrobactin in *V. cholerae* (*82*). Therefore, NRPS in those pathogens is the focus of much research and the target for the development of new chemotherapeutic drugs.

At the beginning of NRPS biosynthesis of aryl-capped siderophores, the aryl acids 2,3-dihydroxybenzoate (DHB) or salicylate (i.e., the aryl caps), are synthesized. These are then used as precursors for condensation with certain amino acids, resulting in production of aryl-capped siderophores. The enzymes that catalyze aryl acid synthesis are regulated by Fur in Gram-negative bacteria (*82*). NRPS assembly lines that condense aryl acids with amino acids work by a multiple-thiol templating process (*84*). An NRPS assembly line is composed of multiple domains that work together to catalyze aryl acid precursor activation, chain elongation, and finally chain termination (*82-83*). Furthermore NRPS can be composed of extra domains which catalyze substrate modification such as N-methylation (M), N-formylation (F), or heterocyclization (Cy) of peptidic backbones (*85*).

Each NRPS system is constructed of multiple domains (Figure 5) (*86*) (i) adenylation (A) domains for the selection and activation of the aryl acid and amino acid as acyl-AMP conjugate; (ii) peptidyl carrier proteins (PCP) domains that covalently tether the activated amino acid or carboxylic acid to their thiol groups of their phosphopantetheinyl arms; (iii) condensation (C) domains that are located downstream of PCP and catalyze chain elongation and forming peptide bond between the activated aryl acid and the activated amino acid. Each C domain has an upstream PCP domain as substrate donor and a proximal downstream PCP domain that is bound to the attacking substrate acceptor; (iv) thioesterase (TE) domain that is responsible for chain termination and release of siderophore. The release of the siderophore by the TE domain could be *via* intermolecular hydrolysis to release free acid or intramolecular cyclization to release a cyclic lactone (e.g., enterobactin).

Many antibiotics are also synthesized by NRPS assembly lines *via* thiotemplate mechanism, resulting in synthesis of effective antibiotics (*87*). This mechanism is different from the synthesis of the peptide backbone in the proteins using mRNAs, tRNAs, and ribosomes as explained previously. Examples of antibiotics synthesized by NRPS include daptomycin (*88*) and penicillin (*89*). Some microbes are able to use their NRPS machinery to synthesize nature products that have antimicrobial, antitumor, or immunosuppressive activities. These products are considered as extremely important source for many pharmaceutical agents (*90*). A deeper understanding of the proteins involved in the NRPS will help in modulation of their activities through the use of small molecule inhibitors that can act as chemotherapeutic agents.

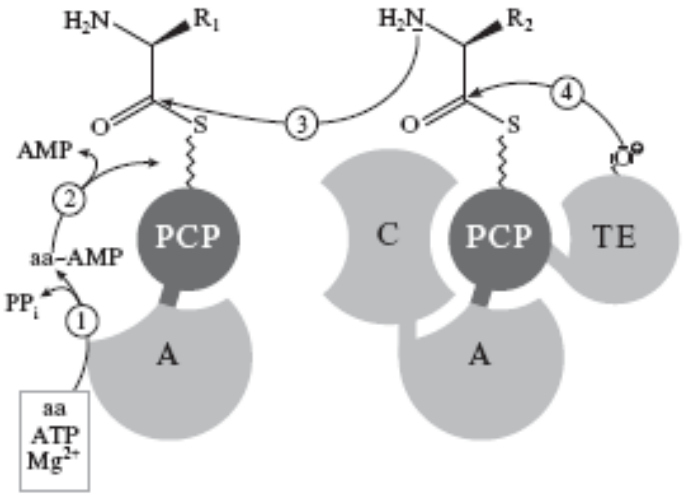

Figure 5: Mechanism of nonribosomal peptide elongation and termination.

(Figure from Marahiel *et al* (*86*))

1: Activation the substrate (e.g., amino acids) via A domain, 2: The activated substrate is transferred to PCP domain and bound to its phosphopantetheinyl group, 3: C domain catalyzes the formation of peptide bond between activated substrate bound to upstream PCP (as donor) and the activated substrate bound to the downstream PCP (as acceptor), and 4: TE domain catalyzes the termination and release of the nonribosomal peptide.

NRPS- Independent Siderophore Biosynthesis

Many siderophores are not polypeptides and are therefore assembled *via* non-ribosomal peptide synthetases-independent mechanisms (*83, 91*). Most hydroxamate and carboxylate siderophores are constructed by NRPS-independent mechanisms. Many enzymes are involved in this mechanism, including ac(et)yltransferases, monoxygenases, aminotransferases, and amino acid ligases (*91*). Aerobactin biosynthesis was the first described NRPS-independent pathway (*91-92*). Siderophores synthesized by NRPS-independent machinery are widely produced by many pathogenic bacteria, including petrobactin produced by *B. anthracis* (*93-94*), alcaligin produced by *B. pertussis* and *B. bronchiseptica* (*95*), and aerobactin produced by *Aerobacter aerogenes* (*96*).

Hybrid NRPS/NRPS-Independent Pathway

Hybrid NRPS/NRPS-independent mechanism can be involved in the biosynthesis of some siderophores such as petrobactin (*97*). Petrobactin is mixed citrate-catecholate siderophore made by *B. anthracis* (*94, 98*). Petrobactin is composed of two catecholate ligands and an α-hydroxycarboxylate ligand for ferric iron chelation. The *B. anthracis asbABCDEF* gene cluster is responsible for petrobactin biosynthesis as reviewed by Barry S. M. and Challis G. L. (*99*).

1.6.4 Siderophore Transport Systems

Siderophore Export Systems

There are three types of transport systems are identified in the siderophore export from the cytoplasm.

(i) **ATP-binding cassette (ABC) transporters** are a large family of transporters that are invoved in both import and export systems (figure 6) (*100-101*). Thus these transporters are considered as one of the important targets for development of antibiotics (*102*). They are composed of two transmembrane domains and two cytoplasmic domains as reviewed by Miethke and Marahiel (*24*). The cytoplasmic domains have the nucleoside triphosphate binding sites (such as ATP). The hydrolysis of the nucleoside triphosphate energizes the transport process. IroC is an example of ABC transporters that transports salmochelin, a glucosylated enterobactin produced by pathogenic *Salmonella* and *E. coli* strains, from the cytoplasm to the periplasm (*103*).

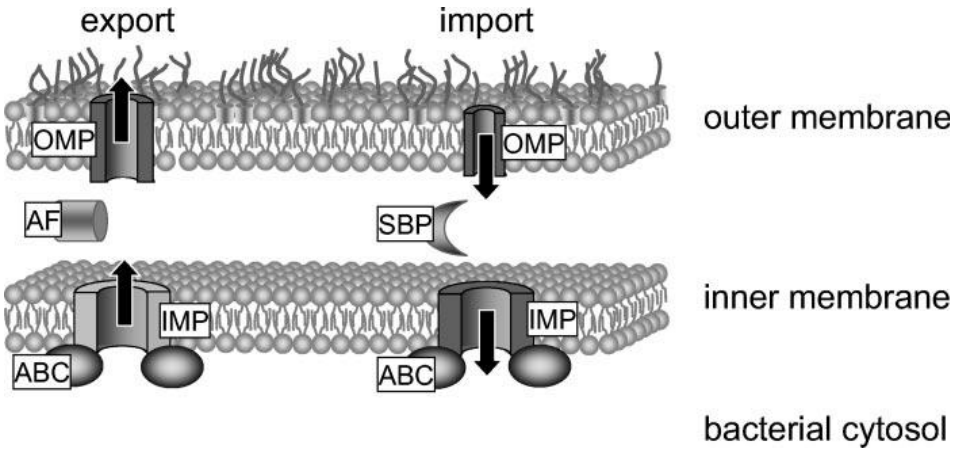

Figure 6: ABC-transport system diagram.

(Figure from Garmory and Titball (*102*))

OMP: outer membrane protein, IMP: inner membrane protein, SBP: solute periplasmic binding protein, and AF: accessory factor that mediates the transport across the periplasm.

(ii) **Resistance, nodulation, and cell division superfamily** (**RND**). This superfamily of transporters is responsible for the export of many compounds. Most of this family uses a transport mechanism that involves a proton antiport system (*104*). The RND transporters are large proteins that are composed of various extracytoplasmic and transmembranne domains (*24*). One of the RND transporters is the AcrB- AcrA-TolC system that mediates the transport of large number of compounds into *E. coli* (*105*). AcrB is an RND transporter across the inner cytoplasmic membrane, AcrA is a membrane fusion protein (MFP), and TolC is an outer membrane chamnel that is mediate the transport across the outer membrane.

(iii) **The major facilitator superfamily** (**MFS**). The MFS superfamily is one of the essential transporter families. The transport by this family involves different mechanisms such as solute/cation symport, solute/cation antiport, or solute uniport (*106*). This family is involved in the export of various compounds such as drugs, siderophores,

and some metabolites (*106*). This family of transporters is constructed of 12, 14, or 24 α-helical transmembrane regions as reviewed by Miethke and Marahiel (*24*). One of the examples of the MFS family involved in siderophore efflux is EntS, which is responsible for enterobactin secretion under iron-limited conditions and it is Fur- regulated (*107*). EntS will be discussed in more detail later in this chapter.

Siderophore Import Systems

Many outer membranes receptors for different ferrisiderophores have been identified, including FhuA for ferrichrome (*108*) and FepA for Fe-enterobactin (*109*) in *E. coli*. Generally, they are composed of a 22-β-strand barrel (C-terminal residues~ 600) and about 150 residues that comprise an N-terminal folded globular domain inside the barrel that form a "plug" domain (*110*). Transport through the receptor is energized by TonB complex. This complex is comprised of three inner membrane proteins (TonB, ExbB, and ExbD) (Figure 7). In this complex TonB interacts with the with the inner cytoplasmic membrane proteins ExbB and ExbD *via* its N-terminal domain (*111*) and interacts with the ferrisiderophore outer membrane receptor *via* its C-terminal domain such as is seen in its interaction with FhuA (*112*). The energy is transferred from the proton motive force energy transduction system (TonB complex) to the outer membrane receptor in order to mediate ferrisiderophore transport into the periplasm. Then an ABC-type transporter mediates the ferrisiderophore complex passage throught the bacterial inner membrane.

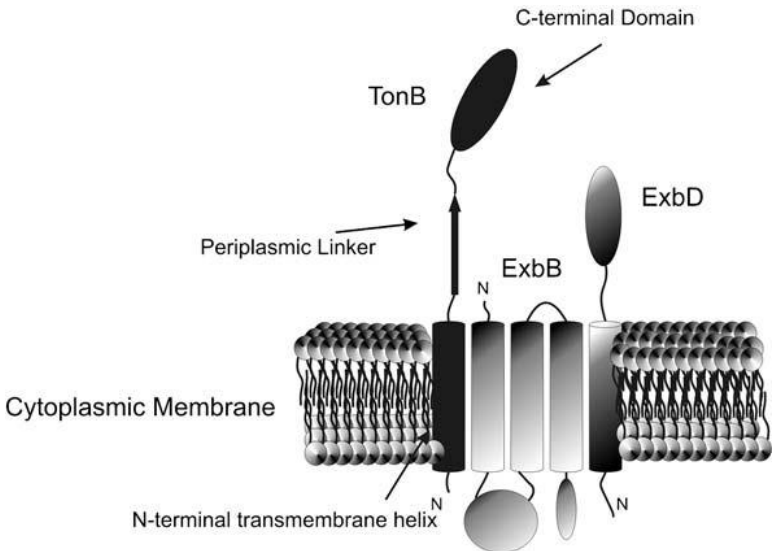

Figure 7: TonB-ExbB-ExbD complex.

(Figure from Chu *et al* (*113*))

TonB is composed of three domains: N-terminal transmembrane domain that interacts with ExbB-ExbD, periplasmic linker domain, and C-terminal domain that interacts with TonB-dependent outer membrane receptor.

1.6.5 Liberation of Iron from Ferric-siderophore Complexes

There are two mechanisms involved in iron release from siderophores in bacteria. Many bacteria have ferri-siderophore ferri-reductases such as *E. coli* (*114*) and *Bacillis* spp. (*115-116*) . These enzymes use NADH or NADPH as cofactors to reduce Fe^{3+} in the siderophore complex, allowing release of Fe^{2+}. Fe^{2+} has lower charge-to-radius ratio than Fe^{3+}. This leads to a decrease in the affinity between Fe^{2+} and the donor atoms in the siderophores which involve in the iron chelation (*44*, *117-118*). Fe^{2+} ions are delivered to the iron-containing molecules (porphyrin, iron-containing proteins, and iron storage proteins).

The second mechanism is the intracellular hydrolysis of siderophores to release iron. In *E. coli*, ferric enterobactin esterase (Fes) catalyzes enterobactin hydrolysis into

2,3-hydrozybenzoylserine (DHBS) moieties. This results in decrease in the chelation affinity and iron release. *E. coli* Fes was purified as monomer with a molecular weight 43 kDa (*119*). It hydrolyzes both free enterobactin and ferric-enterobactin, displaying a 4-fold higher activity with free enterobactin and similar activities toward ferric-enterobactin and aluminum (III)-enterobactin complex hydrolysis (*119*).

1.7 Iron Metabolism Inhibition

One of the essential needs of pathogenic microbes in host cells is iron. Because the free iron concentration inside the host is not enough to support microbial life as we discussed previously, most microbes synthesize and secrete siderophores in order to mobilize and extract iron from its source. The molecular mechanisms of these processes provide many targets for antimicrobial drugs to attack siderophore-mediated iron uptake at the transport level or at the biosynthesis level. Some antimicrobial antibiotics are based on using siderophores as mediators to facilitate the transport of the antibiotic compounds into the microbial cell. Such hybrid compounds are called "Trojan Horse" antibiotics.

"Trojan Horse" Antibiotics

Antibiotics are chemically linked with siderophores so that siderophore uptake systems can be exploited as gates to enter the microbial cell. Because these antibiotics use the siderophore as "Trojan Horse" to enter the cell they are called "Trojan Horse" antibiotics (*120*). Upon entry to the cell, antibiotic moiety is then cleaved from the siderophore in order to be active and to exert its effect. Siderophore antibiotic drugs can be constructed using a semisynthetic method with naturally occurring siderophores, or using a total synthesis method for the whole compound (siderophores and antibiotics)

(*120*). One example of a semisynthesized "Trojan Horse" antibiotic is a β-lactam antibiotic that was linked to pyoverdin from *P. aeruginosa* (*121*).

However, there are also some naturally-produced "Trojan Horse" antibiotics. Microcins is one of the naturally-produced "Trojan Horse" antibiotics that are made by enteric bacteria. MccE492 produced by *K. pneumoniae* is joined to the glucosylated linear enterobactin so it can be recognized by enterobactin and salmochelin outer membrane receptors FepA and IroN, respectively (*122-123*). MccE492 is an antibacterial peptide that induces pore formation in the bacterial membrane (*124*). Another example of the naturally-produced "Trojan Horse" antibiotics is albomycin, made by streptomycetes or actinomycetes. Albomycin is similar to ferrichromes in that it can also be transported by the FhuA outer membrane receptor (*125*). Inside the cell, a serine peptidase catalyzes the release of thioribosyl pyrimidine moiety, a nucleoside analogue, from the siderophore moiety. This nucleoside analogue will then prevent the protein biosynthesis by inhibiting seryl-tRNA synthetases (*126*).

Siderophore Biosynthesis Inhibitors

One of the therapeutic targets against pathogens is the process of siderophore biosynthesis. There are many drugs that are synthesized as inhibitors of siderophores biosynthetic enzymes, and some examples are discussed below.

The first part of the aryl-capped siderophore biosynthesis pathway is the biosynthesis of salicylate or 2,3-dihydroxybenzoate (DHB), which are then activated by adenylation domains using ATP and then used as substrates for the NRPS. Some DHB and salicylate analogue drugs were synthesized to act as inhibitors for DHB and salicylate adenylation domains. A 5'-O-[N-(salicyl)-sulfamoyl] adenosine (SAL-AMS)

blocked the salicylate adenylation domain activities in some microorganisms that use salicylate in siderophore biosynthesis (*127*). In contrast, DhbE, the DHB adenylating domain in bacillibactin biosynthesis, has more of a preference to bind 5'-O-[N-(2,3-dihydroxybenzoyl)-sulfamoyl] adenosine (DHB-AMS) so it exerts a more inhibitory effect than SAL-AMS (*127*). Other substrate analogues have been synthesized in order to inhibit biosynthetic enzymes during siderophore biosynthesis. For example, brominated-enterobactin inhibits IroB, the enzyme that catalyzes C5-glucosylation of enterobactin in most pathogenic *E. coli* species (*128*).

1.8 Enterobactin: the Catecholate Siderophore of *E. coli*

Enterobactin is a cyclic trimer of dihydroxybenzoylserine catecholate siderophore that is produced by all *E. coli* species. Enterobactin was initially discovered in *Salmonella typhimurium* and termed as enterobactin by Pollack and Neiland (*129*), as well as in *E. coli* where it was termed enterochelin by O'Brien and Gibson (*130*). It is composed of three 2,3-DHB subunits such that each subunit forms an amide bond with L-serine, and the three serine residues form the trilactone backbone (enterobactin biosynthesis will be discussed later in more detail). Enterobactin has the highest known binding constant (K_D ~10^{-50} M) for iron compared with other siderophores under physiological conditions (*75*). It binds Fe^{+3} in hexadentate manner *via* its catecholate oxygen atoms (Figure 8).

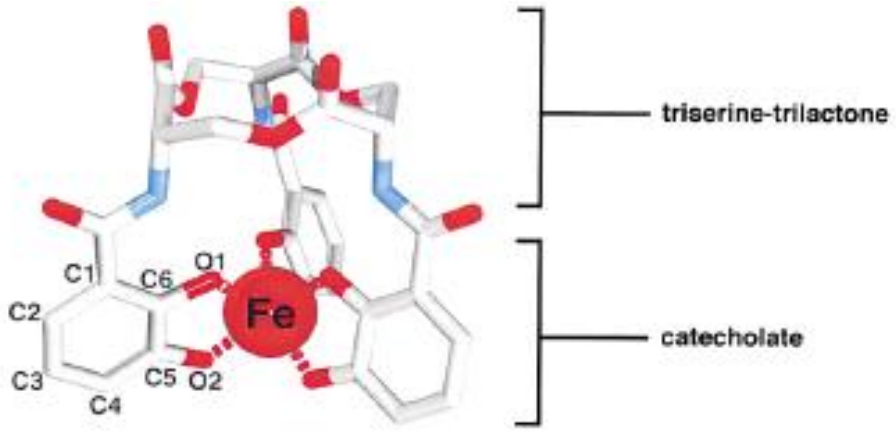

Figure 8: Fe-enterobactin structure.

(Figure from Goetz *et al* (*132*))

Carbon: gray, nitrogen: blue, oxygen: red; iron: red sphere

At the genetic level, enterobactin biosynthetic and transport genes regulated by Fur (*61*). There are six genes (*entA-F*) that encode enterobactin biosynthetic enzymes in *E. coli*. Furthermore, other seven genes (*fepA–G*) encode the proteins involved in ferric-enterobactin uptake and a gene (*entS*) for enterobactin export across the inner cytoplasmic membrane. The enterobactin biosynthetic pathway is broadly divided into two functional modules. In the first module, 2,3-DHB is synthesized from chorismate by sequential reactions catalyzed by EntC, EntB (N-terminal domain), and EntA. In the second functional module (NRPS), enterobactin is constructed from three 2,3-DHB molecules and three L-serine molecules *via* formation of peptide bonds between the 2,3-DHBs and L-serine residues. This module facilitates NRPS by the activities of the sequentially related enzymes EntE, EntD, EntB (C-terminal domain), and EntF. The NRPS reactions are similar to those for peptide antibiotic biosynthesis; here three amide bonds of enterobactin are made non-ribosomally by the protein thiotemplate mechanism

as discussed previously (*131*). After secretion and subsequent iron chelation Fe-enterobactin (Fe-Ent) is transported into the bacterial cell *via* its outer membrane receptor FepA. The TonB-ExbB-ExbD complex is required to transport the Fe-Ent across the bacterial outer membrane. An ABC transporter then transports Fe-Ent into the cytoplasm. In the cytoplasm, a cytoplasmic esterase enzyme (Fes) catalyzes the cytoplasmic breakdown of ferric enterobactin at its triester core in order to release iron for cellular use.

1.8.1 Enterobactin Biosynthesis and Uptake Regulation by Fur

In *E. coli*, iron is involved in many essential biological processes such as respiration, DNA biosynthesis, and amino acid biosynthesis. However the high intracellular free iron concentration can lead to serious problems due to its contribution in the free hydroxyl radical production *via* the Fenton reaction as explained previously. Hence iron metabolism in *E. coli* is highly controlled by Fur (see Section 1.5).

The enterobactin gene cluster is composed of 14 Fur-regulated genes, including six genes for biosynthesis (*entA-F*), seven genes for uptake (*fepA-G*), and *fes* gene, which encodes an esterase that hydrolyzes intracellular ferric-enterobactin to release iron (*82*). The promoter regions of all enterobactin operons contain the Fur box such that under normal conditions in which Fe^{2+} is elevated they are repressed by Fe^{2+}-Fur complex. Another two genes have been identified in enterobactin-dependent bacteria, *ybdA* and *ybdB*. The *ybdA* gene encodes for the cytoplasmic protein EntS that functions to export enterobactin (*107*). The *ybdB* gene encodes for the thioesterase EntH that corrects the misacylation of EntB during enterobactin biosynthesis (*133-134*). The enterobactin gene cluster has been identified in other bacteria, including *Pseudomonas* species, *Salmonella*,

Shigella, and *Klebsiella* (*135-136*). Hence, all of these species have the ability to use enterobactin under condition of iron starvation due to the Fur derepression (*137*).

1.8.2 Enterobactin Biosynthesis

The enterobactin biosynthesis pathway is divided into two modules. In the first module, 2,3-DHB is synthesized from chorismate using the activities of three enzymes EntC, EntB (N-terminal domain), and EntA. Chorismate is the precursor of enterobactin that is converted in the first reaction of the DHB module into isochorismate by the isochorismate synthase, EntC (Figure 9A). Chorismate is also the major precursor of aromatic amino acid biosynthesis (*138*). It is also used as a substrate for isochorismate synthetase (MenF) in menaquinone biosynthesis. *E. coli* has two isochorismate synthases EntC and MenF, which catalyze the same reaction. EntC is required under aerobic and iron-limited conditions whereas MenF is required under anaerobic conditions (*44*).

The second enzyme in the DHB module is isochorismatase, EntB (N-terminal domain). EntB is bifunctional enzyme that functions as an isochorismate lyase *via* its N-terminal domain in the DHB module and as an aryl carrier protein (Ar-CP) *via* its C-terminal domain in the NRPS module (*139*). The EntB N-terminal domain catalyzes hydrolysis of isochorismate into 2,3-dihydro-2,3-dihydroxybenzoate (2,3-diDHB) and pyruvate (Figure 9A). EntA is 2,3-dihydro-2,3-dihydroxybenzoate dehydrogenase that catalyzes the oxidation of EntB N-terminal domain product (2,3-diDHB) into 2,3-dihydroxybenzoate (2,3-DHB) using NAD^+ as cofactor (Figure 9A) (*140*).

In the NRPS module, enterobactin is synthesized from 3 molecules of 2,3-DHB and 3 L-serine residues using the activities of EntE, EntB (C-terminal domain), EntF, and EntD (Figure 9B). EntE is a 2,3-DHB-AMP ligase that catalyzes the first reaction in the

NRPS module. The EntE adenylation (A) domain catalyzes activation of 2,3-DHB (the product of EntA) by adenylation, resulting in the formation of DHB-AMP. EntE also catalyzes the acylation of *holo*-EntB Ar-CP domain by 2,3-DHB (*141*) . EntD is a phosphopantetheine transferase that catalyzes the posttranslational modification of EntB Ar-CP domain and EntF PCP domain to form *holo*-EntB and *holo*-EntF (*131*). This modification activates EntB and EntF to work as aryl and acyl carriers, respectively. The Ar-CP domain name of EntB derived from its function to carry aromatic carboxylic acid while the name of the peptidyl carrier (PCP) domain of EntF is due to its function to hold amino acid.

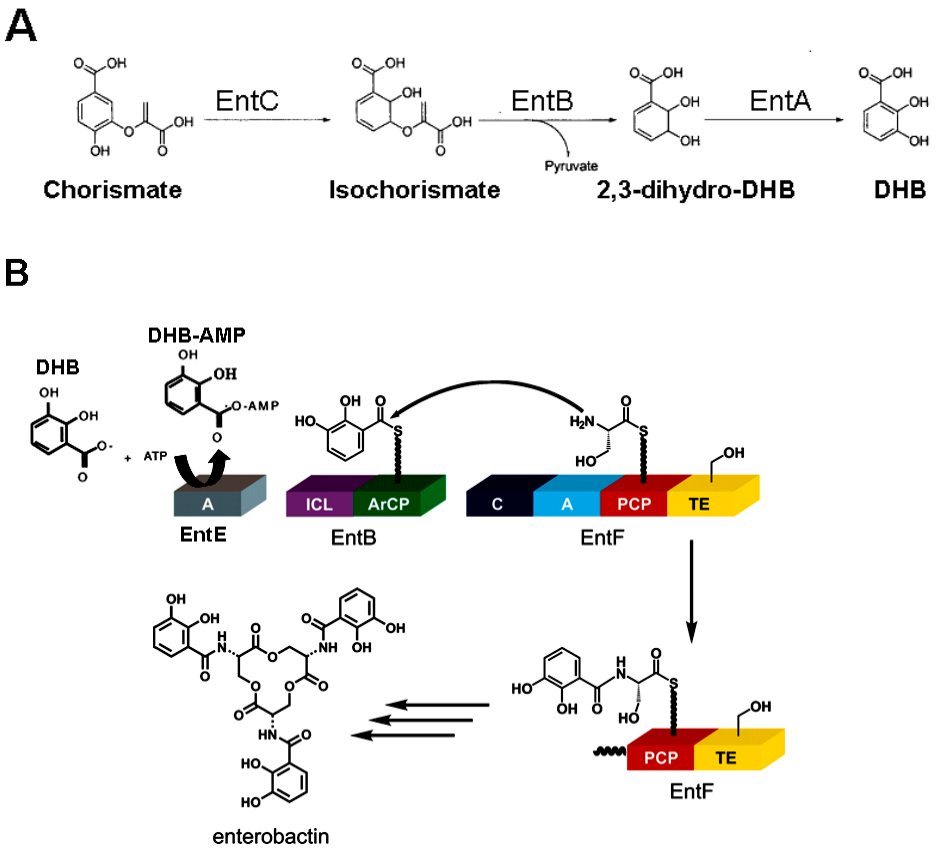

Figure 9: Enterobactin biosynthesis.

A: DHB module (adapted from: (35)) and B: NRPS module (adapted from: (142)).

EntF catalyzes the last reaction in the NRPS module. EntF is composed of four domains (Figure 9B): the adenylation domain (A), the condensation domain (C), the peptidyl carrier protein (PCP) domain, and the thioesterase (TE) domain (*143-144*). In EntF, the A domain adenylates L-serine residues and this is followed by transfer of the activated L-serine residue to the phosphopantetheine group of the PCP domain. The EntF C domain receives 2,3-DHB from *holo*-EntB Ar-CP domain. Then the EntF C domain catalyzes amide bond formation between the 2,3-DHB carboxyl group and the L-serine amino group, forming DHB-Ser-S-PCP in EntF. This is followed by transfer of the 2,3-DHB-Ser (DHBS) moiety from the PCP domain to the TE domain. A second cycle of DHBS synthesis then occurs on the empty EntF C domain. Then the second DHBS is connected to the first DHBS in the TE domain by an ester bond. A third DHBS moiety is synthesized in the empty EntF C-domain and then linked by an ester bond to the second DHBS in the TE domain. At the end of the third cycle, the linear DHBS trimer is cyclized and released from EntF by the TE domain. The NRPS module can be summarized by this equation (*44*):

$$3\ \text{L-Ser} + 3\ \text{DHB} + 6\ \text{ATP} \longrightarrow \text{Enterobactin} + 6\ \text{AMP} + 6\ \text{PPi}$$

EntH is encoded by the Fur-regulated *ybdB* gene. EntH was identified as a thioesterase enzyme that catalyzes the cleaving of any misacylated molecule attached to the phosphopantetheine group of EntB Ar-CP (*133*). This study also showed that an *E. coli* strain lacking *entH* hardly grew under iron-restricted condition in the presence of salicylate, which is a DHB-analogue inhibitor. Salicylate was tethered to the EntB Ar-CP phosphopantetheine group instead of 2,3-DHB causing inhibition of enterobactin biosynthesis.

1.8.3 Enterobactin Secretion

In *E. coli*, a 43 kDa membrane protein was identified and originally called as P43 (*107*). P43 catalyzes the transport of enterobactin across the inner cytoplasmic membrane (Figure 10). This protein belongs to the major facilitator superfamily (MFS) class of membrane proteins which uses the proton motive force to pump the some metabolites through the inner cytoplasmic membrane (*106*). The *ybdA* gene, one of the Fur-regulated enterobactin genes, encodes this transporter. The transporter name was changed to EntS due to its role in enterobactin export as well as the gene ecoded this transporter was changed to *entS* instead of *ybdA* (*107*). EntS mutants have been shown to be defective in enterobactin secretion (*107*).

In *E. coli*, a membrane protein called TolC is responsible for enterobactin secretion through the outer membrane (Figure 10) (*145*). It has been shown that deletion of *tolC* or *entS* resulted in *E. coli* strains that grew poorly under iron-limited conditions (*145*). It was also suggested in this study that enterobactin secretion occurs in two steps. The first step, enterobactin export from the cytoplasm to the periplasm, is mediated by EntS. The second step involves the outer membrane channel protein TolC to transport enterobactin from the periplasm to the extracellular environment.

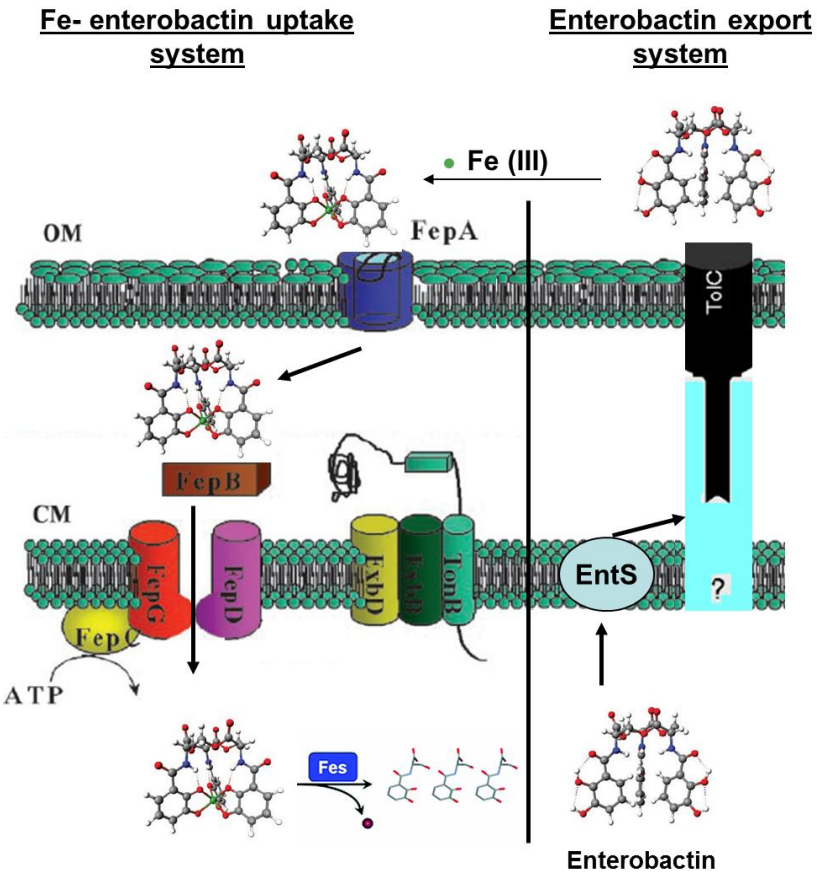

Figure 10: Scheme of enterobactin transport systems.

(Figure adapted from: (*35*, *145*))

Right part represents enterobactin export system and left part represents Fe-Ent uptake system

1.8.4 Fe-Enterobactin (Fe-Ent) Import

E. coli has a specific outer membrane receptor for Ferric-enterobactin called FepA (*146*). FepA not only mediates the Fe-Ent transport but also colicins B and D transport (*147-148*). Colicin B and D are cytotoxins that share similar Binding and translocation domains but have different C-terminal domains (i.e., Killing domains) so they have different mechanisms exerting cytotoxicity. Colicin B kills *E. coli* by creating a pore in

the inner membrane but colicin D works as ribonuclease in the bacterial cytoplasm (*149-150*). The binding stoichiometry of Fe-Ent and colicin B to FepA were studied (*151*). Fe-Ent and colicin B interact with FepA with 1:1 stoichiometry. Enterobactin, colicin B, and colicin D interact with two arginine residues (Arg 286 and Arg316) in a surface loop of FepA (*152*). *E. coli* FepA interacts with Fe-Ent with high affinity (K_D ~17 nM) (*153*).

The crystal structure of FepA has been determined (*154*). FepA is composed of two domains, a C-terminal domain that forms 22-stranded β-barrel and N-terminal domain that forms globular plug inside the barrel. This globular plug occludes the barrel pore. The translocation of Fe-Ent from FepA to the periplasm needs energy provided by the TonB-ExbB-ExbD complex (Figure 10) (*155*). TonB is a periplasmic protein that is embedded in the inner cytoplasmic membrane *via* its N-terminus. ExbB and ExbD, the inner cytoplasmic membrane proteins, mediate proton entry to cytoplasm and consequently energize TonB through conformational changes (*156*). Energy is then transfered from TonB to FepA. This energy induces FepA conformational change leading to rearrangement in the globular plug inside the β-barrel channel, allowing passage of Fe-Ent (*146*).

Once Fe-Ent is translocated to the periplasm, FepB, a periplasmic binding protein, binds Fe-Ent with high affinity and shuttles it to the cytoplasmic membrane ABC transport complex, FepD, FepG, and FepC (Figure 10) (*157-159*). The purified *E. coli* FepB interacts with Fe-Ent and apo-enterobactin with K_D values of 30 nM and 60 nM, respectively (*157*). The transport of Fe-Ent into the cytoplasm is mediated by FepD, FepG, and FepC. FepC has two conformations, only one of which possess a active ATP binding site (*44*). When Fe-Ent binds FepB, FepB interacts with FepD and FepG.

Consequently the FepD-FepG channel opens, leading to change in the conformation of the FepC and forming active ATP binding site. All of these changes mediate the transport of Fe-Ent across the inner cytoplasmic membrane (*44*). ATP hydrolysis by FepC domains leads to a change in FepC conformation, closing FepD-FepG channel, and causing release of FepB. FepE and FepF are inner cytoplasmic permeases which may be involved in the Fe-Ent uptake but there are no details in the literature about the exact roles of FepE and FepF in the Fe-Ent uptake. In *E. coli* cytoplasm, the Fes esterase enzyme catalyzes hydrolysis of Fe-Ent into DHBS in order to release iron (Figure 10) (*160*).

1.8.5 Enterobactin and Pathogenesis

Enterobactin has the highest iron chelation capacity of all siderophores. However enterobactin hydrophobicity makes it less effective inside the host cell due its membrane partitioning, clearance by albumin, and binding by an innate immune protein called lipocalin-2 (*132, 161*). Lipocalin-2 is also called siderocalin or neutrophil gelatinase-associated lipocalin (NGAL). Siderocalin is a 24 kDa protein that interacts with enterobactin, Fe-enterobactin, and related siderophores (*162*). Siderocalin is part of the lipocalins family and functions as a transporter *via* its binding to small hydrophobic molecules followed by binding to cell surface receptors (*163*). Upon bacterial infection, neutrophil cells release siderocalin at the site of infection as a kind of innate immune defense. Then siderocalin sequesters the catecholate related siderophores, including enterobactin.

As a result of the host innate immune defence by siderocalin against enterobactin-producing pathogens, these pathogens have developed a mechanism to modify enterobactin to evade siderocalin binding inside the host. The glucosylated versions of

enterobactin were termed as salmochelins because they were originally identified in Salmonella (*164-165*). The *iroA* gene cluster mediates enterobactin glucosylation, linearization, and transport as salmochelin (*60*). Many Gram-negative enteric bacteria harbor the *iroA* cluster, including extraintestinal *E. coli*, *Salmonella* spp., and *Klebsiella pneumoniae* (*166*). Salmochelin S4 is the glucosylated enterobactin at C5 of two catechol groups (Figure 11).

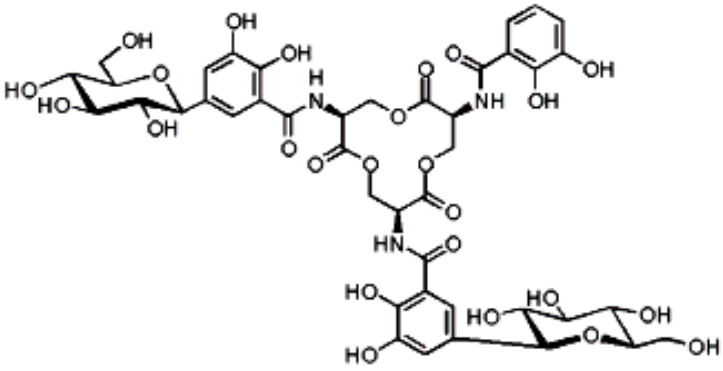

Figure 11: The structure of salmochelin S4.
(Figure from Lin *et al* (*167*))

The *iroA* gene cluster products are IroBCDE and IroN. **IroB** is a glycosyltransferase that catalyzes the enterobactin glucosylation at the C5 of its catechol moiety using uridine-5′-diphosphoglucose (Figure 12) (*168*). It adds the glucosyl group at the C5 of one, two, or three catechol units of enterobactin. Most glycosyltransferases tether glucose residue to nitrogen or oxygen. The glucosylation at a carbon atom instead of oxygen or nitrogen is uncommon. However there are C-glucosylated proteins which are related to the mammalian innate immune system (*169-171*). This glycosidic linkage is essential due to its stability against low pH and the glycosidase activities (*60*). IroB catalyzes the first step in the IroA system so it is essential target for the drug development. Brominated enterobactin at C5 of its catechol groups acts as an IroB

inhibitor (*128*). **IroC** is an ABC transporter that functions to pump salmochelin and enterobactin across the inner cytoplasmic membrane (Figure 13) (*103*). **IroN** is the outer membrane receptor that is responsible for Fe-salmochelin uptake (Figure 13). It has 52 % identity to FepA, the Fe-enterobactin outer membrane receptor. Recently, IroN expression was correlated with a 5- to 10-fold increase in the invasion rate by *E. coli* HB101 (*172*).

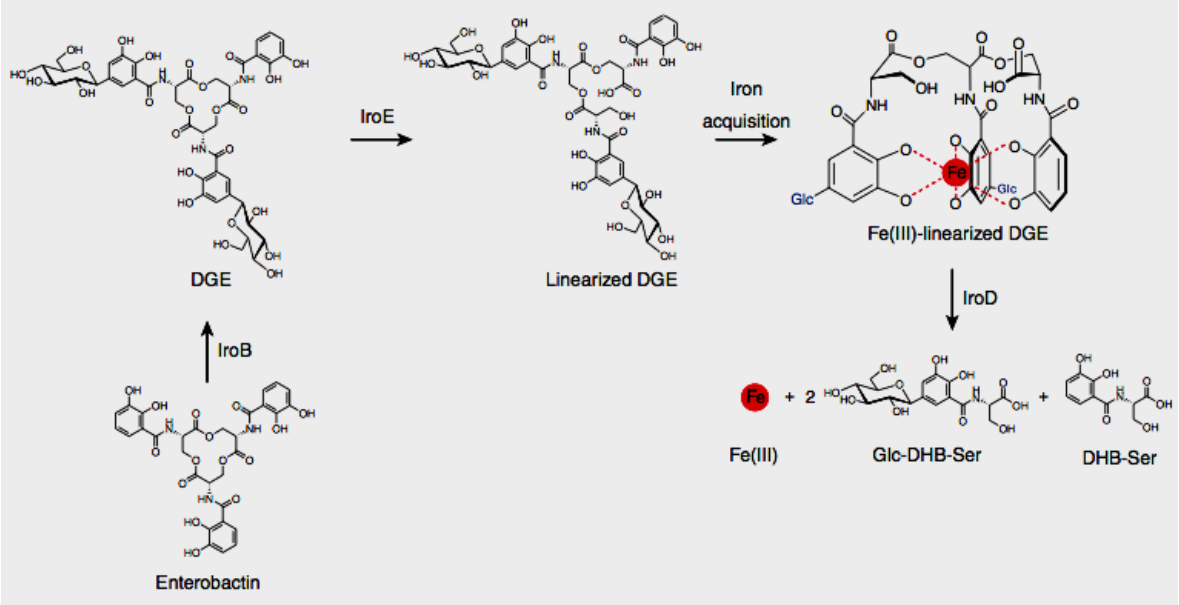

Figure 12: IroB, IroE, and IroD reactions.
(Figure from Fischbach *et al* (*60*))

IroD is an esterase enzyme that catalyzes the hydrolysis of Fe-salmochelin in the cytoplasm to release iron (Figure 12) (*173*). It can hydrolyze Fe-salmochelin into the linear trimer, dimer, and monomer to lower the iron affinity. **IroE** is a periplasmic protein that attaches to the inner cytoplasmic membrane. It catalyzes the hydrolysis of enterobactin and salmochelin to produce the linear trimer (Figure 12) (*173*). The whole IroA system is represented in Figure 13.

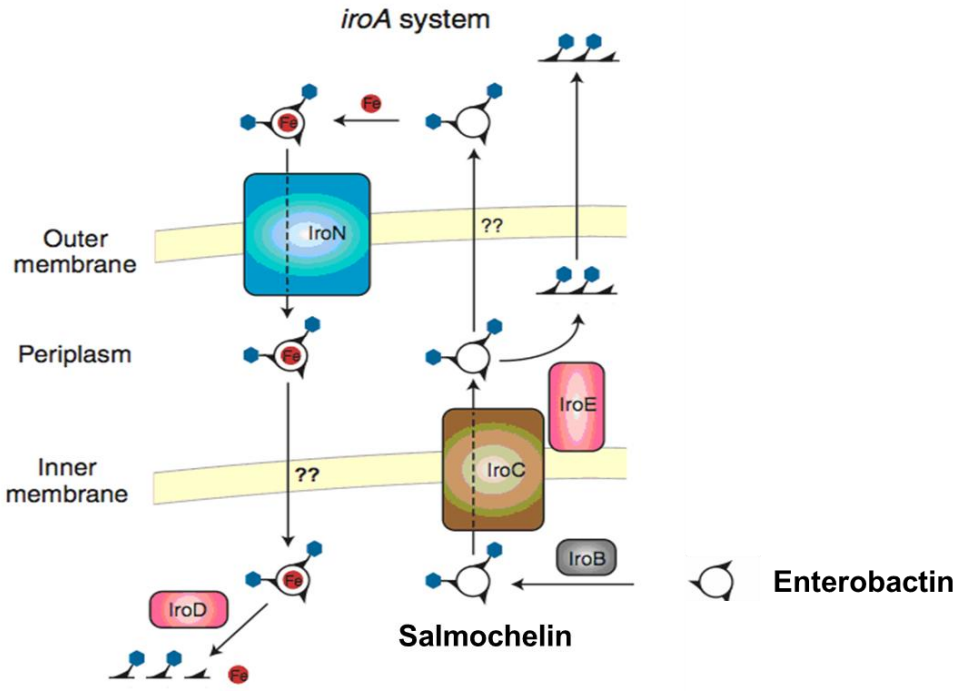

Figure 13: Schematic of IroA system.

(Figure adapted from: (*60*))

1.8.6 Enterobactin Biosynthetic Enzymes

***Isochorismate Synthase*: EntC**

In *E. coli*, there are two isochorismate synthases EntC and MenF. These enzymes are regulated in a different ways. The *entC* gene is expressed under aerobic and iron starvation conditions and is involved in the enterobactin biosynthesis pathway (*174*). The *menF* gene is expressed under anaerobic conditions and used in the menaquinone biosynthesis (*175-176*). It has been reported that each isochorismate synthase (MenF or EntC) is specific to its pathway (*175*). In this study, an *E. coli* mutant with intact *menF* and disrupted *entC* was able to synthesize only menaquinone. In contrast, an *E. coli*

mutant with intact *entC* and disrupted *menF* was able to synthesize enterobactin with traces of menaquinone.

EntC catalyzes the reversible conversion of chorismate to isochorismate, the first reaction in the enterobactin biosynthesis pathway. *E. coli* EntC has been purified as active monomer with a molecular weight of 43 kDa (*174*). The *E. coli* EntC crystal structure has been solved recently (Figure 14) (*177*). EntC is composed of 9 α-helices and 18 β-strands. The α-helices are placed in the protein surface. The β-sheet that is composed of the β-strands 2, 3, 7, and 11 forms an orthogonal β-sandwich with the β-sheet that consists of the β-strands β5, β6, β17, and β18. In this study, many EntC mutations in active site residues were created to get more insights on the mechanism of the catalysis.

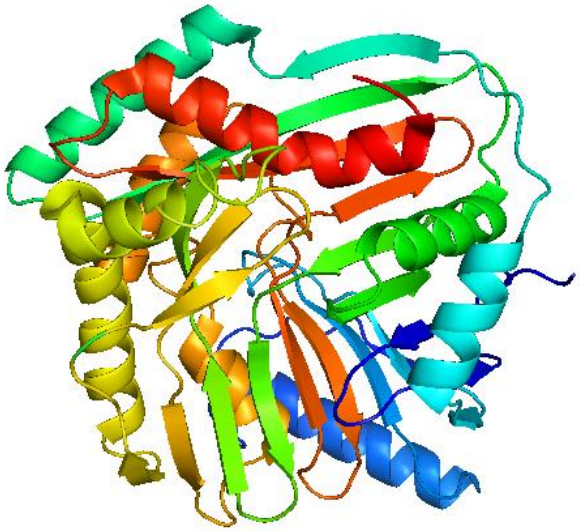

Figure 14: EntC crystal structure as monomer (PDB code: 3HWO).
The N-terminal and C-terminal domains were colored from the blue to red respectively.

***The Bifunctional Enzyme*: EntB**

EntB is bifunctional enzyme which works as an isochorismate lyase (ICL) (also known as isochorismatase) *via* its N-terminal domain and as an aryl carrier protein (Ar-CP) *via* its C-terminal domain (*139*). Thus, EntB contributes to both enterobactin biosynthetic modules. The ICL domain functions in the DHB module and the Ar-CP domain functions in the NRPS module. The isochorismate lyase activity of EntB catalyzes the hydrolysis of isochorismate produced by EntC to 2,3-dihydro-2,3-dihydroxybenzoate (the EntA substrate) and pyruvate. The Ar-CP domain of EntB is phosphopantetheinylated by EntD, the Fur-regulated phosphopantetheinyl transferase, at Ser 245 and then acylated at this site by its upstream partner EntE (*131, 139*). It had previously been reported that enterobactin biosynthesis requires the activity of EntG but there is no separate gene or polypeptide for EntG (*178-179*). Later *entG* gene was identified as the 3' terminus of *entB* gene that encodes the Ar-CP domain of EntB (*180*).

The EntB crystal structure has been solved (Figure 15) (*181*). EntB crystallizes as a dimer (~ 60 kDa). In each monomer, the N-terminal ICL domain composed of a six-stranded β-sheet, three α-helices face the dimerization interface, a long α-helix faces the Ar-CP domain, and a short single-turn helix that is located on the top of one end of the β-sheet. The Ar-CP domain consists of four helices. Ser245 is the site of the postranslational modification by EntD. This residue is placed at the start of the second helix in the Ar-CP domain.

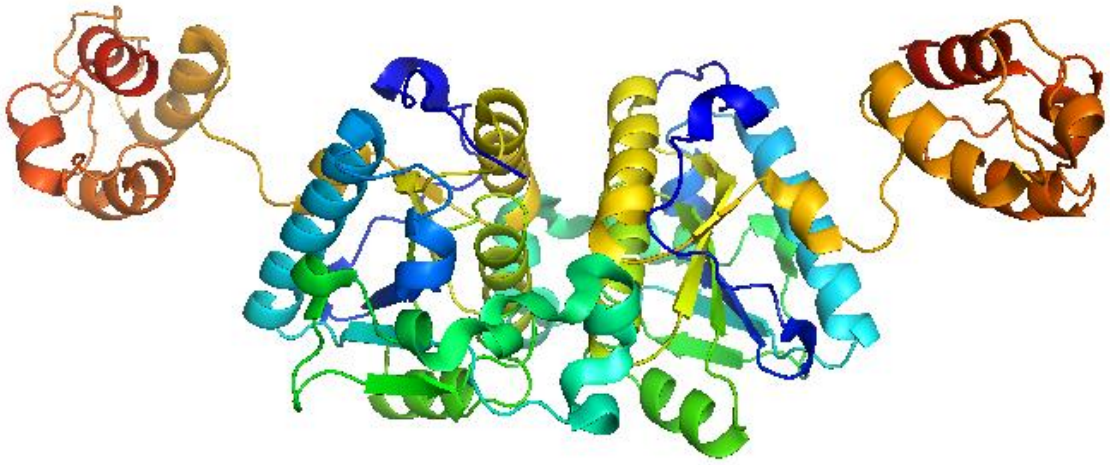

Figure 15: EntB crystal structure as dimer (PDB code: 2FQ1).

The N-terminal and C-terminal domains were colored from the blue to red respectively.

***2,3-Dihydro-2,3-Dihydroxybenzoate Dehydrogenase*: EntA**

EntA is 2,3-dihydro-2,3-dihydroxybenzoate (2,3-diDHB) dehydrogenase that catalyzes the oxidation of 2,3-diDHB to 2,3-DHB (*182*). The EntA crystal structure has been solved (Figure 16) (*183*). The protein was crystallized as tetramer that is formed as a dimer of dimers. In each dimer, the two monomer forms tight interactions with each other through the four four-helix bundle formed by helices 5 and 6 from each monomer. T88 and D89 that are located in the loop that precedes α5 are also involved in the dimer formation. Residues that involved in the tetramer formation are positioned at β7 and the C-terminal loops. EntA has also been purified by gel filtration as an octamer with a native molecular weight 210,000 Da (*140*).

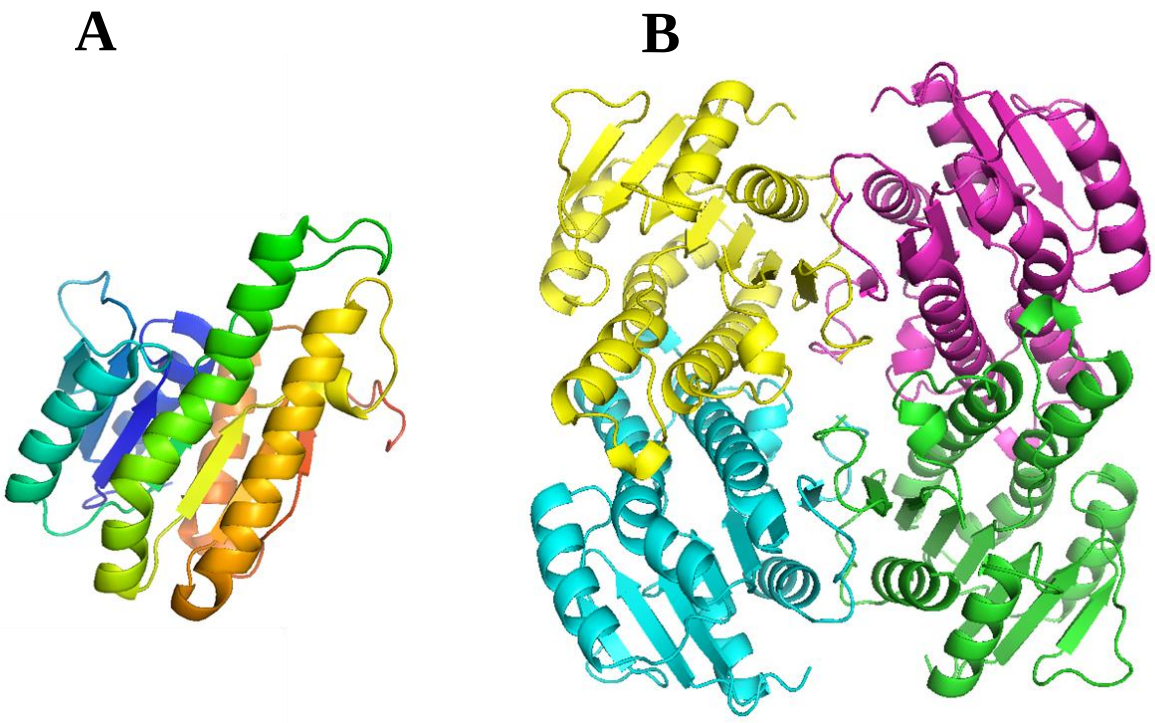

Figure 16: EntA crystal structure (PDB code: 2FWM).

A*: EntA monomer. The N-terminal and C-terminal domains were colored from the blue to red respectively.* ***B:*** *EntA tetramer with colored subunits.*

2,3-DHB-AMP Ligase **: EntE**

EntE is a 2,3-DHB-AMP ligase that catalyzes the first reaction in the NRPS module. It catalyzes the ATP-dependent adenylation of 2,3-DHB. EntE was initially purified as monomer with a molecular weight of 59 kDa (*141*). The EntE three-dimensional structure is currently unknown. EntE is a member of a family of adenylate-forming enzymes that share similar structure. They are composed of a large N-terminal domain of 400–520 residues and a smaller C-terminal domain of approximately 120 residues (*184*). The *P*-loop (phosphate-binding loop or Walker A motif) is a common motif in many ATP-binding proteins (*185*). This loop undergoes opening and closing

movement during catalysis. DhbE is an EntE homologue which is involved in bacillibactin synthesis in *Bacillus subtilis*. The crystal structure of DhbE with and without ligands has been reported (*184*). Based on the DhbE crystal structure, EntE catalysis occurs within its adenylation domain in two steps. The first step is the adenylation of 2,3-DHB and the second step is the transfer of the 2,3-DHB moiety to *holo*-EntB ArCP domain cofactor (*139, 184*).

The release of 2,3-DHB-AMP product from the EntE active site is very slow (*141*). This high affinity of EntE for its product has been exploited in the synthesis of EntE inhibitors (*186*). Here, removal of 2 or 3 hydroxyl group of one of the inhibitors was shown to diminish the inhibitory effect. This highlights the importance of these hydroxyl groups in the interaction between the EntE and its product. The inhibition of aryl acid adenylating enzymes (MbtA, YbtE, EntE, VibE, BasE, and DhbE) by the fluorescent probe *5′-O*-[*N*-(salicyl) sulfamoyl] adenosine (FI-Sal-AMS) has also been investigated (*187*). Here, FI-Sal-AMS was effective to interact and inhibit the aryl acid adenylating enzymes that use salicylic acid or 2,3-DHB as native substrates with K_D values ranging from 9 nM to 369 nM.

Recent studies showed that EntE can be involved in the biosynthsis of P1, P3-diadenosine-5-tetraphosphate (Ap4A) in the absence of *holo*-EntB (*188*). This compound is involved in the regulation of cell division during oxidative stress. This suggests that Ap4A may play a role of slowing bacterial growth under iron depleted conditions until the bacteria obtain iron. A recent report demonstrated that EntE catalysis occurs *via* two half-reactions, following a bi-uni-uni-bi ping-pong mechanism (*189*). The first half of

EntE reaction is adenylation of 2,3-DHB by ATP with release of pyrophosphate. In the second half-reaction, EntE catalyzes the transfer of DHB-AMP to *holo*-EntB, resulting in formation of acylated EntB and AMP as products.

***A Serine-Activating Enzyme*: EntF**

EntF is a monomer protein with a subunit molecular weight of 142 kDa (*190*). EntF is responsible for activating L-serine residue *via* its adenylation domain (A) and then the activated serine residue is transferred to EntF thiolation domain (T) phosphopantetheine group (*144*). The EntF condensation domain (C) catalyzes the condensation of 2,3-DHB acyl group (received from EntB) and the activated serine residue amino group in the T domain (*191*). The thioesterase domain (TE) of EntF was shown to catalyze cyclolactonization and elongation steps in enterobactin biosynthesis (*143*). Mutation of Ser1138 to Ala in the TE domain was shown to abolish enterobactin synthetase activity (*131*). G1027A and M1030A mutations in the T domain disrupted the interaction between T domain and TE domain (*192*).

The EntF T-TE di-domain structure has been solved recently (Figure 17) (*193*). The three helical bundle of T domain is impacted between the globular core and two helices (α4 and α5) of the TE domain. These α4 and α5 helices work as lid that covers both T and TE domains. In this study, it was shown that this lid opens during the interaction to accommodate the phosphopantetheine group attached to T domain active site Ser 48. It was also shown that the T domain interacts with the C domain and The TE domain *via* separate interaction interfaces.

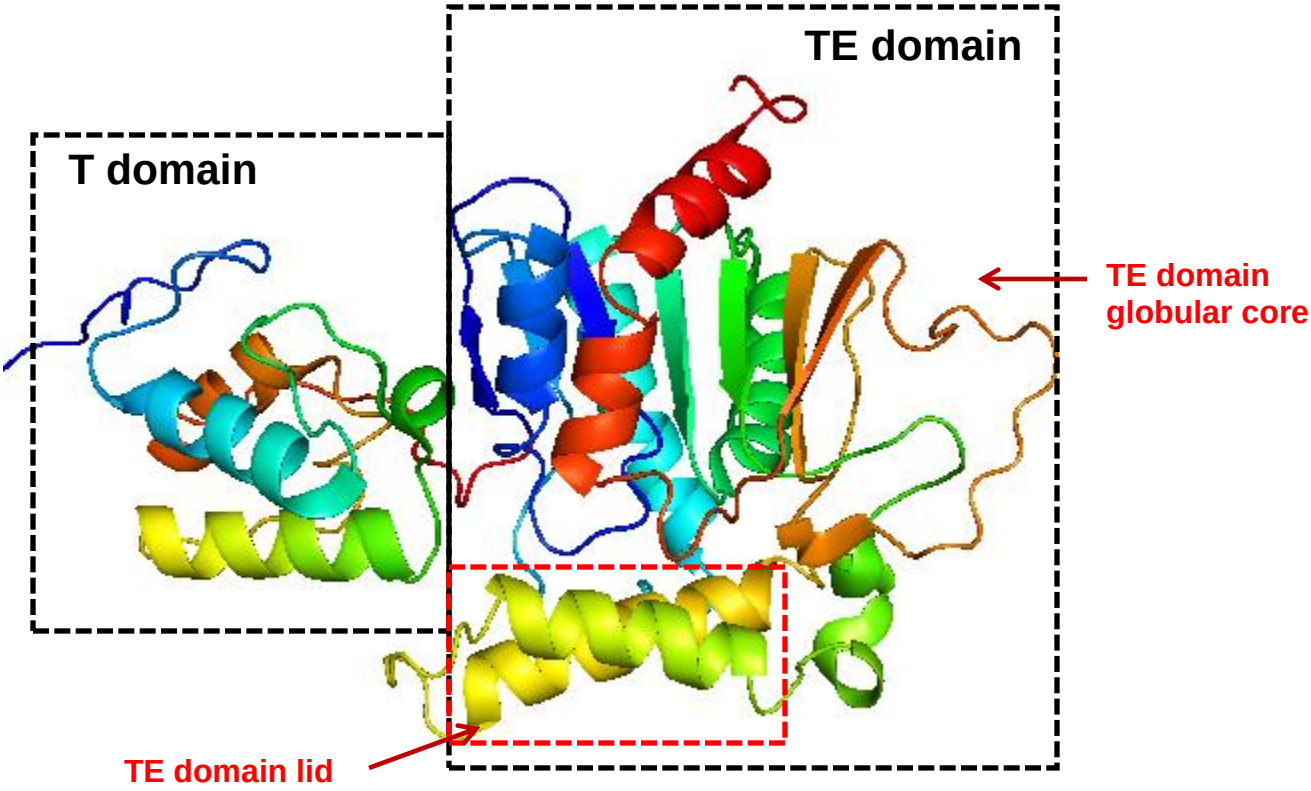

Figure 17: EntF T-TE di-domain structure (PDB code: 2ROQ).

The N-terminal and C-terminal domains were colored from the blue to red respectively.

***Phosphopantetheine transferase*: EntD**

EntD is phosphopantetheine transferase enzyme with a molecular weight approximately of 24 kDa (*194*)**.** It catalyzes the addition of phosphopantetheine (P-pant) moiety of coenzyme A to EntB and EntF, resulting in the formation of the active *holo*-EntB and *holo*-EntF (*131, 139, 195*), *E. coli* has two phosphopantetheine transferases: *holo*-acyl carrier protein synthase (ACPS) and EntD. ACPS catalyzes the transfer of P-pant group to fatty acid synthase ACP, resulting in formation of active *holo*- fatty acid synthase ACP (*196*). EntD is able to transfer the P-pant group to the Ar-CP domain of EntB or the T domain of EntF (*139, 195*). It was shown that EntD was successful in

transferring the P-pant group to apo-EntF but not to apo-ACP (*195*). In contrast, ACPS was able to transfer the P-pant group only to apo-ACP (*195*). These results suggest the specificity of each enzyme to its substrate.

1.8.7 Reported Protein Interactions in the Enterobactin Biosynthesis NRPS Module

Based on the EntB crystal structure (*181*) and the DhbE (EntE homologue) crystal structure (*184*), the EntB and EntE interaction interface residues have been probed by mutagenesis (*181*). In this study, five of the mutations on the EntB aryl carrier domain surface resulted in an increase in EntE specific activity. This suggests that the EntE-EntB interaction might be optimized *in vivo* through EntB conformational change, allowing EntB to interact with other protein partners in the pathway. Such interaction may be necessary to optimize NRPS activities, since it has been shown that EntE activity is stimulated (10-fold increase in k_{cat}) in the presence of *holo*-EntB (*144*).

The EntB-EntF interaction has been indirectly investigated by mutagenesis in the EntB Ar-CP domain. Alanine scanning mutations were performed in helix2 and loop2/helix3 of the Ar-CP domain which have many of highly conserved residues. It was found that EntB Met 249, Phe 264, and Ala 268 constitute an interface for interaction with EntF. Mutation of these residues affected enterobactin biosynthesis and enzymatic coordination of EntB and EntF activities, but they did not affect interaction between EntE and EntB, suggesting that EntB has separate interfaces for interaction with EntF and EntE (*142*). It has been shown that EntB Ar-CP domain residues G242 and D244 play important role in EntB-EntD interaction (*197*). The predicted EntB-EntD interaction interface in this study is different from the previously identified EntB-EntF interaction

interface (*142*). This suggests that EntB Ar-CP domain has non-overlapping interaction interfaces for EntD and EntF. The interaction between EntB Ar-CP domain and EntH was disrupted by a mutation in the EntB Ar-CP residue at position 245 (*133*). In the wild type EntB, Ser 245 is the site of Phosphopantetheinylation by EntD. This observation suggested that the posttranslation modification of EntB-Ar-CP domain at Ser 245 by EntD is essential for the interaction between EntH and EntB Ar-CP domain.

1.9 Scope of Thesis Research

The overall goal of my thesis focuses on detailed studies of the enterobactin biosynthetic enzyme EntE that adenylates 2,3-DHB. My research addresses how EntE binds its DHB substrate, and how it interacts with its partner proteins: EntA, which produces DHB, and EntB, which uses the EntE product (DHB-AMP) as a substrate.

Enterobactin as a siderophore is inactive inside the host due to its elimination by serum albumin and siderocalin (*161-162*). However, enterobactin is used as a substrate for iroB in some pathogenic bacteria such as extraintestinal *E. coli* and *Salmonella (165).* IroB catalyzes the formation of salmochelin, the effective siderophore inside the host as explained previously (*168*). Thus proteins involved in biosynthesis of the salmochelin precursor enterobactin are the center of much research. A comprehensive understanding of these proteins and their interactions is critical in development of new antimicrobial drugs that could inhibit growth of enterobactin utilizing pathogens in a host. The high affinity of EntE to its product DHB-AMP has already been used as a target in the synthesis of DHB-AMP analogues in order to inhibit enterobactin biosynthesis (*186-187*). Furthermore, identification of the protein-protein interactions in this pathway and

the interaction interfaces is also essential. This will assist in the synthesis of peptide aptamers imitating the interaction interfaces that could inhibit interactions and thus disrupt enterobactin biosynthesis in salmochelin-dependent pathogens.

The EntE crystal structure is currently unknown. Therefore, detailed characterization of EntE by homology modeling and eventually solving its structure will provide insights into its function and its catalytic mechanism. Such approaches will also help us to better understand the interactions between EntE and other proteins in the pathway, as well as to enhance our knowledge about the mechanism of related enzymes. Recently, it has been reported that the mammalian cell contains a siderophore similar to enterobactin that play a role in iron homeostasis (*1*). It has been shown in this study that the biosynthesis of this siderophore needs the activities of EntA, EntE, and EntF homologues. Thus my thesis research will also provide insights into the related mammalian enzymes required for the mammalian siderophore biosynthesis.

CHAPTER TWO: LIGAND-INDUCED CONFORMATIONAL REARRANGEMENTS PROMOTE INTERACTION BETWEEN THE *ESCHERICHIA COLI* ENTEROBACTIN BIOSYNTHETIC PROTEINS ENTE AND ENTB

The EntE-EntB interaction was measured in the literature indirectly by two approaches. (i) The first approach is study the effect of EntB Ar-CP domain addition on EntE activity (*144*). This study showed that EntE activity was stimulated (approximately 10 fold increase in k_{cat}) in the presence of EntB Ar-CP domain suggesting that this stimulation resulted from EntE-EntB interaction. (ii) The second approach focuses on study of the predicted interaction interfaces involved EntE-EntB interaction by mutagenesis followed by enzymatic assays (*181*). This study showed that some of the EntB mutations in the Ar-CP domain enhanced its acylation by EntE. This suggests that EntB interaction interface may be optimized by conformational alterations during the interaction with EntE.

This chapter of my thesis addresses the following research areas for the first time: (i) detailed characterization of EntE binding to its substrate 2,3-DHB, (ii) measuring the effect of 2,3-DHB binding on EntE-EntB interaction. Techniques used in this chapter are AUC, ITC, fluorescence spectroscopy, circular dichroism, and pull down assays. Pull-down assays provided the first direct evidence of an EntE-EntB interaction.

The manuscript corresponding to this chapter was published in the *Journal of Molecular Biology*: "Sofia Khalil and Peter D. Pawelek. (2009) Ligand-Induced Conformational Rearrangements Promote Interaction Between The *Escherichia coli* Enterobactin Biosynthetic Proteins EntE And EntB. *J. Mol. Biol*. 393: 658-671"

Summary

Siderophores are small-molecule iron chelators that many bacteria synthesize and secrete in order to survive in iron-depleted environments. Biosynthesis of enterobactin, the *E. coli* catecholate siderophore, requires adenylation of 2,3-DHB by the cytoplasmic enzyme EntE. The 2,3-DHB-AMP product is then transferred to the active site of *holo*-EntB subsequent to formation of an EntE-EntB complex. Here we investigate the binding of 2,3-DHB to EntE, and how 2,3-DHB binding affects EntE-EntB interaction. We overexpressed and purified recombinant forms of EntE and EntB with N-terminal hexahistidine tags (*H6*-EntE and *H6*-EntB). Isothermal titration calorimetry showed that 2,3-DHB binds to *H6*-EntE with a 1:1 stoichiometry and a K_D of 7.4 μM. Fluorescence spectra revealed enhanced 2,3-DHB emission at 440 nm (λ_{ex}=280 nm) when bound to *H6*-EntE due to fluorescence resonance energy transfer (FRET) between EntE intrinsic fluorophore donors and the bound 2,3-DHB acceptor. A FRET signal was not observed when *H6*-EntE was mixed with either 2,5-DHB or 3,5-DHB. The *H6*-EntE-2,3-DHB FRET signal was quenched by *H6*-EntB in a concentration-dependent manner. From these data we were able to determine the EC_{50} of EntE-EntB interaction to be approximately 1.5 μM. We also found by fluorescence and CD measurements that *H6*-EntB can bind 2,3-DHB, resulting in conformational changes in the protein. Additional alterations in the *H6*-EntB near-UV and far-UV CD spectra were observed upon mixture with *H6*-EntE and 2,3-DHB, suggesting that further conformational rearrangements occur in EntB upon interaction with substrate-loaded EntE. We also found that *H6*-EntB as a bait protein pulled down a higher concentration of chromosomally-expressed EntE in the presence of exogenous 2,3-DHB. Taken together, our results show that binding of 2,3-

DHB to EntE and EntB primes these proteins for efficient complexation, thus facilitating direct channeling of the siderophore precursor 2,3-DHB-AMP.

Introduction

Iron is an essential element for most bacteria since it is used for many cellular processes related to metabolism and signaling (*25*). In order to survive in iron-depleted environments, many bacteria synthesize and secrete iron-chelating molecules known as siderophores that have high Fe^{3+}-binding affinities. Siderophores, and the proteins involved in their synthesis, secretion, modification, and uptake, are considered virulence factors in a number of bacterial pathogens (*24*). *Escherichia coli* K12 synthesizes and secretes a single catecholate siderophore called enterobactin, which binds Fe^{3+} with a K_A of approximately 10^{50} M^{-1} (*35*). Upon secretion, enterobactin chelates bioavailable Fe^{3+} from the extracellular environment. Ferric enterobactin is then bound by the *E. coli* outer membrane transporter FepA and imported to the periplasm by a TonB-dependent uptake system (*146*). The ferric siderophore is transported to the inner membrane by the periplasmic binding protein FepB, which docks with the inner membrane-embedded ABC transport complex FepC-FepD-FepG. Upon transport to the cytoplasm *via* the ABC transport complex, ferric enterobactin is degraded by the Fes esterase in order to liberate the iron for various cellular processes. It has recently been reported that extraintestinal strains of *E. coli*, including uropathogenic *E. coli* (UPEC), possess a five-gene cluster known as *iroA* that is responsible for modifying enterobactin to enhance its virulence (*60, 166*). Understanding the molecular mechanisms by which enterobactin is synthesized and secreted by *E. coli* is thus of high priority since such mechanisms may reveal novel antimicrobial targets.

Enterobactin is synthesized in the *E. coli* cytoplasm by seven enzymes: EntC, EntB, EntA, EntE, EntF, EntD, and EntH. The five enzymes directly involved in enterobactin biosynthesis can be grouped into two functional modules: the DHB module (EntC, EntB (N-terminal domain), and EntA) and the non-ribosomal peptide synthesis (NRPS) module (EntE, EntB (C-terminal domain), and EntF). In the DHB module, chorismate is converted to 2,3-DHB through the sequential activities of EntC, EntB, and EntA (*140, 178-179, 198-199*). The DHB module functions upstream of the NRPS module and the two are intrinsically linked through the involvement of the bifunctional EntB protein, in which the N-terminal isochorismate lyase (ICL) domain participates in DHB synthesis while the C-terminal aryl carrier protein (ArCP) domain participates in NRPS. Enterobactin is ultimately produced during NRPS by the condensation of three molecules of 2,3-dihydroxybenzoate (2,3-DHB) and three molecules of L-serine yielding the tricatecholate ester. The enzyme EntD catalyzes the phosphopantetheinylation of the ArCP domains of EntB and EntF (*131, 195*). EntH is a proofreading activity that corrects NRPS misacylation events (*133-134, 200*).

The enzyme EntE catalyzes the adenylation of 2,3-DHB produced by EntA, thus activating it for subsequent steps in the NRPS module (Figure 1). EntE has a subunit size of 59 kDa and is reported to be monomeric (*141*). The EntE product, 2,3-DHB-AMP, is directly transferred to the phosphopantetheine cofactor anchored at the S245 residue in the active site of *holo*-EntB (*131*). Experiments have shown that the turnover number of EntE increases approximately 10-fold in the presence of *holo*-EntB (*144*). In the absence of *holo*-EntB, release of 2,3-DHB-AMP from the EntE active site is slow, due to the high affinity of binding of the product to the enzyme. Site-directed mutagenesis of residues

hypothesized to be at the interaction interface of the EntE - *holo*-EntB complex was reported to have an effect on EntE catalytic activity (*181*).

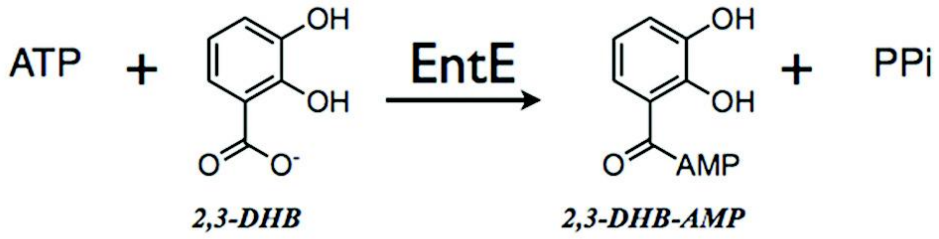

Figure 1: Scheme of reaction catalyzed by *E. coli* EntE.

Although no three-dimensional structure of EntE is currently available, crystal structures of DhbE, a homologous protein involved in the biosynthesis of the *B. subtilis* catecholate siderophore bacillibactin, provide us with some insights into the EntE active site. DhbE has been crystallized in three forms: (*i*) the *apo* form (PDB code: 1mdf), (*ii*) with 2,3-DHB-adenylate bound (PDB code: 1mdb), and (*iii*) with 2,3-DHB and AMP bound (PDB code: 1md9) (*184*). In the substrate-bound structures, 2,3-DHB binds at the floor of a hydrophobic cavity and is stabilized by the active site residue DhbE Y236. The carboxylate moiety of 2,3-DHB is further stabilized by interactions with DhbE residues H234 and K517. The ATP cofactor binds near the entrance of the cavity, proximal to a loop known as the 'P-loop', which closes over the active site during catalysis. Comparison of the *apo*- and *holo*-DhbE structures indicates that the protein undergoes

local conformational changes (i.e., loop movements), but no gross structural rearrangements to the overall fold, upon substrate binding.

EntB is the sequentially-related enterobactin biosynthetic enzyme immediately downstream of EntE. The crystal structure of EntB has been reported (*181*). The 32.5 kDa EntB subunit is composed of two discrete and independently folded domains: an N-terminal isochorismate lyase (ICL) domain (residues 26-208), and a C-terminal aryl carrier protein (ArCP) domain (residues 214-285). Crystallographic data revealed an EntB dimer in the asymmetric unit, with the inter-subunit interface occurring between ICL domains in the dimer. The ICL domain comprises most of the subunit mass (183 residues out of 285 residues in the subunit). Mutagenesis studies revealed that alteration of residues in the ArCP domain affected stimulation of EntE activity by EntB, suggesting their role in the interaction interface (*181*). Thus, there is well established, albeit indirect, evidence for an interaction between EntE and EntB.

Here we investigate the nature of EntE substrate binding and its effects on the EntE-EntB protein-protein interaction. Isothermal titration calorimetry has provided us with unambiguous equilibrium dissociation constant describing binding of 2,3-DHB substrate to EntE. Furthermore, we show that 2,3-DHB can act as a fluorescent sensor of the EntE active site. We exploited this phenomenon to directly measure the EntE-EntB interaction. Our circular dichroism studies and pull-down assays support our fluorescence binding data and show that the formation of an EntE-EntB complex is most efficient in the presence of 2,3-DHB. Our experimental approaches have provided the first direct measurement of the EntE-EntB interaction, and have generated insights into how protein-protein interactions in the enterobactin biosynthetic machinery may be essential in

modulating substrate flux that would result in maximal siderophore production while minimizing deleterious consequences of intracellular accumulation of intermediates.

Materials and Methods

Reagents

Unless otherwise noted, all reagents were purchased from BioShop Canada, Inc. (Burlington, Ontario). 2,3-DHB, 2,5-DHB and 3,5-DHB were purchased from Sigma-Aldrich.

Homology Modeling of EntE

A homology-based model of EntE was obtained using the crystal structure of *B. subtilis holo*-DhbE (with bound 2,3-DHB and AMP) as a template (PDB code: 1md9) (*184*). A structure-based alignment of the EntE amino acid sequence to that of DhbE was obtained using the FFAS03 server (http://ffas.ljcrf.edu/ffas-cgi/cgi/ffas.pl) (*201*). This alignment was used as input for the modeling software Modeller 9v3 (*202*). Structural superposition of the EntE homology model to the DhbE template structure was performed using LSQMAN (*203*) in order to determine RMSD values. Model quality was assessed using the VADAR suite (http://redpoll.pharmacy.ualberta.ca/vadar/) (*204*).

Protein Expression and Purification

Escherichia coli AG-1 (*endA1 recA1 gyrA96 thi-1 relA1 glnV44 hsdR17*(*rK*$^-$ *mK*$^+$)) cells harboring pCA24N plasmids containing the genes encoding EntE and EntB with in-frame N-terminal hexahistidine tags (i.e., pCA24N-EntE and pCA24N-EntB) were obtained from the ASKA repository (*205*). The strains were grown at 37 °C in LB broth containing 30 µg/ml of chloramphenicol to a final OD_{600} between 0.5-0.6. Overexpression of hexahistidine-tagged EntE or hexahistidine-tagged EntB (henceforth

referred to as *H6*-EntE and *H6*-EntB, respectively) was induced in log-phase cells with the addition of IPTG to a concentration of 1 mM. After an additional 3-hour growth at 37 °C, cells were harvested by centrifugation (15 min at 5,000 *g*). Pellets were resuspended in BugBuster Master Mix (Novagen) and incubated for 30 min at room temperature with constant agitation. Cell lysates were centrifuged (50 min at 10,000 *g*) and supernatants were recovered. Clarified lysates containing *H6*-EntE or *H6*-EntB were loaded onto 10-ml Profinity IMAC columns (Bio-Rad Laboratories) connected to a BioLogic DuoFlow FPLC system (Bio-Rad Laboratories). Fractions containing washed *H6*-EntE or *H6*-EntB were eluted by linear imidazole gradients (10 - 500 mM imidazole) in a buffer containing 50 mM Hepes (pH 8.0), 100 mM KCl, and 1.0 mM TCEP. We determined that IMAC purification yielded near-homogenous (> 95% purity) H6-EntE. However, *H6*-EntB required additional purification on a 1-ml UNOsphere Q anion exchange column (Bio-Rad Laboratories) to achieve a near-homogeneous (> 95% purity) *H6*-EntB fraction. Pooled fractions containing purified *H6*-EntE and *H6*-EntB were dialyzed against Buffer A (50 mM Hepes (pH 8.0), 100 mM KCl, 1.0 mM TCEP, and 15% glycerol). Dialyzed samples were stored at -20 ^{o}C. We used the Enzchek pyrophosphate release assay (Invitrogen) to measure *H6*-EntE steady-state enzyme activity and found its specific activity to be comparable to that reported earlier for non-hexahistidine-tagged EntE (*141*). Stability of *H6*-EntE was monitored by enzymatic assays, and no loss of activity was observed after extended (> 14 days) storage at 4 ^{o}C or after long (> 4 weeks) periods of storage at -20 ^{o}C followed by subsequent thawing.

Isothermal Titration Calorimetry

Heat generated by the binding of 2,3-DHB to *H6*-EntE was measured using a VP-ITC isothermal titration microcalorimeter (cell volume = 1.36 ml; Microcal, Inc.). 2,3-DHB dissolved to a concentration of 500 µM in Buffer A was injected into a cell containing 50 µM purified *H6*-EntE dialyzed against Buffer A. Protein concentration was determined by absorption at 280 nm as measured on a Thermo Genesys 10 spectrophotometer and using a molar extinction coefficient predicted from the *H6*-EntE primary amino acid sequence (57,300 M^{-1} cm^{-1}). Data from 24 injections (injection volume = 10 µl) were collected at 293 K while the contents of the cell were stirred at 300 rpm. An initial 2-µl injection was not included in the data analysis. A spacing time of 240 seconds occurred between each injection. Heats of injection were corrected by subtraction of heats of dilution generated by injecting 500 µM 2,3-DHB into the sample cell containing Buffer A. Calorimetry data were analyzed using Origin 5.0 (Microcal, Inc.) by fitting the corrected heats of injection to an equation describing single-site ligand binding. Values of ΔH (in kcal mol^{-1}), S (in cal mol^{-1} K^{-1}) and K_D were obtained from the Origin software.

Fluorescence Spectroscopy

Fluorescence emission and excitation spectra of purified *H6*-EntE and *H6*-EntB in the presence and absence of 2,3-DHB, 2,5-DHB, or 3,5-DHB were collected at room temperature using a Shimadzu RF-5301PC spectrofluorometer. For emission spectra, the excitation wavelength was fixed at 275 nm, 280 nm, or 295 nm and fluorescence emission intensities were recorded from 300 nm to 550 nm. For excitation spectra, the emission wavelength was fixed at 440 nm and fluorescence intensities were collected

upon changing the excitation wavelength from 200 nm to 350 nm. Excitation and emission slits were set to 3 nm. Measurements were performed using a 0.5 ml quartz cuvette (10 mm path length) containing purified *H6*-EntE or *H6*-EntB diluted to a final concentration of 3 μM in Buffer A. Each reported fluorescence spectrum represents the average of three scans (2 nm/sec). Fluorescence intensities were corrected for inner filter effects according to the equation: $F_{corr} = F_{obs} \times 10^{((ODex+ODem)/2)}$, where F_{obs} is the observed fluorescence intensity, OD_{ex} is the optical density of the solution at the excitation wavelength, OD_{em} is the optical density of the solution at the emission wavelength. Fluorescence emission spectra of *H6*-EntE were obtained with varying concentrations of 2,3-DHB (5, 10, 20, 30, 40, 50, 60, 70, and 80 μM). Half-maximal effective concentration (EC_{50}) values describing 2,3-DHB binding to *H6*-EntE were calculated from fluorescence emission data (either intensity increase at 440 nm or decrease at 330 nm) using the computer program Origin 5.0 and fitting the data to a hyperbolic equation to determine EC_{50} values. The EntE-EntB interaction was measured by fluorescence using a solution of *H6*-EntE (2.5 μM) in Buffer A plus 50 μM 2,3-DHB to which increasing concentrations of *H6*-EntB (0.4- 3.4 μM) were added.

In this study, the fluorescence spectra of all protein solutions mixed with a given concentration of 2,3-DHB, 2,5-DHB, or 3,5-DHB were corrected by subtracting fluorescence emission spectra of the appropriate DHB isomer collected at the same concentration in the absence of protein. Furthermore, all corrections for dilution factors were applied when appropriate.

Circular Dichroism

Circular dichroism experiments were performed on a Jasco J-815 CD spectrophotometer connected to a temperature-controlled circulating water bath. Far-UV spectra of *H6*-EntE (7.5 μM) and *H6*-EntB (2.5 μM) solutions were collected at 20 °C between 200 nm and 260 nm (1 nm bandwidth) in 0.2-nm steps at a rate of 100 nm/min (0.25 sec response) using a cell with a path length of 0.2 cm. Each far-UV spectrum presented here is an average of five scans. Near-UV spectra of *H6*-EntE (25 μM) and *H6*-EntB (15.6 μM) were collected at 20 °C between 250 nm and 320 nm (1 nm bandwidth) in 0.2-nm steps at a rate of 20 nm/min (2 sec response) using a cell with a path length of 2.0 cm. Each near-UV spectrum presented here is an average of two scans. Both near-UV and far-UV spectra were collected from solutions of individual proteins and of mixtures of *H6*-EntE and *H6*-EntB. In all cases, protein solutions for CD analysis were dialyzed against 25 mM Tris (pH 8.0), 0.5 mM TCEP, 100 mM KCl, and 15% glycerol and then diluted to the desired concentration in the same buffer. Spectra were collected in the presence and absence of 50 μM 2,3-DHB. Spectra collected in the presence of 50 μM 2,3-DHB were corrected by subtraction of signal contribution from 50 μM 2,3-DHB dissolved in the same buffer in the absence of protein.

Pull-down Assays

Pull-down assays were performed using the ProFound Pull-Down PolyHis Protein:Protein Interaction Kit (Pierce, Rockford, IL). Cobalt chelate columns were equilibrated with washing solution (1:1 mixture of Tris Buffered Saline (25 mM Tris-HCl (pH 7.2), 150 mM NaCl) with ProFound Lysis Buffer, and imidazole to a concentration of 40 mM). *H6*-EntB (130 μg), the bait protein, was immobilized to cobalt chelate

columns by incubation for 1 hour at 4 °C with gentle shaking. Cell lysates containing prey proteins were prepared from *E. coli* BW25113 cells grown for 16 h at 37 ^{o}C in iron-free M63 minimal media in the presence of 75 μM 2,2'-dipyridyl. Lysates were added to the cobalt columns in the presence or absence of 100 μM 2,3-DHB and then incubated at 4 °C with gentle shaking for 2 hours. The columns were washed 8 times with washing solution. Bait-prey protein complexes were eluted by the addition of imidazole to a final concentration of 300 mM. Eluted proteins were separated on 10% SDS-polyacrylamide gels. After electrophoresis, gels were stained using the SilverQuest Silver Staining kit (Invitrogen). Bands of interest were excised from the gels and proteins were subjected to in-gel tryptic digestion. Recovered samples were subjected to LC-MS/MS analysis using Bruker ESI Ion Trap and Agilent LC 1100 mass spectrometers at the McGill Mass Spectrometry Core Facility (McGill University, Montreal). Briefly, samples obtained from gel slices were dried and then resuspended in 97% acetonitrile (ACN)/0.2% formic acid. Resuspended samples were injected in the mass spectrometer, and a gradient of 0-70% (95% water/0.5% ACN to 9.8% water/90%ACN/0.2% formic acid) was used to elute the peptides. The resulting data were searched against the NCBI database using MASCOT (Matrix Science).

Results

Homology Modeling of *E. coli* EntE Predicts Positions of Ligand-Binding Residues and Intrinsic Fluorophores

In order to gain insights into the nature of substrate binding to *E. coli* EntE, as well as the spatial distribution of intrinsic fluorophore residues (Tyr, Trp) throughout the protein, we generated a homology-based model using the structure of the *B. subtilis*

bacillibactin biosynthetic enzyme DhbE (PDB code: 1md9) as a template. These enzymes share 46.5% sequence identity (Figure 2A). The structure-based alignment obtained from the FFAS03 server was used as an input for Modeller 9v3, which produced a three-dimensional model of *E. coli* EntE as output. The EntE model superimposes well with the DhbE structure, with an overall RMSD of 0.271 Å (Figure 2B). The stereochemistry of the model was analyzed using the VADAR suite (*204*). Ramachandran analysis showed that 90% of the model's residues are in the core region, 47% in the allowed region, 1% in the generous region, and no residues were found in the disallowed region. The overall general distribution of the intrinsic fluorophores in the model is such that most of the tyrosine residues populate the interior of the protein whereas most tryptophan residues are surface-exposed. This distribution is consistent with the reported DhbE structure (*184*).

A

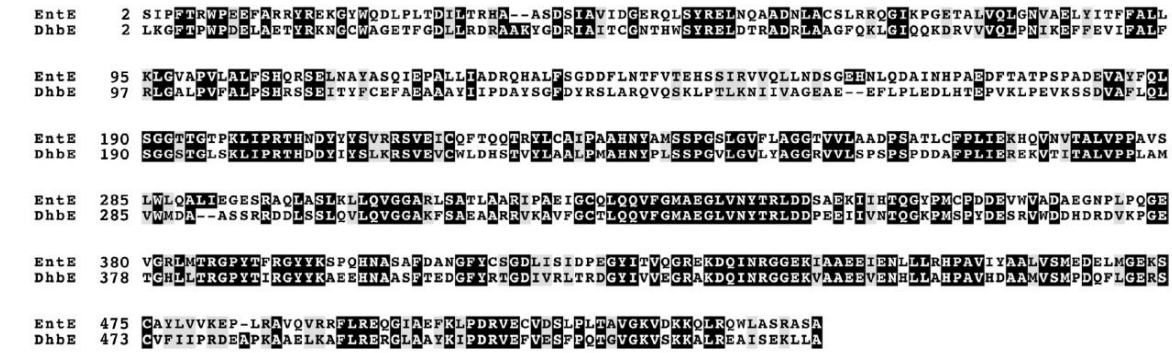

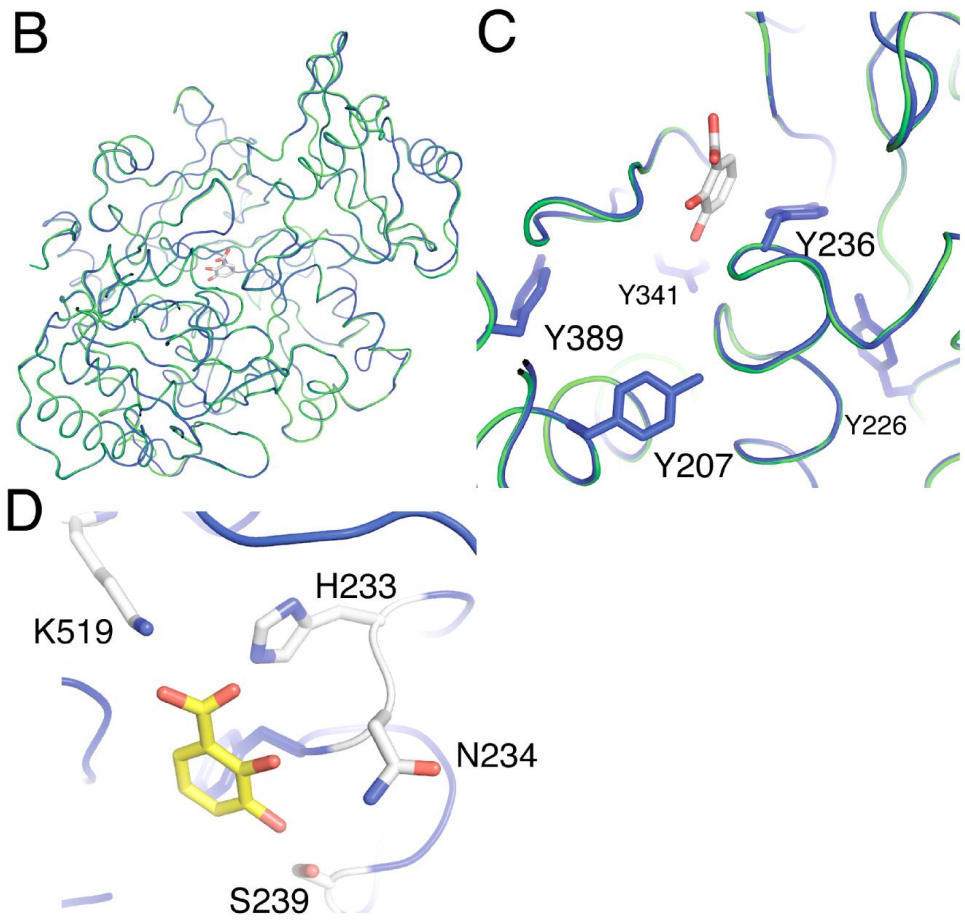

Figure 2: Homology-based model of *E. coli* EntE.

(a) Structure-based alignment of EntE to B. subtilis DhbE primary amino acid sequence. Positions of identity shown as white letters with black background. Positions of similarity shown as black letters on grey background. Residues are numbered according to primary amino acid sequences. (b) Structural superposition of EntE homology model to DhbE structure (PDB code: 1md9). EntE model shown as blue coil. DhbE structure shown as green coil. Position of DHB coordinates from DhbE structure shown as sticks and colored according to element. (c) Close-up view of 2,3-DHB in the active sites of DhbE (green coil) and superimposed EntE (blue coil). EntE tyrosine residues within 10 Å of DHB shown as blue sticks. (d) Close-up view of 2,3-DHB in the active site of the EntE homology model (blue coil) showing EntE residues (white sticks, atoms colored according to element) predicted to form hydrogen bonds with 2,3-DHB substrate (yellow sticks, atoms colored according to element). Molecular graphics were generated using PyMOL (http://www.pymol.org).

We computationally introduced a 2,3-DHB molecule into the active site of our EntE model by using the 2,3-DHB coordinates found in the DhbE active site (Figure 2C). The 2,3-DHB molecule was introduced using the same rotation and translation matrices determined by LSQMAN for optimal EntE-DhbE superposition. Five tyrosine residues were found to be most proximal (distance < 10 Å) to the DHB substrate: Y207, Y226, Y236, Y341, and Y389. All five tryptophan residues in the EntE model were found to be distal (> 15 Å) to the active site. Four of the five tryptophans in the model are surface-exposed. The tryptophan most proximal to the modeled DHB position, W286 (distance =15.6 Å), was the only buried tryptophan found in the model. The model also identified EntE residues that could potentially bind to non-aromatic portions of 2,3-DHB. Residues K519 and H233 are within hydrogen bonding distance of the carboxylate moiety of the substrate and superimpose with DhbE residues previously identified from the crystal structure as stabilizing the carboxylate of bound 2,3-DHB (Figure 2D) (*184*). According to our model, EntE residues N234 and S239 are within hydrogen bonding distance of the 2-hydroxyl and 3-hydroxyl groups of 2,3-DHB, respectively. These residues superimpose with asparagine and serine residues corresponding to 2,3-DHB hydroxyl groups in the substrate-bound DhbE crystal structure.

EntE Has a Single, Micromolar-Affinity Binding Site for Its Substrate 2,3-DHB

We used isothermal titration calorimetry (ITC) to directly measure the binding of 2,3-DHB to purified recombinant hexahistidine-tagged EntE (*H6*-EntE). 2,3-DHB at a concentration of 500 μM was injected into a 50 μM solution of *H6*-EntE and heats of binding were measured over 24 injections (Figure 3, upper panel). Integrated heats of injection of 500 μM 2,3-DHB into buffer were subtracted from the integrated heats of ligand binding to EntE. The corrected heats were plotted as a function of the molar ratio of DHB to *H6*-EntE (Figure 3, lower panel). These data fit well to the single-site binding equation in Origin 5.0, indicating that 2,3-DHB binds to *H6*-EntE with a stoichiometry of 0.92 $\pm$ 0.01, and with an equilibrium dissociation constant (K_D) of 7.35 $\pm$ 0.31 μM. Our ITC data revealed the ΔH of 2,3-DHB binding to *H6*-EntE to be -13.46 $\pm$ 0.15 kcal/mol and the $T\Delta S$ to be -7.03 kcal/mol, such that the overall ΔG of the binding reaction was -6.43 kcal/mol.

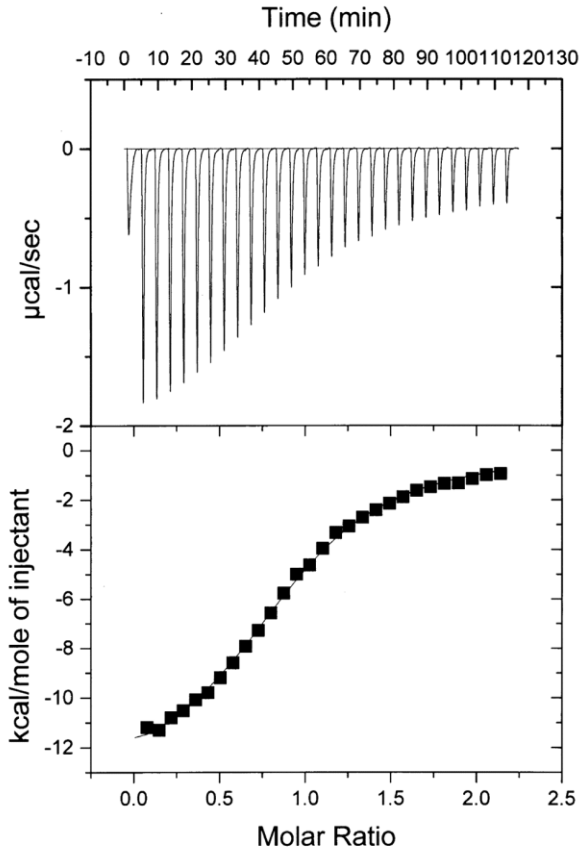

Figure 3: **Isothermal titration calorimetry of *H6*-EntE in the presence and absence of 2,3-DHB**.

Upper panel: Heats of injection of 500 µM 2,3-DHB into a cell containing 50 µM H6-EntE. Lower panel: Data from upper panel integrated and plotted as a function of molar ratio of 2,3-DHB after subtraction of heats generated by injection of 500 µM 2,3-DHB into buffer. Integrated heats shown as black squares. Single-site binding model shown as solid line.

Binding of 2,3-DHB to EntE Results in A Substrate-Specific FRET Signal

We obtained *H6*-EntE fluorescence emission spectra in the presence and absence of 2,3-DHB substrate. Analysis of *H6*-EntE fluorescence emission upon excitation at 280 nm revealed a single emission peak at 330 nm (Figure 4A, black circles). Upon addition of 50 µM 2,3-DHB to 3 µM *H6*-EntE, we observed a decrease in the 330 nm emission peak along with the appearance of a new emission peak at 440 nm (Figure 4A, green circles). This peak coincides with the fluorescence emission maximum of 2,3-DHB (Figure 4A, magenta circles), although in the absence of protein the fluorescence intensity of an equivalent concentration (50 µM) of the substrate was markedly lower. The spectral overlap between tyrosine emission and 2,3-DHB excitation maxima suggests that the increase in 2,3-DHB fluorescence intensity at 440 nm in the presence of *H6*-EntE is due to fluorescence resonance energy transfer (FRET). Fluorescence excitation spectra (λ_{em}= 440 nm) of 2,3-DHB solutions in the presence and absence of *H6*-EntE indicated that the excitation maxima of 2,3-DHB were not significantly altered upon binding to *H6*-EntE, and that a prominent peak occurred around 280 nm in the presence of *H6*-EntE (Figure 4B). Fluorescence emission spectra were also collected at 275 nm, a wavelength that is closer to that of maximal tyrosine excitation and further from that of maximal tryptophan excitation. Excitation at 275 nm was observed to increase the intensity of the emission peak at 440nm relative to excitation at 280 nm (data not shown). The addition of increasing concentrations of 2,3-DHB (5 µM – 80 µM) to a fixed concentration of *H6*-EntE (3 µM) resulted in concentration-dependent increases in fluorescence intensity at 440 nm with corresponding decreases in fluorescence intensity at 330 nm. These concentration-dependent changes in fluorescence intensity reflect 2,3-DHB binding to

H6-EntE since the data fit well to hyperbolic plots describing single-site saturable binding (Figure 4C and 4D). Hyperbolic fits are consistent with EC_{50} values of 12.9 µM (obtained from the increase in fluorescence intensity at 440 nm; Figure 4C) and 9.2 µM (obtained from the quenching of fluorescence intensity at 330 nm; Figure 4D).

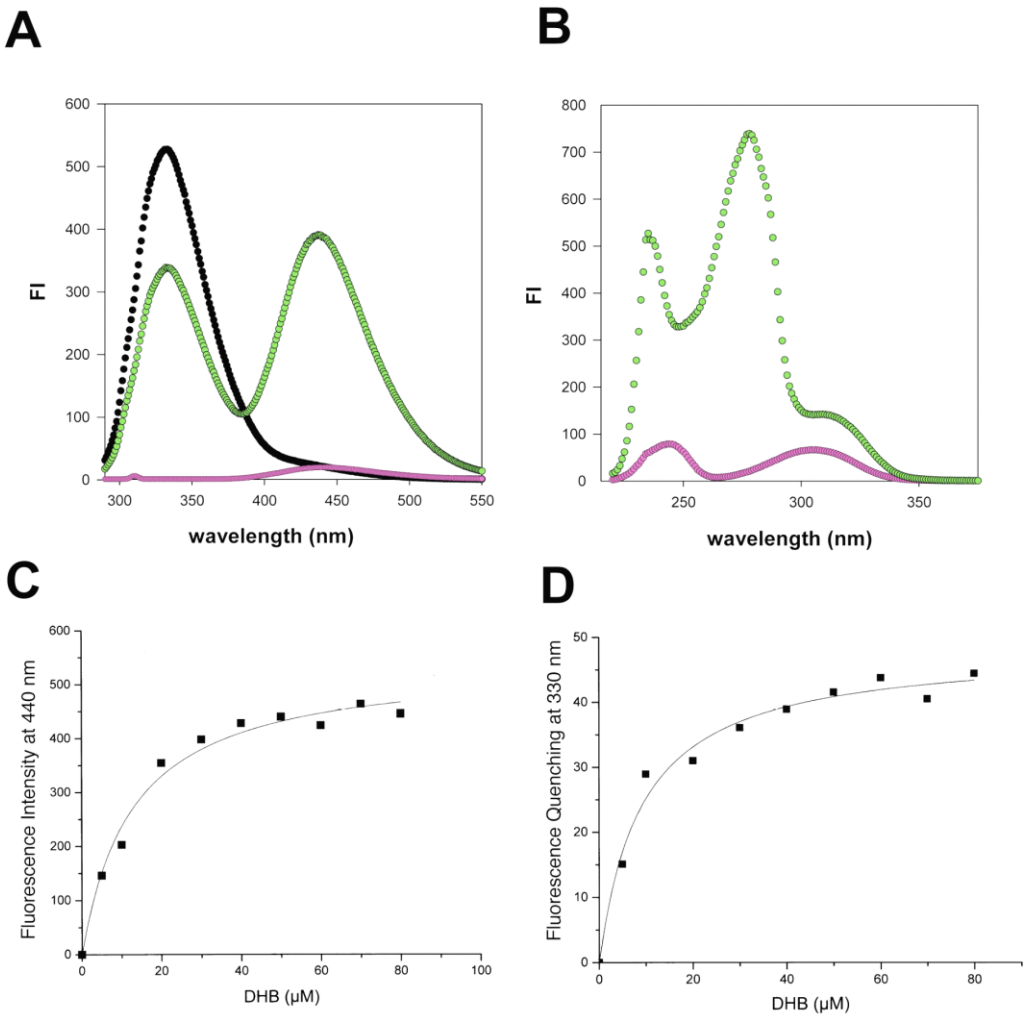

Figure 4: Fluorescence measurements 2,3-DHB binding to *H6*-EntE.

(A) Fluorescence emission spectra (λ_{ex} = 280 nm) of solutions containing: 3 µM H6-EntE (black circles); 50 µM 2,3-DHB (magenta circles); 3 µM H6-EntE and 50 µM 2,3-DHB

(green circles). (B) Fluorescence excitation spectra (λ_{em} = 440 nm) of solutions containing: 50 µM 2,3-DHB (magenta circles); 50 µM 2,3-DHB and 3 µM H6-EntE (green circles). (C) Increase in fluorescence emission at 440 nm as a function of 2,3-DHB concentration. Fluorescence emission at 440 nm corrected by baseline fluorescence emission of H6-EntE in the absence of 2,3-DHB, and by 2,3-DHB emission in the absence of H6-EntE (black squares). Fit of data to hyperbolic curve describing single-site binding (solid line). (D) Quenching of fluorescence emission at 330 nm as a function of 2,3-DHB concentration. Fluorescence quenching was calculated as ($(F_o-F)/F_o$) x 100, where F_o is the initial fluorescence intensity observed at 330 nm in the absence of 2,3-DHB. Fluorescence quenching (black squares). Fit of data to hyperbolic curve describing single-site binding (solid line).

We investigated the specificity of binding of DHB isomers to *H6*-EntE and *H6*-EntB. Fluorescence emission spectra were collected for *H6*-EntB and *H6*-EntE in the presence of equivalent concentrations of 2,3-DHB, 2,5-DHB and 3,5-DHB. We found that the *H6*-EntB emission peak at 330 nm (Figure 5a, black circles) was maximally quenched in the presence of 2,3-DHB (Figure 5A, green circles). We also found that *H6*-EntB intrinsic fluorescence was quenched upon addition of 2,5-DHB (Figure 5A, red circles) and 3,5-DHB (Figure 5A, blue circles), albeit to a lesser extent. When solutions of *H6*-EntE were mixed with the DHB isomers, we found that only 2,3-DHB could quench intrinsic *H6*-EntE fluorescence (Figure 5B, green circles). Furthermore, we only observed a 440 nm emission peak when *H6*-EntE was mixed with 50 µM 2,3-DHB. No quenching of *H6*-EntE intrinsic fluorescence was observed upon addition of equivalent concentrations of 2,5-DHB (Figure 5B, red circles) or 3,5-DHB (Figure 5B, blue circles); furthermore, neither 2,5-DHB nor 3,5-DHB exhibited a 440 nm emission peak in the

presence of *H6*-EntE upon excitation at 280 nm even though both of these DHB isomers also exhibit fluorescence emission maxima at 440 nm (data not shown).

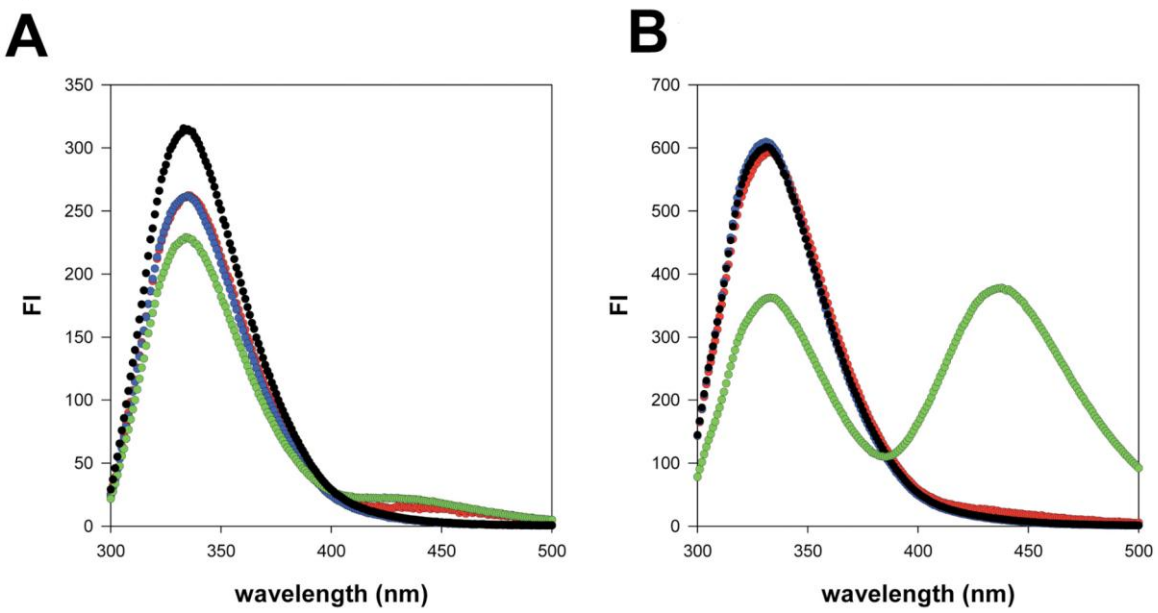

Figure 5: Binding of DHB isomers to *H6*-EntE and *H6*-EntB.

(A) Fluorescence emission spectra (λ_{ex} = 280 nm) of solutions containing: 3 µM H6-EntB (black circles); 3 µM H6-EntB and 50 µM 2,3-DHB (green circles); 3 µM H6-EntB and 50 µM 2,5-DHB (red circles); 3 µM H6-EntB and 50 µM 3,5-DHB (blue circles). (B) Fluorescence emission spectra (λ_{ex} = 280 nm) of solutions containing: 3 µM H6-EntE (black circles); 3 µM H6-EntE and 50 µM 2,3-DHB (green circles); 3 µM H6-EntE and 50 µM 2,5-DHB (red circles); 3 µM H6-EntE and 50 µM 3,5-DHB (blue circles).

Binding of 2,3-DHB to Both EntE and EntB Results in Conformational Changes That Promote Formation of A Transient EntE-EntB Complex

We investigated the effect of EntB-EntE interaction on 2,3-DHB binding to *H6*-EntE using our fluorescence assay. We found that *H6*-EntB quenched 440 nm fluorescence emission of *H6*-EntE-bound 2,3-DHB in a concentration-dependent manner (Figure 6a). Half-maximal quenching of *H6*-EntE-bound 2,3-DHB by *H6*-EntB indicates that the EC_{50} of the EntB-EntE interaction is 1.5 μM, assuming that the observed decrease in fluorescence is due to the EntB-EntE interaction affecting the positioning of 2,3-DHB binding in the *H6*-EntE active site and thus its ability to fluoresce at 440 nm. Representative fluorescence emission spectra are shown for mixtures of 2.5 μM *H6*-EntE and 50 μM 2,3-DHB in the absence of *H6*-EntB (Figure 6b, solid black circles) and in the presence of 3 μM *H6*-EntB (Figure 6b, white circles).

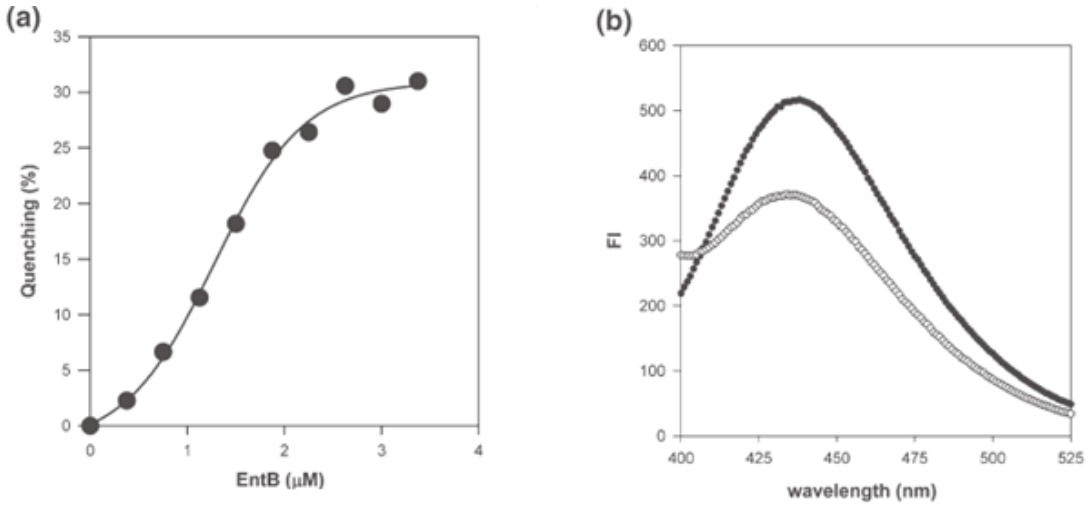

Figure 6: Binding of *H6*-EntB to *H6*-EntE in the presence of 2,3-DHB.

(a) Percentage quenching of the 440 nm H6-EntE-2,3-DHB FRET signal as a function of H6-EntB concentration. Data were fit to a sigmoidal curve describing cooperative binding using SigmaPlot. (b) Fluorescence emission spectra (λ_{ex} = 280 nm) of H6-EntE (2.5 μM) and 2,3-DHB (50 μM) in the absence of H6-EntB (black circles) and in the presence of 3 μM H6-EntB (white circles).

Circular dichroism (CD) was used to measure protein structural changes occurring upon mixture of *H6*-EntE and *H6*-EntB in the presence or absence of 2,3-DHB. All spectra in which proteins were mixed with 2,3-DHB were corrected for ellipticity signal contributions from 2,3-DHB in the absence of protein. Far-UV CD spectra revealed that both *H6*-EntE (Figure 7A, blue circles) and *H6*-EntB (Figure 7A, red circles) in solution exhibited similar major ellipticity minima at 210 nm and 222 nm. The addition of a saturating concentration of 2,3-DHB to *H6*-EntE (Figure 7B, blue circles) did not significantly alter its far-UV CD spectrum, indicating no large changes in secondary structure occurred upon substrate binding. A decrease in the ellipticity minima in the *H6*-EntB spectrum was observed upon the addition of 2,3-DHB (Figure 7B, red circles). Far-UV spectra were also obtained for mixtures of *H6*-EntE and *H6*-EntB in the presence and absence of 2,3-DHB. Spectra of the {*H6*-EntE+*H6*-EntB} mixtures in which the *H6*-EntB signals were subtracted revealed no significant changes in *H6*-EntE far-UV spectra in the presence or absence of 2,3-DHB (Figure 7A and 7B, cyan circles). In contrast, a spectrum of the {*H6*-EntE+*H6*-EntB} + 2,3-DHB mixture in which the *H6*-EntE signal was subtracted revealed a significant change in *H6*-EntB far-UV spectrum (Figure 7B, magenta circles).

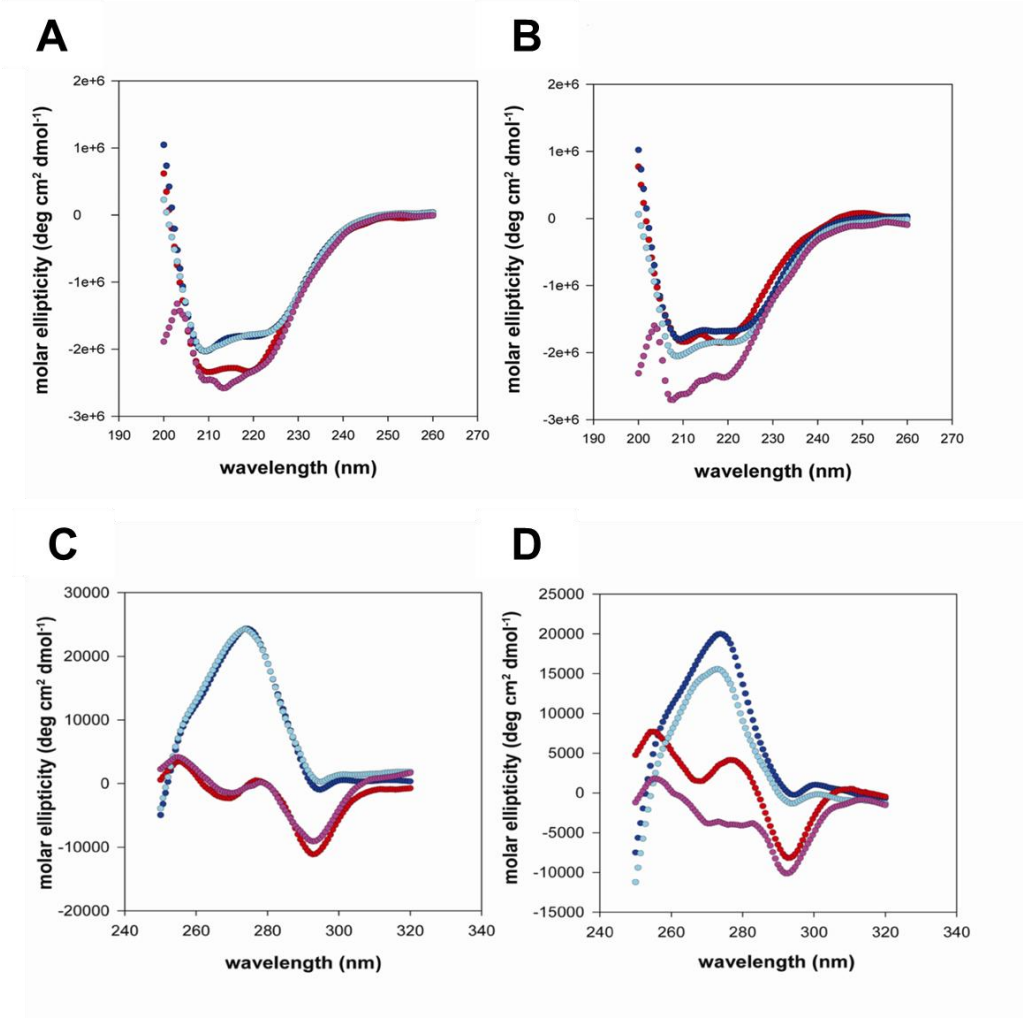

Figure 7: Circular dichroism spectra of *H6*-EntE and *H6*-EntB in the presence and absence of DHB.

(A) Far-UV circular dichroism spectra of protein solutions in the absence of 2,3-DHB: H6-EntE (blue circles); H6-EntB (red circles); mixture of {H6-EntE+H6-EntB} with H6-EntB signal subtracted (cyan circles); mixture of {H6-EntE+H6-EntB} with H6-EntE signal subtracted (magenta circles). (B) Far-UV circular dichroism spectra of protein solutions in the presence of 50 µM 2,3-DHB: H6-EntE (blue circles); H6-EntB (red circles); mixture of {H6-EntE + H6-EntB} with H6-EntB signal subtracted (cyan circles); mixture of {H6-EntE + H6-EntB} with H6-EntE signal subtracted (magenta circles). (C) Near-UV circular dichroism spectra of protein solutions in the absence of 2,3-DHB: H6-EntE (blue circles); H6-EntB (red circles); mixture of {H6-EntE+H6-EntB} with H6-EntB signal subtracted (cyan circles); mixture of {H6-EntE+H6-EntB} with H6-EntE

signal subtracted (magenta circles). (D) Near-UV circular dichroism spectra of protein solutions in the presence of 50 μM 2,3-DHB: H6-EntE (blue circles); H6-EntB (red circles); mixture of {H6-EntE+H6-EntB} with H6-EntB signal subtracted (cyan circles); mixture of {H6-EntE+H6-EntB} with H6-EntE signal subtracted (magenta circles).

The near-UV CD spectrum of *H6*-EntE in the absence of 2,3-DHB (Figure 7C, blue circles) indicates a dominant positive peak centered between 270 nm and 280 nm, indicative of contributions from tyrosine residues. This spectrum did not change when *H6*-EntE was mixed with 2,3-DHB (Figure 7D, blue circles). In the absence of 2,3-DHB, the *H6*-EntB near-UV spectrum (Figure 7C, red circles) revealed two minor positive peaks at 255 nm and 277 nm, and a major negative peak at 290 nm. In the presence of 2,3-DHB, the *H6*-EntB near-UV spectrum exhibits a similar overall shape, but with altered peak magnitudes compared to the –DHB spectrum (Figure 7D, red circles). As with our far-UV experiments, we collected near-UV spectra of {*H6*-EntE+*H6*-EntB} mixtures in the presence and absence of 2,3-DHB. The spectrum of the {*H6*-EntE+*H6*-EntB} –DHB mixture in which the *H6*-EntB signal was subtracted (Figure 7C, cyan circles) revealed no major change relative to the *H6*-EntE spectrum (Figure 7C, blue circles). We observed a small reduction in overall ellipticity of the {*H6*-EntE+*H6*-EntB} +DHB spectrum after subtraction of the *H6*-EntB signal (Figure 7D, cyan circles) when compared to the *H6*-EntE spectrum (Figure 7D, blue circles). In contrast, large changes in the peak amplitudes at 255 nm and 277 nm were observed in a spectrum of the {*H6*-EntE+*H6*-EntB} mixture in which the *H6*-EntE signal was subtracted (Figure 7D, magenta circles) compared to the *H6*-EntB +DHB spectrum obtained in the absence of H6-EntE (Figure 7D, red circles).

H6-EntB Bait Protein Efficiently Pulls Down Chromosomally-Expressed *E. coli* EntE Only in the Presence of Exogenous 2,3-DHB

To investigate the ability of our recombinantly expressed *H6*-EntB to form complexes with *E. coli* partner proteins *in situ*, we used *H6*-EntB as a bait protein to pull down chromosomally-expressed interacting partners from lysates of *E. coli* cells grown in M63 minimal media in the presence of the iron chelator 2,2'-dipyridyl. This iron-depleted media condition was employed in order to induce expression of chromosomally-encoded enterobactin biosynthetic proteins by derepression of Fur. Pull down assays were achieved by binding *H6*-EntB bait protein to Co^{2+}-chelate resin, flowing over cell lysates, and gently washing away unbound proteins. When exposed to lysates pre-incubated with exogenous 2,3-DHB, the *H6*-EntB bait protein was able to pull down a major protein band migrating at approximately 60 kDa as determined by SDS-PAGE analysis (Figure 8, band 'd'), which corresponds to the molecular weight of *E. coli* EntE. In the absence of exogenous 2,3-DHB, a minor band migrating at this position was observed to be pulled down (Figure 8, lane -DHB, band 'a'). Bands migrating at approximately 34 kDa, the expected molecular weight of *H6*-EntB, were observed +/- exogenous 2,3-DHB (Figure 8, bands 'b' and 'e'). Below this band, we also observed a second major band migrating at approximately 25 kDa (Figure 8, bands 'c' and 'f').

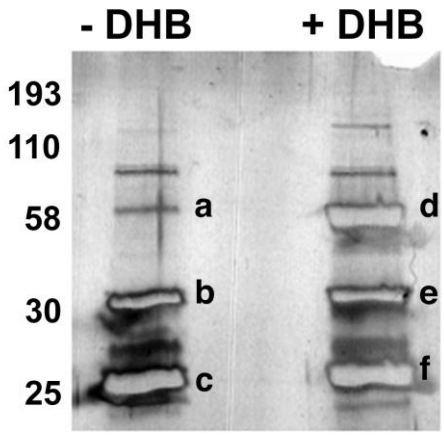

Figure 8: Pull-down assay of proteins binding to *H6*-EntB bait.
Silver-stained 10% SDS-polyacrylamide gel of proteins eluted from Co^{2+}-chelate beads. Numbers to left of gel represent positions of bands of known molecular weight markers (not shown). Lane '-DHB': proteins isolated from beads exposed to lysate of iron-starved E. coli BW25113 with no exogenously added 2,3-DHB. Lane '+DHB': proteins isolated from beads exposed to lysate of iron-starved E. coli BW25113 cells with exogenously-added 2,3-DHB (100 µM). The identity of proteins in bands 'b'-'f' were determined by LC-MS/MS analysis of bands excised from gel. Bands 'a' and 'd': E. coli EntE; Bands 'b' and 'e': E. coli EntB; Bands 'c' and 'f': E. coli EntB (proteolysed).

We were able to perform mass spectrometry analysis on tryptic peptides recovered from the proteins corresponding to bands 'b'-'f'; all other bands contained insufficient amounts of protein for this analysis. Table 1 shows the peptides recovered from bands 'd', 'e', and 'f' shown in Figure 8; all of these peptides were obtained from lysates spiked with exogenous 2,3-DHB prior to pull-down. Peptides corresponding to EntE in band 'd' (Table 1, rows 3-21) represent 57% total EntE sequence coverage. Peptides corresponding to EntB in band 'e' (Table 1, rows 22-37) represent 66% total EntB sequence coverage. Peptides corresponding to EntB in band 'f' (Table 1, rows 38-41) represent 18% total EntB sequence coverage. Peptides were also recovered from

bands ‘a’-‘c’ obtained from –DHB samples (data not shown). In the absence of exogenous 2,3-DHB, no peptides corresponding to EntE could be identified by mass spectrometry, although the silver-stained gel shows a faint band (Figure 8, band ‘a’) at its expected position. The low amount of protein in this band likely resulted in poor peptide recovery such that any EntE signals were below the sensitivity threshold of the mass spectrometer. Mass spectrometry data of peptides recovered from band ‘b’ (-DHB) were comparable to peptides recovered from band ‘e’ (+DHB) (57 peptides corresponding to EntB, representing 78% sequence coverage). Consistent with our analysis of band ‘f’, twelve peptides corresponding to EntB were also obtained from band ‘c’ (-DHB), representing 30% sequence coverage.

Table 1.: MASCOT analysis of peptides recovered from pull-down assay of iron-depleted *E. coli* BW25113 lysates and identified by mass spectrometry.

Band on Gel[a]	DHB[b]	Protein	Residue Range	Delta Avg. (Da)[c]	Frequency[d]
d	+	EntE	8 – 14	0.2490	2
d	+	EntE	20 – 33	0.2722	20
d	+	EntE	34 – 47	0.3206	7
d	+	EntE	53 – 66	0.2264	16
d	+	EntE	96 – 109	0.6179	8
d	+	EntE	110 – 128	0.3726	11
d	+	EntE	129 – 150	0.2852	1
d	+	EntE	203 – 212	0.1955	3
d	+	EntE	213 – 225	0.4819	1
d	+	EntE	271 – 296	0.2850	5
d	+	EntE	312 – 343	0.4175	1
d	+	EntE	320 – 343	0.4190	33
d	+	EntE	351 – 382	0.4925	2
d	+	EntE	397 – 430	0.4962	2
d	+	EntE	442 – 453	0.2739	39
d	+	EntE	454 – 473	0.2801	3
d	+	EntE	474 – 481	0.2641	1
d	+	EntE	503 – 520	0.4018	2
d	+	EntE	507 – 520	0.2502	5
e	+	EntB	6 – 21	0.4196	2
e	+	EntB	22 – 30	0.2724	5
e	+	EntB	69 – 81	0.4872	2
e	+	EntB	89 – 101	0.3311	15
e	+	EntB	112 – 123	0.3618	15
e	+	EntB	112 – 125	0.2588	1
e	+	EntB	132 – 139	0.2146	1
e	+	EntB	144 – 167	0.2988	3
e	+	EntB	168 – 183	0.2271	7
e	+	EntB	200 – 215	0.4174	17
e	+	EntB	220 – 247	0.4461	18
e	+	EntB	220 – 254	0.6332	1
e	+	EntB	257 – 269	0.2950	2
e	+	EntB	257 – 269	0.2950	2
e	+	EntB	258 – 269	0.2689	2
e	+	EntB	270 – 278	0.2102	3
f	+	EntB	6 – 21	0.2932	1
f	+	EntB	22 – 30	0.2004	1
f	+	EntB	112 – 123	0.2211	2
f	+	EntB	200 – 215	0.2270	1

[a] see Figure 8; [b] exogenous 2,3-DHB added to lysate prior to pull-down; [c] |(observed peptide mass) – (expected peptide mass from sequence)|; [d] frequency of observed peptide recovered from gel slice.

Discussion

The *E. coli* enzyme EntE is an essential component of the enterobactin biosynthetic pathway. Recently this protein has been the focus of studies probing ligand binding specificity (*134, 200*) as well as identifying novel compounds that can act as tight-binding EntE inhibitors (*127*). From previously reported kinetic characterizations we know that the release of the product 2,3-DHB-AMP is slow and rate-determining. By isothermal titration calorimetry we determined a direct, unambiguous measurement of the equilibrium binding constant (K_D) of 2,3-DHB binding to EntE (7.3 μM). This value is approximately three-fold higher than the reported 2,3-DHB K_m value (2.7 μM) (*141*). It should be noted that the reported K_m value was determined in the presence of ATP substrate as well as 2,3-DHB. If we assume that the reported K_m reflects 2,3-DHB binding affinity during the EntE-catalyzed reaction in the presence of all substrates, then our higher K_D value for 2,3-DHB binding (obtained in the absence of ATP) suggests that ATP binding and subsequent closure of the P-loop reduces 2,3-DHB dissociation, thus potentiating formation of the 2,3-DHB-AMP product. Although an equilibrium binding constant has not been reported for 2,3-DHB-AMP binding to EntE, it has been found to be a competitive inhibitor of the substrate, with a K_i value of 4.5 nM (*186*). It is clear from our data, in conjunction with these previous findings, that the binding affinity of EntE for the 2,3-DHB substrate is much lower than that for the 2,3-DHB-AMP product. High-affinity binding of the 2,3-DHB-AMP product to EntE ensures its efficient channeling to the *holo*-EntB ArCP domain. That the affinity of binding of the 2,3-DHB substrate is lower than that of the product suggests that considerable dissociation of the substrate to the bulk phase might occur prior to its adenylation. However, it is likely that

subsequent binding of the ATP co-substrate with closure of the P-loop would prevent this dissociation.

Our fluorescence emission spectra of *H6*-EntE showed that in the absence of 2,3-DHB there is a single emission maximum at 330 nm upon excitation at 280 nm. When we added 2,3-DHB to *H6*-EntE, we observed a new and large emission peak at 440 nm upon excitation at 280 nm, the wavelength of maximal tyrosine excitation. Based on our experimental observations coupled with insights from our EntE homology model, we conclude that this emission peak is due to fluorescence resonance energy transfer (FRET) between EntE intrinsic fluorophore donors and the bound 2,3-DHB acceptor. In the absence of *H6*-EntE, we observe that 2,3-DHB emits maximally at 440 nm with a maximal excitation wavelength of 306 nm. Thus there is a spectral overlap between EntE intrinsic tyrosine fluorescence emission (λ_{em} = 305 nm) and our observed 2,3-DHB excitation maximum. Our fluorescence excitation spectra did not reveal a significant shift in the 2,3-DHB excitation maxima when the substrate is bound to EntE (there is a slight 3 nm red shift in 2,3-DHB λ_{ex} to 309 nm) indicating that observed fluorescence at 440 nm is not due to an alteration in the fluorescence properties of 2,3-DHB itself when bound to the EntE active site. When we collected spectra at an excitation wavelength of 275 nm instead of 280 nm, we observed an increase in the 440 nm peak, not a decrease. This suggests that the FRET signal we observe is mostly due to excitation by instrinsic tyrosine donors proximal to the EntE active site, although we cannot rule out some contribution to the FRET signal by more distal tryptophan donors. Regardless of the exact nature of the EntE FRET donor residues, it is clear that the increase in observed fluorescence emission at 440 nm is due to 2,3-DHB binding to *H6*-EntE. This increase is

saturable with increasing 2,3-DHB concentrations and follows hyperbolic single-site binding behavior that allowed us to obtain an EC_{50} value of 2,3-DHB binding to *H6*-EntE that agrees with our ITC outcomes.

Until now, our knowledge of the exact residues involved in EntE substrate binding has been limited. According to our EntE homology model, 2,3-DHB binds in an active site cavity proximal to five tyrosine residues. The closest of these residues is EntE Y236, which appears to be able to form a stacking interaction with the aromatic moiety of 2,3-DHB. In the DhbE structure, Y236 does indeed stack with bound 2,3-DHB. In our EntE model the Y236 aromatic ring is orthogonal to the 2,3-DHB aromatic moiety, although the model indicates that the tyrosine side-chain has sufficient rotational degrees of freedom to facilitate stacking. In addition to Y236, our homology model reveals additional EntE residues that we predict to be involved in 2,3-DHB binding. In the DhbE structure, residues H234 and K517 stabilize the carboxylate moiety of the substrate (*184*). In our model, the side chains of EntE residues H233 and K519 superimpose with these DhbE carboxylate-binding residues, predicting their role in substrate binding in the EntE active site. In addition, our model predicts that EntE residues N234 and S239 bind the 2- and 3-hydroxyl groups of 2,3-DHB. Here it is worth noting that our ITC data show that binding of 2,3-DHB to EntE has a negative entropy component. Binding of 2,3-DHB to EntE is therefore enthalpy driven, and not primarily due to hydrophobic stacking interactions with Y236. This is supported by our fluorescence studies that clearly show that EntE specifically binds 2,3-DHB. Neither 2,5-DHB nor 3,5-DHB upon mixture with *H6*-EntE cause a quenching of intrinsic *H6*-EntE fluorescence, nor do these isomers generate a FRET signal at 440 nm upon excitation at 280 nm. The selectivity of *H6*-EntE

binding to 2,3-DHB can be explained by the side-chain positions of the hydrogen bond donors N234 and S239 relative to the bound substrate as predicted by our model. In contrast, C5 of the bound 2,3-DHB is proximal to a loop containing EntE residues V306, G307, G308. None of these residues could stabilize a DHB isomer containing a hydroxyl group at position C5. Based on our model, in conjunction with our experimental data, we propose that EntE residues N234 and S239 are essential for determining EntE substrate-binding specificity.

Two recent studies have suggested that misacylation of EntB may occur due to the ability of EntE to adenylate non-physiological DHB isomers. In the one study, a ~ 30% reduction in *in vitro* enterobactin biosynthesis was observed when 1,500 µM 2,4-DHB and 3,4-DHB were mixed with 2,3-DHB in a cell-free assay, showing that misacylation interfered with downstream NRPS processes (*200*). In the other study, it was found that *holo*-EntB could be acylated with 2,4-DHB and 3,4-DHB when in the presence of EntE and 500 µM of either DHB isomer (*134*). In these experiments, the concentrations of DHB isomers used was far in excess of the K_D of 2,3-DHB binding to EntE as determined by ITC in this study. Our fluorescence experiments do not indicate any binding of 2,5-DHB or 3,5-DHB to EntE at what is likely to be a more physiologically relevant concentration (50 µM), although the possibility remains that binding of these isomers may have occurred in a manner such that a FRET signal was not generated. While *H6*-EntE is selective for 2,3-DHB binding under our experimental conditions, we found that all DHB isomers examined (2,3-DHB, 2,5-DHB, and 3,5-DHB) were able to quench *H6*-EntB intrinsic fluorescence to some degree. It is significant that 2,3-DHB was found to quench *H6*-EntB intrinsic fluorescence most efficiently,

suggesting a binding preference for this isomer. Our far-UV and near-UV circular dichroism data also established that 2,3-DHB can bind to *H6*-EntB, resulting in conformational changes to the enzyme. These results were unexpected, since 2,3-DHB is not a substrate for the ICL domain of EntB nor the ArCP domain. Based on our results, we propose that EntB may possess an allosteric site that binds 2,3-DHB to regulate 2,3-DHB synthesis by feedback inhibition. It is reasonable that EntB would be a target for such regulation, since EntC, the first enzyme in the pathway, has been shown to be highly reversible (*174*). Given its reversibility, it is unlikely that the conversion of chorismate to isochorismate is the committed step of enterobactin biosynthesis, which would make the EntB-catalyzed conversion of isochorismate to 2,3-dihydro-dihydroxybenzoate the likely first committed step of the pathway. Our data suggest that not only could the 2,3-DHB module be feedback-attenuated in the presence of excess intracellular 2,3-DHB binding to EntB, but also that interaction with EntE would be promoted through ligand-induced conformational changes in EntB, thus enhancing NRPS and enterobactin formation further decreasing intracelluar 2,3-DHB levels.

We used the FRET signal generated by 2,3-DHB binding to the EntE active site as a tool to measure interaction of *H6*-EntE with *H6*-EntB. We found that addition of *H6*-EntB to a solution of *H6*-EntE saturated with 2,3-DHB resulted in significant quenching of the observed 2,3-DHB-EntE FRET signal. We conclude that this quenching reflects a conformational change in the EntE active site upon interaction with EntB, resulting in alterations to the geometry and distance of the bound 2,3-DHB substrate relative to intrinsic EntE FRET donor residues and a subsequent decrease in the FRET signal. We observed that upon increasing EntB concentration, the 2,3-DHB-EntE FRET signal

decreases until apparent saturation is achieved. Saturation of the quenching effect cannot be simply due to sequestration of 2,3-DHB as a result of its binding to *H6*-EntB, since the concentration of 2,3-DHB (50 μM) was far greater than the concentration of *H6*-EntB (3 μM) used in this assay. Our fluorescence data describing the EntE-EntB interaction fit to a sigmoidal curve, suggesting positive binding cooperativity. The EntB concentration at which quenching of the FRET signal is half-maximal gives us an EC_{50} value of the interaction affinity, which is in the low micromolar range, suggesting that EntE and EntB interact transiently. Since EntB must deliver acylated 2,3-DHB to EntF during NRPS, low-affinity protein-protein interactions would allow EntB to interact in an asynchronous manner with both upstream and downstream partners in the NRPS assembly line. We also found that mixture of *H6*-EntB with *H6*-EntE in the presence of 2,3-DHB resulted in additional changes in near-UV CD signal intensities at wavelengths corresponding to contributions from aromatic chromophores in each protein. Such changes in the near-UV CD signal is generally due to alterations in the local environment of aromatic amino acids contributing to the signal. We therefore conclude that our observed changes in the near-UV CD signals of *H6*-EntE and *H6*-EntB upon their mixture in the presence of 2,3-DHB are due to conformational rearrangements upon formation of the EntE-EntB interaction interface. These rearrangements may include conformational alterations of surface-exposed aromatic residues at the interface upon entering a more symmetric and ordered environment, and/or gross structural rearrangements in the EntB protein upon interaction with EntE.

Our pull-down assays establish that the EntB-EntE interaction can occur *in situ* between *H6*-EntB and chromosomally-expressed *E. coli* EntE. Furthermore, the presence

of exogenously added 2,3-DHB greatly enhances the efficiency of EntE pull down by *H6*-EntB. This is consistent with our CD data, which show gross EntB conformational rearrangements upon mixture with EntE only when 2,3-DHB is present. The binding of 2,3-DHB to EntE appears to subtly alter the surface of EntE in such a way that an EntB-EntE interaction interface is optimized. The conformational rearrangements in *H6*-EntB observed by circular dichroism at both secondary- and tertiary-structure levels occur as a consequence of its interaction with substrate-loaded EntE. Our pull-down data show that binding of chromosomally-expressed EntE to *H6*-EntB bait is greatly enhanced in the presence of exogenously added (100 μM) 2,3-DHB, confirming that efficient formation of the EntE-EntB complex depends on ligand-loaded EntE and EntB.

That efficient pull-down did not occur in the absence of exogenously added 2,3-DHB strengthens our argument that the pool of free intracellular 2,3-DHB is normally low, presumably due to its direct channeling through the enterobactin biosynthetic machinery. Some further insights into EntB conformational flexibility may be obtained from our pull-down data. On our SDS-polyacrylamide gel of pull-down products, we observed bands at approximately 25 kDa (Figure 8, bands 'c' and 'f') containing EntB peptides. We conclude that this is the result of EntB proteolysis. The ArCP domain of EntB resides between residues 214 – 285. The most C-terminal EntB peptide that we observed by mass spectrometry comprises residues 200 – 215 (Table 1, row 41). Although only five peptides were recovered from the 25-kDa band obtained in the presence of exogenous 2,3-DHB, we also recovered 12 peptides from the 25-kDa band pulled down in the absence of DHB (Figure 8, band 'c', -DHB). The most C-terminal EntB peptide from this dataset also corresponded to residues 200 – 215. Band 'c'

therefore corresponds to the ICL domain of EntB, with proteolysis likely occurring in the linker region between the EntB ICL and ArCP domains. This suggests that in solution the interdomain region of EntB is solvent-exposed and flexible, and may thus play a role in EntB conformational rearrangements. It is also worth noting that we have measured EntE-EntB interaction in the absence of ATP, implying that ATP can still access the EntE active site subsequent to formation of the EntE-EntB complex. This opens up some intriguing lines of inquiry regarding the order of substrate binding and protein interaction.

In this study we have shown that binding of 2,3-DHB to the *E. coli* enterobactin biosynthetic enzyme EntE can be measured in a rapid and sensitive manner using fluorimetry. Observed changes in intrinsic EntE fluorescence upon binding of 2,3-DHB can be clearly explained by the spatial distribution of tyrosine and tryptophan residues predicted by our homology model of the EntE structure. EntE and homologous AMP ligases from pathogenic bacteria are becoming targets for the development of novel synthetic inhibitors that rely on the high affinity of binding of DHB-AMP product (*186-187*). Fluorescence-based assays of the binding of DHB-like analogues, or of the inhibition of 2,3-DHB binding in the case of non-fluorescent inhibitors could result in a more high-throughput approach to the development of such drugs. The fluorescence phenomenon that we have reported here also allows us to use 2,3-DHB as a reporter of the EntE active site environment. Most importantly, we used this fluorescence phenomenon to measure the interaction of EntE with its immediate downstream enzymatic partner EntB. Taken together, our data show that EntE only interacts efficiently with EntB in the presence of 2,3-DHB. This transient complex is formed presumably to facilitate channeling of 2,3-DHB-AMP. Our results lead us to hypothesize

that the enterobactin biosynthetic machinery has evolved to minimize free intracellular 2,3-DHB, which may be toxic to the bacterium (e.g., by inhibiting chorismate-dependent cellular processes such as aromatic amino acid biosynthesis), or which may inhibit other aspects of enterobactin biosynthesis and secretion (e.g., competing with enterobactin for binding to recognition sites on the efflux transporter EntS).

CHAPTER THREE: A PROTEIN-PROTEIN INTERACTION FACILITATES CONFORMATIONAL REMODELING OF THE *ESCHERICHIA COLI* 2,3-DIHYDROXYBENZOATE-AMP LIGASE (ENTE) ACTIVE SITE BY 2,3-DIHYDRO-2,3-DIHYDROXYBENZOATE DEHYDROGENASE (ENTA)

The previous chapter focused on EntE interaction with its downstream partner protein EntB. In this chapter, a novel EntE interaction with its upstream partner protein EntA was characterized. All the protein-protein interactions involved in enterobactin biosynthesis up to this point were localized to the NRPS module (*142, 181, 195, 197, 206*). Here, for the first time the EntA-EntE interaction was detected, establishing a direct link between the functional modules of enterobactin biosynthesis (the DHB and the NRPS modules). Methods used in this chapter included AUC, fluorescence spectroscopy, fluorescence polarization, crosslinking, pull-down assays, and enzymatic assays. In this chapter, we also revealed that EntA-EntE interaction is likely dependent on EntA conformation.

The manuscript of this chapter has been accepted for publication in Biochemistry under the title: "Enzymatic Adenylation of 2,3-Dihydroxybenzoate is Enhanced by a Protein-Protein Interaction Between *Escherichia coli* 2,3-Dihydro-2,3-Dihydroxybenzoate Dehydrogenase (EntA) and 2,3-Dihydroxybenzoate-Amp Ligase (EntE)" Sofia Khalil and Peter D. Pawelek. (2010).

Summary

The *E. coli* siderophore enterobactin is synthesized in response to iron starvation. EntA produces 2,3-dihydroxybenzoate (2,3-DHB), an enterobactin biosynthetic intermediate. EntE then adenylates 2,3-DHB, activating it for attachment to EntB. Using sedimentation velocity analytical ultracentrifugation we found that *H6*-EntA undergoes concentration-dependent dimer-tetramer self-association (K_D = 12.3 μM). We further found that EntA can form a specific complex with its downstream partner EntE. Pull-down assays revealed that recombinant *H6*-EntA bait could pull down EntE from *E. coli* lysates, whereas recombinant *H6*-EntE bait could pull down both EntA and EntB from lysate in the presence of 2,3-DHB. Addition of the crosslinker SMCC to a mixture of *H6*-EntA and *H6*-EntE resulted in a crosslinked product with a size greater than 250 kDa, suggesting a complex stoichiometry of one EntA tetramer and four EntE monomers. The effect of EntA on EntE activity was also examined. Addition of a 4-fold excess of *H6*-EntA to an *H6*-EntE assay mixture resulted in a 6-fold stimulation of *H6*-EntE activity. *H6*-EntA was also found to perturb the FRET signal between *H6*-EntE donor residues and *H6*-EntE-bound 2,3-DHB. By following the EntA-dependent decrease in the *H6*-EntE–2,3-DHB FRET signal, EntA–EntE binding behavior was found to be sigmoidal, suggesting positive cooperativity in the interaction (Hill coefficient = 3.66; $K_{0.5}$ = 1.94 μM). Taken together, our results establish that EntA and EntE form a complex that optimizes EntE catalysis by active site remodeling. The observed sigmoidal binding behavior is likely due in part to higher-affinity binding of EntE to tetrameric EntA.

Introduction

Under iron-limiting conditions, most bacteria synthesize and secrete small molecules known as siderophores in order to obtain iron from the extracellular environment (*24*). Siderophores, and the proteins involved in their synthesis, secretion, and modification are considered virulence factors in many pathogenic bacteria (*60, 166, 207-209*). In extraintestinal environment, *Escherichia coli* obtains ferric iron predominantly *via* the biosynthesis and secretion of enterobactin, a catecholate-type siderophore (*35, 130*). Enterobactin consists of three 2,3-dihydroxybenzoic acid (2,3-DHB) moieties linked by amide bonds to three L-serine subunits cyclized in a triserine trilactone core (Scheme 1A). High-affinity chelation occurs through the hexadentate coordination of the three 2,3-DHB catechol groups of enterobactin to one Fe^{3+} atom (association constant ~ $1x10^{50}$ M^{-1}) (*75*). This extraordinary affinity for ferric iron is needed to effectively scavenge low-abundance extracellular Fe^{3+}, and to compete with high-affinity chelators such as mammalian serum transferrin (*210*).

The biosynthesis and secretion of enterobactin requires the proteins expressed from eight genes (*entA-F*, *entH*, and *entS*). Proteins encoded by the genes *fepA-G* then facilitate TonB-dependent uptake of ferric-enterobactin from the extracellular environment. These genes are all under the control of the Fur repressor, such that expression is only up-regulated when levels of intracellular iron are low (*137, 211-212*). Enterobactin biosynthesis involves six enzyme activities that can be broadly grouped into two major arms that are functionally distinct. The DHB synthesis arm includes the activities of EntC (*199*), EntB (N-terminal isochorismate lyase (ICL) domain) (*213*), and EntA (*140*); these activities function sequentially to catalyze the conversion of

chorismate into 2,3-DHB. The NRPS arm includes the activities of EntD (*194*), EntE (*214*), EntB (C-terminal aryl carrier protein (ArCP) domain), and EntF (*215*); activities in the NRPS arm function in concert to condense the three molecules each of 2,3-DHB and L-serine into one enterobactin molecule (*82, 142*). EntH has been shown to be a proofreading activity that ensures proper acylation of EntB during the NRPS process (*134, 200*). The inner-membrane protein EntS secretes enterobactin from the cytoplasm into the periplasm, and is necessary for efficient enterobactin export (*107*).

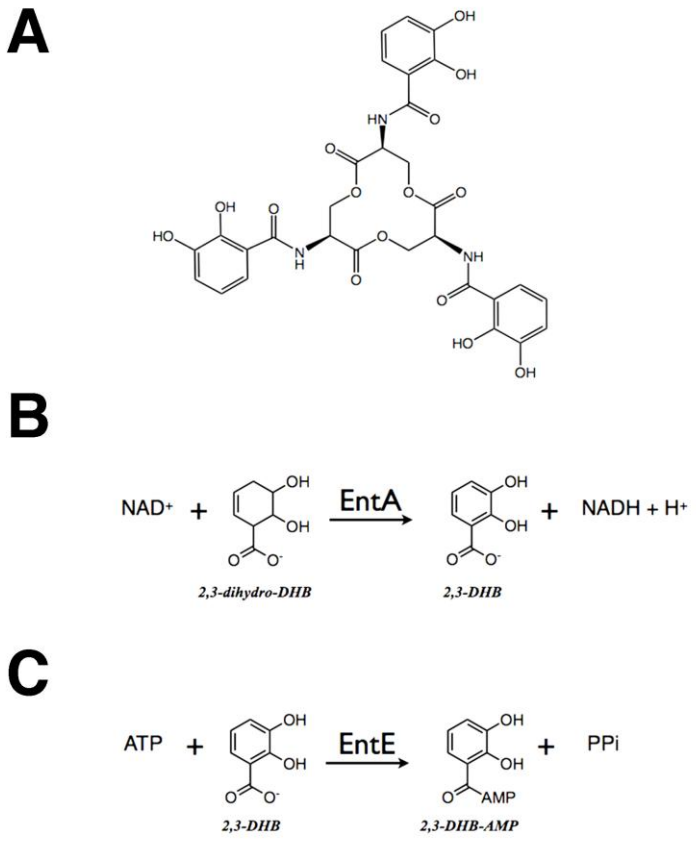

Scheme 1: (A) Chemical structure of enterobactin. (B) Reaction catalyzed by *E. coli* EntA. (C) Reaction catalyzed by *E. coli* EntE.

We now know that the majority of proteins in a cell form specific complexes with one or more partner proteins in order to carry out their biological activities, and many such interactions are now targets in the development of novel chemotherapeutics (*216-219*). To what extent do protein-protein interactions play a role in enterobactin biosynthesis? Protein interactions within the NRPS arm have already been reported (*142, 144, 181, 197, 206*). EntE activity has been shown to be significantly enhanced (~10-fold increase in k_{cat}) in the presence of phoshopantetheinylated EntB (*i.e.*, *holo*-EntB) (*144*). Residues comprising the EntB–EntE interaction interface have been identified through mutagenic studies (*181*). We have recently reported that EntE–EntB complexation is optimal in the presence of exogenous 2,3-DHB, and that the EntE–EntB interaction was of relatively low affinity (EC_{50} ~ 1.5 μM) (*206*). Evidence of an EntB–EntF interaction has also been reported involving the participation of the EntB C-terminal aryl carrier protein (ArCP) domain (*142*).

The enzymes EntA and EntE are found at the interface of the two major arms of enterobactin biosynthesis. EntA (2,3-dihydro-2,3-dihydroxybenzoic acid dehydrogenase; E.C. 1.3.1.28) catalyzes the final reaction in the DHB synthesis arm (Scheme 1B). EntA has a subunit molecular mass of 26,249 Da (*140*). The EntA crystal structure revealed EntA to be tetrameric, being composed of a dimer of dimers (*183*). EntE (2,3-dihydroxybenzoic acid-AMP ligase; E.C. 2.7.7.58) catalyzes the first reaction in the NRPS arm by activating 2,3-DHB, the product of EntA, through ATP-dependent adenylation (Scheme 1C). EntE has a subunit molecular mass of 59,112 Da and is monomeric, being a member of the adenylate-forming family of enzymes (*131, 141, 184, 187*). The EntE-catalyzed activation of 2,3-DHB facilitates its attachment to the

phosphopantetheine moiety of the downstream NRPS enzyme *holo*-EntB. The EntE catalytic mechanism has been elucidated in a recent report showing that EntE catalyzes two half-reactions in a bi-uni-uni-bi ping-pong mechanism: (*i*) in the first half reaction 2,3-DHB binds to EntE followed by the co-substrate ATP. 2,3-DHB is then adenylated followed by release of pyrophosphate (PPi); (*ii*) in the second half-reaction, EntE-2,3-DHB-AMP binds to *holo*-EntB resulting in transfer of 2,3-DHB to the phosphopantetheine group on EntB Ser245, thus producing *acyl-holo*-EntB, and this is followed by release of AMP from EntE (*189*). Interestingly, it has also shown that in the absence of *holo*-EntB, EntE catalyzes the slow production of P^1,P^3-diadenosine-5'-tetraphosphate (Ap4A), a molecule that is involved in modulation of cellular stress (*188*). This highlights not only the importance of the EntE–EntB interaction during normal enterobactin biosynthesis, but also a potential protective role for EntE when expressed in the absence of EntB.

Here we report the first evidence of a protein-protein interaction between the sequentially related enzymes EntA and EntE, thus establishing a direct, physical link between the DHB synthesis and NRPS arms of enterobactin biosynthesis. Through the use of various *in vitro* assays, we show that EntA and EntE specifically interact to form a protein-protein complex. The nature of this interaction appears to be significantly affected by the oligomeric structure of EntA, which undergoes a concentration-dependent transition from dimer to tetramer at low-micromolar concentrations. Reminiscent of the effect of EntB interaction on EntE activity, we report here that the EntA–EntE interaction also results in stimulation of EntE activity through a conformational remodeling of the EntE active site. EntA exerts an activating role in first half-reaction (2,3-DHB

adenylation), similar to how EntB exerts an activating role in the second half-reaction (2,3-DHB transfer to *holo*-EntB). EntE activity therefore appears to be optimal when the enzyme is assembled into a protein complex, either EntA–EntE or EntE–EntB. The discoveries reported here further highlight the integral role of protein-protein interactions in networking the enterobactin biosynthetic pathway.

Materials and Methods

Reagents

Most reagents were purchased from Bioshop Canada, Inc. (Burlington, Ont.). 2,3-dihydroxybenzoic acid (2,3-DHB) was purchased from Sigma-Aldrich (St. Louis, Mo.). Inorganic pyrophosphatase was purchased from Invitrogen (Carlsbad, Ca.).

Protein Expression and Purification

Hexahistidine-tagged EntA (*H6*-EntA) and EntE (*H6*-EntE) were purified from *Escherichia coli* AG-1 cells (obtained from the ASKA repository (*205*) harboring appropriate pCA24N-based expression constructs. Each protein was expressed with an in-frame hexahistidine tag and spacer region at the N-terminus (MRGSHHHHHHTDPALRA...), and a short extension at the C-terminus (...GLCGR[STOP]). Recombinant *H6*-EntA and *H6*-EntE were overexpressed and purified using immobilized metal affinity chromatography as reported previously (*206*). In this study, all protein concentrations were determined by measuring absorbance at 280 nm and using molar extinction coefficients predicted from primary amino acid sequences (ε = 57,300 M^{-1} cm^{-1} and 20,970 M^{-1} cm^{-1} for EntE and EntA, respectively). Protein concentrations are reported as concentrations of monomer subunit unless otherwise indicated.

Analytical Ultracentrifugation

Sedimentation velocity experiments were performed in a Beckman XL-I analytical ultracentrifuge with a four-place An-60Ti rotor. Runs were initiated after extensive thermal equilibration (> 5 hr) of the rotor and sample-containing cells at 20 ^{o}C. Solutions containing 50 mM Tris (pH 7.5), 150 mM NaCl, 0.5 mM TCEP, and varying concentrations of *H6*-EntA or *H6*-EntE were centrifuged at 40,000 rpm over approximately 10h. A total of 250 absorbance scans were collected per run in which optical density at 280 nm was measured. Sedimentation velocity data were fit to *g*(*s**) and *g*^(*s**) distributions using the computer program DCDT+ (v2.2.1) (*220*). A number of scans (~ 17 scans per analysis) from each run were selected. Fits to *g*(s*) distributions were used for qualitative graphical comparison of concentration-dependent sedimentation behavior. Fits of *g*^(*s**) distributions (in which concentration distributions were not based on zero-time extrapolations), were used to quantitatively determine weight-averaged sedimentation coefficients. The program SEDPHAT (*221*) was used for global analysis of concentration-dependent EntA oligomerization. SEDPHAT global analysis was performed using four sedimentation velocity runs (*H6*-EntA at 2 μM, 4 μM, 8 μM, and 18 μM; 250 scans per run). The data were fit to the monomer-dimer self-association model of SEDPHAT, in which EntA dimer was modelled as the 'monomer' and EntA tetramer was modelled as the 'dimer', assuming that the *H6*-EntA dimer sedimented as a stable non-dissociating species over the concentration range examined, consistent with the reported EntA crystal structure in which EntA subunits are arranged as a dimer of dimers (*183*). Estimations of $S_{20,W}$ values for EntA dimer and EntA tetramer, which are required in the SEDPHAT global analysis, were obtained by hydrodynamic bead modeling using

the computer program HYDROPRO (*222*) with the EntA PDB structure (2FWM) as input (either all 4 chains of the tetrameric biological assembly, or the 2 chains from the structure that comprise the physiological dimer). The fit to the SEDPHAT self-association model was optimized using both simplex and Marquardt-Levenberg algorithms. For both DCDT+ and SEDPHAT analyses, the program SEDNTERP (v1.09) (*223*) was used as appropriate for estimation of the following parameters at 20 ^{o}C: solution viscosity, solution density, protein partial specific volumes (as predicted from primary amino acid sequences).

Pull-Down Assays

The ProFound Pull-Down PolyHis Protein:Protein Interaction Kit (Pierce, Rockford, IL) was used to study *in situ* interactions formed between hexahistidine-tagged recombinant bait proteins (*H6*-EntA or *H6*-EntE) and chromosomally-expressed prey proteins from *E. coli* lysates in the presence or absence of exogenous 2,3-DHB (100 µM). Pull-down assays were performed at room temperature as described previously (*206*). Bait proteins and co-eluting proteins were recovered and separated on 10% SDS-polyacrylamide gels. Proteins in bands excised from the gel were trypsinized and analyzed by LC-MS/MS at the McGill Mass Spectrometry Core Facility (McGill University, Montreal) as described previously (*206*).

Chemical Crosslinking

Recombinant proteins were covalently crosslinked using the Controlled Protein-Protein Crosslinking Kit (Pierce). In a typical crosslinking reaction, *H6*-EntA was dialyzed against phosphate-buffered saline (pH 7.2) and then incubated with a 50-fold molar excess of the heterobifunctional crosslinker sulfo-SMCC for 30 minutes at room

temperature. Purified maleimide-activated *H6*-EntA-SMCC conjugate (22 μM) was then incubated with purified *H6*-EntE (2.5 μM) for 60 minutes at room temperature. Crosslinking reactions were concentrated using Microcon YM-30 centrifugal filter units (Millipore). Concentrated proteins were then denatured and separated on a 10 % SDS-polyacrylamide gel. Peptides recovered from bands containing crosslinked proteins were analyzed by LC-MS/MS as described above.

Enzyme Activity Assays

A pyrophosphate release assay adapted from Rusnak *et al.* (*141, 144*) was used to monitor the effect of *H6*-EntA on *H6*-EntE activity. Reaction mixtures (100 μL total volume) containing *H6*-EntE (1 μM) and *H6*-EntA (0.25 μM and 4 μM), 0.2 units of *E. coli* inorganic pyrophosphatase, 75 mM Tris (pH 8.0), 10 mM $MgCl_2$, 5 mM ATP, 5 mM DTT, and 2 mM salicylate were incubated at 37 ^{o}C and aliquots were withdrawn at 30 sec time intervals. Inorganic phosphate produced by the coupled enzyme reactions was measured spectrophotometrically by mixture with an ammonium molybdate–malachite green solution, resulting in the formation of a chromophore that maximally absorbs at 620 nm (*224*). A control experiment was also performed in which EntE activity was assayed as above, but in the presence of 4 μM bovine serum albumin instead of *H6*-EntA. *H6*-EntE initial velocities were measured as the production of inorganic pyrophosphate as a function of time.

Fluorescence Spectroscopy

Fluorescence emission spectra (λ_{ex} = 280 nm) were collected at 20 ^{o}C using a Shimadzu RF-5301PC spectrofluorimeter. Solutions of *H6*-EntE (3 μM) plus 2,3-DHB (60 μM) in Buffer A (50 mM Hepes (pH 8.0) and 1.0 mM TCEP, 15% glycerol) with or without *H6*-EntA (3 μM) were supplemented with KCl to a final concentration of either 100 mM or 300 mM. Slit widths (excitation and emission) were set to 3 nm. Each spectrum presented is the average of 3 scans. Fluorescence emission data were corrected for background, dilution, and inner filter effects as appropriate.

Fluorescence Anisotropy

Fluorescence anisotropy measurements were performed on a Varian Cary Eclipse spectrofluorimeter equipped with automated polarizers. Measurements were collected for solutions containing Buffer A plus 100 mM KCl and supplemented with various combinations of 2,3-DHB (20 μM), *H6*-EntA (15 μM) and *H6*-EntE (7 μM). Measurements of 2,3-DHB fluorescence anisotropy in the presence and absence of proteins were collected in triplicate at 20 °C at wavelengths of maximal 2,3-DHB excitation and emission (310 nm and 440 nm, respectively). Anisotropy (*r*) values were calculated according to the following equation (adapted from Lakowicz (*225*)):

$$r = (I_{VV} - I_{VH}) / (I_{VV} + 2I_{VH}) \quad (1)$$

where I_{VV} is the fluorescence emission intensity read at 440 nm with polarizers positioned in a parallel orientation, and I_{VH} is the fluorescence emission intensity read at 440 nm with the polarizers in a perpendicular orientation.

Fluorescence-Based Equilibrium-Binding Assay

The 2,3-DHB–*H6*-EntE FRET signal (*206*) of solutions containing Buffer A plus 100 mM KCl, 3 μM *H6*-EntE, 60 μM 2,3-DHB, and varying concentrations of *H6*-EntA (0.5 μM to 7 μM) was measured as the fluorescence emission intensity of the solution monitored at 440 nm upon excitation at 280 nm. Fluorescence emission data were collected at 20 °C using a Varian Cary Eclipse spectrofluorimeter equipped with a Peltier temperature controller. Fluorescence emission intensities were corrected for inner-filter effects, dilutions, and background. To analyze equilibrium-binding data collected in these experiments, $[EntA]_{bound}$ and $[EntA]_{free}$ at a given $[EntA]_{total}$ were calculated from changes in *H6*-EntE-bound 2,3-DHB fluorescence emission intensity (ΔF) measured at 440 nm in the presence of varying concentrations of *H6*-EntA:

$$\Delta F = F_0 - F \qquad (2)$$

where F_0 is the corrected fluorescence emission intensity of 2,3-DHB bound to *H6*-EntE in the absence of *H6*-EntA, and F is the corrected fluorescence emission intensity of 2,3-DHB bound to *H6*-EntE at a given *H6*-EntA concentration.

Binding assays were performed in triplicate in order to determine mean values for changes in fluorescence intensities as a function of [EntA]. To normalize for slight variations in F_o between replicates, we expressed the change in fluorescence intensity ($\Delta F/F_0$) at a given $[EntA]_{total}$ by dividing this value by the maximal change in fluorescence intensity observed in a given replicate at a saturating concentration of *H6*-EntA ($(\Delta F/F_0)_{max}$). We define the resulting ratio as fractional binding: ($\Delta F/F_0$)/

$(\Delta F/F_0)_{max}$, where $(\Delta F/F_0)_{max}$ was obtained from plotting $(\Delta F/F_0)$ as a function of $[EntA]_{total}$ and fitting the plotted data to the equation describing a dose-response curve in Origin 8.1 (OriginLab Corp., Northampton, Mass.); the curve maxima obtained from these fits were used to determine $(\Delta F/F_0)_{max}$. We used fractional binding to directly relate the observed decrease in 2,3-DHB fluorescence emission at 440 nm to the fraction of *H6*-EntE in complex with *H6*-EntA, as shown below:

$$[EntA]_{bound} = [EntE]_{total} \times (\Delta F/F_0)/ (\Delta F/F_0)_{max} \quad (3)$$

In all fluorescence titration experiments in this study, $[EntE]_{total}$ was 3 µM. Since $[EntA]_{total}$ was experimentally determined by measuring OD_{280}, we derived the concentration of *H6*-EntA in the free fraction as follows:

$$[EntA]_{free} = [EntA]_{total} - [EntA]_{bound} \quad (4)$$

Equilibrium binding data were fit to the Hill equation:

$$(\Delta F/F_0)/ (\Delta F/F_0)_{max} = [EntA]_{free}^{n} / (K_{0.5}^{n} + [EntA]_{free}^{n}) \quad (5)$$

where n is the Hill coefficient, and $K_{0.5}$ is the concentration of $[EntA]_{free}$ at which 50% binding is observed. Non-linear fits of equilibrium-binding data to the Hill equation were performed using Origin 8.1

Results

Protein Expression and Purification

Preparations of recombinant, *H6*-EntA and *H6*-EntE were each expressed in *E. coli* AG-1 cells and purified by a single IMAC affinity chromatography step. The purity of proteins eluted from the IMAC columns were assessed by SDS-polyacrylamide gel electrophoresis and found to be near-homogeneous (purity > 95%). Yields obtained were typically in the range of 20-30 mg of purified protein per litre of culture.

Analytical Ultracentrifugation

We performed sedimentation velocity analytical ultracentrifugation (AUC) experiments on solutions of purified *H6*-EntA and *H6*-EntE in order to gain insights into the oligomeric state of these proteins as a function of concentration. We employed the program DCDT+ to perform model-independent, time-derivative $g(s^*)$ analyses of our sedimentation velocity data, resulting in a graphical representation of the abundance of sedimenting species as a function of $S_{20,W}$ (Figure 1). We observed that *H6*-EntE consistently sedimented as a monomer with a $S_{20,W}$ value of approximately 4.0, independent of *H6*-EntE concentration between 2.5 µM and 13 µM (Figure 1A). In contrast, large changes in *H6*-EntA sedimentation behavior were observed upon alteration *H6*-EntA concentration. Over a concentration range of 2 µM to 18 µM, *H6*-EntA sedimented as a single peak, but that peak position shifted significantly with increasing concentration (Figure 1B). Concentration-dependent changes in sedimentation coefficients of sedimenting species are indicative of reversible self-association occurring between sedimenting species during the AUC experiment. In such a situation, the $g(s^*)$ distribution reflects an averaged reaction boundary of the reversible association and not

to discrete sedimenting species (*226*). We used the *g*^(*s**) analysis function of DCDT+ to quantitatively determine $S_{20,W}$ values for *H6*-EntE and *H6*-EntA at different concentrations (Table 1). Consistent with our *g*(*s**) analyses, the $S_{20,W}$ of *H6*-EntE did not change significantly over the concentration range examined (Table 1, rows 1-3). The *H6*-EntA $S_{20,W}$ increased from 3.87 $\pm$ 0.35 at a total loading concentration of 2 µM to 5.70 $\pm$ 0.09 at 18 µM (Table 1, rows 4-7). A plot (not shown) of *H6*-EntA $S_{20,W}$ vs. loading concentration revealed that the sedimentation coefficients followed a hyperbola-like trend with *H6*-EntA concentration, indicative of self-association over the observed concentration range.

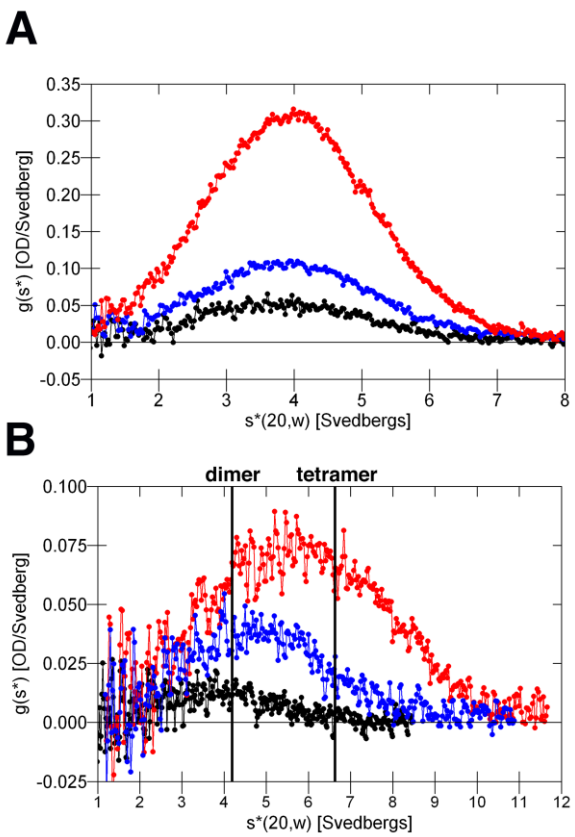

Figure 1: Sedimentation velocity analytical ultracentrifugation of *H6*-EntE and *H6*-EntA.

(A) g(s) distributions fit to sedimentation velocity data obtained at 20 ^{o}C from H6-EntE solutions at the following concentrations: 2.5 µM (black circles); 4.5 µM (blue circles); 13 µM (red circles). (B) g(s*) distributions fit to sedimentation velocity data obtained at 20 ^{o}C from H6-EntA solutions at the following concentrations: 2 µM (black circles); 8 µM (blue circles); 18 µM (red circles). For clarity, the g(s*) distribution of H6-EntA at 4 µM is not shown in this figure, but the $S_{20,W}$ for H6-EntA at this concentration is reported in Table 1. The left vertical line represents the $S_{20,W}$ of dimeric EntA calculated by HYDROPRO. The right vertical line represents the $S_{20,W}$ of tetrameric EntA calculated by HYDROPRO.*

Table 1: Sedimentation velocity analytical ultracentrifugation of purified *H6*-EntE and *H6*-EntA.

Protein	Conc.[a] (μM)	$S_{20,W}$ [b]	c/c_{tot} [c]	r.m.s.d.[d]
EntE	2.5	3.93 ± 0.17	0.859	n/a
EntE	4.5	4.04 ± 0.07	0.879	n/a
EntE	13.0	3.93 ± 0.04	0.869	n/a
EntA	2.0	3.87 ± 0.35	0.866	0.01057
EntA	4.0	4.48 ± 0.23	0.869	0.01054
EntA	8.0	4.97 ± 0.15	0.883	0.01077
EntA	18.0	5.70 ± 0.09	0.864	0.01553

[a] *Protein concentration determined by A_{280} and expressed as micromolar concentration of monomer subunits.*

[b] *Weight-average sedimentation coefficients determined by fits to g^(s*) distributions using DCDT+. Standard errors to fits also shown.*

[c] *Ratio of absorbance contribution of sedimenting species identified by g^(s*) analysis to total absorbance in cell.*

[d] *Local root mean square deviations of fits to self-association model using SEDPHAT global analysis. 'n/a' = not applicable.*

We used SEDPHAT to assess the fit of our sedimentation velocity data to a model describing dimer-tetramer self-association (given that the *H6*-EntA sedimenting species at 2 µM had an $S_{20,W}$ similar to that of the 60 kDa *H6*-EntE monomer and that *H6*-EntA also adopts a globular fold, we concluded that at this concentration *H6*-EntA was predominantly in the dimeric (~ 56 kDa) form). For SEDPHAT global analysis we required sedimentation coefficients for EntA dimer and EntA tetramer. Since our sedimentation velocity data indicated that our samples contained mixtures of *H6*-EntA dimer and tetramer over the concentration range examined, we could not experimentally determine sedimentation coefficients for discrete *H6*-EntA dimer or tetramer. We therefore employed hydrodynamic bead modelling using the program HYDROPRO, with the published X-ray crystallographic structure of EntA (PDB code: 2FWM) as input. According to our HYDROPRO analyses, the EntA dimer was predicted to have an $S_{20,W}$ value of 4.23, and the EntA tetramer to have an $S_{20,W}$ value of 6.71. These positions are shown in Figure 1B as vertical lines. The HYDROPRO-predicted $S_{20,W}$ of the EntA dimer is consistent with our experimental $S_{20,W}$ of *H6*-EntA determined by *g*^(*S**) analysis at the lowest concentration that we examined (2 µM), indicating that *H6*-EntA is mostly dimer at this concentration. At the upper boundary of our concentration range (18 µM), our experimentally-derived $S_{20,W}$ value of 5.70 is significantly less than that predicted for homogeneous EntA tetramer, suggesting that at this concentration *H6*-EntA was present as both dimers and tetramers, with the majority of the protein being in the tetrameric form. Sedimentation velocity data from the four runs (250 absorbance scans per run) collected between 2 µM and 18 µM *H6*-EntA fit well to the SEDPHAT monomer-dimer self-association model (here *H6*-EntA dimer was modelled as 'monomer' and *H6*-EntA

tetramer was modelled as 'dimer', assuming no dissociation of dimer to monomer over this concentration range). The reduced chi-squared (χ_r^2) value of the global fit was 1.46, which is acceptable given that a χ_r^2 value of 1.00 represents a perfect fit to the model (*221*). The root mean square deviations of fits of local datasets to the global SEDPHAT self-association model were also found to be acceptable (each R.M.S.D. was less than 0.016; Table 1, column 5). The K_D of the *H6*-EntA dimer-tetramer equilibrium was determined by SEDPHAT global analysis to be 12.30 μM (or 6.15 μM if total *H6*-EntA is expressed as dimer equivalents).

Pull-Down Assays

We previously showed that recombinant *H6*-EntB when used as a bait protein could pull down chromosomally-expressed EntE from *E. coli* lysates, and further that pull-down efficiency increased substantially in the presence of exogenous 2,3-DHB (*206*). Here we used purified, recombinant *H6*-EntE and *H6*-EntA bait proteins in pull-down experiments to identify respective binding partners from *E. coli* lysates in the presence and absence of exogenous 2,3-DHB. Bait proteins were immobilized to Co^{+2}-chelate beads and then incubated with lysates from *E. coli* BW25113 cells grown under iron-restricted conditions (M63 minimal medium plus 75 μM 2,-2'-dipyridyl), resulting in expression of the enterobactin biosynthetic machinery by derepression of Fur. We initially used *H6*-EntA as a bait protein to determine what partner proteins could be pulled down from *E. coli* cell lysates in the presence and absence of 2,3-DHB (Figure 2A). We found that *H6*-EntA bait was able to pull down a protein migrating at approximately 60 kDa by SDS-PAGE analysis independent of whether or not exogenous 2,3-DHB (100 μM) was added to the cell lysate (Figure 2A, band 'a', -DHB and +DHB,

respectively). Trypsinized proteins recovered from these bands were analyzed by LC-MS/MS, and the recovered peptides were found to correspond to *E. coli* EntE (Appendix Table1, rows 1-41). The bands visible above the 'a' (-DHB and +DHB) bands were also present in a control experiment (in which the lysate was applied to the empty column) and therefore do not represent a prey protein that specifically binds to *H6*-EntA (data not shown). In a second pull-down experiment, we used *H6*-EntE as a bait protein to pull down partner proteins from iron-restricted *E. coli* cell lysates with or without exogenously added 2,3-DHB (Figure 2B). *H6*-EntE bait was also able to pull down a protein migrating at approximately 30 kDa (Figure 2B, band 'd', +DHB) that was determined by LC-MS/MS to be *E. coli* EntB (Appendix Table1, rows 42-57). This band was only observed when exogenous 2,3-DHB was added to the lysate prior to equilibration with immobilized *H6*-EntE bait. We also found that *H6*-EntE pulled down in a DHB-independent manner a protein migrating at approximately 26 kDa (Figure 2B, band 'e', -DHB and +DHB, respectively). Mass spectrometry of proteins extracted from the 'e' (-DHB) and 'e' (+DHB) bands confirmed that they contained peptides corresponding to *E. coli* EntA (Appendix Table 1, rows 58-78).

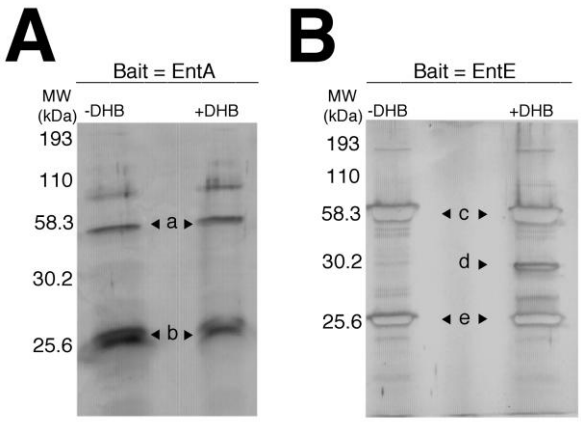

Figure 2: Pull down assays of EntA–EntE and EntE–EntB complexes formed *in situ*. *(A) Silver-stained 10% SDS-polyacrylamide gel of E. coli proteins co-eluted from Co^{+2}-chelate beads when H6-EntA was used as bait. (B) Same as (A), but with H6-EntE being used as bait. -DHB: proteins eluted from beads exposed to iron-restricted E. coli BW25113 lysate in the absence of exogenous 2,3-DHB. +DHB: proteins eluted from the beads exposed to iron-restricted E. coli BW25113 lysate in the presence of exogenous 2,3-DHB (100 μM). Positions of migration of protein molecular weight standards (Kaleidoscope Pre-Stained Markers, Bio-Rad Laboratories) are shown on the left side of each gel. Labels a-e indicate bands in which proteins were extracted and identified by LC-MS/MS: (a) E. coli EntE from lysate, (b) EntA (bait), (c) EntE (bait), (d) E. coli EntB from lysate, (e) E. coli EntA from lysate. Peptide sequences identified by LC-MS/MS for recovered chromosomally-expressed E. coli prey proteins are shown in Appendix Table 1.*

Chemical Crosslinking

A solution of *H6*-EntA was incubated with the heterobifunctional crosslinker SMCC resulting in covalent attachment of the *n*-hydroxysuccinimide moiety of the crosslinker to primary amines on *H6*-EntA. Maleimide-activated *H6*-EntA (22 μM) was then mixed with a solution of *H6*-EntE (2.5 μM) in order to form crosslinks between *H6*-EntE cysteine residues and the *H6*-EntA-SMCC conjugate. Resolution of crosslinked products on an SDS-polyacrylamide gel revealed the presence of a single band corresponding to a large (> 250 kDa) complex in addition to bands corresponding to uncrosslinked *H6*-EntA and *H6*-EntE. This additional band was observed in the presence of SMCC, but not in the absence of SMCC (Figure 3). The size of the +SMCC band is consistent with a crosslinked product containing four EntE monomers and four EntA monomers. Analysis of tryptic peptides from proteins recovered from the > 250 kDa band revealed that it contained both *E. coli* EntA and EntE sequences (Appendix Table 2), confirming that this band represented a crosslinked EntA–EntE complex.

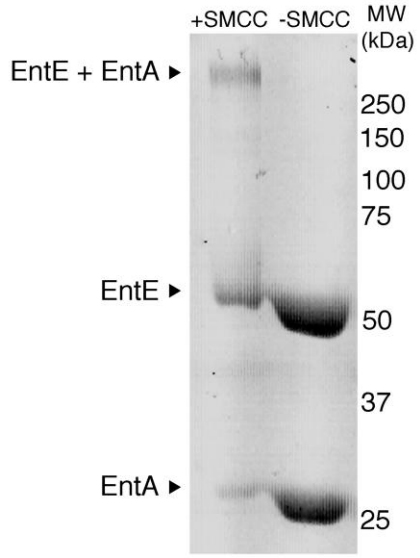

Figure 3: Covalent crosslinking of maleimide-activated EntA to EntE using the heterobifunctional crosslinker SMCC.

Left lane: Mixture of purified EntE and SMCC-activated EntA. Right lane: Mixture of purified EntE and untreated (-SMCC) EntA. Proteins were separated by SDS-PAGE and sizes were estimated by co-electrophoresis with molecular weight standards (Kaleidoscope Precision Plus, Bio-Rad Laboratories). Positions of standards are shown as numerals on the right side of the gel. Labels on the left side of the gel correspond to proteins identified by LC-MS/MS mass spectrometry from excised bands (see Appendix Table 2). Although the crosslinking reaction was performed with 22 μM maleimide-activated EntA and 2.5 μM EntE, the abundance of the bands on the gel do not reflect this ratio. This is likely due to loss of protein during concentration in Microcon YM-30 centrifugal filtration units, as well as aggregation of a portion of maleimide-activated EntA due to self-crosslinking.

EntE Activity Assays

Since we found that *H6*-EntE can form a complex with *H6*-EntA, we were interested in determining the effect of *H6*-EntA interaction on *H6*-EntE activity. It was previously reported that EntE turnover increases approximately 10-fold in the presence of its downstream partner protein, *holo*-EntB (*144*), suggesting that protein interactions could remodel the EntE active site. Here we found that addition of purified *H6*-EntA at concentrations of 0.25 μM and 4 μM to a solution containing 1 μM of purified *H6*-EntE resulted in 3-fold (Figure 4, black inverted triangles) and 6-fold (Figure 4, black triangles) increases in *H6*-EntE initial velocity, respectively, relative to the initial velocity of *H6*-EntE-catalyzed production of pyrophosphate product in the absence of *H6*-EntA (Figure 4, black squares). We did not observe any significant change in *H6*-EntE activity upon the addition of a control protein (bovine serum albumin at a concentration of 4 μM (Figure 4, black circles), demonstrating that the observed increase in *H6*-EntE activity was specific to *H6*-EntA.

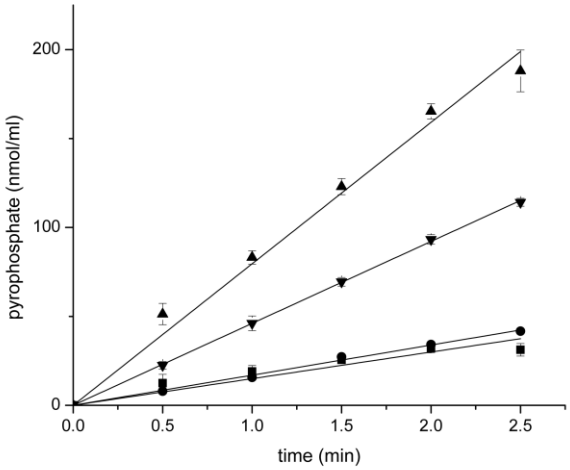

Figure 4: Stimulation of *H6*-EntE activity by *H6*-EntA.

Initial velocities of H6-EntE (straight lines) fit to the production of pyrophosphate as a function of time. H6-EntE alone (black squares); H6-EntE plus 0.25 μM H6-EntA (black inverted triangles); H6-EntE plus 4 μM H6-EntA (black triangles); H6-EntE plus 4 μM bovine serum albumin (black circles). Data shown are averaged values of triplicate readings. Error bars represent standard deviation from averaged values.

Effect of *H6*-EntA on the *H6*-EntE–DHB FRET Signal

The observed stimulatory effect of *H6*-EntA on *H6*-EntE activity led us to investigate if conformational changes at the *H6*-EntE active site did indeed occur upon formation of the EntA–EntE complex. We used fluorescence spectroscopy to further investigate the EntA–EntE interaction by observing the effect of *H6*-EntA on the *H6*-EntE–2,3-DHB FRET signal that we reported previously (*206*). The corrected fluorescence emission spectrum of the *H6*-EntE (3 μM) plus 2,3-DHB (60 μM) solution containing 100 mM KCl in the absence of *H6*-EntA is shown in Figure 5 (dashed line). The maximum at 440 nm corresponds to 2,3-DHB fluorescence emission upon excitation of *H6*-EntE intrinsic fluorophores at 280 nm. When the experiment was repeated with the addition of 3 μM *H6*-EntA, the observed corrected spectrum exhibited a 1.75-fold decrease in the peak maximum at 440 nm (Figure 5, solid line). We performed a similar experiment with *H6*-EntA present, but increased the concentration of KCl from 100 mM to 300 mM (Figure 5, dotted line). We found that this increase in ionic strength almost restored the *H6*-EntE–2,3-DHB FRET signal to its initial intensity, even in the presence of *H6*-EntA. We did not observe any KCl-dependent effect on the *H6*-EntE–2,3-DHB FRET signal in the absence of *H6*-EntA. This specificity suggests that the restoration of the FRET signal at 300 mM KCl is due to a salt-dependent disruption of an EntA–EntE complex.

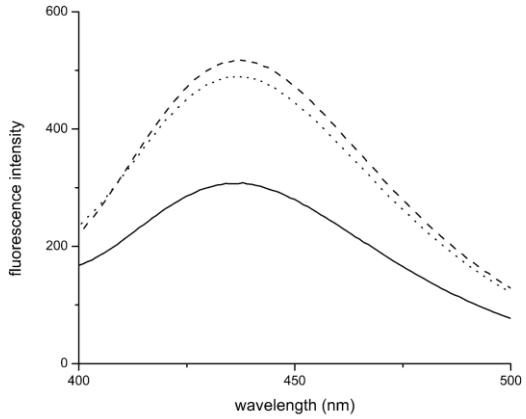

Figure 5: Perturbation of the 2,3-DHB– *H6*-EntE FRET signal by *H6*-EntA.
Fluorescence emission spectra collected at 20 ^{o}C show 2,3-DHB fluorescence emission around 440 nm upon excitation of mixtures of 2,3-DHB with H6-EntE plus or minus H6-EntA at 280 nm. 3 µM H6-EntE, 60 µM 2,3-DHB (dashed line); 3 µM H6-EntE, 60 µM 2,3-DHB, 3 µM H6-EntA in a buffer containing 100 mM KCl (solid line); 3 µM H6-EntE, 60 µM 2,3-DHB, 3 µM H6-EntA in a buffer containing 300 mM KCl (dotted line).

Fluorescence Anisotropy Experiments

In order to determine the binding status of 2,3-DHB during EntA–EntE interaction, we measured the fluorescence anisotropy of 2,3-DHB in the absence and presence of *H6*-EntA and/or *H6*-EntE. We observed that in the absence of protein, fluorescence anisotropy (*r*) of 2,3-DHB at a concentration of 20 µM was near zero, indicating a rapid rate of rotational diffusion in solution (Figure 6, black bar). The addition of 15 µM *H6*-EntA to the 2,3-DHB solution did not result in a significant increase in 2,3-DHB anisotropy (Figure 6, dark grey bar). The addition of *H6*-EntE (7 µM) to 2,3-DHB results in a relatively large increase in 2,3-DHB anisotropy, consistent with its ability to bind 2,3-DHB as a substrate (Figure 6, light grey bar). The addition of both *H6*-EntA (15 µM) and *H6*-EntE (7 µM) (Figure 6, white bar) resulted in observed

2,3-DHB anisotropy similar to that of 2,3-DHB plus *H6*-EntE, showing that *H6*-EntA binding to *H6*-EntE does not cause dissociation of 2,3-DHB from *H6*-EntE.

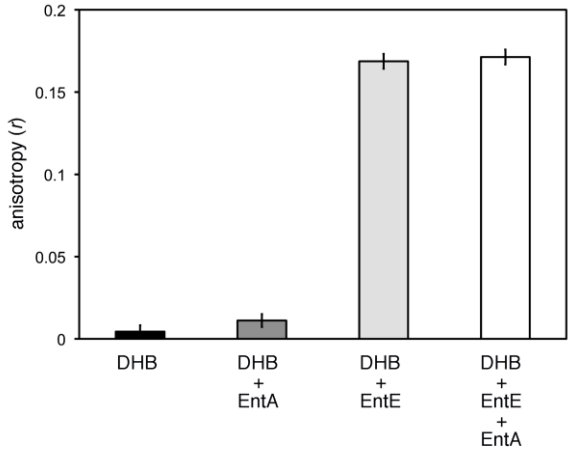

Figure 6: Fluorescence anisotropy of 2,3-DHB.

Fluorescence anisotropy measurements (λ_{ex} = 310 nm; λ_{em} = 440 nm) collected at 20 ^{o}C of 2,3-DHB alone and in the presence of H6-EntE and/or H6-EntA. Black bar: 20 µM 2,3-DHB; dark grey bar: 20 µM 2,3-DHB, 15 µM H6-EntA; light grey bar: 20 µM 2,3-DHB, 7 µM H6-EntE; white bar: 20 µM 2,3-DHB, 15 µM H6-EntA, 7 µM H6-EntE.

Fluorescence-Based Equilibrium-Binding Assay

Having found that the change in the *H6*-EntE–2,3-DHB FRET signal by *H6*-EntA was due to the EntA–EntE interaction, we followed the decrease in this signal as a function of *H6*-EntA concentration to measure the equilibrium-binding behavior of EntA–EntE complexation. By varying the concentration of *H6*-EntA relative to a fixed concentration of *H6*-EntE plus 2,3-DHB, we found that *H6*-EntA was able to decrease the *H6*-EntE–2,3-DHB FRET signal in a saturable, concentration-dependent manner. At 20 ^{o}C the decrease in the FRET signal was initially shallow followed by a transition to a steeper decrease commencing at an *H6*-EntA concentration of approximately 4 µM

(Figure 7A). We used our SEDPHAT-derived equilibrium association constant for the *H6*-EntA dimer-tetramer equilibrium (K_A = 1.63 x 10^5 M^{-1} when total *H6*-EntA is expressed as dimer equivalents) to estimate the fraction of tetrameric EntA at a given $[EntA]_{total}$. The following equation, adapted from Cole (*227*), was used to relate the concentration of EntA dimer at a given $[EntA]_{total}$ (here expressed as dimer equivalents):

$$[EntA]_{dimer} = (-1 + (1 + 8K_A[EntA]_{total\_as\_dimer})^{1/2}) / 4K_A \quad (6)$$

We were thus able to estimate at each *H6*-EntA concentration used in our fluorescence-based equilibrium-binding assay the fraction of EntA occurring in the tetrameric form (Figure 7A, inset). According to these calculations, the amount of tetrameric *H6*-EntA found when $[EntA]_{total}$ is at a saturating concentration (7 μM) in our fluorescence assay is about 2.8 μM (*i.e.*, fraction of *H6*-EntA as tetramer at this concentration was estimated to be 0.4), which is approximately equimolar with the fixed concentration of *H6*-EntE in our binding assay (3.0 μM). *H6*-EntA-dependent changes in the 2,3-DHB–*H6*-EntE FRET signal were used to determine fractional binding ($(\Delta F/F_o)/(\Delta F/F_o)_{max}$). Fractional binding values were then used to calculate $[EntA]_{bound}$ and $[EntA]_{free}$ at a given $[EntA]_{total}$ (see Experimental Procedures). At 20 ^oC the observed change in fractional binding as a function of $[EntA]_{free}$ was sigmoidal in character (Figure 7B). These data fit well (R^2 = 0.975) to the Hill equation. The Hill coefficient (n) determined from the non-linear fit was 3.66, and the $K_{0.5}$ value was determined to be 1.94 μM. A Scatchard replot of our binding data revealed a concave-down trend (Figure 7B, inset).

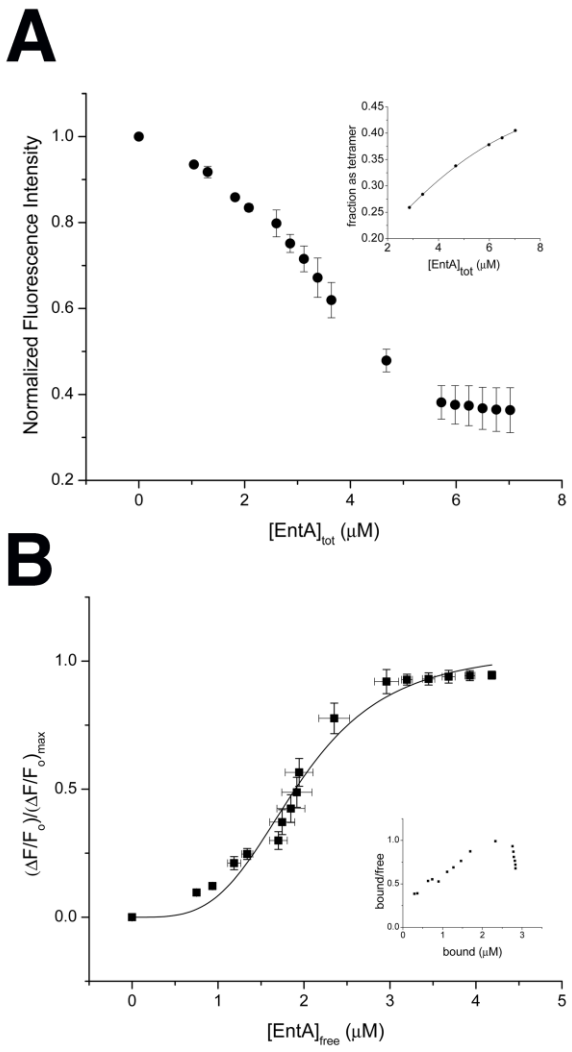

Figure 7: Fluorescence-based equilibrium binding assay of the EntA–EntE interaction.

Binding of H6-EntA to H6-EntE corresponds to the decrease in the 2,3-DHB– H6-EntE FRET signal at 440 nm upon increasing concentration of H6-EntA. (A) Decrease in fluorescence emission at 440 nm (λ_{ex} = 280 nm) as a function of $[EntA]_{total}$ at 20 ^{o}C (black circles). Data shown are averaged values of readings taken in triplicate and normalized to correct for small changes in F_o between replicates; error bars represent standard deviations from averaged values. Fluorescence emission at 440 nm is due to 2,3-DHB emission resulting from FRET via H6-EntE donor residues excited at 280 nm. Inset: Estimate of the fraction of $[EntA]_{total}$ occurring as tetramer at concentrations used in the fluorescence assay. Fractions as tetramer were determined using the K_A of dimer-

tetramer equilibrium determined by SEDPHAT global analysis of H6-EntA sedimentation velocity AUC data in an equation relating $[EntA]_{dimer}$ *concentration to total loading concentration expresed as EntA dimers. Fraction as tetramer =* $([EntA]_{total\_as\_dimer} - [EntA]_{dimer}) / [EntA]_{total\_as\_dimer}$*. The solid line represents a non-linear fit of the data to a second-order polynomial describing Equation (6) (see Results). (B) Hill plot showing the change in fractional binding* $((\Delta F/F_0)/ (\Delta F/F_0)_{max})$ *as a function of* $[EntA]_{free}$ *(black squares). Error bars along the y-axis reflect standard deviations of averaged fractional binding determinations from three experiments; error bars along the x-axis reflect standard deviations of averaged* $[EntA]_{free}$ *determinations from three experiments. Inset shows Scatchard replot of same data, in which* $[EntA]_{bound}$ *= fractional binding x* $[EntE]_{total}$*. See Experimental Procedures for details on how* $[EntA]_{bound}$ *and* $[EntA]_{free}$ *were determined.*

Discussion

Protein-protein interactions are now recognized to play a key role in many metabolic processes mediated by sequential enzyme activities (*228-230*). Such interactions may facilitate the direct channeling of metabolic intermediates, resulting in optimization of catalysis, sequestration of intermediates to protect against diversion to other pathways, or to protect against degradation of labile intermediates (*231-233*). The biosynthesis of the *E. coli* siderophore enterobactin is a cytoplasmic enzyme-mediated process in which protein-protein interactions are now recognized to be essential. Prior to this study, all protein-protein interactions relevant to enterobactin biosynthesis had been localized to proteins involved in the NRPS arm (EntE, EntB, EntF, EntD) (*142, 181, 195, 197, 206*). Here we report the first experimental evidence of a protein-protein interaction between EntA and EntE, thus establishing a direct link between the DHB synthesis and NRPS arms. Formation of an EntA–EntE complex during enterobactin biosynthesis could serve to facilitate substrate channeling, thus minimizing dissociation of 2,3-DHB into the

bulk medium and favoring direct, rapid entry of this intermediate into the NRPS arm. Such channeling would be advantageous since excessive accumulation of intracellular 2,3-DHB during enterobactin biosynthesis in *E. coli* under iron-limiting conditions could interfere with iron uptake processes potentially requiring molecular recognition of enterobactin 2,3-DHB moeities as part of their function (*e.g.*, Fes, EntS).

Here we found through our enzyme assays that *H6*-EntE activity increased significantly upon addition of *H6*-EntA, and in a manner dependent on *H6*-EntA concentration. We propose that our observed stimulation of EntE activity is due to optimization of the EntE active site through conformational changes occurring upon EntA binding. Our finding that *H6*-EntA perturbs the FRET signal between 2,3-DHB and *H6*-EntE intrinsic fluorophore donor residue(s) supports this. Complexation of EntA with EntE therefore likely results in conformational changes at the EntE active site causing translocation of bound 2,3-DHB towards the ATP co-substrate and away from FRET donor residues such as Tyr236 predicted to be found at the floor of the EntE active site, consistent with the structure of the EntE homologue DhbE (*184, 206*). Our fluorescence anisotropy experiments clearly show that 2,3-DHB is not dissociated upon formation of the EntA–EntE complex, thus excluding this as an alternate explanation for EntA-induced reduction in the observed FRET signal. Taken together, our data show that EntA induces a conformational remodeling of the EntE active site upon EntA–EntE complex formation, resulting in a re-positioning of 2,3-DHB within the substrate-binding cavity of EntE such that the rate of EntE-catalyzed 2,3-DHB adenylation in the first half-reaction of the EntE mechanism is increased due to a closer proximity to ATP (Scheme 2).

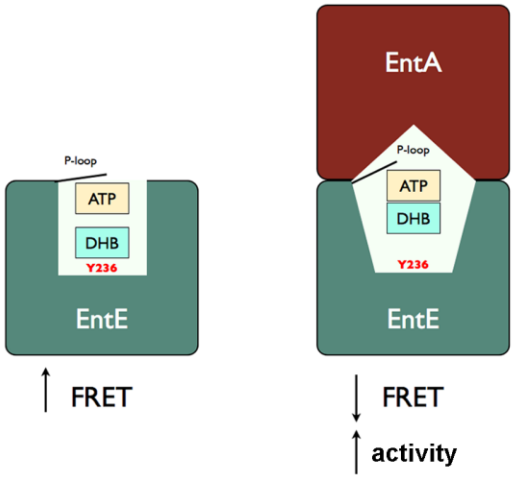

Scheme 2: Proposed model of the attenuation of the EntE–2,3-DHB FRET signal upon EntA interaction. EntE Y236 is shown as a putative FRET donor at the base of the EntE active site.

We also found that the decrease in the 2,3-DHB–*H6*-EntE FRET signal was dependent on the concentration of *H6*-EntA, and we exploited this phenomenon to gain insights into the equilibrium-binding aspects of EntA–EntE complexation. Our equilibrium-binding data at 20 ^{o}C fit well to the Hill Equation, with a Hill coefficient greater than one (n = 3.66; Figure 7B). A Hill coefficient of that magnitude, along with the concave-down behavior observed in the Scatchard replot of our binding data, suggests positive cooperativity in the EntA–EntE interaction (*i.e.*, EntE affinity for EntA increases as a function of EntA concentration). Concordant with this binding behavior, our AUC data show that the oligomeric structure of EntA changes over the concentration range used in our equilibrium-binding assay. We found that EntA exists as a mixture of dimers and tetramers at concentrations between 2 µM and 18 µM, with a transition from being

predominantly dimer at 2 μM to being predominantly tetramer at 18 μM. The sigmoidal binding behavior observed in the EntA–EntE interaction is therefore likely due at least in part to EntE binding with higher affinity to EntA in the tetrameric form. However, it appears that EntE can also interact with EntA in non-tetrameric forms (*i.e.*, dimer) since we observed stimulation of EntE activity in the presence of EntA at a concentration of 0.25 μM, where the concentration of EntA tetramer would be negligible according to our analysis of EntA self-association.

When taken together, our experimental data demonstrate that the EntE interacts with EntA, and appears to form a higher-affinity complex with EntA in the tetrameric form compared to EntA in the dimeric form. Our crosslinking experiment detected only a large (> 250 kDa) crosslinked species that contained both *H6*-EntA and *H6*-EntE (Figure 3), consistent with a complex comprised of four EntE monomers binding to one EntA tetramer (~ 360 kDa). The effect of intracellular concentration on the oligomeric state of EntA may play a regulatory role during enterobactin biosynthesis, with activation of the process occurring upon EntA tetramerization only at sufficiently high intracellular concentrations. Our pull-down assays also showed that recombinant *H6*-EntE bait could pull down both chromosomally-expressed EntA and EntB *in situ* from *E. coli* lysates when exogenous 2,3-DHB was present. This supports our previous study (*206*) where we showed that the EntE–EntB interaction affinity increases significantly in the presence of exogenous 2,3-DHB, due to 2,3-DHB binding to EntB as an allosteric regulator. The most likely explanation for our pull-down data is that EntA and EntB formed discrete and independent complexes with the immobilized *H6*-EntE bait during the pull-down experiment. Consistent with this, we observed that *H6*-EntA bait could pull down EntE

but not EntB, and in our previous study that *H6*-EntB bait could pull down EntE but not EntA. An alternative explanation for our pull-down data could be that *H6*-EntE in the presence of 2,3-DHB pulled down both EntA and EntB as an EntA–EntE–EntB complex. Although this is enticing, we currently do not have further evidence to support the existence of such a ternary complex.

To summarize our findings in the context of what is currently known about EntA, EntE, and EntB, we propose in Scheme 3 a model outlining the roles of dynamic protein-protein interactions in enterobactin biosynthetic steps involving EntE. In this model, EntE initially forms a complex with tetrameric EntA, facilitating direct channeling of 2,3-DHB from EntA to the EntE active site. ATP would then enter the EntE active site and the first half-reaction (adenylation of 2,3-DHB) would occur at an optimal rate along with release of pyrophosphate. Assuming partial channeling of 2,3-DHB between EntA and EntE active sites, some free 2,3-DHB would be released into the cytoplasm that could then bind at an allosteric site on *holo*-EntB, thus activating it for interaction with EntE. EntA would then dissociate from EntE (perhaps as a result of ATP hydrolysis), thus allowing EntE–DHB–AMP to interact with *holo*-EntB. The resulting EntE–EntB complex would allow for direct transfer of the 2,3-DHB moiety to PPant-Ser245, thus forming *acyl-holo*-EntB along with the release of AMP. Dissociation of *acyl-holo*-EntB from the EntE would then occur such that the 2,3-DHB moiety could be delivered to the NRPS scaffold protein EntF for condensation with activated L-serine. Upon dissociation of *acyl-holo*-EntB, the EntE–EntA complex would be regenerated, resulting in turnover of the process. This model is consistent with recent reports elucidating the EntE mechanism in the context of its two half-reactions (*188-189*), such that the EntA–EntE interaction

optimizes the first half-reaction (2,3-DHB adenylation), and the EntE–EntB interaction optimizes the second half-reaction (transfer of 2,3-DHB to *holo*-EntB).

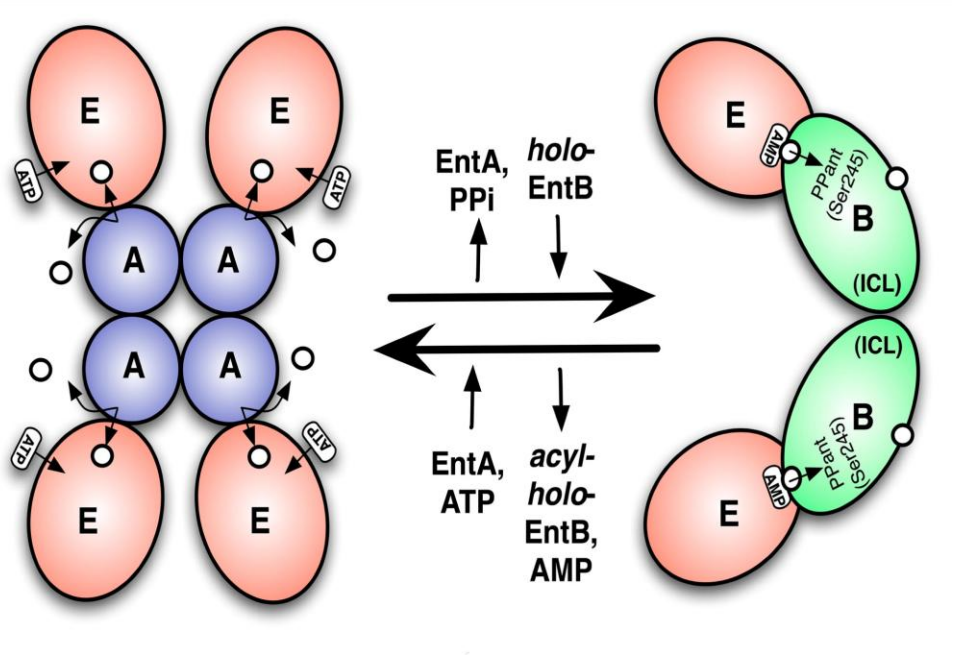

Scheme 3: Proposed mechanism of EntA–EntE and EntE–EntB complex assembly during enterobactin biosynthesis.

This model proposes that protein-protein interactions enhance the two EntE half-reactions in a manner consistent with what is known about the EntE catalytic mechanism. First half reaction: Four EntE monomers (red ellipsoids) bind with optimal affinity to one EntA tetramer (blue circles indicate EntA monomers). Partial channeling then occurs in which some 2,3-DHB (small circles) produced by EntA is directly transferred to the EntE active site, while some is released into the cytoplasm that will act as a signal to recruit holo-EntB to EntE. Subsequent to 2,3-DHB binding, ATP will then bind at the EntE active site. While in complex with EntA, EntE catalyzes the production of 2,3-DHB-AMP, followed by release of pyrophosphate (PPi) and EntA. Second half reaction: holo-EntB (subunits shown as green elliposids; dimerization occurring through isochorismate lyase (ICL) domains, consistent with the EntB structure), with 2,3-DHB bound at an allosteric site, forms a complex with EntE–DHB–AMP. 2,3-DHB is then directly transferred to the phosphopantetheine (PPant) group attached to EntB Ser245, resulting in the production of acyl-holo-EntB. EntE and AMP dissociate from acyl-holo-EntB,

allowing it to participate in downstream NRPS steps. Dissociated EntE complexes with EntA, followed by another round of DHB adenylation upon binding of 2,3-DHB (via transfer from EntA) and ATP.

Here we have shown that *E. coli* enterobactin biosynthesis is even more highly networked by protein-protein interactions than previously thought. We have established that there is a direct link between the DHB synthesis and NRPS arms of enterobactin biosynthesis as facilitated by the EntA–EntE interaction. Our study, in conjunction with previous reports, provides strong evidence that EntE has evolved such that its enzymatic activity is only fully optimized when the protein is participating in a protein-protein interaction that facilitates conformational remodeling of the EntE active site. Significantly, it has recently been reported that an endogenous catecholate siderophore occurs in mammals, with a homologue of *E. coli* EntA (BDH2) being essential for its biosynthesis; furthermore, a mammalian homologue of *E. coli* EntE has also been identified (*1*). Our elucidation of the protein-protein interaction network necessary for *E. coli* enterobactin biosynthesis therefore provides not only further insights into a biological process that is essential for bacterial survival under iron-limiting conditions, but also provides insights that will be useful in interpreting the newly identified BDH2-dependent system that has been shown to play a role in mammalian iron homeostasis.

CHAPTER FOUR: IDENTIFICATION OF *ESCHERICHIA COLI* ENTA RESIDUES NECESSARY FOR INTERACTION WITH ENTE: TARGETED DISRUPTION OF THE ENTA-ENTE COMPLEX

Continuing our characterization of the EntA-EntE interaction that was the focus of the last chapter, the EntA-EntE interaction interface was mapped and characterized in this chapter for the first time. Here, phage display was used to identify the EntE interaction interface on the EntA surface. Site-directed mutagenesis was then used to measure the contribution of two of the identified interface residues of EntA in the interaction with EntE. Techniques used to study EntA variants predicted to differentially interact with EntE compared to wild-type include: AUC, circular dichroism, fluorescence spectroscopy, cross-linking experiments, and growth phenotype assays. The manuscript corresponding to this chapter is in preparation for submission to a peer-reviewed journal.

Summary

Enterobactin biosynthesis needs the activities of six enzymes (EntA-EntF). The activities of EntC, EntB (N-terminal domain), and EntA are required for biosynthesis of 2,3-dihydroxybenzoate (2,3-DHB). The activities of EntE, EntB (C-terminal domain), EntD, and EntF are required for the condensation of 2,3-DHB with L-serine *via* non-ribosomal peptide synthesis (NRPS). We previously showed that the DHB biosynthesis and NRPS processes are directly linked by EntA-EntE interaction. Here we performed a fine-mapping of the EntA-EntE interaction interface by phage display. We localized EntE-interacting residues to an alpha helix near the N-terminus of EntA, proximal to the EntA dimerization interface. *H6*-EntA variants containing single-site mutations (Q64A and A68Q) and a double-site mutation (Q64A/A68Q) were created. Our cross-linking experiments demonstrated a weak interaction between *H6*-EntE and *H6*-EntA (Q64A) variant. Near-UV CD spectra did not display any changes in the *H6*-EntE and *H6*-EntA (Q64A) or *H6*-EntA (Q64A/A68Q) spectra upon mixing. Our fluorescence assays showed a weak interaction between *H6*-EntE and *H6*-EntA variants (Q64A and Q64A/A68Q), supporting our CD results. Growth phenotype experiments revealed that an *E. coli entA*-knockout strain transformed with gene encoding *H6*-EntA (Q64A) variant or *H6*-EntA (Q64A/A68Q) variant grew more poorly in iron-free M63 minimal media in the presence of 2,2-dipyridyl. Taken together, our results show that EntA residues Q64 and A68 are necessary for efficient formation of the EntA-EntE complex. Disruption of the EntA-EntE interaction by mutations at these positions appears to be due a combination of direct disruption of the EntA-EntE interaction interface as well as an interference in the ability of EntA variant proteins to form tetramers.

Introduction

Most microorganisms have developed different ways to get iron from the extracellular environment under conditions of iron starvation. One of such strategy involves the synthesis and export of low-molecular-weight compounds named siderophores that have high affinity for ferric iron. More than 500 siderophores have so far been identified (*57*). Siderophores compete with other iron chelators to sequester iron from the extracellular environment. Iron is an essential micronutrient for most microorganisms. It is involved in many important biological processes, including enzyme catalysis and electron transport. Since iron availability inside a host cell is limited, siderophores from pathogenic bacteria are considered virulence factors. For example, siderophores have been identified as virulence factors in a number of diseases inflicted by pathogenic microorganisms: cystic fibrosis pathogenesis (*234*), pulmonary infections caused by *Klebsiella pneumonia* (*235*), *Pseudomonas aeruginosa* pathogenesis (*236*), *Escherichia coli* k1 in neonatal meningitis (*207*), extraintestinal *Escherichia coli* pathogenesis (*172*), and avian pathogenic *Escherichia coli* infection (*237*). Much work has been done to gain understanding of siderophore biosynthesis and transport systems.

E. coli and other enteric bacteria synthesize and secrete the catecholate siderophore, enterobactin, which is a cyclic triester of 2,3-dihydroxybenzoylserine (DHBS). Enterobactin is secreted in response to iron deficiency in the cell. It has the highest affinity for ferric ions ($K_D \sim 10^{-50}$ M (*75*)). The outer membrane protein FepA binds ferric enterobactin and transports it to the periplasm (*146*) where FepB shuttles the ferric siderophore to the multisubunit inner membrane permease complex FepCDG (*44, 157-159*). In many bacteria, the iron uptake and homeostasis pathways are down-

regulated by ferric uptake regulator (Fur) protein in response to iron availability (*238*). Several pathogens including *E. coli* (*130*), *Salmonella typhimurium* (*239*), and *Klebsiella pneumoniae* (*240*), produce enterobactin by derepression of Fur in response to iron-limiting conditions. Thus enterobactin biosynthesis, export, and import pathways are a crucial target in the development of novel antimicrobial drugs.

The biosynthesis of enterobactin needs the activities of six enzymes: EntC, EntB, EntA, EntE, EntD, and EntF. The first three enzymes in the pathway (EntC, EntB (N-terminal domain), and EntA) comprise the DHB biosynthesis module that involves the formation of 2,3-dihydroxybenzoate (2,3-DHB) from chorismate (*140, 177, 213*). EntE, EntB (Ar-CP domain), EntD, and EntF comprise the non-ribosomal-peptide synthesis (NRPS) module (*131, 139, 141, 143*). In the NRPS module three molecules of 2,3-DHB are condensed with three L-serine residues to form enterobactin. EntH has been shown to be a proofreading activity to prevent or reverse misacylation of EntB and EntF during NRPS (*133*). Enterobactin can be further modified by *iroA* system in extraintestinal *E. coli* in order to evade the host innate immune system (*241*).

EntA is a 2,3-dihydro-2,3-dihydroxybenzoate dehydrogenase (E.C. 1.3.1.28). It catalyzes the last reaction of the DHB biosynthesis module, which is the oxidation of 2,3-dihydro-2,3-dihydroxybenzoate (2,3-diDHB) to 2,3-dihydroxybenzoate (2,3-DHB) (*140*). The crystal structure of EntA has been determined (*183*). EntE, 2,3-DHB-AMP ligase (E.C. 2.7.7.58), catalyzes the first reaction of the NRPS module, which is the activation of 2,3-DHB (i.e., the product of EntA) *via* adenylation to form 2,3-DHB-AMP (*141*). The crystal structure of EntE is currently unknown. The crystal structure of DhbE, an EntE homologue from *Bacillus subtilis*, was determined in the presence and absence of bound

DHB and AMP (*184*). In our previous work (Chapter 2), we generated an EntE homology model using DhbE as a template (*206*). This model provided insights into the nature of binding of the 2,3-DHB substrate to the EntE active site. We also previously demonstrated that the functional modules involved in DHB biosynthesis and NRPS are directly linked by a protein-protein interaction between EntA and EntE (Chapter 3) (*242*). In that study we demonstrated that EntA quaternary structure is dependent on its concentration. EntA in solution is in equilibrium between dimeric and tetrameric forms, with conversion to the tetrameric form occurring with increasing EntA concentration. At low micromolar EntA concentrations the dimeric form is predominant, with a transition to predominantly tetrameric EntA occurring at a concentration greater than 20 μM. We also demonstrated that EntE has a higher affinity for EntA in the tetrameric form at 20°C. Thus EntA oligomerization likely plays a regulatory role in enterobactin biosynthesis, such that EntA tetramerization enhances EntA-EntE interaction.

In this report, we used phage display to identify EntA residues involved in interaction with EntE. Based on our phage display results, we generated EntA variants to observe the effects of EntA mutagenesis at these positions on EntE interaction *in vitro* and *in vivo*. The effect of EntA mutations on the interaction with EntE was characterized *in vitro* using cross-linking experiments, fluorescence spectroscopy, and circular dichroism. Here we found that single-site mutation at EntA residue 64 and double-site mutation at EntA residues 64 and 68 had a significant effect on the ability of variants harboring these mutations to interact with EntE in solution. We also studied the effect of EntA mutations *in vivo* by conducting growth phenotype experiments in which we transformed genes encoding EntA variants with mutations at residues 64 and 64/68 into

an *E. coli entA*-knockout strain. Growth of resulting transformants under iron-restricted conditions was found to be very poor relative to *entA*-knockout cells transformed with a gene encoding wild-type EntA.

Materials and Methods

Reagents

All chemicals were purchased from Bioshop Canada, Inc. (Burlington, Ontario) except 2,3-DHB, which was purchased from Sigma-Aldrich (St. Louis, Mo.)

Phage Display

The Ph.D.-12^{TM} phage display peptide library kit (New England Biolabs) was used to pan a phage library containing random 12-mer peptide sequences (~ 1 x 10^{13} pfu/ml) against immobilized *H6*-EntE. Panning was carried out by incubating 10 µl of a library of phage-displayed peptides (~1 x 10^{11} pfu/ml) in a well of a plastic tray coated with approximately 100 µg of purified *H6*-EntE. Unbound phage were washed away using a buffer containing 50 mM Tris (pH 8.6), 150 mM NaCl, and 0.1% (v/v) Tween 20. Bound phages were eluted by the addition of a solution containing 0.2 M glycine-HCl (pH 2.2) and bovine serum albumin (1 mg/ml). Eluted phages were amplified in *E. coli* ER2738 cells, and two additional binding/amplification cycles were performed. After three rounds, clones were selected by picking individual plaques containing amplified phage developed on plated lawns of *E. coli* ER2738 cells. Each plaque represented a clonal phage population containing a single 12-mer peptide sequence. Single-stranded DNA was isolated from phage amplified from plaque picks using the QIAGEN M13 Kit (QIAGEN Inc, Chatsworth, CA) and sequenced at the McGill University and Génome Québec Innovation Centre. Amino acid sequences of 12-mer peptides from isolated

phage particles were predicted from DNA sequence data. The dataset of unique peptide sequences isolated from *H6*-EntE-bound phage particles was analyzed using the RELIC server (http://relic.bio.anl.gov/) that employs algorithms developed from statistical analyses of published phage display outcomes (*243*).

Site-Directed Mutagenesis

Single-site mutagenesis of *H6*-EntA was performed on the construct obtained from the ASKA repository (*205*) used previously for expression and purification of wild-type, recombinant hexahistinde-tagged EntA (henceforth referred to as *H6*-EntA) (*242*). This construct was used as a template in site-directed mutagenesis experiments employing the Quik-Change Site-Directed Mutagenesis Kit (Stratagene) along with two mutagenic oligonucleotide primers for each mutant generated. The mutagenic oligonucleotides were designed to substitute EntA Gln64 to Ala (Q64A) (forward primer: 5'-GGT CGC GCA AGT GTG TGC GCG ACT GTT AGC TGA AAC G-3'; reverse primer: 5'-CGT TTC AGC TAA CAG TCG CGC ACA CAC TTG CGC GAC C-3') or EntA Ala68 to Gln (A68Q) (forward primer: 5'-TGT CAG CGA CTG TTA CAG GAA ACG GAG CGA CTG G-3'; reverse primer: 5'-CCA GTC GCT CCG TTT CCT GTA ACA GTC GCT GAC A-3'). The reaction mixture contained the pCA24N-*H6-entA* construct (5-50 ng), mutagenic forward and reverse primers (125 ng each), 1 μl of dNTP mixture (10 mM), and DNA polymerase (0.05 U/μl). The number, duration, and temperature of the PCR cycles were performed according to the manufacturer's instructions. Double-stranded plasmids obtained from site directed mutagenesis were purified using QIAGEN DNA Mini Prep Kit and verified by sequencing. Plasmids containing the mutations were transformed into competent *E. coli* AG-1 cells (Stratagene)

for expression and purification of *H6*-EntA mutants. An EntA double mutant (Q64A/A68Q) was created by TOP Gene Technologies (Montreal, Canada) using the pCA24N-*H6*-*entA* construct.

Expression and Purification of EntA Wild-Type and Variant Proteins

Constructs containing DNA sequences encoding in-frame N-terminal hexahistidine tagged EntE, EntA, or EntA variants (Q64A, A68Q, or Q64A/A68Q) were transformed into competent AG-1 cells. Transformants were grown in LB broth containing 30 μg/ml of chloramphenicol at 37 °C to an OD_{600} of 0.6. Protein expression was induced with the addition of IPTG to a final concentration of 1 mM followed by further incubation at 37 ^{o}C for 3 hours. Cell lysis was performed using the BugBuster Master Mix lysis buffer (Novagen). Clarified lysates were applied to a 10-ml Profinity IMAC column connected to a BioLogic DuoFlow FPLC system (Bio-Rad Laboratories). The column was washed using Buffer A (50 mM Hepes (pH 8.0), 100 mM KCl, 1 mM TCEP, and 10 mM imidazole). The hexahistidine-tagged proteins were eluted using a linear gradient of imidazole (10 mM to 500 mM) in Buffer A. Fractions containing the highest OD_{280} fractions were analyzed by SDS-PAGE, pooled, and dialyzed against Buffer B (50 mM Hepes (pH 8.0), 100 mM KCl, 1 mM TCEP, and 15 % glycerol) followed by storage at – 20 °C.

Analytical Ultracentrifugation

Sedimentation velocity experiments performed in a Beckman XL-I analytical ultracentrifuge with a four-place An-60Ti rotor. *H6*-EntA, *H6*-EntA (Q64A), *H6*-EntA (A68Q), and *H6*-EntA (Q64A/A68Q) were dialyzed into Buffer C (50 mM Tris buffer (pH 8.0), 150 mM NaCl and 0.5 mM TCEP) and adjusted to final concentrations of 2 μM

and 20 µM by dilution with Buffer C. Sedimentation velocity experiments were performed as described previously (*206*). Samples were centrifuged at 40,000 rpm for approximately 10 h at 20 °C; for each run a total of 250 absorbance scans were collected in which optical density at 280 nm was measured. Data were analyzed by fitting to the $g(s^*)$ and $g^\wedge(s^*)$ distributions using the computer program DCDT+ (v2.2.1) (*220*). Approximately 20 scans were selected from each run of 250 scans for analysis. Solvent density, viscosity, and protein partial specific volumes used as input parameters for DCDT+ were obtained using the program SEDNTERP (*223*).

Chemical Crosslinking of Protein Complexes

In this study, protein-protein complexes were covalently crosslinked using the Controlled Protein-Protein Crosslinking Kit (Pierce). The crosslinking reaction mixture contained 0.8 mg/ml of *H6*-EntA, *H6*-EntA (Q64A) or *H6*-EntA (A68Q)) and 50-fold molar excess of sulfo-SMCC prepared in phosphate-buffered saline (pH 7.2). The mixture was incubated for 30 minutes at room temperature, followed by removal of unreacted sulfo-SMCC using a D-salt™ dextran desalting column. The highest OD_{280} fractions containing maleimide-activated *H6*-EntA or *H6*-EntA variants were pooled (22 µM), mixed with *H6*-EntE (2.5 µM) and incubated for 60 minutes at room temperature. Complex formation was analyzed by SDS-polyacrylamide gel electrophoresis. Bands corresponding to crosslinked species were excised and analyzed for protein content by LC-MS/MS at the McGill Mass Spectrometry Core Facility (McGill University, Montreal).

Fluorescence Spectroscopy

The interaction between *H6*-EntE and *H6*-EntA (wild-type or *H6*-EntA variants) was monitored by measuring the reduction in *H6*-EntE-bound 2,3-DHB FRET signal at 440 nm (*206*). Fluorescence intensities were measured at 20 ^{o}C using a Varian Cary Eclipse spectrofluorimeter equipped with a Peltier temperature controller. Fluorescence intensity measurements (excitation wavelength: 280 nm; emission wavelength: 440 nm) of a mixture of *H6*-EntE solutions (2.5 μM) and 60 μM 2,3-DHB were collected in the presence and absence of each *H6*-EntA variant (Q64A, A68Q, Q64A/A68Q) at a concentration of 6 μM. Measurements were corrected for background, protein dilution, and the inner filter effect as appropriate.

Far-UV Circular Dichroism Spectroscopy

Far-UV CD spectra of *H6*-EntE (1.25 μM), wild-type *H6*-EntA or *H6*-EntA variants (1.25 μM), and a mixture of *H6*-EntE with wild-type *H6*-EntA or *H6*-EntA variants (1.25 μM) were recorded over the range 200-260 nm in 0.2-cm path-length rectangular cell. Proteins were exchanged into a Tris buffer (pH 8.0, adjusted using H_2SO_4), 0.5 mM TCEP, 100 mM KCl, and 15% glycerol) and then diluted to the appropriate concentrations in the same buffer. Spectra were recorded at 20°C by averaging 5 wavelength scans (1 nm bandwidth) in 0.2-nm steps at a rate of 100 nm/min, and 0.25 sec response.

Near-UV Circular Dichroism Spectroscopy

Near-UV CD spectra of *H6*-EntE (20μM), *H6*-EntA wild type or *H6*-EntA variants (20 μM), and a mixture of *H6*-EntE with wild-type *H6*-EntA or *H6*-EntA variants were recorded over the range 250-320 nm in 2-cm path-length rectangular cell.

Proteins used for near-UV CD experiments were dialyzed and diluted in buffer B. Spectra were recorded at 20°C by averaging 3 wavelength scans (1 nm bandwidth) in 0.2-nm steps at a rate of 20 nm/min, and 2 sec response.

Growth Phenotype Assay

Competent *E. coli* BW25113 (*entA*::*kanR*) cells (*lacI*q *rrnB*$_{T14}$ Δ*lacZ*$_{WJ16}$ *hsdR514* Δ*araBAD*$_{AH33}$ Δ*rhaBAD*$_{LD78}$) (*244*) were transformed with pCA24N-based expression constructs encoding *H6*-EntA (wild type), *H6*-EntA (Q64A), *H6*-EntA (A68Q), *H6*-EntA (Q64A/A68Q)). Cells were also transformed with empty pCA24N vector as a control. Cultures containing 5 ml LB with 30 μg/μl chlormophenicol were inoculated with one colony of each transformant and grown at 37 °C overnight with constant shaking at 225 RPM. After overnight growth, cultures were diluted 1:60 in LB media containing 30 μg/μl chlormophenicol and grown at 37 °C and 225 rpm until an OD_{600} ~ 0.4 was achieved. Log-phase cultures were then diluted 1:800 (all cultures having equivalent cell densities) in iron-free M63 minimal media containing 30 μg/μl chlormophenicol in the presence of 2,2'-dipyridyl (65 μM). The strains were grown for 42 hours and cell densities were measured at 600 nm. Soluble whole cell lysates of each culture were prepared using BugBuster Master Mix lysis buffer (Novagen) followed by recovery of supernatants after centrifugation at 10,000g for 1 hr at 4^{o} C.

Western Blot Analysis

Western blot analysis was performed using the Immune-Blot Assay Kit (Bio-Rad Laboratories). Total protein (50 μg) of the clarified lysate prepared from each growth assay culture (see above) was applied to SDS-polyacrylamide gel (12%). After the electrophoresis, proteins were transferred to PVDF membrane at 4^{o} C for 1 hour at 100

Volt using the Bio-Rad Western Blotting system. The membrane was incubated in the blocking solution (TTBS containing 3 % BSA) overnight at 4 °C. Subsequently, the membrane was washed with TTBS and incubated overnight in the anti-His_6 antibody (1:5000 dilution) solution. This was followed by two washing steps (each 10 minutes) using TTBS prior to incubation with the secondary antibody solution (Goat Anti-Mouse IgG/horseradish peroxidase conjugate (GAM-HRP)). After one hour incubation with GAM-HRP, the membrane was washed and resolved using colorimetric assay reagents supplied with the Bio-Rad Immune-Blot Assay kit.

Results

Identification of EntA Residues Involved in the Interaction with EntE Using Phage Display

We used phage display in order to identify potential residues occurring at the EntA-EntE protein interaction interface. The Ph.D.-12™ phage display peptide library was used to pan against immobilized *H6*-EntE to obtain a set of unique EntE-binding peptide sequences. Upon successive rounds of panning, we obtained 47 unique phage-derived 12-mer peptides (Table 1). These peptides were used as inputs for the RELIC server program RELIC-MATCH (https://relic.bio.anl.gov/programs.aspx). RELIC-MATCH analysis identified a subset of the 47-peptide set that aligned as a cluster to EntA primary amino acid sequence (Figure 1A). Such a cluster indicates a high probability that these peptide sequences reflect an EntE-binding site within the EntA sequence. Examination of the EntA crystal structure (PDB code: 2fwm) revealed that these residues occur on the EntA surface, specifically at the exterior face of EntA helix α4 (Figure 1B). Residues within this cluster were compared and quantified using a

scoring function for the corresponding residues in EntA sequence (Table 2) (*243*). This method suggests a maximum similarity score at position 66 of EntA primary sequence (Leu 66), and approximately equal similarity scores at positions 64 and 68 (Gln64 and Ala68). We also found that some of our phage-derived EntE-binding peptide sequences aligned to the *E. coli* EntB primary sequence, suggesting potential EntB residues at the EntE interaction interface on that protein (data not shown).

Table 1: Phage-derived 12-mer peptides isolated from *H6*-EntE-bound phage particles.

***H6*-EntE phage peptides**	
ADANRHSTLRER	TPLWQHLLSGRA
ADANRRSTLRER	TPPWVTVLLSRQ
ADSRRALLAQRA	TPQWQQLLSFRQ
ADSWRALLAQRA	TPSWATLLAQRA
ASPWHQLLAERR	TYRMDIMSIKTV
ATSWKEMLAERQ	WHDITSLRQYSF
DSPPIFDATLPK	TPWEEVLLSRLR
DWREILGARSQV	DPVWVNILTSRQ
EHVLWQQLLTSR	AQWQETLSERAR
ENWRLTLLQRNG	KCCYYDHSHALS
GGLHWTEILRSR	HSLRSDWPLRPG
GGVHWSEILSYR	ELTGWRLLLAQR
GRLQQHEIFRSG	KVVDLYSGWNRS
KTPWQEMLASRI	HVLWQHVVDLCR
PPMWADMLLARS	GPFLPLTSLHWR
SCKQVLEHRQGM	NWRETMGVRSQV
SIDGRSIISSRN	SDWTHVLSQRAL
SLDWTELLRLRT	KIYDLSLLHPST
SMPQWQELLKVR	QPAWQQTLINRS
SPLWQDIILTRS	SWMETLRTRNMS
SPTYHSSTGLND	SLSNYQIAGNGL
SSPSWRDVLLSR	TVSWQALLEMRQ
STGDWREILRNR	TPAWQATLLGRQ
TDWRTQLHLRQG	

EntE phage peptide sequences (each 12 amino acids) obtained from a phage display experiment with EntE used as an immobilized target protein in the biopanning procedur

Table 2: Relic match analysis of EntE phage peptides.

Position	EntA Residue	Similarity score
61	Q	7.62
62	V	10.61
63	C	26.41
64	Q	47.33
65	R	57.77
66	L	68.31
67	L	60.01
68	A	44.68
69	E	30.43
70	T	19.30

Similarity scores in this table were obtained from the RELIC MATCH analysis of the 47 unique phage-derived 12-mer peptides (see Table 1) aligning to the EntA primary sequence.

A

mdvadaaqvaqvcqrllaeterldalvnaagilrmgatdqlskedwqqtf 100

ASPWHQLLAERR
ATSWKEMLAERQ
EHVLWQQLLTSR
KTPWQEMLASRI
PPMWADMLLARS
TPLWQHLLSGRA
TPQWQQLLSFRQ

B

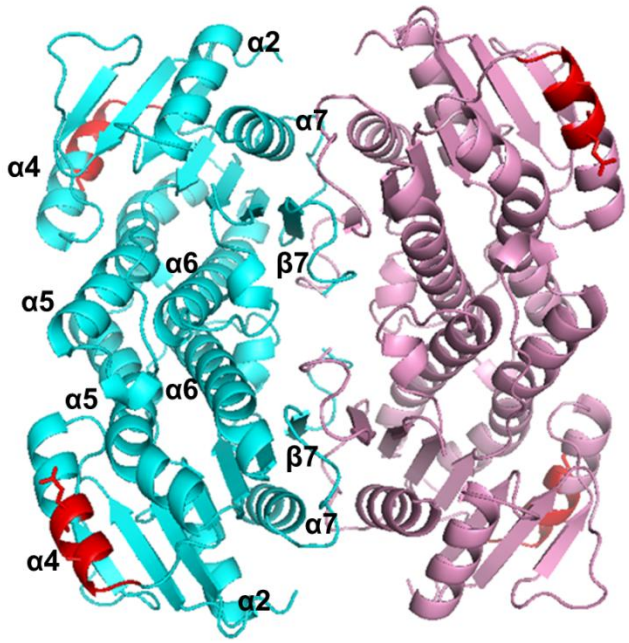

Figure 1: Identification of EntA-EntE interaction interface.

(A) RELIC MATCH output showing alignment between phage-derived EntE-binding peptides and the E. coli EntA primary sequence. (B) EntA tetramer crystal structure (PDB code: 2fwm) with the predicted EntE interaction interface identified by phage display coloured in red. The red sticks show EntA residues which are selected for mutagenesis in this study (Gln64 and Ala68). EntA was crystalized as a dimer of dimers. The cyan and pink colors represent the physiological dimers that comprise the tetramer.

Expression and Purification of EntA Variants

Based on our phage display results, we generated single-site and double-site EntA mutations at residues (Gln64, Ala68) predicted to interact with EntE. *H6*-EntA variants (Q64A, A68Q, and Q64A/A68Q) were purified by FPLC using immobilized metal affinity chromatography (Profinity IMAC column). According to SDS-PAGE analysis, all the purified variants have approximately the same subunit molecular weight ~ 28 kDa and a purity of > 95% (Figure 2A).

Circular Dichroism Spectroscopy of EntA Variants

CD spectra in the far-UV and near-UV were collected in order to measure effects of *H6*-EntA amino acid conversions (Q64A, A68Q, Q64A/A68Q) on EntA secondary structure or tertiary structure. Far-UV spectra showed that wild-type *H6*-EntA in solution has major ellipticity minima at 210 nm and 222 nm (Figure 2B, black circles). Far UV-CD spectra also revealed a minor increase in the helicity of *H6*-EntA (Q64A) (Figure 2B, white circles) whereas a significant helicity increase was observed for the double mutant (Q64A/A68Q) relative to wild-type *H6*-EntA (Figure 2B, white triangles). *H6*-EntA (A68Q) far-UV spectrum is almost the same like that of wild-type EntA (Figure 2B, black triangles). Near-UV spectra demonstrated the same changes in the spectra of *H6*-EntA (Q64A) (Figure 2C, white circles) and *H6*-EntA (A68Q) (Figure 2C, black triangles) relative to wild-type *H6*-EntA spectrum (Figure 2C, black circles). These changes likely reflect some conformational alteration in the environment of EntA chromophores upon amino acid replacement. No changes were observed in the near-UV spectrum of *H6*-EntA (Q64A/A68Q) compared to wild-type H6-EntA spectrum (Figure 2C, white triangles).

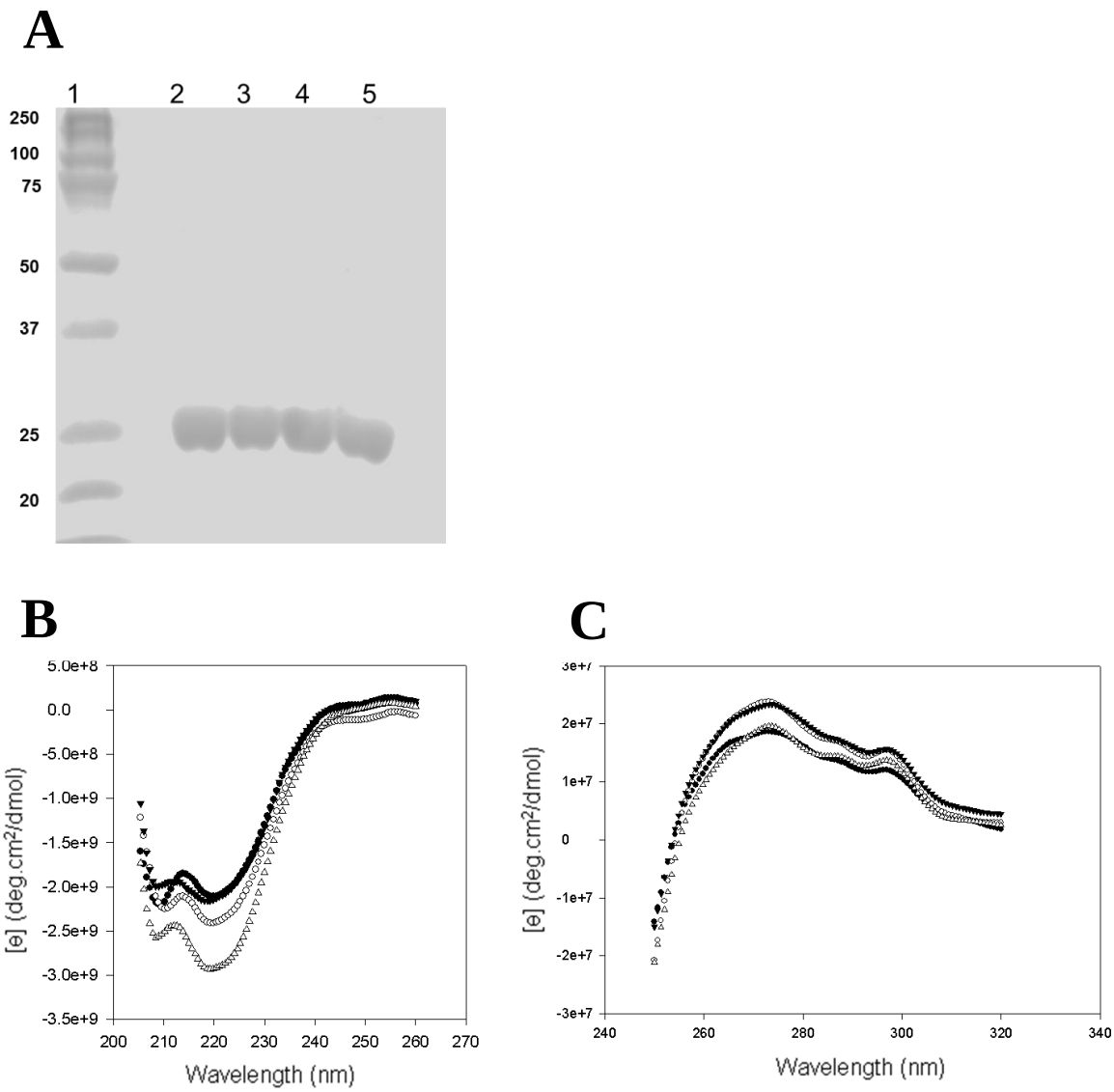

Figure 2: *H6*-EntA variants purification using IMAC and characterization using circular dichroism.

A: *Coomassie-stained 10 % SDS-polyacrylamide gel of EntA wild type and EntA variants purified by IMAC chromatography. The proteins were overexpressed in AG-1 cells grown in LB media. Protein marker (lane 1), EntA wild type (lane 2), EntA (Q64A) (lane 3), EntA (A68Q) (lane 4), and EntA (Q64A/A68Q) (lane 5).* ***B and C:*** *Far-UV and Near-UV spectra of wild-type EntA and variant proteins, respectively.* ***EntA*** *(black circles), EntA (Q64A) (white circles), EntA (A68Q) (black triangles), and EntA (Q64A/A68Q) (white triangles).*

Analytical Ultracentrifugation of EntA Variants

Sedimentation velocity analytical ultracentrifugation data of *H6*-EntA variants were analyzed using DCDT^{+}. The sedimentation data were fitted to *g*^(*s**) distributions, allowing for a model-independent estimation of sedimentation coefficients. In our previous work (Chapter 3), we demonstrated that EntA occurs in solution as a mixture of dimers and tetramers with shift toward the tetrameric form with increasing EntA concentration; dimeric EntA has an $S_{20,\,w}$ value of 4.23, and tetrameric EntA has an $S_{20,\,w}$ value of 6.71 (*242*). In this study, fits of sedimentation velocity data collected on EntA variants to the *g*^(*s**) distribution using DCDT+ revealed that EntA mutations affect the distribution of dimers and tetramers in solution. While we did not see any significant change in the $S_{20,\,w}$ values of *H6*-EntA variants at 2 μM (Table 3, rows 1-4 and Figure 3A), we did observe pronounced effects on $S_{20,\,w}$ values at an elevated concentration (20 μM) (Table 3, rows 5-8 and Figure 3B). *H6*-EntA (A68Q) variant has $S_{20,\,w}$ value (6.81), indicating that this variant occurs mostly as tetramer as wild-type *H6*-EntA (Table 3, row 6 and Figure 3B, blue squares). *H6*-EntA (Q64A) $S_{20,\,w}$ value (4.97) indicates that this variant has more dimer than tetramer at 20 μM (Table 3, rows 7 and Figure 3B, green diamonds). The double mutant *H6*-EntA (Q64A/A68Q) occurs mostly as dimer ($S_{20,\,w}$ value 3.95), even at a concentration (20 μM) at which wild-type *H6*-EntA is predominantly tetrameric (Table 3, row 8 and Figure 3B, black circles).

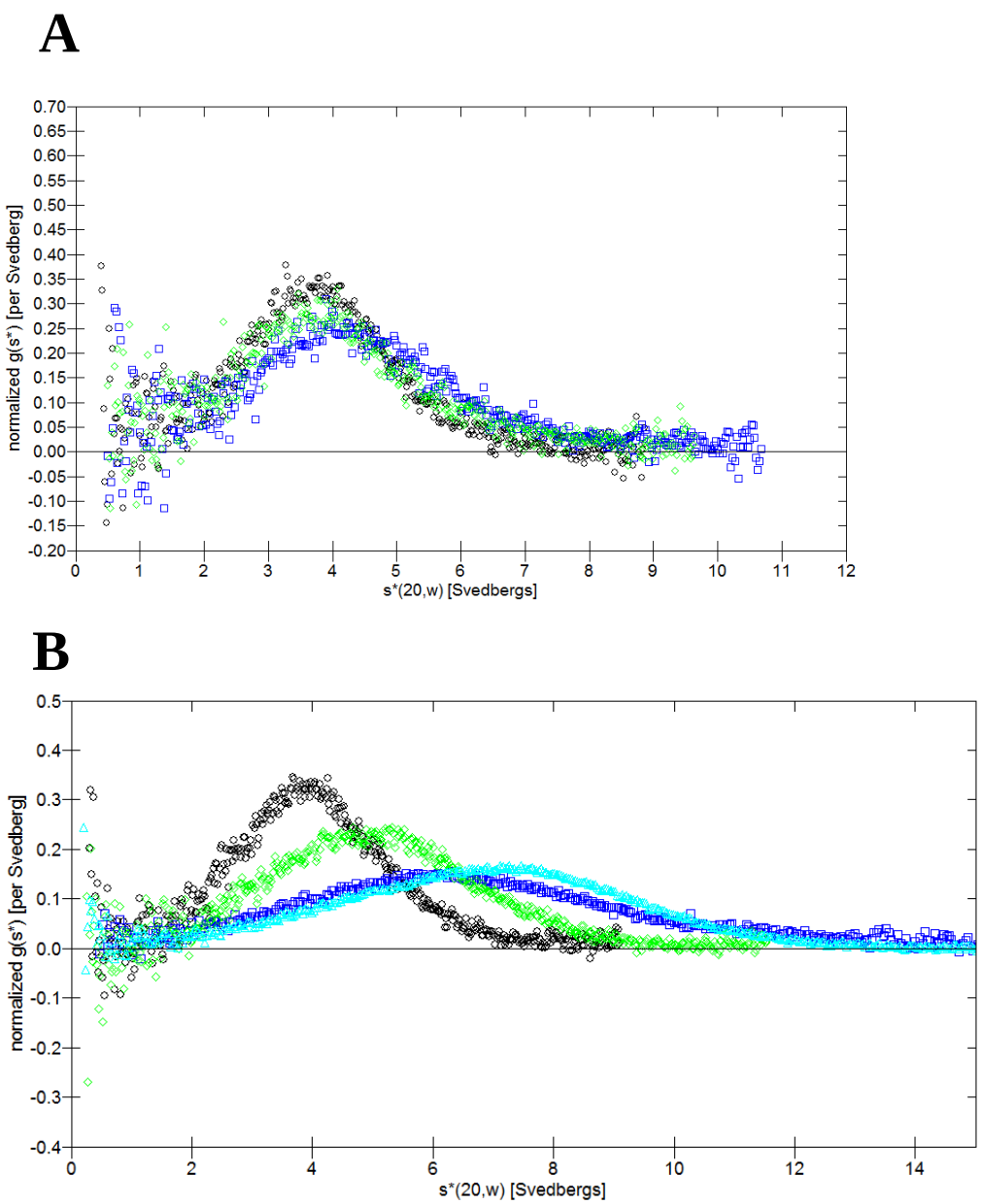

Figure 3: g(s*) distribution fits of *H6*-EntA variants sedimentation velocity analytical ultracentrifugation data.

*EntA wild-type and variant protein concentrations are 2 µM (**A**) and 20 µM (**B**). H6-EntA (light blue triangles), H6-EntA (Q64A) (green diamonds), H6-EntA (A68Q) (blue squares), and H6-EntA (Q64A/A68Q) (black circles).*

Table 3: Sedimentation velocity analytical ultracentrifugation of purified *H6*-EntA variants.

EntA variant	Concentration (µM)	$S_{20,w}$
H6-EntA[a]	2	3.87 ± 0.350
H6-EntA (A68Q)	2	4.26 ± 0.105
H6-EntA (Q64A)	2	3.90 ± 0.096
H6-EntA (Q64A/A68Q)	2	3.60 ± 0.072
H6-EntA	20	6.60 ± 0.058
H6-EntA (A68Q)	20	6.81 ± 0.110
H6-EntA (Q64A)	20	4.97 ± 0.082
H6-EntA (Q64A/A68Q)	20	3.96 ± 0.068

Protein concentrations were measured by absorbance at 280 nm; all EntA concentrations were expressed for monomer subunits. Weight-average sedimentation coefficients ($S_{20,W}$) were determined by g^(s) distribution analysis using DCDT+.*

[a] *wild-type H6-EntA $S_{20,W}$ value determined at 2 µM in chapter three.*

Chemical Crosslinking

We previously measured the *H6*-EntA-*H6*-EntE interaction using the heterobifunctional crosslinker sulfo-SMCC (*242*). In this report we used the same crosslinker in order to measure the interaction between *H6*-EntE and *H6*-EntA variants (Q64A and A68Q) (Figure 4). Maleimide-activated EntA variant proteins (22 µM) were mixed with *H6*-EntE (2.5 µM). When we used the maleimide-activated *H6*-EntA in the crosslinking mixture, we observed a conjugate band migrating according to a size greater than 250 kDa (Figure 4, lane 2). The protein contents of this band were found by LC-MS/MS to contain EntE and EntA (data not shown). When maleimide-activated *H6*-EntA (Q64A) or (A68Q) was used in the crosslinking reaction mixture, the same conjugate band (> 250 kDa) was observed, but the densities of this band varied between the *H6*-EntA variants. Mixture of *H6*-EntA (Q64A) with *H6*-EntE resulted in the formation of a

very faint conjugate band (Figure 4, lane 4). Mixture of *H6*-EntA (A68Q) and *H6*-EntE resulted in a conjugate band with a density approximately the same as that seen for wild-type *H6*-EntA (Figure 4, lane 6). All conjugate bands in this experiment were found by LC-MS/MS to contain both EntE and EntA.

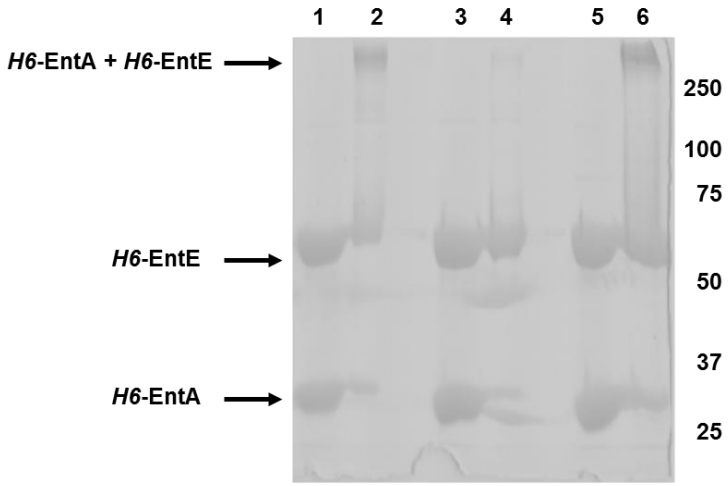

Figure 4: The effect of EntA mutations on ability to crosslink with EntE *in vitro*. *Protein size markers are represented by their molecular weight (kDa) on the right side of the gel. Lane 1: Wild-type H6-EntA mixed with H6-EntE in the absence of sulfo-SMCC. Lane 2: Wild-type H6-EntA mixed with H6-EntE in the presence of sulfo-SMCC. Lane 3: H6-EntA (Q64A) mixed with H6-EntE in the absence of sulfo-SMCC. Lane 4: H6-EntA (Q64A) mixed with H6-EntE in the presence of sulfo-SMCC. Lane 5: H6-EntA (A68Q) mixed with H6-EntE in the absence of sulfo-SMCC. Lane 6: H6-EntA (A68Q) mixed with H6-EntE in the presence of sulfo-SMCC.*

Circular Dichroism Spectroscopy of Mixtures of *H6*-EntA and *H6*-EntE

Circular dichroism spectra of protein mixtures (*i.e.*, *H6*-EntE + *H6*-EntA (wild-type or variants)) were collected, and spectra of corresponding individual proteins were subtracted from the protein mixture spectra in order to measure any observable alterations in the protein secondary or tertiary structure of individual proteins upon mixing with potential partner proteins. Using this approach, we observed increases in the near-UV spectra (260-320 nm) of *H6*-EntA and *H6*-EntA (A68Q) upon mixture with *H6*-EntE (Figure 5A and 5C). A corresponding change in the *H6*-EntE near-UV spectrum at the 275 nm band was observed in the presence of *H6*-EntA or *H6*-EntA (A68Q) (Figure 6, white squares and white triangles). We did not see any changes in *H6*-EntE and *H6*-EntA (Q64A) or *H6*-EntA (Q64A/A68Q) spectra upon mixing (Figure 5B and 5D; Figure 6, black triangles and black squares). These results suggest that the EntA variant proteins (Q64A) and (Q64A/A68Q) cannot efficiently interact with EntE.

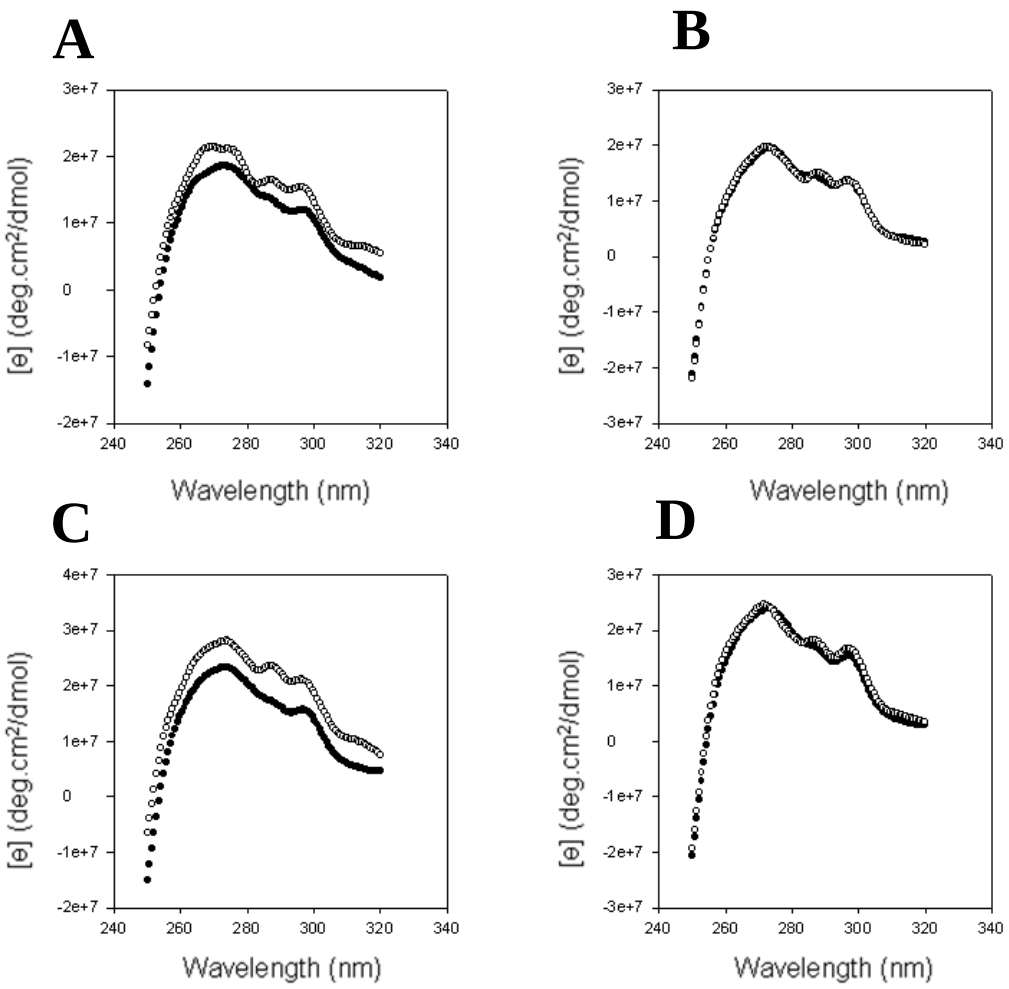

Figure 5: Near-UV CD spectra of EntA variants upon mixing with EntE.

*Black circles: near-UV spectra of H6-EntA (or H6-EntA variants). White circles: near-UV spectra of a mixture of H6-EntA (or H6-EntA variants) with H6-EntE in which H6-EntE signal was subtracted. (**A**) H6-EntA wild type, (**B**) H6-EntA (Q64A), (**C**) H6-EntA (A68Q), and (**D**) H6-EntA (Q64A/A68Q)*

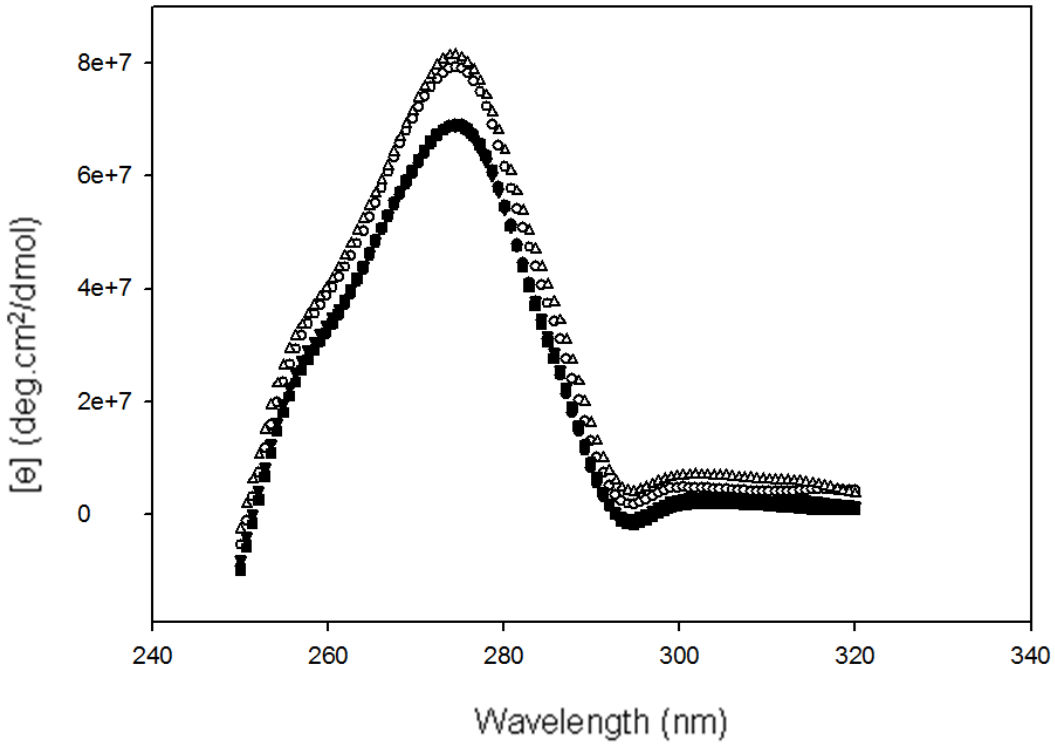

Figure 6: Near-UV CD spectra of EntE upon mixing with EntA variants.

H6-EntE near-UV spectra (black diamonds). The remaining near-UV spectra are of H6-EntE in the presence of wild-type H6-EntA or H6-EntA variants. H6-EntE spectra upon mixture with wild-type H6-EntA (white circles), H6-EntE spectra upon mixture with H6-EntA (Q64A) (black triangles), H6-EntE spectra upon mixture with H6-EntA (A68Q) (white triangles), and H6-EntE spectra upon mixture with H6-EntA (Q64A/A68Q) (black squares).

Fluorescence Spectroscopy

We previously reported that 2,3-DHB when bound to *H6*-EntE results in a FRET signal at 440 nm upon excitation of EntE intrinsic fluorophores at 280 nm (Chapter 2) (*206*). We also used this FRET signal to measure EntE interaction with its upstream partner protein EntA (*242*). In both of those studies we found that addition of EntE partner proteins (EntB or EntA) reduces the *H6*-EntE-2,3-DHB FRET signal at 440 nm in a saturable manner. Here we used the *H6*-EntE-2,3-DHB FRET signal to measure the interaction between *H6*-EntE and *H6*-EntA variants (Figure 7). We expressed the reduction in the *H6*-EntE-2,3-DHB FRET signal at 440 nm as a percentage change in $\Delta F/F0$. $\Delta F = F0 - F$ (F0 is the fluorescence intensity of *H6*-EntE-2,3-DHB solution at 440 nm in the absence of *H6*-EntA or *H6*-EntA variants, and F is the fluorescence intensity of *H6*-EntE-2,3-DHB solution at 440 nm in the presence of *H6*-EntA or *H6*-EntA variants).

Addition of *H6*-EntA (A68Q) to *H6*-EntE plus 2,3-DHB solution resulted in a minor (approximately 10%) decrease in the $\Delta F/F0$ value (Figure 7, light gray bar). This suggests that *H6*-EntA (A68Q) variant still efficiently interacts with *H6*-EntE, in agreement with our CD and crosslinking experiments. An approximately 20% decrease in the $\Delta F/F0$ value was observed upon addition of *H6*-EntA (Q64A) to the *H6*-EntE+2,3-DHB mixture, reflecting a more pronounced negative effect of this mutation on the EntA-EntE interaction (Figure 7, dark gray bar). The largest reduction in the $\Delta F/F0$ value was observed upon addition of *H6*-EntA (Q64A/A68Q) to the *H6*-EntE+2,3-DHB solution (Figure 7, black bar), indicating that the Q64A/A68Q mutation had the most disruptive effect on EntA-EntE interaction.

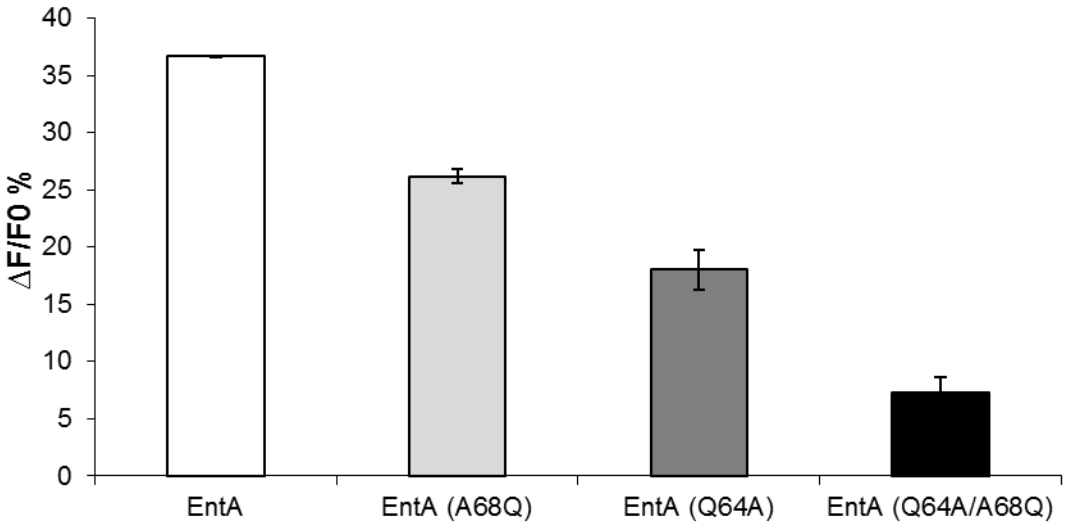

Figure 7: Effect of amino acid conversions in EntA on the interaction with EntE+DHB as measured by fluorescence spectroscopy.

The figure shows the reduction percent of the H6-EntE-bound 2,3-DHB FRET signal at 440 nm upon mixing with 6 μM EntA or EntA variants. White bar: Reduction percent of H6-EntE-2,3-DHB FRET signal in the presence of wild-type H6-EntA. Light gray bar: Reduction percent of FRET signal in the presence of H6-EntA (A68Q). Dark gray bar: Reduction percent of FRET signal in the presence of H6-EntA (Q64A). Black bar: Reduction percent of FRET signal in the presence of H6-EntA (Q64A/A68Q). The reduction percent values are the average of three replicates and the error bars are the standard deviations of replicate values.

Growth Phenotype Assays:

In our previous study, we showed that addition of *H6*-EntA to an *H6*-EntE assay mixture resulted in a significant increase in EntE activity (Chapter 3) (*242*). These results suggested that EntA-EntE interaction could increase enterobactin biosynthesis efficiency *in vivo*, thus affecting bacterial growth under iron-limiting conditions. Here we measured the effect of EntA amino acid conversions of residues predicted by phage display on *E. coli* cell growth under iron-limiting conditions. We transformed an *entA*$^{-}$ *E. coli* strain

with constructs expressing *H6*-EntA mutations (Q64A, A68Q, Q64A/A68Q), and measured the ability of these transformants to grow in iron-restricted media containing 2,2'-dipyridyl. In the absence of 2,2'-dipyridyl, *entA*$^-$ cells expressing *H6*-EntA (A68Q) (Figure 8A, dark gray bar {-Dipyridyl}) exhibited growth similar to that of *entA*$^-$ cells expressing wild-type *H6*-EntA (Figure 8A, black bar {-Dipyridyl}). In contrast, transformants expressing *H6*-EntA (Q64A) exhibited an approximately 25 % reduction in growth (Figure 8A, light gray bar {- Dipyridyl}), and transformants expressing *H6*-EntA (Q64A/A68Q) exhibited approximately 40 % reduction in cell growth (Figure 8A, white bar {- Dipyridyl}) relative to *H6*-EntA wild type. In agreement with the growth in the absence of 2,2-dipyridyl, cells expressing *H6*-EntA (A68Q) grew at levels similar to wild-type *H6*-EntA in the presence of 2,2'-dipyridyl (Figure 8A, dark gray bar {+ Dipyridyl}). *EntA*$^-$ cells expressing *H6*-EntA (Q64A) and *H6*-EntA (Q64A/A68Q) exhibited an 80 % reduction in the growth in the presence of 2,2'-dipyridyl (Figure 8A, light gray bar and white bar, respectively {+ Dipyridyl}). Western blot analysis revealed that all *H6*-EntA variants are similarly expressed in the transformants used in our growth experiments (Figure 8C). We did not observe any growth for *entA*$^-$ cells transformed with empty pCA24N vector (data not shown)

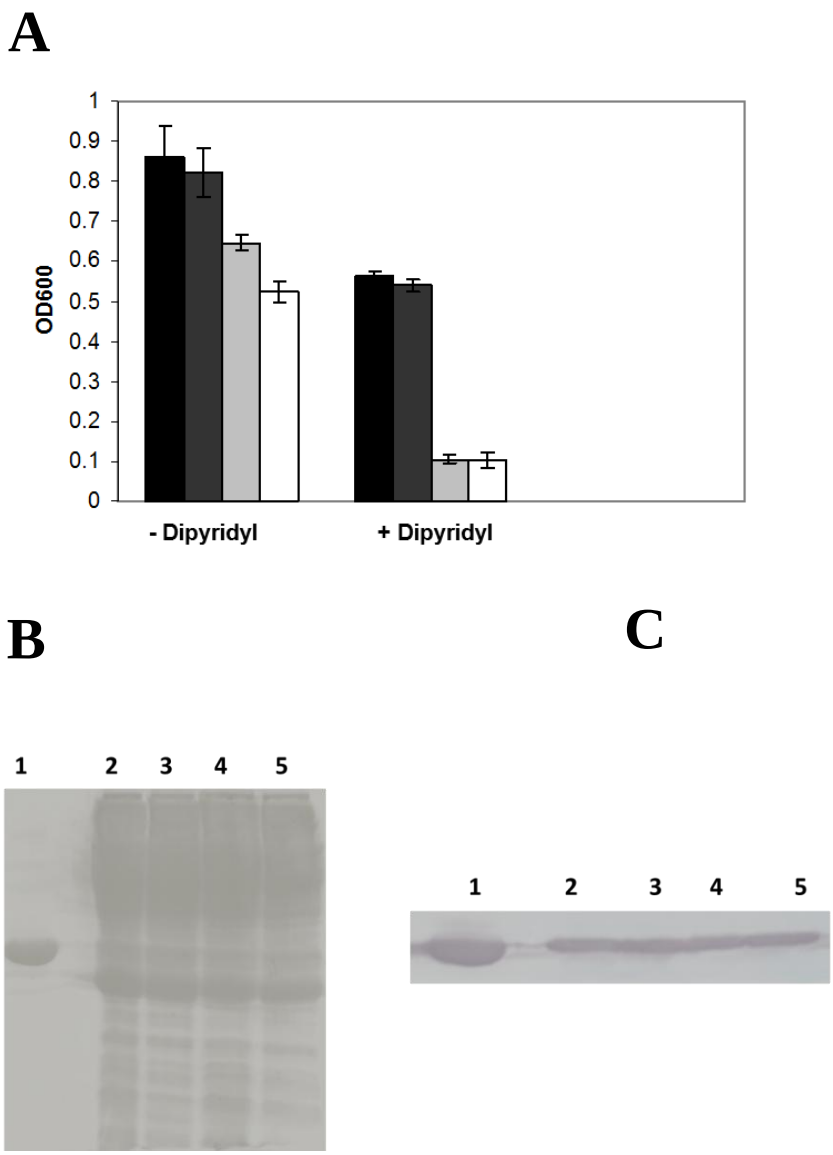

Figure 8: Monitoring the effect of amino acid conversions in EntA on EntA-EntE interaction *in vivo* through growth phenotype assays.

(A) *Densities (OD_{600}) of entA⁻ cells transformed with constructs expressing wild-type and variant EntA proteins after growth in M63 minimal media in the presence and absence of 65 μM 2,2'-Dipyridyl for 42 hours. H6-EntA wild type (black bars), H6-EntA (A68Q) (dark grey bars), H6-EntA (Q64A) (light grey bars), and H6-EntA (Q64A/A68Q) (white bars).* ***(B)*** *Coomassie-stained SDS-PAGE of E. coli BW25113 soluble whole-cell lysates (entA⁻ cells transformed with constructs expressing wild-type H6-EntA or H6-EntA variants); each lane contains 50 μg total protein from each lysate. Here the cells*

were grown in M63 media for 42 hours. Lane 1: purified H6-EntA, 5 μg. Lanes 2-5: proteins recovered from soluble whole-cell lysates expressing wild-type or variant H6-EntA proteins. Lane 2: wild-type H6-EntA, Lane 3: H6-EntA (Q64A), Lane 4: H6-EntA (A68A), Lane 5: H6-EntA (Q64A/A68Q). ***(C)*** *Western blot analysis of SDS-PAGE of E. coli BW25113 soluble whole-cell lysates. Lane 1: purified H6-EntA, 2.5 μg. Lanes 2-5: proteins recovered from soluble whole-cell lysates expressing wild-type or variant H6-EntA proteins (50 μM each). Lane 2: H6-EntA wild type, Lane 3: H6-EntA (Q64A), Lane 4: H6-EntA (A68A), Lane 5: H6-EntA (Q64A/A68Q).*

Discussion

It is now known that the majority of proteins function in biochemical processes as proteins complexes (*228-230*). One function of protein-protein interactions is to enhance the process in which they involve. Such enhancement might occur indirectly through the sequestration of intermediates by direct channeling between the partner protein active sites without release into the bulk phase (*231-233*). Identification and characterization of residues occurring at protein-protein interaction interfaces are now recognized as active targets in the development and design of new drugs and antimicrobial agents (*219*). In the case of pathogenic bacteria infecting mammalian hosts, enterobactin is not itself a virulence factor due to its removal by circulating albumin in serum and by the innate immune system protein NGAL (*132, 161*). However, in bacteria harboring the *iroA* gene cluster, enterobactin can be glycosylated and secreted as salmochelin, which is not recognized by NGAL and has less hydrophobicity (*166*). Therefore inhibition of the growth of salmochelin-secreting pathogens can be targeted at stages prior to glycosylation starting at enterobactin biosynthesis. Protein-protein interactions have been established to play an important role in enterobactin biosynthesis (*142, 144, 181, 206*). The enterobactin biosynthetic enzyme EntE catalyzes the first reaction in the NRPS

module. In terms of overall enterobactin biosynthesis, EntE acts as a central enzyme that can form complexes both with its downstream partner EntB and its upstream partner EntA (*206, 242*), with the EntA-EntE interaction facilitating a direct physical link between the DHB and NRPS modules. Here we show through *in vivo* assays that this interaction is necessary for bacterial growth under iron-limiting conditions, likely through the enhancement of enterobactin biosynthesis *in vivo*. Therefore, disruption of the EntA-EntE interaction appears to be a good target in the development of new antibiotics against bacteria that use enterobactin-based siderophores as virulence factors.

In order to identify amino acid residues in the EntA-EntE interaction interface, we used phage display to pan random peptide sequences against immobilized *H6*-EntE. Using this approach, we obtained a set of unique peptides that aligned to the EntA primary sequence, suggesting a region on EntA potentially involved in a direct interaction with EntE. According to the EntA crystal structure (*183*), EntA residues Gln64 and Ala68, which we identified by phage display as being EntE-interacting residues, occur on the exterior face of the α4 helix, and proximal to the EntA physiological dimer interface (Figure 1B). We therefore targeted these residues for mutagenesis to investigate their role in the EntA-EntE interaction, both *in vitro* and *in vivo*. Our crosslinking experiments showed only a very faint conjugate band could be formed by mixing *H6*-EntE with maleimide-activated *H6*-EntA (Q64A), suggesting that the Q64A mutation diminishes the ability of EntA to interact with EntE. In contrast, crosslinking reactions containing *H6*-EntA (A68Q) resulted in the presence of an EntA-EntE conjugate band at levels comparable to that seen when wild-type EntA was used.

Previously we showed that a reduction in *H6*-EntE-2,3-DHB FRET signal occurred in the presence of *H6*-EntA, presumably due to conformational alterations in the EntE active site upon EntA-EntE interaction (*242*). Here our *H6*-EntE-2,3-DHB FRET assay demonstrated a significant decrease in the FRET signal reduction upon addition of *H6*-EntA (Q64A) compared to wild-type *H6*-EntA or *H6*-EntA (A68Q), indicating the pronounced negative effect of Q64A mutation on the EntA-EntE interaction, consistent with our crosslinking data. A further decrease in the *H6*-EntE-2,3-DHB FRET signal reduction was observed when the double mutant *H6*-EntA (Q64A/A68Q) was used, suggesting that multiple mutations in EntA helix α4 can completely abrogate the EntA-EntE interaction. Our circular dichroism data indicated changes in the near-UV spectra of *H6*-EntE in the presence of *H6*-EntA or *H6*-EntA (A68Q). These spectral changes reflect conformational rearrangements of relevant chromophores occurring upon EntA-EntE interaction, and our results show that the EntA (A68Q) mutation does not significantly affect the interaction. In contrast, no CD spectral changes were observed upon mixing *H6*-EntE with *H6*-EntA (Q64A) or with *H6*-EntA (Q64A/A68Q), indicating that these variant proteins likely do not interact efficiently with *H6*-EntE. In support of our *in vitro* data, our *in vivo* growth studies revealed that attempted rescue of the *entA*$^-$ phenotype by transformation with constructs expressing *H6*-EntA variants Q64A and Q64A/A68Q resulted in diminished bacterial growth under iron-limiting conditions. The similar levels of expression of EntA variants expressed in transformed *entA*$^-$ BW25113 cells as revealed by our Western blot suggests that the observed effect on the bacterial growth is likely the result of amino acid substitutions at positions 64 and 68 in expressed EntA variants, and

not due to these conversions having a negative effect on protein expression at the transcriptional or translational level.

The EntA crystal structure indicates that positions 64 and 68 occur on an alpha helix 4 near the dimer interface within the EntA biological subunit. Do the (Q64A) and (Q64A/A68Q) mutations of EntA therefore disrupt EntA-EntE interaction due to their participation in the interaction interface, or is the oligomeric state of EntA altered upon mutation at these positions? In our previous study of EntA oligomeric structure in solution, we found that EntA behaves in solution as a mixture of dimers and tetramers (*242*). EntA undergoes reversible conversion between the two oligomeric forms in a concentration-dependent manner. At low EntA concentrations, EntA dimers are the predominant form. Upon increasing EntA concentration, the distribution shifts towards the tetrameric form until EntA tetramers become predominant at high (> 18 μM) EntA concentrations. In this study, our sedimentation velocity analytical ultracentrifugation experiments on *H6*-EntA variants revealed that some of EntA mutations cause a shift in the distribution of EntA dimers and tetramers in solution. Since the EntA oligomeric structure is dependent on concentration, we maintained *H6*-EntA variant at constant concentrations in our AUC experiments. Thus any alteration in EntA quaternary structure would reflect the effect of the EntA conversions. *H6*-EntA (A68Q) in solution has $S_{20,W}$ value 6.81 at 20 μM, which is almost equal to that of wild-type *H6*-EntA ($S_{20,W}$ = 6.6). This indicates that EntA tetramers are predominant in *H6*-EntA and *H6*-EntA (A68Q) solutions at this concentration, consistent with our results that *H6*-EntA (A68Q) is able to interact with EntE with similar efficiency as wild-type *H6*-EntA. However, the Q64A mutation of EntA shifts the distribution towards the dimeric form, resulting in an

observed $S_{20,W}$ value of 4.97. A pronounced shift toward the dimeric form was observed for the Q64A/A68Q mutation ($S_{20,W}$ value of 3.95).

EntA was crystallized as a dimer of dimers, in which each physiological EntA dimer in the tetramer is composed of two EntA monomer subunits that interact strongly with each other (*183*) (Figure 1B, cyan and pink colored dimers). This EntA physiological dimer formation is supported by the four-helix bundle that contains α5 and α6 from each monomer. Formation of the four-helix bundle results in the burying of most of the residues that constitute the physiological dimer interface. The 'non-physiological dimer' in this structure is composed of the monomeric subunits at the dimer-tetramer interface (Figure 1B, cyan-colored subunit plus the corresponding pink-colored subunit). EntA subunits in the non-physiological dimer interact through the C-terminal loops and β7 from each subunit, giving less buried surface at the interaction interface compared to the physiological dimer.

An explanation of the effect of Q64A and Q64A/A68Q conversions on EntA oligomeric structure is not immediately apparent. There are two possible reasons for the effects we observed. The EntA replacements studied in this report occur on the solvent-exposed face of helix α4. The A68 side chain is completely exposed to the solvent while the Q64 side chain is partially facing α5 and the solvent (Figure 9, red sticks). The segment of α4 that is proximal to α5 is rich in hydrophobic residues (A56, A57, V59, A60, C63, Q64, L67, and A68) (Figure 9, yellow and red sticks). In contrast, the α5 residues that face α4 are mostly polar (N109, L110, Q113, T114, Q117, and R120) (Figure 9, orange sticks). Since most of α5 residues facing α4 are hydrophilic, Q64 in α4 might have the most important role in stabilizing α4-α5 interaction *via* a hydrogen bond

interaction with Q113 on α5. Thus there is the possibility that the transition to the dimeric forms upon amino acid conversions at these positions resulted from disruption of α4-α5 interaction followed by diminishing the stability of α5 to participate in physiological dimer formation. Since the crystal structure of EntA indicates that the tetrameric form is a dimer of physiological dimers, this would mean that the dimeric forms of the EntA variants observed in our AUC experiments are due to non-physiological dimer formation (i.e. between subunits found normally at the dimer-tetramer interface). The EntA residue A68 might participate in the α4-α5 interaction stabilization to a lesser extent, which may also explain why we observed that *H6*-EntA (Q64A) was more predominantly dimeric than EntA (A68Q). This effect was also likely cumulative in the double mutant (Q64A/A68Q) such that non-physiological dimers occurred as the predominant form.

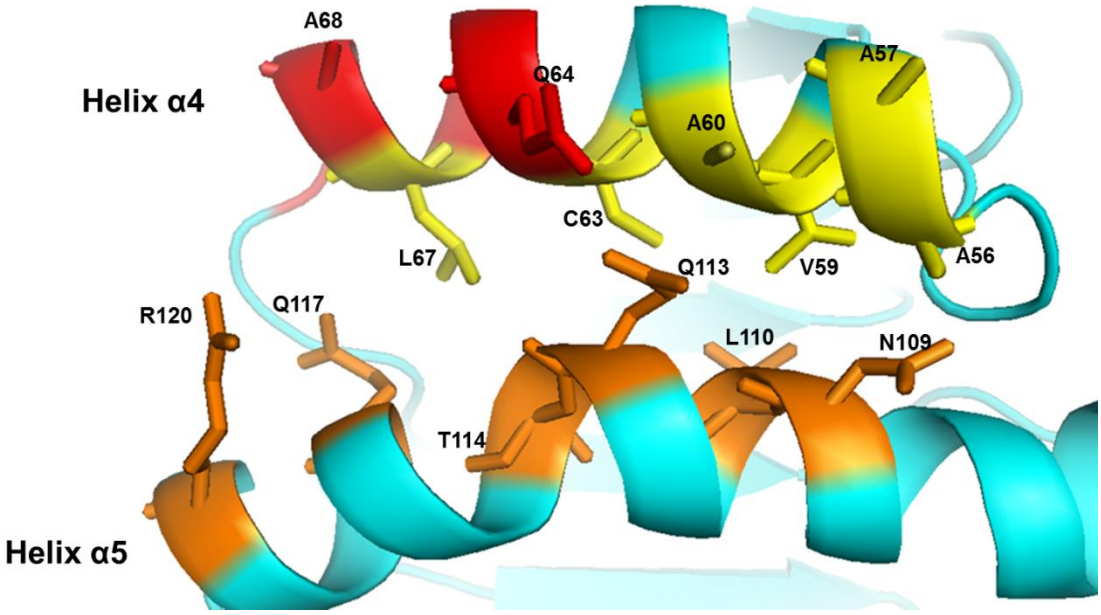

Figure 9: EntA residues involved in the interaction between helix α4 and helix α5. *Residues in helix α4 are shown as yellow sticks except residues selected for mutagenesis, which are shown as red sticks. Residues in helix α5 are shown as orange sticks.*

The alternate possibility is that the observed increase in the helicity of both *H6*-EntA (Q64A) and (Q64A/A68Q) resulted from changes in EntA folding caused by amino acid conversions at these positions. The small increase in the *H6*-EntA (Q64A) helicity correlated with a shift towards the dimeric form as revealed by our AUC experiments. The larger increase in helicity of the *H6*-EntA (Q64A/A68Q) variant correlated with almost a complete conversion to the dimeric form as observed by AUC. This suggests a direct relation between the observed increase in helicity content and the dimer-tetramer distribution in the solution for these EntA variants. This possible alteration in the variant EntA structure might bring residues 64 and 68 to closer to the tetramerization interface, causing a steric disruption of tetramer formation. In this case, the dimeric forms observed for the variant proteins in our AUC experiments would represent the physiological dimers.

In summary, we have provided here initial evidence of EntA residues occurring at EntA-EntE interaction interface. Our fine-mapping has not only identified residues in EntA that are involved in EntE interaction, but as well EntA residues necessary for tetramer formation. In Chapter 3, we showed that EntE likely has a higher affinity for EntA in the tetrameric form compared to the dimeric form (*242*). In this chapter, the negative effect of Q64A and Q64A/A68Q mutations on the EntA-EntE interaction are likely be due to (i) the participation of these residues at the EntA-EntE interaction interface, or (ii) to the conversion of EntA oligomeric structure to a dimeric form (either physiological or non-physiological), thus lowering the binding affinity of EntE to these variant proteins, or (iii) a combination of (i) and (ii). We also showed that EntA variants (Q64A and Q64A/A68Q) could not interact efficiently with EntE *in vitro*, and could also

not support bacterial growth under iron-limiting conditions *in vivo* when expressed in *entA*$^{-}$ cells. These residues thus provide promising targets in the design new chemotherapeutic agents that could hinder the growth of enterobactin-dependent pathogens inside the host.

CHAPTER FIVE: OVERALL SUMMARY AND GENERAL DISCUSSION

OVERALL SUMMARY

The overall goal of this research project is to better understand the enterobactin biosynthetic enzyme EntE and its binding to its substrate 2,3-DHB as well as its interaction with the upstream and downstream partner proteins EntA and EntB, respectively. My thesis is divided into three research-related chapters:

In **the first research chapter (Chapter 2 in this thesis)**, biophysical techniques were used to study the interaction of EntE with its substrate 2,3-DHB, in addition to characterization its interaction with the downstream partner EntB in the presence and absence of 2,3-DHB. The results of this chapter showed that the EntE-EntB interaction is stimulated by 2,3-DHB. Furthermore, EntB undergoes significant conformational changes upon 2,3-DHB binding that allow it to interact efficiently with EntE. This study demonstrated the first reported detailed description of this interaction that is essential for enterobactin biosynthesis.

In **the second research chapter (Chapter 3 in this thesis)**, a novel protein-protein interaction between EntE and EntA was characterized *in vitro*. Biophysical techniques and enzymatic assays were used in this chapter. The results of this chapter demonstrated that EntA quaternary structure is highly dependent on its concentration. Fluorescence and AUC experiments suggested that EntA quaternary structure likely plays a critical role in EntA-EntE interaction. Pull down assays provided additional evidence for EntE interactions with EntA and EntB. This suggests that EntE is a key enzyme in the enterobactin biosynthesis that is able to interact with more than one protein.

The third research chapter (Chapter 4 in this thesis) focuses on identification and characterization of the EntE interaction interface on the EntA surface. Phage display

was used to determine EntA residues that constitute the interaction interface for EntE. Based on the phage display results, *H6*-EntA variants containing single-site and double-site mutations were created. Here, *in vitro* studies showed that *H6*-EntA (Q64A) and *H6*-EntA (Q64A/A68Q) variants exhibited a very weak binding to *H6*-EntE. Transformation of *entA*-knockout strains with *entA* genes encoding for those *H6*-EntA variants restricted their growth in iron-depleted media compared to *entA*-knockout strain transformed with wild-type *entA* gene.

GENERAL DISCUSSION

2,3-DHB Functions as a FRET Sensor in EntE Active Site

EntE, 2,3-DHB-AMP ligase, is one of the key enzymes involved in enterobactin biosynthesis. It catalyzes 2,3-DHB adenylation, resulting in 2,3-DHB-AMP formation. EntE then catalyzes the transfer of 2,3-DHB to the *holo*-EntB phosphopantetheine moiety, resulting in formation of acylated *holo*-EntB with release of AMP (*139, 141*). Adenylate forming enzymes are widely distributed in the biosynthesis of many siderophores. Some of them catalyze the adenylation of 2,3-DHB such as EntE in enterobactin biosynthesis by *E. coli (141),* and DhbE in bacillibactin biosynthesis by *Bacillus subtilis (184).* Altenatively, some of these enzymes adenylate salicylate instead of 2,3-DHB such as in the case of MbtA in mycobactin biosynthesis by *Mycobacterium tuberculosis* (*245*), PchD in pyochelin biosynthesis by *Pseudomonas aeruginosa (246),* and YbtE in yersiniabactin biosynthesis by *Yersinia pestis (247).* These enzymes have around 40-50 % sequence identity (*206, 248*). Recently, many studies have focused on the adenylate forming enzymes involved in different siderophore biosynthesis processes, revealing the attempts to inhibit these enzymes using small molecule product mimics (*127, 248-249*).

In the second chapter, we characterized 2,3-DHB binding to *H6*-EntE using circular dichroism, fluorescence spectroscopy, and ITC. Here we found that *apo-H6*-EntE has an emission peak at 330 nm upon excitation the protein at 280 nm. In contrast, 2,3-DHB has a very small emission peak at 440 nm when excited at 280 nm. Addition of 2,3-DHB to *H6*-EntE solution resulted in a decrease in *H6*-EntE emission peak at 330 nm with a significant increase in the 2,3-DHB emission peak at 440 nm (Chapter 2, Figure

4A). As a result of the overlap between EntE tyrosine fluorophores emission maximum wavelength (305 nm) and 2,3-DHB excitation maximum wavelength (306 nm), we conclude that the peak at 440 nm resulted from fluorescence resonance energy transfer (FRET). This FRET occurred between EntE intrinsic fluorophores as donor and 2,3-DHB as acceptor (Chapter 2, Figure 2C).

The increase at 440 nm was saturable with increasing 2,3-DHB concentrations and was fit to a hyperbolic single-site binding equation, giving EC_{50} value of 2,3-DHB binding to *H6*-EntE that agrees with the K_D value (7.35 $\pm$ 0.31 μM) determined by ITC (Chapter 2, Figure 3 and Figure 4C, 4D). This dissociation constant value reflects lower affinity of 2,3-DHB binding to *H6*-EntE than the expected affinity based on the reported EntE-2,3-DHB K_m value (2.7 μM) by Rusnak, F. *et al* (*141*). The DhbE crystal structure determined by May *et al* revealed that 2,3-DHB binding is followed by ATP binding at the entrance of the active site, and followed by P-loop closure at the top of the active site during the catalysis (*184*). Thus the lower affinity of 2,3-DHB binding in our fluorescence assay can be attributed to the absence of ATP. ATP binding would increase the 2,3-DHB affinity by preventing its dissociation from EntE active site. The affinity of EntE binding to its product 2,3-DHB-AMP has not been determined. However, adenylate product analogues were used as competitive inhibitors of EntE and DhbE with Ki values of 4.5 nM and 85 nM, respectively (*186-187*). This suggests a higher affinity of these adenylate forming enzymes for their products relative to their substrate. The higher affinity of these enzymes for their product is likely achieved by the P-loop closure as reported by May and coworkers (*184*). Thus, this higher affinity was a good target in the synthesis of inhibitors in order to hinder the siderophore biosynthesis processes that use

these enzymes (*186-187*). The high affinity of EntE binding to 2,3-DHB-AMP likely ensures the effective channeling of 2,3-DHB directly from EntE active site to *holo*-EntB active site without release to the cytoplasm.

The Specificity of EntE Binding to 2,3-DHB

An EntE homology model was generated using the *Bacillus subtilis* homologue DhbE (*184*). EntE has five tyrosine residues in the active site (Chapter 2, Figure 2C). The nearest tyrosine residue to 2,3-DHB is Y236, and this residue likely stabilizes 2,3-DHB *via* hydrophobic interactions, in agreement with DhbE crystal structure reported by May *et al* (*184*). In our EntE homology model, H233 and K519 are predicted to stabilize the DHB-carboxylate moiety. These residue side chains superimpose with the 2,3-DHB-carboxylate stabilizing residues (H234 and K517) in DhbE active site, indicating their role in DHB binding. Our EntE model also anticipates the involvement of EntE active site residues N234 and S239 in 2,3-DHB binding *via* its C-2 and C-3 hydroxyl groups, respectively (Chapter 2, Figure 2D). In the second chapter, our data showed that the mixing of neither 2,5 DHB nor 3,5 DHB with EntE resulted in FRET (Chapter 2, Figure 5B). These results revealed the selective binding of EntE to its natural substrate 2,3-DHB. Although most of catecholate siderophores use 2,3-DHB as iron-binding group (*44*), there are some siderophores that use other DHB isomers as iron-binding groups. For example, 3,4-DHB is found in petrobactin produced by *Bacillus anthracis* and *Bacillus cereus* (*98*), and 2,5-DHB is found in a mammalian siderophore produced by a mammalian cell (*1*). The hydroxyl group positions in the DHB moiety of these siderophores may play a role in the recognition of these DHB isomers by their enzymes or in siderophore recognition by their receptors. The specificity of 2,3-DHB binding to

EntE can be interpreted by the presence of N234 and S239 in the our EntE model active site close to the 2 and 3 hydroxyl groups of 2,3-DHB, respectively. This suggests the role of these residues in stabilizing 2,3-DHB binding by forming hydrogen bonds with the C-2 and C-3 hydroxyl groups. In contrast, the hydroxyl group at C5 in 2,5 DHB or 3,5 DHB isomers would be proximal to a loop containing to V306, G307, G308. None of these residues can form hydrogen bond to stabilize 2,5 DHB or 3,5 DHB binding. Thus our data and EntE model predict the involvement of EntE active site residues N234 and S239 in the binding of 2,3-DHB.

The Role of 2,3-DHB in EntE-EntB Interaction

Gehring and coworkers revealed that EntB is bifunctional enzyme with isochorismatase activity (ICL domain) that catalyzes the second reaction in the DHB module, and aryl carrier protein activity (Ar-CP domain) that catalyzes EntE downstream reaction (*139*). It has also been reported that *holo*-EntB stimulated EntE activity approximately 10-fold (*144*). This suggests that the EntE-EntB interaction likely stimulates the direct channeling of 2,3-DHB to *holo*-EntB active site, regenerating EntE for another round of catalysis. In the second chapter, we studied the 2,3-DHB binding to both EntE and EntB and its effect on the interaction between these proteins. All DHB isomers were able to quench EntB intrinsic fluorescence (Chapter 2, Figure 5A). 2,3-DHB were found to have the most quenching effect on EntB emission spectra, suggesting that EntB favors the binding of this isomer. This is the first study to demonstrate 2,3-DHB binding to EntB. Although 2,3-DHB is not the natural substrate of EntB, our data suggest that EntB might have an allosteric site to bind 2,3-DHB. EntC catalyzes a reversible reaction in the first step of enterobactin biosynthesis pathway (*174*) but the

EntB ICL domain catalyzes irreversible reaction in the second step of that pathway (*139*). This suggests that EntB ICL domain-catalyzed reaction is likely the first committed step of this pathway. Thus 2,3-DHB binding to EntB might have a regulatory role such as feedback inhibition of the DHB module in case of surplus production of 2,3-DHB.

We found that *H6*-EntB is able to quench *H6*-EntE-bound 2,3-DHB FRET signal at 440 nm in a saturable manner with increasing *H6*-EntB concentrations. According to our FRET assay, *H6*-EntE and *H6*-EntB interact with EC_{50} value in the low micromolar range, suggesting the proteins interact transiently probably for substrate channeling (Chapter 2, Figure 6). The changes in the near-UV spectra of each protein upon mixing reflecting EntE-EntB interaction were observed only in the presence of 2,3-DHB (Chapter 2, Figure 7B and 7D). We therefore conclude that 2,3-DHB binding to EntB is likely to induce conformational changes in EntB to ensure efficient interaction with EntE. This conclusion is consistent with studies reported by Drake *et al* (*181*). They showed that some mutations in the EntB Ar-CP domain increased the rate of EntB acylation by EntE, suggesting that EntB conformation alteration might be required to optimize the interaction interface for its interaction with EntE. Our pull-down assays support our CD and fluorescence data in this respect. We found that our purified *H6*-EntB was able to efficiently pull down *E. coli* EntE only in the presence of exogenous 2,3-DHB, revealing the essential role of 2,3-DHB in EntE-EntB interaction (Chapter 2, Figure 8). Studies in Chapter Two were the first-reported characterizations of EntE-2,3-DHB binding and the role of 2,3-DHB in the EntE-EntB interaction.

The Effect of the Protein Concentration on EntE and EntA Quaternary Structure

EntA and EntE oligmeric structures were studied in the third chapter as a function of the protein concentration at 20 °C using AUC. Here we found that *H6*-EntE presents in solution as monomer independent on its concentration (Chapter 3, Figure 1A). In contrast, *H6*-EntA oligomeric structure is dependent on *H6*-EntA concentration in solution. Here we found that *H6*-EntA behaves in solution as a mixture of dimer and tetramer. It was shown by Sundlov and coworkers that EntA crystallizes as a dimer of dimers (*183*). Our AUC analysis revealed that *H6*-EntA undergoes reversible conversion between the dimeric and tetrameric forms depending on its concentration (Chapter 3, Figure 1B). The dimer-tetramer distribution shifts toward the tetramer form upon increasing *H6*-EntA concentration gradually until *H6*-EntA tetramer becomes the predominant form (over 18 μM). The dependence of EntA oligomeric structure on its concentration might have a regulatory role in the enterobactin biosynthesis process. A similar example of self-association behavior affecting function is seen with tumor suppressor protein p53 oligomerization that described by Weinberg and coworkers (*250*). They found that a truncated form of p53 containing the oligomerization and DNA binding domains behaves as a mixture of dimers and tetramers. In that study, the dimeric form of p53 is predominant at submicromolar concentrations but the tetrameric form is predominant at high concentrations. The tetrameric form of p53 interacts with higher affinity to DNA compared to the dimeric form.

DHB Biosynthesis and NRPS Modules are Coordinated by the EntA-EntE Interaction

It has been shown that protein-protein interactions play a crucial role in the enterobactin NRPS module *(142, 181, 195, 197, 206)*. In the third chapter, for the first time we showed that enterobactin biosynthetic functional modules (DHB and NRPS modules) are directly linked through EntA-EntE interaction. EntA catalyzes the last reaction in the DHB module while EntE catalyzes the first reaction in the NRPS module (Chapter 3, Scheme 1B and 1C). The interaction between these enzymes is likely to facilitate enterobactin biosynthesis, probably by direct intermediate channeling. The role of protein-protein interactions in mediating substrate channeling between active sites has been identified in many processes. For example, it was shown by Tsuji and coworkers that protein-protein interactions between the modules of the polyketide synthase complex play a major role in intermediate channeling (*251*). It was also revealed by Winkel that intermediate channeling *via* protein-protein interactions plays an essential role in some of the plant metabolic processes (*252*). Moreover protein-protein interactions facilitate the substrate channeling between enzymes involved in the purine biosynthesis (*253*). Here we propose that EntA-EntE interaction will promote the growth of the bacteria that use enterobactin related siderophores inside the host. Such an interaction is a promising target for development of antimicrobial drugs.

In the third chapter of this thesis, *H6*-EntE activity was shown to be significantly enhanced upon *H6*-EntA addition to the *H6*-EntE reaction mixture (Chapter 3, Figure 4), supporting our assumption that this interaction will increase the efficiency of enterobactin biosynthesis. It has been reported by Ehmann *et al* that EntE activity is also stimulated by

the *holo*-EntB Ar-CP domain (*144*). The increase in EntE activity might result from optimization of EntE active site upon conformational changes that occur during its interaction with EntA. This assumption is supported by the observed decrease in *H6*-EntE-bound 2,3-DHB FRET upon EntA-EntE interaction. Here we assume that EntA-EntE interaction alters the position of 2,3-DHB in the active site, such that 2,3-DHB moved away from the FRET donors (resulted in the observed quenching of the FRET signal), and toward ATP (resulted in the observed increase in EntE activity) (Chapter 3, Scheme 2).

Sulfo-SMCC crosslinking experiments gave us a direct evidence for EntA-EntE interaction at 20°C. Here, the sulfo-SMCC-activated *H6*-EntA was able to form a complex with *H6*-EntE with a molecular weight over 250 kDa (Chapter 3, Figure 3). In the crosslinking experiment, *H6*-EntA concentration was 22 μM, suggesting that EntA tetramers are the predominant forms based on the AUC analysis of EntA self-association. Thus the SDS-PAGE band containing crosslinked EntA and EntE probably reflects a complex of EntA tetramer with four EntE subunits (predicted mass ~360 kDa). Our pull down assays provide us with further direct evidence for EntA-EntE complex formation *in situ* in *E. coli* lysates. *H6*-EntA bait was able to pull down chromosomally expressed *E. coli* EntE in a manner independent on 2,3-DHB (Chapter 3, Figure 2A {band a}). *H6*-EntE bait was able to pull down chromosomally expressed *E. coli* EntA independent on the presence of exogenous 2,3-DHB (Chapter 3, Figure 2B {band e}). Moreover, *H6*-EntE bait was also able to pull down *E. coli* EntB only in the presence of 2,3-DHB (Chapter 3, Figure 2B {band d}). This supports our observation in the second chapter that EntE and EntB interacts more efficiently in the presence of 2,3-DHB. There are two

possible explanations for pulling down both *E. coli* EntB and *E. coli* EntA by *H6*-EntE bait in the presence of 2,3-DHB. The major explanation is that EntE forms discrete complexes with EntB and EntA. This possibility is supported by the ability of *H6*-EntA bait to pull down only *E. coli* EntE, and *H6*-EntB bait to pull down only *E. coli* EntE. An alternate explanation is that formation of an EntA-EntE-EntB ternary complex can occur but we do not have further evidence for this.

Characterization of the EntA-EntE Interaction

In the second chapter of my thesis, we demonstrated that *H6*-EntE binding to 2,3-DHB resulted in a FRET signal at 440 nm. The FRET signal was used to measure the EntE-EntB interaction, giving an EC_{50} value of ~ 1.5 μM (*206*). In the third chapter, we were able to use this fluorescence binding assay to measure the EntA-EntE interaction at 20 °C. Here *H6*-EntA was able to decrease *H6*-EntE-2,3-DHB FRET signal in a manner dependent on *H6*-EntA concentration. Our anisotropy assay demonstrated that 2,3-DHB remains bound to *H6*-EntE upon *H6*-EntA interaction (Chapter 3, Figure 6). Thus the decrease in the *H6*-EntE-2,3-DHB FRET signal is likely due to a conformational change in EntE active site which alters the position and orientation of EntE FRET fluorophore donors and the acceptor 2,3-DHB. The equilibrium binding data at 20 °C revealed a sigmoidal binding behavior with a Hill coefficient greater than one and a concave-down scatchard plot. Furthermore, the equilibrium binding curve of EntA-EntE interaction has biphasic behavior. At low *H6*-EntA concentrations, the equilibrium binding response exhibited a shallow reduction in the *H6*-EntE-2,3-DHB FRET signal. As we increased *H6*-EntA concentration, a steep reduction in the *H6*-EntE-bound 2,3-DHB FRET signal was observed, suggesting higher affinity of EntE toward EntA upon increasing EntA

concentration. Our AUC analysis showed that increasing EntA concentration accompanied by a transition from EntA dimer to EntA tetramer. Thus the higher reduction in the *H6*-EntE-bound 2,3-DHB FRET upon increasing *H6*-EntA concentration might reflect a higher affinity of EntE toward EntA in the tetrameric form. This suggests that the sigmoidicity and the high Hill coefficient are likely due to positive cooperativity in the interaction. The enhancement of protein-protein interaction by oligomerization has been shown in many systems. For example, it was demonstrated by Terawaki *et al* that the mammalian PD-L1 protein interaction with its receptor PD-1 was stimulated upon tetramerization as seen by approximately 100 fold increase in the association constant relative to that determined for interaction involved monomeric PD-L1 (*254*). The interaction between PD-L1 and its receptor PD1 play an essential role in the immune reactions (*255*). Another example is seen with p53-DNA binding as revealed by Weinberg and coworkers (*250*). They showed that p53 interaction with its DNA sequence is highly cooperative with a Hill coefficient greater than one, and enhanced by tetramerization. In that study, mutation affecting p53 oligomerization lowers the interaction affinity between the mutated p53 and DNA by approximately six-fold. Our results do not rule out that EntE interaction with EntA in the dimeric form since our results showed stimulation in *H6*-EntE activity upon adding *H6*-EntA at 0.25 μM, where EntA would be predominantly as dimer according our analysis of EntA self-association. Taken together, our experiments revealed that EntE likely has higher affinity to EntA in the tetrameric form at 20°C. This suggests that EntA oligomeric state might play an important role in the regulation of enterobactin biosynthesis, such that the biosynthesis is enhanced upon EntA tetramerization.

Characterization of the EntA-EntE Interaction Interface

Characterization of protein-protein interaction interfaces is the focus of much research. Many studies have focused on identification of the interaction interfaces between enzymes involved in enterobactin biosynthesis (*142, 181, 195, 197*). Residues of acyl carrier protein domain (ACP) of polyketide synthase that comprise the interaction interface for phosphopantetheinyl transferse were studied by Weissman *et al (256)*. It was also shown that that the bacterial chemotaxis mechanism is highly dependent on protein-protein interactions (*257*). Moreover, Carter and coworkers identified the *E. coli* TonB (cytoplasmic membrane protein) and FhuD (periplasmic protein) interaction interface (*258*). In that study, they showed the ternary complex formation of FhuA-TonB-FhuD, FhuD is a periplasmic protein that transports ferrichrome from the FhuA receptor to an ABC transporter for import of the ferric siderophore to the cytoplasm.

Much research focuses on development of small molecules inhibitors in attempt to disrupt the protein interaction interfaces, providing useful targets for the development of antimicrobial and chemotherapeutic drugs (*219, 259*). For example, small peptide inhibitors have been used to disrupt the interaction between the pilus adhesin (FimH) and periplasmic chaperone (FimC) in Uropathogenic *E. coli (260).* A small molecule inhibitor of the interaction between cytokine interleulin-2 (IL-2) and its receptor IL-2R was studied by Arkin *et al* (*261*). Furthermore, small molecules inhibitors have been used to inhibit the antiapoptotic protein (BCL2) interaction with the proapoptotic protein BAK as reviewed by Arkin and Wells (*262*).

Phage display was used to identify the interaction interface between EntA and EntE in the fourth chapter of this study. Here, a phage display library was used to pan

random peptide sequences against immobilized *H6*-EntE. This technique provides us with 47 unique peptide sequences that aligned with EntA primary sequence using RELIC MATCH program (Chapter 4, Table 1 and Figure 1A). EntA residues Gln64 and Ala68 identified to be in the interaction interface for EntE were selected for mutagenesis in attempt to disrupt the interaction. Our crosslinking experiments showed that maleimide-activated *H6*-EntA (Q64A) formed a very faint conjugate band with *H6*-EntE, suggesting a weak interaction between *H6*-EntE and *H6*-EntA (Q64A) (Chapter 4, Figure 4). In contrast, maleimide-activated *H6*-EntA (A68Q) formed a complex band with *H6*-EntE with a density almost the same like that seen when wild-type EntA was used (Chapter 4, Figure 4). Near-UV spectra changes reflecting EntA-EntE interaction were only observed upon mixing *H6*-EntE with wild-type *H6*-EntA or *H6*-EntA (A68Q) (Chapter 4, Figure 5 and 6). This suggests that A68Q mutation did not affect the ability of EntA to interact with EntE but Q64A and Q64A/A68Q mutations are likely disrupting the interaction. Moreover, our fluorescence binding assay showed that *H6*-EntA Q64A mutation had a negative effect on its interaction with *H6*-EntE. This assay also revealed that *H6*-EntA Q64A/A68Q mutation had a more pronounced effect than Q64A mutation on the interaction (Chapter 4, Figure 7), indicating that multiple mutations in the interaction interface can completely disrupt the interaction. Our *in vivo* growth assays support our *in vitro* studies, showing that *entA*$^{-}$ BW25113 cells transformed with gene encoding for *H6*-EntA (Q64A) and *H6*-EntA (Q64A/A68Q) were unable to grow under iron-limited condition (Chapter 4, Figure 8A). Taken together, our *in vitro* and *in vivo* studies in Chapter Four revealed that *H6*-EntA Q64A and Q64A/A68Q mutations have a pronounced effect on disrupting the EntA-EntE interaction. This suggests that the helix

containing EntA residues 64 and 68 would make a good target for the development of a small molecule inhibitor of the EntA-EntE interaction.

EntA Mutations Interrupt EntA Tetramer Construction

Wild-type *H6*-EntA behaves in solution as a mixture of dimer and tetramer with transition toward the tetramer forms upon increasing EntA concentration (Chapter 3, Figure 1B and Table 1, row 4-7). In the fourth chapter, we found *H6*-EntA (A68Q) has $S_{20,W}$ value which almost equal to that of wild-type *H6*-EntA at 20 µM (Chapter 4, Figure 3B and Table 3, row 6) , indicating that both *H6*-EntA (A68Q) and wild-type *H6*-EntA present predominantly as tetramer. In contrast, the *H6*-EntA (Q64A) $S_{20,W}$ value determined at 20 µM suggests that EntA of this variant has more dimers (Chapter 4, Figure 3B and Table 3, row 7). The *H6*-EntA (Q64A/A68Q) $S_{20,W}$ value determined at 20 µM indicates that EntA of this variant is predominantly dimer (Chapter 4, Figure 3B, Table 3, row 8). Thus the negative effect of Q64A and Q64A/A68Q mutations on EntA-EntE interaction likely resulted from their position in the interaction interface and/or the dimer formation upon mutation.

EntA was crystalized as a tetramer by Sundlov *et al* (*183*). This tetramer is composed of two physiological dimers as explained previously. The mechanism by which Q64A and Q64A/A68Q mutations interrupt the tetramerization of EntA is not obvious. However there are two possible interpretations for dimer formation in these variants. In the first interpretation, the non-physiological dimer is formed as a result of the physiological dimer interface disruption (Chapter 4, Figure 1B {one cyan colored subunit plus the corresponding pink colored subunit}). This effect likely resulted from the role of Gln64 and Ala68 that they might play in interaction between helices α4 and α5. In the

second interpretation, the physiological dimer is formed as a result of the tetramer interface disruption (Chapter 4, Figure 1B {cyan or pink colored dimers}). The observed change in the protein helicity of *H6*-EntA (Q64A) and *H6*-EntA (Q64A/A68Q) variants likely resulted from changes in the conformation of these variants upon mutation. The positions of Gln64 and Ala68 in these variants might be close to the tetramerization interface as a result of the conformation alteration, causing interruption of the tetramer interface.

Thesis Studies in Context of What Have Been Currently Published

Mechanistic studies on EntE by Sikora and coworkers revealed that EntE reaction divided into two half-reactions *(189).* The first half-reaction of EntE is 2,3-DHB adenylation (2,3-DHB-AMP formation) while the second half-reaction is acylation of *holo*-EntB by the activated 2,3-DHB with release of AMP. Sikora *et al* also reported that EntE catalyzes the formation of P^1,P^3-diadenosine-5'-tetraphosphate (Ap4A) in the absence of *holo*-EntB *(188).* 2,3-DHB-AMP, the product of the first half-reaction of EntE, is attacked by another molecule of ATP in the absence of *holo*-EntB, resulting in formation of Ap4A. In contrast in the presence of *holo*-EntB, 2,3-DHB-AMP is attacked by the phosphopantetheine group of *holo*-EntB, resulted in the formation of acylated *holo*-EntB.

Our findings, along with what is currently known about EntE (Chapter 5, Scheme 1), suggest that EntE activity in the two half-reactions is only optimized by interactions with its protein partners. This likely occurs by conformational change of the EntE active site upon its interaction with both upstream and downstream protein partners. This is predicted by the observed quenching of the EntE bound 2,3-DHB FRET signal upon the

interaction with EntA and EntB (Chapter 2 and 3). Here we propose that the first half-reaction of EntE is enhanced by its interaction with the upstream partner EntA (Chapter 3). This likely resulted from stimulation of 2,3-DHB-AMP formation, probably by channeling of 2,3-DHB from EntA to EntE (Scheme 1A (I)). This interaction is likely dependent on EntA conformation, such that EntE interacts with higher affinity to EntA in the tetrameric form (Chapter 3 and 4).

The second half-reaction of EntE is enhanced by its interaction with the downstream partner EntB as reported by Ehmann *et al* (*144*). Consistent with our studies in the second chapter, some of the released 2,3-DHB likely binds to an allosteric site on *holo*-EntB and primes it to interact with EntE (Scheme 1B). Our finding in Chapter Two that EntB needs to be optimized by conformational changes prior to its interaction with EntE is consistent with what reported by Drake *et al* as (*181*). The EntE-EntB interaction occurs in the second half-reaction of EntE, probably to facilitate 2,3-DHB channeling to *holo*-EntB, consisting with what has been published *(188-189)*. After *holo*-EntB is acylated by EntE (attach the 2,3-DHB moiety to PPant-Ser245 of *holo*-EntB), acylated *holo*-EntB will be released to interact with the downstream enzyme (EntF) in the pathway. Lai *et al* reported that mutations in EntB interaction interface for EntF did not disrupt its interaction with EntE, suggesting that EntB has separate interaction interfaces for each interaction (*142*). After EntB dissociates from EntE, EntE will be ready for another interaction with EntA and another cycle of the catalysis. Our studies in Chapter Four showed that EntA (Q64A) and EntA (Q64A/A68Q) variants demonstrated very weak interaction with EntE. The effect of these mutations might have resulted from their presence in the interaction interface and/or the conversion of EntA to the dimeric form

upon the mutation, lowering the interaction affinity of EntE to these variants (Scheme1A (II)).

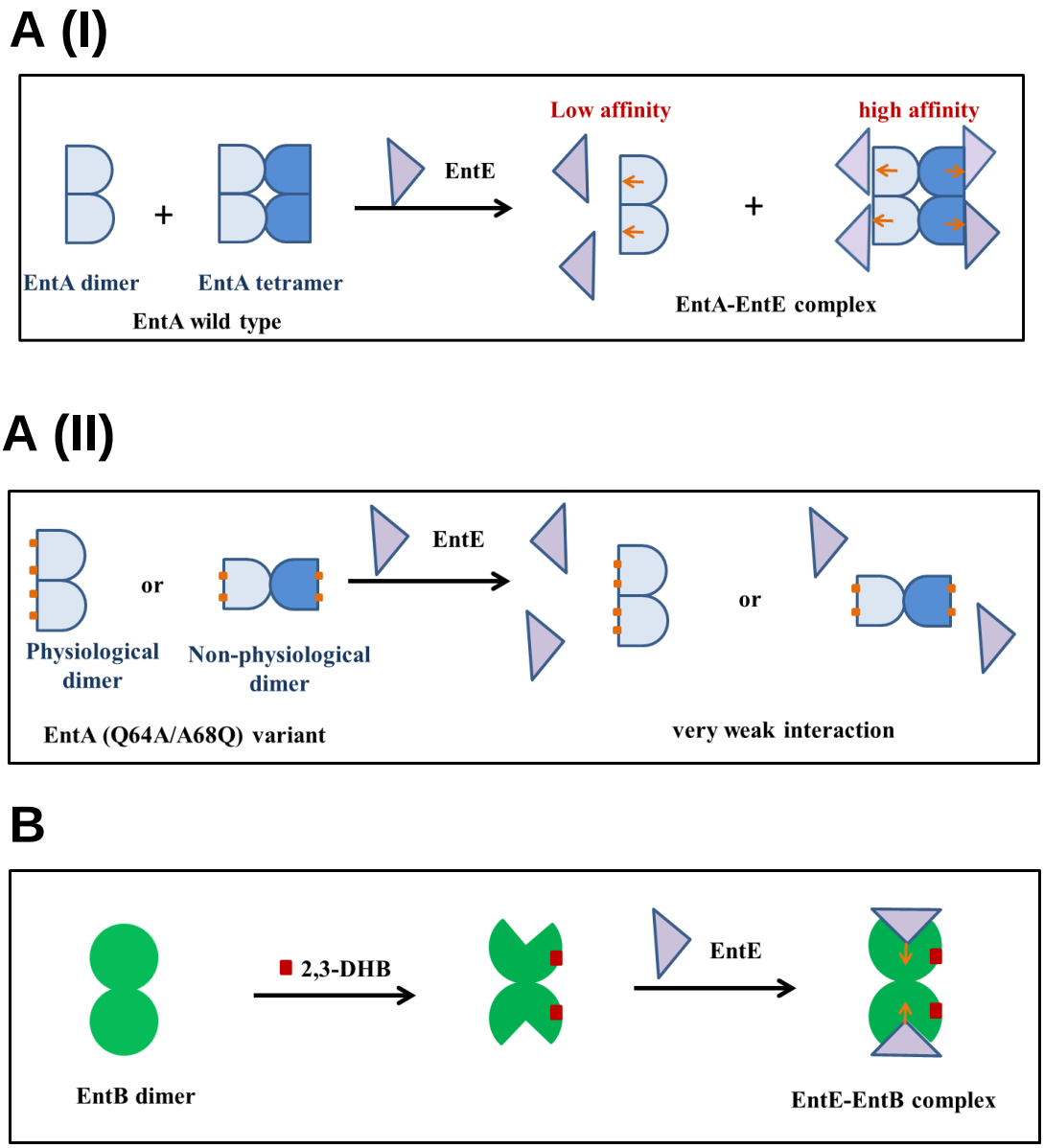

Scheme 1: Proposed mechanism of EntE interaction with EntA and EntB in context of our studies, along with what have been reported about EntA, EntE, and EntB.

A(I): *Representation of the EntA-EntE interaction in the first half-reaction of EntE. EntA crystal structure revealed that EntA tetramer composed of two physiological homo-dimers (light blue and dark blue dimers). The third chapter studies revealed that EntA in equilibrium between the dimeric and tetrameric form in solution. This chapter results*

also suggested that EntE interacts with higher affinity to EntA in the tetrameric form. This interaction is probably to mediate 2,3-DHB channeling from EntA active site to EntE active site as represented by orange arrows. ***A(II):*** *Disruption of EntA-EntE interaction. The fourth chapter studies showed that EntA mutations (e.g. Q64A/A68Q) likely disrupt the interaction through promotion of dimer (physiological or non-physiological) formation of EntA and/or disruption of the interaction interface. The mutagenized EntA residues (Gln64 and Ala68) were represented as orange squares. The dimer formation in these variants correlated with change in EntA conformation as predicted by our CD data. The change in EntA conformation upon the mutation might contribute to the weak interaction with EntE. EntA conformational change upon mutation was not represented in the diagram.* ***B:*** *Representation of the EntE-EntB interaction in the second half-reaction of EntE. 2,3-DHB (red squares) binds to EntB and prepares it to efficiently interact with EntE, probably by EntB conformational change as predicted by our studies in the second chapter. EntE-EntB interaction likely facilitates 2,3-DHB-AMP channeling from EntE active site to EntB active site as shown by the orange arrows.*

Our studies in this report advance our knowledge about protein-protein interaction network involved in enterobactin biosynthesis. Furthermore our studies provide a rapid fluorescence assay for further exploration of EntE active site (Chapter 2). This assay has already proved useful in monitoring EntE interaction with EntB and EntA (Chapter 2 and 3). Moreover, studies in the fourth chapter demonstrated the essential role of Gln64 and Ala68 residues of EntA in the interaction with EntE as well as in EntA tetramer formation. Here, Q64A and Q64A/A68Q mutations of EntA were able to restrict the bacterial growth in iron free media. The studies in this chapter also suggest that inhibition of EntA tetramer formation might play an essential role in disruption of EntA-EntE interaction. Hence this chapter identifies novel targets for development of antibacterial drug against bacteria that produce enterobactin-related siderophores.

Recently, Devireddy *et al* showed that the mammalian cell has a mammalian siderophore involved in the iron homeostasis (*1*). They found that the biosynthesis of this siderophore requires EntA and EntE homologues. Thus our findings provide insights not only into the related bacterial proteins involved in other sidrophores biosynthesis but also into the homologue proteins involved in the mammalian siderophore biosynthesis.

APPENDIX

Table 1: LC-MS/MS analysis of peptides recovered from pull-down experiments.

Band on gel[a]	DHB	Protein[b]	Residue range	Δ average (Da)	Frequency
a	-	EntE	8–14	0.2090	3
a	-	EntE	20-33	0.1872	20
a	-	EntE	34-47	0.3550	5
a	-	EntE	53-66	0.2664	13
a	-	EntE	96-109	0.3416	6
a	-	EntE	110-128	0.1487	13
a	-	EntE	129-150	0.2552	1
a	-	EntE	203-212	0.1931	2
a	-	EntE	213-225	0.4219	1
a	-	EntE	214-225	0.2835	9
a	-	EntE	271-296	0.3510	5
a	-	EntE	312-319	0.2254	2
a	-	EntE	312-343	0.3875	1
a	-	EntE	320-343	0.3651	46
a	-	EntE	351-382	0.4411	4
a	-	EntE	397-430	0.5838	7
a	-	EntE	442-453	0.2914	32
a	-	EntE	454-473	0.3019	6
a	-	EntE	474-481	0.2441	3
a	-	EntE	503-520	0.4168	5
a	-	EntE	507-520	0.2647	7
a	+	EntE	8-14	0.2490	3
a	+	EntE	20-33	0.2072	23
a	+	EntE	34-47	0.3150	6
a	+	EntE	53-66	0.3064	27
a	+	EntE	96-109	0.3616	10
a	+	EntE	110-128	0.2887	25
a	+	EntE	129-150	0.2852	1
a	+	EntE	203-212	0.1931	3
a	+	EntE	203-213	0.2115	1
a	+	EntE	213-225	0.4046	2
a	+	EntE	214-225	0.2835	12
a	+	EntE	271-296	0.4110	1
a	+	EntE	320-343	0.3251	37
a	+	EntE	351-382	0.5311	4
a	+	EntE	442-453	0.2714	38
a	+	EntE	442-473	0.7680	1
a	+	EntE	454-473	0.2719	6
a	+	EntE	474-481	0.2441	3
a	+	EntE	503-520	0.4168	6
a	+	EntE	507-520	0.2447	13
d	+	EntB	6-21	0.4159 0.2804	3

d	+	EntB	22-30	0.6489	3
d	+	EntB	31-64	0.5085	1
d	+	EntB	69-81	0.1835	2
d	+	EntB	89-101	0.1911	8
d	+	EntB	112-123	0.3488	19
d	+	EntB	112-125	0.1946	1
d	+	EntB	132-139	0.2939	1
d	+	EntB	144-167	0.3269	4
d	+	EntB	168-183	0.2819	6
d	+	EntB	200-215	0.4203	9
d	+	EntB	216-247	1.1891	1
d	+	EntB	220-247	0.3917	16
d	+	EntB	220-254	0.2475	3
d	+	EntB	257-269	0.2502	3
d	+	EntB	270-278	0.3086	2
e	-	EntA	26-41	0.7873	25
e	-	EntA	42-75	0.3000	31
e	-	EntA	76-94	0.2135	1
e	-	EntA	83-94	0.3665	24
e	-	EntA	104-129	0.2845	1
e	-	EntA	133-148	0.3146	7
e	-	EntA	149-162	0.2366	1
e	-	EntA	163-178	0.1632	33
e	-	EntA	179-193	0.2125	4
e	-	EntA	194-205	0.1686	14
e	+	EntA	26-41	0.5327	32
e	+	EntA	42-75	0.3043	27
e	+	EntA	76-82	0.3	1
e	+	EntA	76-94	0.2535	1
e	+	EntA	83-94	0.2765	44
e	+	EntA	104-129	0.3645	25
e	+	EntA	133-148	0.3446	11
e	+	EntA	149-162	0.2366	1
e	+	EntA	163-178	0.2032	43
e	+	EntA	179-193	0.2725	2
e	+	EntA	194-205		8

[a] *Band from SDS-polyacrylamide gel shown in Figure 2 of Chapter Three. Letter corresponds to letter label beside band in figure.*

[b] *Only LC-MS/MS data of peptides recovered from SDS-PAGE bands corresponding to pulled down prey proteins are shown in this table.*

Table 2: LC-MS/MS analysis of peptides recovered from SMCC crosslinking experiment.

Protein[a]	Residue range	Δ average (Da)	Frequency
EntE	8-14	0.2290	2
EntE	20-33	0.1272	18
EntE	34-47	0.3950	3
EntE	53-66	0.2664	5
EntE	68-96	0.6431	1
EntE	96-109	0.3189	3
EntE	110-128	0.2487	3
EntE	203-212	0.1731	2
EntE	203-213	0.2685	1
EntE	213-225	0.4519	1
EntE	214-225	0.2235	3
EntE	271-296	0.2610	5
EntE	312-343	0.4175	2
EntE	320-343	0.2200	20
EntE	351-382	0.0001	3
EntE	442-453	0.2714	31
EntE	454-473	0.2817	4
EntE	474-481	0.2841	2
EntE	503-520	0.3868	3
EntE	507-520	0.2447	2
EntA	83-94	0.1935	1
EntA	104-129	0.3065	1
EntA	133-148	0.4445	2
EntA	194-205	0.1725	1

[a] *Identified protein from band in SDS-polyacrylamide gel migrating with size > 250 kDa in +SMCC lane (Chapter 3, Figure 3). Non-crosslinked EntA and EntE peptides (i.e., from other bands in same gel) are not shown in this table.*

REFERENCES

1. Devireddy, L. R., Hart, D. O., Goetz, D. H., and Green, M. R. (2010) A mammalian siderophore synthesized by an enzyme with a bacterial homolog involved in enterobactin production, *Cell 141*, 1006-1017.
2. Crichton, R. R., and Boelaert, J. R. (2001) *Inorganic biochemistry of iron metabolism : from molecular mechanisms to clinical consequences*, 2nd ed., Wiley, Chichester ; New York.
3. Baes, C. F., and Mesmer, R. E. (1976) *The hydrolysis of cations*, Wiley, New York.
4. Ratledge, C., and Dover, L. G. (2000) Iron metabolism in pathogenic bacteria, *Annu Rev Microbiol 54*, 881-941.
5. Bagg, A., and Neilands, J. B. (1987) Molecular mechanism of regulation of siderophore-mediated iron assimilation, *Microbiol Rev 51*, 509-518.
6. Chipperfield, J. R., and Ratledge, C. (2000) Salicylic acid is not a bacterial siderophore: a theoretical study, *Biometals 13*, 165-168.
7. Neilands, J. B., Van der Helm, D., and Winkelmann, G. (1987) *Iron transport in microbes, plants, and animals*, VCH, Weinheim, Federal Republic of Germany ; New York, NY.
8. Boukhalfa, H., and Crumbliss, A. L. (2002) Chemical aspects of siderophore mediated iron transport, *Biometals 15*, 325-339.
9. Dhungana, S., and Crumbliss, A. L. (2005) Coordination chemistry and redox processes in siderophore-mediated iron transport, *Geomicrobiology Journal 22*, 87-98.
10. Kruszewski, M. (2003) Labile iron pool: the main determinant of cellular response to oxidative stress, *Mutat Res 531*, 81-92.
11. Touati, D. (2000) Iron and oxidative stress in bacteria, *Arch Biochem Biophys 373*, 1-6.
12. Pierre, J. L., and Fontecave, M. (1999) Iron and activated oxygen species in biology: the basic chemistry, *Biometals 12*, 195-199.
13. Pierre, J. L., Fontecave, M., and Crichton, R. R. (2002) Chemistry for an essential biological process: the reduction of ferric iron, *Biometals 15*, 341-346.
14. Honda, K., Smith, M. A., Zhu, X., Baus, D., Merrick, W. C., Tartakoff, A. M., Hattier, T., Harris, P. L., Siedlak, S. L., Fujioka, H., Liu, Q., Moreira, P. I., Miller, F. P., Nunomura, A., Shimohama, S., and Perry, G. (2005) Ribosomal RNA in Alzheimer disease is oxidized by bound redox-active iron, *J Biol Chem 280*, 20978-20986.
15. Castellani, R. J., Moreira, P. I., Liu, G., Dobson, J., Perry, G., Smith, M. A., and Zhu, X. (2007) Iron: the Redox-active center of oxidative stress in Alzheimer disease, *Neurochem Res 32*, 1640-1645.
16. Mainous, A. G., 3rd, Gill, J. M., and Everett, C. J. (2005) Transferrin saturation, dietary iron intake, and risk of cancer, *Ann Fam Med 3*, 131-137.
17. Ward, P. P., Paz, E., and Conneely, O. M. (2005) Multifunctional roles of lactoferrin: a critical overview, *Cell Mol Life Sci 62*, 2540-2548.

18. Baker, H. M., Anderson, B. F., and Baker, E. N. (2003) Dealing with iron: common structural principles in proteins that transport iron and heme, *Proc Natl Acad Sci U S A 100*, 3579-3583.
19. Sigel, A., and Sigel, H. (1998) Metal ions in biological systems, volume 35: iron transport and storage microorganisms, plants, and animals, *Met Based Drugs 5*, 262.
20. Harrison, P. M. (1979) Iron storage in bacteria, *Nature 279*, 15-16.
21. Andrews, S. C. (1998) Iron storage in bacteria, *Adv Microb Physiol 40*, 281-351.
22. Carrondo, M. A. (2003) Ferritins, iron uptake and storage from the bacterioferritin viewpoint, *EMBO J 22*, 1959-1968.
23. Lawson, D. M., Treffry, A., Artymiuk, P. J., Harrison, P. M., Yewdall, S. J., Luzzago, A., Cesareni, G., Levi, S., and Arosio, P. (1989) Identification of the ferroxidase centre in ferritin, *FEBS Lett 254*, 207-210.
24. Miethke, M., and Marahiel, M. A. (2007) Siderophore-based iron acquisition and pathogen control, *Microbiol Mol Biol Rev 71*, 413-451.
25. Wandersman, C., and Delepelaire, P. (2004) Bacterial iron sources: from siderophores to hemophores, *Annu Rev Microbiol 58*, 611-647.
26. Tong, Y., and Guo, M. (2009) Bacterial heme-transport proteins and their heme-coordination modes, *Arch Biochem Biophys 481*, 1-15.
27. Cope, L. D., Thomas, S. E., Hrkal, Z., and Hansen, E. J. (1998) Binding of heme-hemopexin complexes by soluble HxuA protein allows utilization of this complexed heme by *Haemophilus influenzae*, *Infect Immun 66*, 4511-4516.
28. Cope, L. D., Yogev, R., Muller-Eberhard, U., and Hansen, E. J. (1995) A gene cluster involved in the utilization of both free heme and heme:hemopexin by *Haemophilus influenzae* type b, *J Bacteriol 177*, 2644-2653.
29. Moon, R. B., and Richards, J. H. (1972) Conformation studies of various hemoglobins by natural-abundance 13 C NMR spectroscopy, *Proc Natl Acad Sci U S A 69*, 2193-2197.
30. Wejman, J. C., Hovsepian, D., Wall, J. S., Hainfeld, J. F., and Greer, J. (1984) Structure of haptoglobin and the haptoglobin-hemoglobin complex by electron microscopy, *J Mol Biol 174*, 319-341.
31. Lewis, L. A., Sung, M. H., Gipson, M., Hartman, K., and Dyer, D. W. (1998) Transport of intact porphyrin by HpuAB, the hemoglobin-haptoglobin utilization system of *Neisseria meningitidis*, *J Bacteriol 180*, 6043-6047.
32. Morton, D. J., Whitby, P. W., Jin, H., Ren, Z., and Stull, T. L. (1999) Effect of multiple mutations in the hemoglobin- and hemoglobin-haptoglobin-binding proteins, HgpA, HgpB, and HgpC, of *Haemophilus influenzae* type b, *Infect Immun 67*, 2729-2739.
33. Lewis, L. A., and Dyer, D. W. (1995) Identification of an iron-regulated outer membrane protein of *Neisseria meningitidis* involved in the utilization of hemoglobin complexed to haptoglobin, *J Bacteriol 177*, 1299-1306.
34. Rohde, K. H., and Dyer, D. W. (2004) Analysis of haptoglobin and hemoglobin-haptoglobin interactions with the *Neisseria meningitidis* TonB-dependent receptor HpuAB by flow cytometry, *Infect Immun 72*, 2494-2506.
35. Raymond, K. N., Dertz, E. A., and Kim, S. S. (2003) Enterobactin: an archetype for microbial iron transport, *Proc Natl Acad Sci U S A 100*, 3584-3588.

36. Imbert, M., and Blondeau, R. (1998) On the iron requirement of *lactobacilli* grown in chemically defined medium, *Curr Microbiol 37*, 64-66.
37. Jens Harder (1993) Ribonucleotide reductases and their occurrence in microorganisms: A link to the RNA/DNA transition, *FEMS Microbiol Rev* 12 (4), 273-292.
38. Riera, J., Robb, F. T., Weiss, R., and Fontecave, M. (1997) Ribonucleotide reductase in the *archaeon Pyrococcus* furiosus: a critical enzyme in the evolution of DNA genomes?, *Proc Natl Acad Sci U S A 94*, 475-478.
39. Booker, S., and Stubbe, J. (1993) Cloning, sequencing, and expression of the adenosylcobalamin-dependent ribonucleotide reductase from *Lactobacillus leichmannii*, *Proc Natl Acad Sci U S A 90*, 8352-8356.
40. Torrents, E., Grinberg, I., Gorovitz-Harris, B., Lundstrom, H., Borovok, I., Aharonowitz, Y., Sjoberg, B. M., and Cohen, G. (2007) NrdR controls differential expression of the *Escherichia coli* ribonucleotide reductase genes, *J Bacteriol 189*, 5012-5021.
41. Bullen, J. J., and Griffiths, E. (1999) *Iron and infection : molecular, physiological and clinical aspects*, 2nd ed., John Wiley, Chichester ; New York.
42. Kammler, M., Schon, C., and Hantke, K. (1993) Characterization of the ferrous iron uptake system of *Escherichia coli*, *J Bacteriol 175*, 6212-6219.
43. Tsolis, R. M., Baumler, A. J., Heffron, F., and Stojiljkovic, I. (1996) Contribution of TonB- and Feo-mediated iron uptake to growth of *Salmonella typhimurium* in the mouse, *Infect Immun 64*, 4549-4556.
44. Crosa, J. H., Mey, A. R., and Payne, S. M. (2004) *Iron transport in bacteria*, ASM Press, Washington, D.C.
45. Noto, J. M., and Cornelissen, C. N. (2008) Identification of TbpA residues required for transferrin-iron utilization by *Neisseria gonorrhoeae*, *Infect Immun 76*, 1960-1969.
46. Shouldice, S. R., Skene, R. J., Dougan, D. R., Snell, G., McRee, D. E., Schryvers, A. B., and Tari, L. W. (2004) Structural basis for iron binding and release by a novel class of periplasmic iron-binding proteins found in gram-negative pathogens, *J Bacteriol 186*, 3903-3910.
47. NM, O. B.-S., Veith, P. D., Dashper, S. G., and Reynolds, E. C. (2003) *Porphyromonas gingivalis* gingipains: the molecular teeth of a microbial vampire, *Curr Protein Pept Sci 4*, 409-426.
48. Lee, B. C. (1995) Quelling the red menace: haem capture by bacteria, *Mol Microbiol 18*, 383-390.
49. Schmitt, M. P. (1997) Utilization of host iron sources by *Corynebacterium diphtheriae*: identification of a gene whose product is homologous to eukaryotic heme oxygenases and is required for acquisition of iron from heme and hemoglobin, *J Bacteriol 179*, 838-845.
50. Ochsner, U. A., Johnson, Z., and Vasil, M. L. (2000) Genetics and regulation of two distinct haem-uptake systems, phu and has, in *Pseudomonas aeruginosa*, *Microbiology 146 (Pt 1)*, 185-198.
51. Stoebner, J. A., and Payne, S. M. (1988) Iron-regulated hemolysin production and utilization of heme and hemoglobin by *Vibrio cholerae*, *Infect Immun 56*, 2891-2895.

52. Torres, A. G., and Payne, S. M. (1997) Haem iron-transport system in enterohaemorrhagic *Escherichia coli* O157:H7, *Mol Microbiol 23*, 825-833.
53. Zhu, W., Wilks, A., and Stojiljkovic, I. (2000) Degradation of heme in gram-negative bacteria: the product of the hemO gene of *Neisseriae* is a heme oxygenase, *J Bacteriol 182*, 6783-6790.
54. Izadi, N., Henry, Y., Haladjian, J., Goldberg, M. E., Wandersman, C., Delepierre, M., and Lecroisey, A. (1997) Purification and characterization of an extracellular heme-binding protein, HasA, involved in heme iron acquisition, *Biochemistry 36*, 7050-7057.
55. Letoffe, S., Wecker, K., Delepierre, M., Delepelaire, P., and Wandersman, C. (2005) Activities of the *Serratia marcescens* heme receptor HasR and isolated plug and beta-barrel domains: the beta-barrel forms a heme-specific channel, *J Bacteriol 187*, 4637-4645.
56. Drechsel, H., and Jung, G. (1998) Peptide siderophores, *J Pept Sci 4*, 147-181.
57. Carrano, C. J., and Winkelmann, G. (1997) *Transition metals in microbial metabolism*, Harwood Academic Publishers, Amsterdam.
58. Neilands, J. B. (1995) Siderophores: structure and function of microbial iron transport compounds, *J Biol Chem 270*, 26723-26726.
59. Alvin L. Crumbliss and James M. Harrington (2009) Iron sequestration by small molecules: Thermodynamic and kinetic studies of natural siderophores and synthetic model compounds, *Adv. Inorg. Chem.* 61, 179-250.
60. Fischbach, M. A., Lin, H., Liu, D. R., and Walsh, C. T. (2006) How pathogenic bacteria evade mammalian sabotage in the battle for iron, *Nat Chem Biol 2*, 132-138.
61. Hantke, K. (2001) Iron and metal regulation in bacteria, *Curr Opin Microbiol 4*, 172-177.
62. Masse, E., Salvail, H., Desnoyers, G., and Arguin, M. (2007) Small RNAs controlling iron metabolism, *Curr Opin Microbiol 10*, 140-145.
63. Fourel, G., Phalipon, A., and Kaczorek, M. (1989) Evidence for direct regulation of diphtheria toxin gene transcription by an Fe2+-dependent DNA-binding repressor, DtoxR, in *Corynebacterium diphtheriae*, *Infect Immun 57*, 3221-3225.
64. Hill, P. J., Cockayne, A., Landers, P., Morrissey, J. A., Sims, C. M., and Williams, P. (1998) SirR, a novel iron-dependent repressor in *Staphylococcus epidermidis*, *Infect Immun 66*, 4123-4129.
65. Oguiza, J. A., Tao, X., Marcos, A. T., Martin, J. F., and Murphy, J. R. (1995) Molecular cloning, DNA sequence analysis, and characterization of the *Corynebacterium diphtheriae* dtxR homolog from *Brevibacterium lactofermentum*, *J Bacteriol 177*, 465-467.
66. Pohl, E., Haller, J. C., Mijovilovich, A., Meyer-Klaucke, W., Garman, E., and Vasil, M. L. (2003) Architecture of a protein central to iron homeostasis: crystal structure and spectroscopic analysis of the ferric uptake regulator, *Mol Microbiol 47*, 903-915.
67. Schiering, N., Tao, X., Zeng, H., Murphy, J. R., Petsko, G. A., and Ringe, D. (1995) Structures of the apo- and the metal ion-activated forms of the diphtheria tox repressor from *Corynebacterium diphtheriae*, *Proc Natl Acad Sci U S A 92*, 9843-9850.

68. Pecqueur, L., D'Autreaux, B., Dupuy, J., Nicolet, Y., Jacquamet, L., Brutscher, B., Michaud-Soret, I., and Bersch, B. (2006) Structural changes of *Escherichia coli* ferric uptake regulator during metal-dependent dimerization and activation explored by NMR and X-ray crystallography, *J Biol Chem 281*, 21286-21295.
69. Helmann, J. D. (2002) The extracytoplasmic function (ECF) sigma factors, *Adv Microb Physiol 46*, 47-110.
70. Braun, V., Mahren, S., and Ogierman, M. (2003) Regulation of the FecI-type ECF sigma factor by transmembrane signalling, *Curr Opin Microbiol 6*, 173-180.
71. Rossi, M. S., Paquelin, A., Ghigo, J. M., and Wandersman, C. (2003) Haemophore-mediated signal transduction across the bacterial cell envelope in *Serratia marcescens*: the inducer and the transported substrate are different molecules, *Mol Microbiol 48*, 1467-1480.
72. Michel, L., Gonzalez, N., Jagdeep, S., Nguyen-Ngoc, T., and Reimmann, C. (2005) PchR-box recognition by the AraC-type regulator PchR of *Pseudomonas aeruginosa* requires the siderophore pyochelin as an effector, *Mol Microbiol 58*, 495-509.
73. Hider, R. C. (2002) Design of therapeutic chelating agents, *Biochem Soc Trans 30*, 751-754.
74. Tseng, C. F., Burger, A., Mislin, G. L., Schalk, I. J., Yu, S. S., Chan, S. I., and Abdallah, M. A. (2006) Bacterial siderophores: the solution stoichiometry and coordination of the Fe(III) complexes of pyochelin and related compounds, *J Biol Inorg Chem 11*, 419-432.
75. Harris, W. R., Carrano, C. J., Cooper, S. R., Sofen, S. R., Avdeef, A. E., McArdle, J. V., and Raymond, K. N. (1979) Coordination chemistry of microbial iron transport compounds. 19. Stability constants and electrochemical behavior of ferric enterobactin and model complexes, *J Am Chem Soc* 101, 6097-6104.
76. Loomis, L. D., and Raymond, K. N. (1991) Solution Equilibria of Enterobactin and Metal Enterobactin Complexes, *Inorganic Chemistry 30*, 906-911.
77. Valdebenito, M., Crumbliss, A. L., Winkelmann, G., and Hantke, K. (2006) Environmental factors influence the production of enterobactin, salmochelin, aerobactin, and yersiniabactin in *Escherichia coli* strain Nissle 1917, *Int J Med Microbiol 296*, 513-520.
78. Delorenzo, V., and Martinez, J. L. (1988) Aerobactin Production as a Virulence Factor - a Reevaluation, *European Journal of Clinical Microbiology & Infectious Diseases 7*, 621-629.
79. Johnson, J. R., Moseley, S. L., Roberts, P. L., and Stamm, W. E. (1988) Aerobactin and other virulence factor genes among strains of *Escherichia coli* causing urosepsis: association with patient characteristics, *Infect Immun 56*, 405-412.
80. Wilson, M. K., Abergel, R. J., Arceneaux, J. E., Raymond, K. N., and Byers, B. R. (2010) Temporal production of the two *Bacillus anthracis* siderophores, petrobactin and bacillibactin, *Biometals 23*, 129-134.
81. Renshaw, J. C., Robson, G. D., Trinci, A. P. J., Wiebe, M. G., Livens, F. R., Collison, D., and Taylor, R. J. (2002) Fungal siderophores: structures, functions and applications, *Mycol Res 106*, 1123-1142.

82. Crosa, J. H., and Walsh, C. T. (2002) Genetics and assembly line enzymology of siderophore biosynthesis in bacteria, *Microbiol Mol Biol R 66*, 223-249.
83. Barry, S. M., and Challis, G. L. (2009) Recent advances in siderophore biosynthesis, *Curr Opin Chem Biol 13*, 205-215.
84. Marahiel, M. A., Stachelhaus, T., and Mootz, H. D. (1997) Modular Peptide Synthetases Involved in Nonribosomal Peptide Synthesis, *Chem Rev 97*, 2651-2674.
85. Schwarzer, D., Finking, R., and Marahiel, M. A. (2003) Nonribosomal peptides: from genes to products, *Nat Prod Rep 20*, 275-287.
86. Marahiel, M. A., and Essen, L. O. (2009) Chapter 13. Nonribosomal peptide synthetases mechanistic and structural aspects of essential domains, *Methods Enzymol 458*, 337-351.
87. Walsh, C. T., Chen, H., Keating, T. A., Hubbard, B. K., Losey, H. C., Luo, L., Marshall, C. G., Miller, D. A., and Patel, H. M. (2001) Tailoring enzymes that modify nonribosomal peptides during and after chain elongation on NRPS assembly lines, *Curr Opin Chem Biol 5*, 525-534.
88. Miao, V., Coeffet-Legal, M. F., Brian, P., Brost, R., Penn, J., Whiting, A., Martin, S., Ford, R., Parr, I., Bouchard, M., Silva, C. J., Wrigley, S. K., and Baltz, R. H. (2005) Daptomycin biosynthesis in *Streptomyces roseosporus*: cloning and analysis of the gene cluster and revision of peptide stereochemistry, *Microbiology 151*, 1507-1523.
89. Schofield, C. J., Baldwin, J. E., Byford, M. F., Clifton, I., Hajdu, J., Hensgens, C., and Roach, P. (1997) Proteins of the penicillin biosynthesis pathway, *Curr Opin Struct Biol 7*, 857-864.
90. McDaniel, R., Thamchaipenet, A., Gustafsson, C., Fu, H., Betlach, M., and Ashley, G. (1999) Multiple genetic modifications of the erythromycin polyketide synthase to produce a library of novel "unnatural" natural products, *Proc Natl Acad Sci U S A 96*, 1846-1851.
91. Challis, G. L. (2005) A widely distributed bacterial pathway for siderophore biosynthesis independent of nonribosomal peptide synthetases, *Chem bio chem 6*, 601-611.
92. de Lorenzo, V., and Neilands, J. B. (1986) Characterization of iucA and iucC genes of the aerobactin system of plasmid ColV-K30 in *Escherichia coli*, *J Bacteriol 167*, 350-355.
93. Cendrowski, S., MacArthur, W., and Hanna, P. (2004) *Bacillus anthracis* requires siderophore biosynthesis for growth in macrophages and mouse virulence, *Mol Microbiol 51*, 407-417.
94. Koppisch, A. T., Browder, C. C., Moe, A. L., Shelley, J. T., Kinkel, B. A., Hersman, L. E., Iyer, S., and Ruggiero, C. E. (2005) Petrobactin is the primary siderophore synthesized by *Bacillus anthracis* str. Sterne under conditions of iron starvation, *Biometals 18*, 577-585.
95. Moore, C. H., Foster, L. A., Gerbig, D. G., Jr., Dyer, D. W., and Gibson, B. W. (1995) Identification of alcaligin as the siderophore produced by *Bordetella pertussis* and *B. bronchiseptica*, *J Bacteriol 177*, 1116-1118.

96. Gibson, F., and Magrath, D. I. (1969) The isolation and characterization of a hydroxamic acid (aerobactin) formed by *Aerobacter aerogenes* 62-I, *Biochim Biophys Acta 192*, 175-184.
97. Kadi, N., and Challis, G. L. (2009) Chapter 17. Siderophore biosynthesis a substrate specificity assay for nonribosomal peptide synthetase-independent siderophore synthetases involving trapping of acyl-adenylate intermediates with hydroxylamine, *Methods Enzymol 458*, 431-457.
98. Wilson, M. K., Abergel, R. J., Raymond, K. N., Arceneaux, J. E., and Byers, B. R. (2006) Siderophores of *Bacillus anthracis*, *Bacillus cereus*, and *Bacillus thuringiensis*, *Biochem Biophys Res Commun 348*, 320-325.
99. Barry, S. M., and Challis, G. L. (2009) Recent advances in siderophore biosynthesis, *Curr Opin Chem Biol 13*, 205-215.
100. Bouige, P., Laurent, D., Piloyan, L., and Dassa, E. (2002) Phylogenetic and functional classification of ATP-binding cassette (ABC) systems, *Curr Protein Pept Sci 3*, 541-559.
101. Davidson, A. L., and Chen, J. (2004) ATP-binding cassette transporters in bacteria, *Annu Rev Biochem 73*, 241-268.
102. Garmory, H. S., and Titball, R. W. (2004) ATP-binding cassette transporters are targets for the development of antibacterial vaccines and therapies, *Infect Immun 72*, 6757-6763.
103. Crouch, M. L., Castor, M., Karlinsey, J. E., Kalhorn, T., and Fang, F. C. (2008) Biosynthesis and IroC-dependent export of the siderophore salmochelin are essential for virulence of *Salmonella enterica* serovar Typhimurium, *Mol Microbiol 67*, 971-983.
104. Tseng, T. T., Gratwick, K. S., Kollman, J., Park, D., Nies, D. H., Goffeau, A., and Saier, M. H., Jr. (1999) The RND permease superfamily: an ancient, ubiquitous and diverse family that includes human disease and development proteins, *J Mol Microbiol Biotechnol 1*, 107-125.
105. Yu, E. W., Aires, J. R., and Nikaido, H. (2003) AcrB multidrug efflux pump of *Escherichia coli*: composite substrate-binding cavity of exceptional flexibility generates its extremely wide substrate specificity, *J Bacteriol 185*, 5657-5664.
106. Pao, S. S., Paulsen, I. T., and Saier, M. H., Jr. (1998) Major facilitator superfamily, *Microbiol Mol Biol Rev 62*, 1-34.
107. Furrer, J. L., Sanders, D. N., Hook-Barnard, I. G., and McIntosh, M. A. (2002) Export of the siderophore enterobactin in *Escherichia coli*: involvement of a 43 kDa membrane exporter, *Mol Microbiol 44*, 1225-1234.
108. Locher, K. P., Rees, B., Koebnik, R., Mitschler, A., Moulinier, L., Rosenbusch, J. P., and Moras, D. (1998) Transmembrane signaling across the ligand-gated FhuA receptor: crystal structures of free and ferrichrome-bound states reveal allosteric changes, *Cell 95*, 771-778.
109. Pierce, J. R., Pickett, C. L., and Earhart, C. F. (1983) Two fep genes are required for ferrienterochelin uptake in *Escherichia coli* K-12, *J Bacteriol 155*, 330-336.
110. Chakraborty, R., Storey, E., and van der Helm, D. (2007) Molecular mechanism of ferricsiderophore passage through the outer membrane receptor proteins of *Escherichia coli*, *Biometals 20*, 263-274.

111. Higgs, P. I., Larsen, R. A., and Postle, K. (2002) Quantification of known components of the *Escherichia coli* TonB energy transduction system: TonB, ExbB, ExbD and FepA, *Mol Microbiol 44*, 271-281.
112. Pawelek, P. D., Croteau, N., Ng-Thow-Hing, C., Khursigara, C. M., Moiseeva, N., Allaire, M., and Coulton, J. W. (2006) Structure of TonB in complex with FhuA, *E. coli* outer membrane receptor, *Science 312*, 1399-1402.
113. Chu, B. C., Peacock, R. S., and Vogel, H. J. (2007) Bioinformatic analysis of the TonB protein family, *Biometals 20*, 467-483.
114. Fischer, E., Strehlow, B., Hartz, D., and Braun, V. (1990) Soluble and membrane-bound ferrisiderophore reductases of *Escherichia coli* K-12, *Arch Microbiol 153*, 329-336.
115. Arceneaux, J. E., and Byers, B. R. (1980) Ferrisiderophore reductase activity in *Bacillus megaterium*, *J Bacteriol 141*, 715-721.
116. Gaines, C. G., Lodge, J. S., Arceneaux, J. E., and Byers, B. R. (1981) Ferrisiderophore reductase activity associated with an aromatic biosynthetic enzyme complex in *Bacillus subtilis*, *J Bacteriol 148*, 527-533.
117. Richens, D. T. (2005) Ligand substitution reactions at inorganic centers, *Chem Rev 105*, 1961-2002.
118. Wilkins, R. G. (1991) *Kinetics and mechanism of reactions of transition metal complexes*, 2nd thoroughly rev. ed., VCH Publishers, New York, N.Y.
119. Brickman, T. J., and McIntosh, M. A. (1992) Overexpression and purification of ferric enterobactin esterase from *Escherichia coli*. Demonstration of enzymatic hydrolysis of enterobactin and its iron complex, *J Biol Chem 267*, 12350-12355.
120. Mollmann, U., Heinisch, L., Bauernfeind, A., Kohler, T., and Ankel-Fuchs, D. (2009) Siderophores as drug delivery agents: application of the "Trojan Horse" strategy, *Biometals 22*, 615-624.
121. Budzikiewicz, H. (2001) Siderophore-antibiotic conjugates used as trojan horses against *Pseudomonas aeruginosa*, *Curr Top Med Chem 1*, 73-82.
122. Destoumieux-Garzon, D., Thomas, X., Santamaria, M., Goulard, C., Barthelemy, M., Boscher, B., Bessin, Y., Molle, G., Pons, A. M., Letellier, L., Peduzzi, J., and Rebuffat, S. (2003) Microcin E492 antibacterial activity: evidence for a TonB-dependent inner membrane permeabilization on *Escherichia coli*, *Mol Microbiol 49*, 1031-1041.
123. Patzer, S. I., Baquero, M. R., Bravo, D., Moreno, F., and Hantke, K. (2003) The colicin G, H and X determinants encode microcins M and H47, which might utilize the catecholate siderophore receptors FepA, Cir, Fiu and IroN, *Microbiology 149*, 2557-2570.
124. Lagos, R., Wilkens, M., Vergara, C., Cecchi, X., and Monasterio, O. (1993) Microcin E492 forms ion channels in phospholipid bilayer membrane, *FEBS Lett 321*, 145-148.
125. Pramanik, A., and Braun, V. (2006) Albomycin uptake via a ferric hydroxamate transport system of *Streptococcus pneumoniae* R6, *J Bacteriol 188*, 3878-3886.
126. Stefanska, A. L., Fulston, M., Houge-Frydrych, C. S., Jones, J. J., and Warr, S. R. (2000) A potent seryl tRNA synthetase inhibitor SB-217452 isolated from a *Streptomyces* species, *J Antibiot (Tokyo) 53*, 1346-1353.

127. Miethke, M., Bisseret, P., Beckering, C. L., Vignard, D., Eustache, J., and Marahiel, M. A. (2006) Inhibition of aryl acid adenylation domains involved in bacterial siderophore synthesis, *FEBS J 273*, 409-419.
128. Lin, H., Fischbach, M. A., Gatto, G. J., Jr., Liu, D. R., and Walsh, C. T. (2006) Bromoenterobactins as potent inhibitors of a pathogen-associated, siderophore-modifying C-glycosyltransferase, *J Am Chem Soc 128*, 9324-9325.
129. Pollack, J. R., and Neilands, J. B. (1970) Enterobactin, an iron transport compound from *Salmonella typhimurium*, *Biochem Biophys Res Commun 38*, 989-992.
130. O'Brien, I. G., and Gibson, F. (1970) The structure of enterochelin and related 2,3-dihydroxy-N-benzoylserine conjugates from *Escherichia coli*, *Biochim Biophys Acta 215*, 393-402.
131. Gehring, A. M., Mori, I., and Walsh, C. T. (1998) Reconstitution and characterization of the *Escherichia coli* enterobactin synthetase from EntB, EntE, and EntF, *Biochemistry 37*, 2648-2659.
132. Goetz, D. H., Holmes, M. A., Borregaard, N., Bluhm, M. E., Raymond, K. N., and Strong, R. K. (2002) The neutrophil lipocalin NGAL is a bacteriostatic agent that interferes with siderophore-mediated iron acquisition, *Mol Cell 10*, 1033-1043.
133. Leduc, D., Battesti, A., and Bouveret, E. (2007) The hotdog thioesterase EntH (YbdB) plays a role *in vivo* in optimal enterobactin biosynthesis by interacting with the ArCP domain of EntB, *J Bacteriol 189*, 7112-7126.
134. Chen, D., Wu, R., Bryan, T. L., and Dunaway-Mariano, D. (2009) In vitro kinetic analysis of substrate specificity in enterobactin biosynthetic lower pathway enzymes provides insight into the biochemical function of the hot dog-fold thioesterase EntH, *Biochemistry 48*, 511-513.
135. Crosa, J. H. (1989) Genetics and molecular biology of siderophore-mediated iron transport in bacteria, *Microbiol Rev 53*, 517-530.
136. Curtiss, R., and Neidhardt, F. C. (1996) *Escherichia coli and Salmonella : cellular and molecular biology*, 2nd ed., ASM Press, Washington, D.C.
137. Carpenter, B. M., Whitmire, J. M., and Merrell, D. S. (2009) This is not your mother's repressor: the complex role of fur in pathogenesis, *Infect Immun 77*, 2590-2601.
138. Herrmann, K. M. (1995) The shikimate pathway: early steps in the biosynthesis of aromatic compounds, *Plant Cell 7*, 907-919.
139. Gehring, A. M., Bradley, K. A., and Walsh, C. T. (1997) Enterobactin biosynthesis in *Escherichia coli*: isochorismate lyase (EntB) is a bifunctional enzyme that is phosphopantetheinylated by EntD and then acylated by EntE using ATP and 2,3-dihydroxybenzoate, *Biochemistry 36*, 8495-8503.
140. Liu, J., Duncan, K., and Walsh, C. T. (1989) Nucleotide sequence of a cluster of *Escherichia coli* enterobactin biosynthesis genes: identification of entA and purification of its product 2,3-dihydro-2,3-dihydroxybenzoate dehydrogenase, *J Bacteriol 171*, 791-798.
141. Rusnak, F., Faraci, W. S., and Walsh, C. T. (1989) Subcloning, expression, and purification of the enterobactin biosynthetic enzyme 2,3-dihydroxybenzoate-AMP

ligase: demonstration of enzyme-bound (2,3-dihydroxybenzoyl) adenylate product, *Biochemistry 28*, 6827-6835.
142. Lai, J. R., Fischbach, M. A., Liu, D. R., and Walsh, C. T. (2006) A protein interaction surface in nonribosomal peptide synthesis mapped by combinatorial mutagenesis and selection, *Proc Natl Acad Sci U S A 103*, 5314-5319.
143. Shaw-Reid, C. A., Kelleher, N. L., Losey, H. C., Gehring, A. M., Berg, C., and Walsh, C. T. (1999) Assembly line enzymology by multimodular nonribosomal peptide synthetases: the thioesterase domain of *E. coli* EntF catalyzes both elongation and cyclolactonization, *Chem Biol 6*, 385-400.
144. Ehmann, D. E., Shaw-Reid, C. A., Losey, H. C., and Walsh, C. T. (2000) The EntF and EntE adenylation domains of *Escherichia coli* enterobactin synthetase: sequestration and selectivity in acyl-AMP transfers to thiolation domain cosubstrates, *Proc Natl Acad Sci U S A 97*, 2509-2514.
145. Bleuel, C., Grosse, C., Taudte, N., Scherer, J., Wesenberg, D., Krauss, G. J., Nies, D. H., and Grass, G. (2005) TolC is involved in enterobactin efflux across the outer membrane of *Escherichia coli*, *J Bacteriol 187*, 6701-6707.
146. Ma, L., Kaserer, W., Annamalai, R., Scott, D. C., Jin, B., Jiang, X., Xiao, Q., Maymani, H., Massis, L. M., Ferreira, L. C., Newton, S. M., and Klebba, P. E. (2007) Evidence of ball-and-chain transport of ferric enterobactin through FepA, *J Biol Chem 282*, 397-406.
147. Devanathan, S., and Postle, K. (2007) Studies on colicin B translocation: FepA is gated by TonB, *Mol Microbiol 65*, 441-453.
148. Barnard, T. J., Watson, M. E., Jr., and McIntosh, M. A. (2001) Mutations in the *Escherichia coli* receptor FepA reveal residues involved in ligand binding and transport, *Mol Microbiol 41*, 527-536.
149. Dover, L. G., Evans, L. J., Fridd, S. L., Bainbridge, G., Raggett, E. M., and Lakey, J. H. (2000) Colicin pore-forming domains bind to *Escherichia coli* trimeric porins, *Biochemistry 39*, 8632-8637.
150. Graille, M., Mora, L., Buckingham, R. H., van Tilbeurgh, H., and de Zamaroczy, M. (2004) Structural inhibition of the colicin D tRNase by the tRNA-mimicking immunity protein, *EMBO J 23*, 1474-1482.
151. Payne, M. A., Igo, J. D., Cao, Z., Foster, S. B., Newton, S. M., and Klebba, P. E. (1997) Biphasic binding kinetics between FepA and its ligands, *J Biol Chem 272*, 21950-21955.
152. Newton, S. M., Allen, J. S., Cao, Z., Qi, Z., Jiang, X., Sprencel, C., Igo, J. D., Foster, S. B., Payne, M. A., and Klebba, P. E. (1997) Double mutagenesis of a positive charge cluster in the ligand-binding site of the ferric enterobactin receptor, FepA, *Proc Natl Acad Sci U S A 94*, 4560-4565.
153. Thulasiraman, P., Newton, S. M., Xu, J., Raymond, K. N., Mai, C., Hall, A., Montague, M. A., and Klebba, P. E. (1998) Selectivity of ferric enterobactin binding and cooperativity of transport in gram-negative bacteria, *J Bacteriol 180*, 6689-6696.
154. Buchanan, S. K., Smith, B. S., Venkatramani, L., Xia, D., Esser, L., Palnitkar, M., Chakraborty, R., van der Helm, D., and Deisenhofer, J. (1999) Crystal structure of the outer membrane active transporter FepA from *Escherichia coli*, *Nat Struct Biol 6*, 56-63.

155. Braun, V., Gaisser, S., Herrmann, C., Kampfenkel, K., Killmann, H., and Traub, I. (1996) Energy-coupled transport across the outer membrane of *Escherichia coli*: ExbB binds ExbD and TonB in vitro, and leucine 132 in the periplasmic region and aspartate 25 in the transmembrane region are important for ExbD activity, *J Bacteriol 178*, 2836-2845.
156. Postle, K. (1993) TonB protein and energy transduction between membranes, *J Bioenerg Biomembr 25*, 591-601.
157. Sprencel, C., Cao, Z., Qi, Z., Scott, D. C., Montague, M. A., Ivanoff, N., Xu, J., Raymond, K. M., Newton, S. M., and Klebba, P. E. (2000) Binding of ferric enterobactin by the *Escherichia coli* periplasmic protein FepB, *J Bacteriol 182*, 5359-5364.
158. Stephens, D. L., Choe, M. D., and Earhart, C. F. (1995) *Escherichia coli* periplasmic protein FepB binds ferrienterobactin, *Microbiology 141 (Pt 7)*, 1647-1654.
159. Ozenberger, B. A., Nahlik, M. S., and McIntosh, M. A. (1987) Genetic organization of multiple fep genes encoding ferric enterobactin transport functions in *Escherichia coli*, *J Bacteriol 169*, 3638-3646.
160. Abergel, R. J., Zawadzka, A. M., Hoette, T. M., and Raymond, K. N. (2009) Enzymatic hydrolysis of trilactone siderophores: where chiral recognition occurs in enterobactin and bacillibactin iron transport, *J Am Chem Soc 131*, 12682-12692.
161. Konopka, K., and Neilands, J. B. (1984) Effect of serum albumin on siderophore-mediated utilization of transferrin iron, *Biochemistry 23*, 2122-2127.
162. Abergel, R. J., Clifton, M. C., Pizarro, J. C., Warner, J. A., Shuh, D. K., Strong, R. K., and Raymond, K. N. (2008) The siderocalin/enterobactin interaction: a link between mammalian immunity and bacterial iron transport, *J Am Chem Soc 130*, 11524-11534.
163. Flower, D. R. (2000) Beyond the superfamily: the lipocalin receptors, *Biochim Biophys Acta 1482*, 327-336.
164. Hantke, K., Nicholson, G., Rabsch, W., and Winkelmann, G. (2003) Salmochelins, siderophores of *Salmonella enterica* and uropathogenic *Escherichia coli* strains, are recognized by the outer membrane receptor IroN, *Proc Natl Acad Sci U S A 100*, 3677-3682.
165. Muller, S. I., Valdebenito, M., and Hantke, K. (2009) Salmochelin, the long-overlooked catecholate siderophore of *Salmonella*, *Biometals 22*, 691-695.
166. Fischbach, M. A., Lin, H., Zhou, L., Yu, Y., Abergel, R. J., Liu, D. R., Raymond, K. N., Wanner, B. L., Strong, R. K., Walsh, C. T., Aderem, A., and Smith, K. D. (2006) The pathogen-associated *iroA* gene cluster mediates bacterial evasion of lipocalin 2, *Proc Natl Acad Sci U S A 103*, 16502-16507.
167. Lin, H., Fischbach, M. A., Liu, D. R., and Walsh, C. T. (2005) In vitro characterization of salmochelin and enterobactin trilactone hydrolases IroD, IroE, and Fes, *J Am Chem Soc 127*, 11075-11084.
168. Fischbach, M. A., Lin, H., Liu, D. R., and Walsh, C. T. (2005) In vitro characterization of IroB, a pathogen-associated C-glycosyltransferase, *Proc Natl Acad Sci U S A 102*, 571-576.

169. Hofsteenge, J., Blommers, M., Hess, D., Furmanek, A., and Miroshnichenko, O. (1999) The four terminal components of the complement system are C-mannosylated on multiple tryptophan residues, *J Biol Chem 274*, 32786-32794.
170. Hartmann, S., and Hofsteenge, J. (2000) Properdin, the positive regulator of complement, is highly C-mannosylated, *J Biol Chem 275*, 28569-28574.
171. Krieg, J., Glasner, W., Vicentini, A., Doucey, M. A., Loffler, A., Hess, D., and Hofsteenge, J. (1997) C-Mannosylation of human RNase 2 is an intracellular process performed by a variety of cultured cells, *J Biol Chem 272*, 26687-26692.
172. Feldmann, F., Sorsa, L. J., Hildinger, K., and Schubert, S. (2007) The salmochelin siderophore receptor IroN contributes to invasion of urothelial cells by extraintestinal pathogenic *Escherichia coli* in vitro, *Infect Immun 75*, 3183-3187.
173. Zhu, M., Valdebenito, M., Winkelmann, G., and Hantke, K. (2005) Functions of the siderophore esterases IroD and IroE in iron-salmochelin utilization, *Microbiology 151*, 2363-2372.
174. Liu, J., Quinn, N., Berchtold, G. A., and Walsh, C. T. (1990) Overexpression, purification, and characterization of isochorismate synthase (EntC), the first enzyme involved in the biosynthesis of enterobactin from chorismate, *Biochemistry 29*, 1417-1425.
175. Dahm, C., Muller, R., Schulte, G., Schmidt, K., and Leistner, E. (1998) The role of isochorismate hydroxymutase genes entC and menF in enterobactin and menaquinone biosynthesis in *Escherichia coli*, *Biochim Biophys Acta 1425*, 377-386.
176. Subramaniapillai Kolappan, Jacque Zwahlen, Rong Zhou, James J. Truglio, Peter J. Tonge, and Caroline Kisker. (2007) Lysine 190 Is the Catalytic Base in MenF, the Menaquinone-Specific Isochorismate Synthase from *Escherichia coli*: Implications for an Enzyme Family, *Biochemistry 46* (4), 946–953.
177. Sridharan, S., Howard, N., Kerbarh, O., Blaszczyk, M., Abell, C., and Blundell, T. L. (2010) Crystal structure of *Escherichia coli* enterobactin-specific isochorismate synthase (EntC) bound to its reaction product isochorismate: implications for the enzyme mechanism and differential activity of chorismate-utilizing enzymes, *J Mol Biol 397*, 290-300.
178. Woodrow, G. C., Young, I. G., and Gibson, F. (1975) Mu-induced polarity in the *Escherichia coli* K-12 ent gene cluster: evidence for a gene (entG) involved in the biosynthesis of enterochelin, *J Bacteriol 124*, 1-6.
179. Nahlik, M. S., Fleming, T. P., and McIntosh, M. A. (1987) Cluster of genes controlling synthesis and activation of 2,3-dihydroxybenzoic acid in production of enterobactin in *Escherichia coli*, *J Bacteriol 169*, 4163-4170.
180. Staab, J. F., and Earhart, C. F. (1990) EntG activity of *Escherichia coli* enterobactin synthetase, *J Bacteriol 172*, 6403-6410.
181. Drake, E. J., Nicolai, D. A., and Gulick, A. M. (2006) Structure of the EntB multidomain nonribosomal peptide synthetase and functional analysis of its interaction with the EntE adenylation domain, *Chem Biol 13*, 409-419.
182. Sakaitani, M., Rusnak, F., Quinn, N. R., Tu, C., Frigo, T. B., Berchtold, G. A., and Walsh, C. T. (1990) Mechanistic studies on trans-2,3-dihydro-2,3-dihydroxybenzoate dehydrogenase (EntA) in the biosynthesis of the iron chelator enterobactin, *Biochemistry 29*, 6789-6798.

183. Sundlov, J. A., Garringer, J. A., Carney, J. M., Reger, A. S., Drake, E. J., Duax, W. L., and Gulick, A. M. (2006) Determination of the crystal structure of EntA, a 2,3-dihydro-2,3-dihydroxybenzoic acid dehydrogenase from *Escherichia coli*, *Acta Crystallogr D Biol Crystallogr 62*, 734-740.
184. May, J. J., Kessler, N., Marahiel, M. A., and Stubbs, M. T. (2002) Crystal structure of DhbE, an archetype for aryl acid activating domains of modular nonribosomal peptide synthetases, *Proc Natl Acad Sci U S A 99*, 12120-12125.
185. Saraste, M., Sibbald, P. R., and Wittinghofer, A. (1990) The P-loop--a common motif in ATP- and GTP-binding proteins, *Trends Biochem Sci 15*, 430-434.
186. Callahan, B. P., Lomino, J. V., and Wolfenden, R. (2006) Nanomolar inhibition of the enterobactin biosynthesis enzyme, EntE: synthesis, substituent effects, and additivity, *Bioorg Med Chem Lett 16*, 3802-3805.
187. Neres, J., Wilson, D. J., Celia, L., Beck, B. J., and Aldrich, C. C. (2008) Aryl acid adenylating enzymes involved in siderophore biosynthesis: fluorescence polarization assay, ligand specificity, and discovery of non-nucleoside inhibitors via high-throughput screening, *Biochemistry 47*, 11735-11749.
188. Sikora, A. L., Cahill, S. M., and Blanchard, J. S. (2009) Enterobactin synthetase-catalyzed formation of P(1),P(3)-diadenosine-5'-tetraphosphate, *Biochemistry 48*, 10827-10829.
189. Sikora, A. L., Wilson, D. J., Aldrich, C. C., and Blanchard, J. S. (2010) Kinetic and inhibition studies of dihydroxybenzoate-AMP ligase from *Escherichia coli*, *Biochemistry 49*, 3648-3657.
190. Reichert, J., Sakaitani, M., and Walsh, C. T. (1992) Characterization of EntF as a serine-activating enzyme, *Protein Sci 1*, 549-556.
191. Roche, E. D., and Walsh, C. T. (2003) Dissection of the EntF condensation domain boundary and active site residues in nonribosomal peptide synthesis, *Biochemistry 42*, 1334-1344.
192. Zhou, Z., Lai, J. R., and Walsh, C. T. (2006) Interdomain communication between the thiolation and thioesterase domains of EntF explored by combinatorial mutagenesis and selection, *Chem Biol 13*, 869-879.
193. Frueh, D. P., Arthanari, H., Koglin, A., Vosburg, D. A., Bennett, A. E., Walsh, C. T., and Wagner, G. (2008) Dynamic thiolation-thioesterase structure of a non-ribosomal peptide synthetase, *Nature 454*, 903-906.
194. Coderre, P. E., and Earhart, C. F. (1989) The entD gene of the *Escherichia coli* K12 enterobactin gene cluster, *J Gen Microbiol 135*, 3043-3055.
195. Lambalot, R. H., Gehring, A. M., Flugel, R. S., Zuber, P., LaCelle, M., Marahiel, M. A., Reid, R., Khosla, C., and Walsh, C. T. (1996) A new enzyme superfamily - the phosphopantetheinyl transferases, *Chem Biol 3*, 923-936.
196. Lambalot, R. H., and Walsh, C. T. (1995) Cloning, overproduction, and characterization of the *Escherichia coli* holo-acyl carrier protein synthase, *J Biol Chem 270*, 24658-24661.
197. Lai, J. R., Fischbach, M. A., Liu, D. R., and Walsh, C. T. (2006) Localized protein interaction surfaces on the EntB carrier protein revealed by combinatorial mutagenesis and selection, *J Am Chem Soc 128*, 11002-11003.

198. Nahlik, M. S., Brickman, T. J., Ozenberger, B. A., and McIntosh, M. A. (1989) Nucleotide sequence and transcriptional organization of the *Escherichia coli* enterobactin biosynthesis cistrons entB and entA, *J Bacteriol 171*, 784-790.
199. Ozenberger, B. A., Brickman, T. J., and McIntosh, M. A. (1989) Nucleotide sequence of *Escherichia coli* isochorismate synthetase gene entC and evolutionary relationship of isochorismate synthetase and other chorismate-utilizing enzymes, *J Bacteriol 171*, 775-783.
200. Guo, Z. F., Sun, Y., Zheng, S., and Guo, Z. (2009) Preferential hydrolysis of aberrant intermediates by the type II thioesterase in *Escherichia coli* nonribosomal enterobactin synthesis: substrate specificities and mutagenic studies on the active-site residues, *Biochemistry 48*, 1712-1722.
201. Jaroszewski, L., Rychlewski, L., Li, Z., Li, W., and Godzik, A. (2005) FFAS03: a server for profile--profile sequence alignments, *Nucleic Acids Res 33*, W284-288.
202. Sali, A., and Blundell, T. L. (1993) Comparative protein modelling by satisfaction of spatial restraints, *J Mol Biol 234*, 779-815.
203. Kleywegt, G. J. (1999) Experimental assessment of differences between related protein crystal structures, *Acta Crystallogr D Biol Crystallogr 55*, 1878-1884.
204. Willard, L., Ranjan, A., Zhang, H., Monzavi, H., Boyko, R. F., Sykes, B. D., and Wishart, D. S. (2003) VADAR: a web server for quantitative evaluation of protein structure quality, *Nucleic Acids Res 31*, 3316-3319.
205. Kitagawa, M., Ara, T., Arifuzzaman, M., Ioka-Nakamichi, T., Inamoto, E., Toyonaga, H., and Mori, H. (2005) Complete set of ORF clones of *Escherichia coli* ASKA library (a complete set of E. coli K-12 ORF archive): unique resources for biological research, *DNA Res 12*, 291-299.
206. Khalil, S., and Pawelek, P. D. (2009) Ligand-induced conformational rearrangements promote interaction between the *Escherichia coli* enterobactin biosynthetic proteins EntE and EntB, *J Mol Biol 393*, 658-671.
207. Dam, T. (2005) Siderophores--potential candidate in the therapy of neonatal meningitis, *J Med Microbiol 54*, 613.
208. Wiles, T. J., Kulesus, R. R., and Mulvey, M. A. (2008) Origins and virulence mechanisms of uropathogenic *Escherichia coli*, *Exp Mol Pathol 85*, 11-19.
209. Flo, T. H., Smith, K. D., Sato, S., Rodriguez, D. J., Holmes, M. A., Strong, R. K., Akira, S., and Aderem, A. (2004) Lipocalin 2 mediates an innate immune response to bacterial infection by sequestrating iron, *Nature 432*, 917-921.
210. Braun, V., and Killmann, H. (1999) Bacterial solutions to the iron-supply problem, *Trends Biochem Sci 24*, 104-109.
211. Stojiljkovic, I., and Hantke, K. (1995) Functional domains of the *Escherichia coli* ferric uptake regulator protein (Fur), *Mol Gen Genet 247*, 199-205.
212. Sheikh, M. A., and Taylor, G. L. (2009) Crystal structure of the *Vibrio cholerae* ferric uptake regulator (Fur) reveals insights into metal co-ordination, *Mol Microbiol 72*, 1208-1220.
213. Rusnak, F., Liu, J., Quinn, N., Berchtold, G. A., and Walsh, C. T. (1990) Subcloning of the enterobactin biosynthetic gene entB: expression, purification, characterization, and substrate specificity of isochorismatase, *Biochemistry 29*, 1425-1435.

214. Staab, J. F., Elkins, M. F., and Earhart, C. F. (1989) Nucleotide sequence of the *Escherichia coli* entE gene, *FEMS Microbiol Lett 50*, 15-19.
215. Rusnak, F., Sakaitani, M., Drueckhammer, D., Reichert, J., and Walsh, C. T. (1991) Biosynthesis of the *Escherichia coli* siderophore enterobactin: sequence of the entF gene, expression and purification of EntF, and analysis of covalent phosphopantetheine, *Biochemistry 30*, 2916-2927.
216. Gavin, A. C., Bosche, M., Krause, R., Grandi, P., Marzioch, M., Bauer, A., Schultz, J., Rick, J. M., Michon, A. M., Cruciat, C. M., Remor, M., Hofert, C., Schelder, M., Brajenovic, M., Ruffner, H., Merino, A., Klein, K., Hudak, M., Dickson, D., Rudi, T., Gnau, V., Bauch, A., Bastuck, S., Huhse, B., Leutwein, C., Heurtier, M. A., Copley, R. R., Edelmann, A., Querfurth, E., Rybin, V., Drewes, G., Raida, M., Bouwmeester, T., Bork, P., Seraphin, B., Kuster, B., Neubauer, G., and Superti-Furga, G. (2002) Functional organization of the yeast proteome by systematic analysis of protein complexes, *Nature 415*, 141-147.
217. Devos, D., and Russell, R. B. (2007) A more complete, complexed and structured interactome, *Curr Opin Struct Biol 17*, 370-377.
218. Bagnasco, L., Tortolina, L., Biasotti, B., Castagnino, N., Ponassi, R., Tomati, V., Nieddu, E., Stier, G., Malacarne, D., and Parodi, S. (2007) Inhibition of a protein-protein interaction between INI1 and c-Myc by small peptidomimetic molecules inspired by Helix-1 of c-Myc: identification of a new target of potential antineoplastic interest, *FASEB J 21*, 1256-1263.
219. Wells, J. A., and McClendon, C. L. (2007) Reaching for high-hanging fruit in drug discovery at protein-protein interfaces, *Nature 450*, 1001-1009.
220. Philo, J. S. (2006) Improved methods for fitting sedimentation coefficient distributions derived by time-derivative techniques, *Anal Biochem 354*, 238-246.
221. Schuck, P. (2003) On the analysis of protein self-association by sedimentation velocity analytical ultracentrifugation, *Anal Biochem 320*, 104-124.
222. Garcia De La Torre, J., Huertas, M. L., and Carrasco, B. (2000) Calculation of hydrodynamic properties of globular proteins from their atomic-level structure, *Biophys J 78*, 719-730.
223. Hayes, D.B., Laue, T., and Philo, J. (1995) *Sednterp: Sedimentation Interpretation Program*, Alliance Protein Laboratories, Thousand Oaks, Ca.
224. Sousa, E. H., Garay, P. A., Tinianow, J. N., and Gerber, N. C. (2006) Development of a spectrophotometric assay for cyclase activity, *Anal Biochem 348*, 57-63.
225. Lakowicz, J. R. (2006) *Principles of fluorescence spectroscopy*, 3rd ed., Springer, New York.
226. Stafford, W. F. (2000) Analysis of reversibly interacting macromolecular systems by time derivative sedimentation velocity, *Methods Enzymol 323*, 302-325.
227. Cole, J. L. (1996) Characterization of human cytomegalovirus protease dimerization by analytical centrifugation, *Biochemistry 35*, 15601-15610.
228. Srere, P. A. (1987) Complexes of sequential metabolic enzymes, *Annu Rev Biochem 56*, 89-124.
229. Jorgensen, K., Rasmussen, A. V., Morant, M., Nielsen, A. H., Bjarnholt, N., Zagrobelny, M., Bak, S., and Moller, B. L. (2005) Metabolon formation and

metabolic channeling in the biosynthesis of plant natural products, *Curr Opin Plant Biol 8*, 280-291.
230. Durek, P., and Walther, D. (2008) The integrated analysis of metabolic and protein interaction networks reveals novel molecular organizing principles, *BMC Syst Biol 2*, 100.
231. An, S., Kumar, R., Sheets, E. D., and Benkovic, S. J. (2008) Reversible compartmentalization of de novo purine biosynthetic complexes in living cells, *Science 320*, 103-106.
232. Fukushima, T., Decker, R. V., Anderson, W. M., and Spivey, H. O. (1989) Substrate channeling of NADH and binding of dehydrogenases to complex I, *J Biol Chem 264*, 16483-16488.
233. Spivey, H. O., and Ovadi, J. (1999) Substrate channeling, *Methods 19*, 306-321.
234. Mossialos, D., and Amoutzias, G. D. (2009) Role of siderophores in cystic fibrosis pathogenesis: foes or friends?, *Int J Med Microbiol 299*, 87-98.
235. Lawlor, M. S., O'Connor, C., and Miller, V. L. (2007) Yersiniabactin is a virulence factor for *Klebsiella pneumoniae* during pulmonary infection, *Infect Immun 75*, 1463-1472.
236. Lamont, I. L., Beare, P. A., Ochsner, U., Vasil, A. I., and Vasil, M. L. (2002) Siderophore-mediated signaling regulates virulence factor production in *Pseudomonas aeruginosa*, *Proc Natl Acad Sci U S A 99*, 7072-7077.
237. Caza, M., Lepine, F., Milot, S., and Dozois, C. M. (2008) Specific roles of the iroBCDEN genes in virulence of an avian pathogenic *Escherichia coli* O78 strain and in production of salmochelins, *Infect Immun 76*, 3539-3549.
238. Andrews, S. C., Robinson, A. K., and Rodriguez-Quinones, F. (2003) Bacterial iron homeostasis, *FEMS Microbiol Rev 27*, 215-237.
239. Pollack, J. R., Ames, B. N., and Neilands, J. B. (1970) Iron transport in *Salmonella typhimurium*: mutants blocked in the biosynthesis of enterobactin, *J Bacteriol 104*, 635-639.
240. Perry, R. D., and San Clemente, C. L. (1979) Siderophore synthesis in *Klebsiella pneumoniae* and *Shigella sonnei* during iron deficiency, *J Bacteriol 140*, 1129-1132.
241. Smith, K. D. (2007) Iron metabolism at the host pathogen interface: lipocalin 2 and the pathogen-associated iroA gene cluster, *Int J Biochem Cell Biol 39*, 1776-1780.
242. Sofia Khalil and Peter D. Pawelek (2010) A Protein-protein interaction facilitates conformational remodeling of the *Escherichia coli* 2,3-dihydroxybenzoate-AMP ligase (EntE) active site by 2,3-dihydro-2,3-dihydroxybenzoate dehydrogenase (EntA) (submitted to *Biochemisty*).
243. Rodi, D. J., Soares, A. S., and Makowski, L. (2002) Quantitative assessment of peptide sequence diversity in M13 combinatorial peptide phage display libraries, *J Mol Biol 322*, 1039-1052.
244. Datsenko, K. A., and Wanner, B. L. (2000) One-step inactivation of chromosomal genes in *Escherichia coli* K-12 using PCR products, *Proc Natl Acad Sci U S A 97*, 6640-6645.
245. Quadri, L. E., Sello, J., Keating, T. A., Weinreb, P. H., and Walsh, C. T. (1998) Identification of a *Mycobacterium tuberculosis* gene cluster encoding the

biosynthetic enzymes for assembly of the virulence-conferring siderophore mycobactin, *Chem Biol 5*, 631-645.
246. Quadri, L. E., Keating, T. A., Patel, H. M., and Walsh, C. T. (1999) Assembly of the *Pseudomonas aeruginosa* nonribosomal peptide siderophore pyochelin: In vitro reconstitution of aryl-4, 2-bisthiazoline synthetase activity from PchD, PchE, and PchF, *Biochemistry 38*, 14941-14954.
247. Gehring, A. M., Mori, I. I., Perry, R. D., and Walsh, C. T. (1998) The nonribosomal peptide synthetase HMWP2 forms a thiazoline ring during biogenesis of yersiniabactin, an iron-chelating virulence factor of *yersinia pestis*, *Biochemistry 37*, 17104.
248. Ferreras, J. A., Ryu, J. S., Di Lello, F., Tan, D. S., and Quadri, L. E. (2005) Small-molecule inhibition of siderophore biosynthesis in *Mycobacterium tuberculosis* and *Yersinia pestis*, *Nat Chem Biol 1*, 29-32.
249. Neres, J., Labello, N. P., Somu, R. V., Boshoff, H. I., Wilson, D. J., Vannada, J., Chen, L., Barry, C. E., 3rd, Bennett, E. M., and Aldrich, C. C. (2008) Inhibition of siderophore biosynthesis in *Mycobacterium tuberculosis* with nucleoside bisubstrate analogues: structure-activity relationships of the nucleobase domain of 5'-O-[N-(salicyl)sulfamoyl]adenosine, *J Med Chem 51*, 5349-5370.
250. Weinberg, R. L., Veprintsev, D. B., and Fersht, A. R. (2004) Cooperative binding of tetrameric p53 to DNA, *J Mol Biol 341*, 1145-1159.
251. Tsuji, S. Y., Cane, D. E., and Khosla, C. (2001) Selective protein-protein interactions direct channeling of intermediates between polyketide synthase modules, *Biochemistry 40*, 2326-2331.
252. Winkel, B. S. (2004) Metabolic channeling in plants, *Annu Rev Plant Biol 55*, 85-107.
253. Zhang, Y., Morar, M., and Ealick, S. E. (2008) Structural biology of the purine biosynthetic pathway, *Cell Mol Life Sci 65*, 3699-3724.
254. Terawaki, S., Tanaka, Y., Nagakura, T., Hayashi, T., Shibayama, S., Muroi, K., Okazaki, T., Mikami, B., Garboczi, D. N., Honjo, T., and Minato, N. (2007) Specific and high-affinity binding of tetramerized PD-L1 extracellular domain to PD-1-expressing cells: possible application to enhance T cell function, *Int Immunol 19*, 881-890.
255. Liang, S. C., Latchman, Y. E., Buhlmann, J. E., Tomczak, M. F., Horwitz, B. H., Freeman, G. J., and Sharpe, A. H. (2003) Regulation of PD-1, PD-L1, and PD-L2 expression during normal and autoimmune responses, *Eur J Immunol 33*, 2706-2716.
256. Weissman, K. J., Hong, H., Popovic, B., and Meersman, F. (2006) Evidence for a protein-protein interaction motif on an acyl carrier protein domain from a modular polyketide synthase, *Chem Biol 13*, 625-636.
257. Bren, A., and Eisenbach, M. (2000) How signals are heard during bacterial chemotaxis: protein-protein interactions in sensory signal propagation, *J Bacteriol 182*, 6865-6873.
258. Carter, D. M., Miousse, I. R., Gagnon, J. N., Martinez, E., Clements, A., Lee, J., Hancock, M. A., Gagnon, H., Pawelek, P. D., and Coulton, J. W. (2006) Interactions between TonB from *Escherichia coli* and the periplasmic protein FhuD, *J Biol Chem 281*, 35413-35424.

259. Cegelski, L., Marshall, G. R., Eldridge, G. R., and Hultgren, S. J. (2008) The biology and future prospects of antivirulence therapies, *Nat Rev Microbiol 6*, 17-27.
260. Larsson, A., Johansson, S. M., Pinkner, J. S., Hultgren, S. J., Almqvist, F., Kihlberg, J., and Linusson, A. (2005) Multivariate design, synthesis, and biological evaluation of peptide inhibitors of FimC/FimH protein-protein interactions in uropathogenic *Escherichia coli*, *J Med Chem 48*, 935-945.
261. Arkin, M. R., Randal, M., DeLano, W. L., Hyde, J., Luong, T. N., Oslob, J. D., Raphael, D. R., Taylor, L., Wang, J., McDowell, R. S., Wells, J. A., and Braisted, A. C. (2003) Binding of small molecules to an adaptive protein-protein interface, *Proc Natl Acad Sci U S A 100*, 1603-1608.
262. Arkin, M. R., and Wells, J. A. (2004) Small-molecule inhibitors of protein-protein interactions: progressing towards the dream, *Nat Rev Drug Discov 3*, 301-317.